

UNIVERSITY OF BELGRADE
FACULTY OF PHYSICS

Jelena R. Pešić

**INVESTIGATION OF SUPERCONDUCTIVITY
IN GRAPHENE AND RELATED MATERIALS
USING AB-INITIO METHODS**

dissertation

Belgrade, 2017

UNIVERZITET U BEOGRADU
FIZIČKI FAKULTET

Jelena R. Pešić

**ISTRAŽIVANJE SUPERPROVODNOSTI U
GRAFENU I SLIČNIM MATERIJALIMA
KORIŠĆENJEM AB-INITIO METODA**

disertacija

Beograd, 2017

Mentor:

dr Radoš Gajić,
naučni savetnik,
Institut za fiziku, Univerzitet u Beogradu

Članovi komisije:

dr Kurt Hingerl
professor
Johannes Kepler University, Linz , Austria

dr Ivanka Milošević
redovni profesor
Fizi ki fakultet, Univerzitet u Beogradu

dr Milan Knežević
redovni profesor
Fizi ki fakultet, Univerzitet u Beogradu

dr Djordje Spasojević
vanredni profesor
Fizi ki fakultet, Univerzitet u Beogradu

dr Zoran Popović
naučni savetnik
INN Vin a, Univerzitet u Beogradu

Datum odbrane: 4. Decembar 2017

Acknowledgements

First I would like to thank my mentor Professor dr. Radoš Gajić. His continuous guidance, and trust have not only helped me to complete my thesis work, but also led me the way to be an open-minded scientist. His passion and dedication, as well as his high standards toward science have deeply impacted me, which would be a great benefit for my future academic career. I've learned not only about science, solid state physics, superconductivity and nanomaterials but as well about creative thinking. I consider myself fortunate to graduate under his guidance.

I am especially grateful to my colleague dr. Vladimir Damljanović, for great cooperation and support. His commitment and patience were invaluable to me. I am thankful for advice that originated from applications of symmetry to phonon- and band-structure calculations and for reading and commenting my thesis.

I am rather grateful to Professor dr. Kurt Hingerl from Johannes Kepler University, Linz, Austria for providing me access to their computational resources and for helpful discussions, comments and suggestions. I was very fortunate to coauthor several papers with Professor Hingerl and to engage in writing of few international projects of cooperation with him and his group. The long-term cooperation that exists between our groups was of a great value to me.

Also am very grateful to my colleagues: dr. Aleksandar Matković for teaching me the process of the micromechanical exfoliation and for many useful discussions about physics of the graphene, dr. Borislav Vasić and dr. Marko Spasenović for cooperation on several experimental publications and many helpful comments that improved my understanding of experimental physics, and dr. Igor Popov for many interesting explanations of fine particularities of DFT calculations. They all together have helped me many times during my studies through comments, advices, and ideas. I am grateful to dr. Aleksandar Milosavljević for including me in cooperation with University of Potsdam and their joint project on DNA origami structures.

I am grateful to Professor dr. Milivoj R. Belić from Texas A&M University at Qatar, for helpful discussions, comments and suggestions and for managing of QNRF project in past few years.

I would like to thank my colleagues and fellow PhD students Jasna Vujin, Tijana Tomašević-Ilić and Andrijana Šolajić who I am sharing with, not only, scientific work but PhD student life.

Also, I would like to thank all the colleagues from Graphene Laboratory as well

as, from the Center of Solid State Physics and New Materials, for their help and for creating a friendly work environment. Specially I would like to express my gratitude to the head of the center of Solid State Physics and New Materials Professor dr. Zoran V. Popović.

I would like to thank Professor dr. Nebojša Romčević for his support and for all the help in managing the industry project "Graphene based functional inks and printing of Radio-frequency identification tags". I would like to thank Professor dr. Radomir Žikić for support and wonderful cooperation throughout all time of my research at Institute of Physics. I was engaged in writing several projects with Professor Žikić and his group which was great experience. Working with him and his group was always enlightening and pleasant experience.

I would like to thank members of committee, Professor dr. Ivanka Milošević, Professor dr. Milan Knežević, Professor dr. Zoran S. Popović and Professor dr. Djordje Spasojević.

I would like to thank Professor dr. Ilko Bald and dr. Julia Prinz from University of Potsdam, Germany. A fruitful collaboration between our research groups have resulted with several joint publications on graphene and organic nanostructures.

I am grateful to Professor dr. Emmanuele Cappeluti, Istituto dei Sistemi Complessi CNR, Italy for interesting discussions and advices about superconductivity. The ongoing cooperation with Professor Cappeluti was of great value to me and his passion for understanding superconductivity from both theoretical and experimental aspect, was always great inspiration to me.

I would like to thank Professor dr. Ivanka Holclajtner-Antunović for providing Raman spectra (Figures 1.10 and 1.11).

I would like to acknowledge financial support by the Serbian Ministry of Science through Projects OI 171005 and by Industry project "Graphene based functional inks and printing of Radio-frequency identification tags" (in period 2014-2015) and by project of bilateral cooperation with Republic of China titled "Crystal Growth and peculiar physics of normal state of ReBCO crystals" and by Qatar National Research Foundation through Project "Intercalated graphene: effects of substrates on functionalities", NPRP 7-665-1-125.

Podaci o doktorskoj disertaciji

Naslov doktorske disertacije

”ISTRAŽIVANJE SUPERPROVODNOSTI U GRAFENU I SLIČNIM MATERI-
JALIMA KORIŠĆENJEM AB-INITIO METODA”

Rezime

Disertacija istražuje superprovodnost u dopiranom grafenu i monosloju magnezijum-diborida, novog superprovodnog 2D materijala. Za sve proračune su korišćenje ab-initio tehnike zasnovane na teoriji funkcionala gustine. Pokazano je da primenom dvo-osovinskog istezanja elektron-fononska interakcija se može prilagođavati u grafenu dopiranom litijumom tako da se kritična temperatura može povećati do 29 K. Vibracione osobine grafena dopiranog litijumom i drugim alkalnim metalima (Ba i Ca) su detaljno proučavane da bi se bolje razumelo elektron-fononsko kuplovanje i poreklo superprovodnosti u grafenu. Takodje slika o grafenu dopiranom litijumom je kompletirana istraživanjem optičkih osobina ovog materiala.

Inspirisani strukturnom i elektronskom sličnošću sa grafitom i grafenom, niskodimenzioni limit magnezijum-diborida je proučavan. Njegove elektronske i fononske osobine su detaljno diskutovane. Pokazano je da je MgB_2 u monosloju superprovodan na 18 K i da isto kao kod grafena, na elektron-fononsku interakciju se može uticati primenom dvo-osovinskog naprezanja, čime se povećava kritična temperatura do 31 K. Rezultati prikazani u ovoj disertaciji ne samo da izučavaju superprovodnost u grafenu i grafenu-sličnim materijalima već opštije izučavaju pitanja i perspektive istraživanja superprovodnosti u nisko-dimenzionim materijalima korišćenjem ab-initio metoda.

U disertaciji uz ab-initio izučavanje materijala, tehničko pitanje proračuna se takodje diskutuje. Testirano je korišćenje hardverskog ubrzanja, grafičkih procesora, sa posebnim fokusom na proračune nisko-dimensionih materijala.

Dodatno je predstavljena sinteza dvo-dimenzionih materijala primenom tehnike mikromehaničke eksfolijacije. Prikazano je kako uzorci dobijeni na ovaj način mogu se koristiti za različite primene, a demonstrirano je kako se grafen može koristiti kao zaštitni sloj za organske nanostrukture. Uzorci dobijeni mikromehaničkom eksfoli-

jacijom su najvišeg kvaliteta i ne samo da mogu da se koriste za aplikacije, već i za fundamentalna istraživanja (npr superprovodnost).

Ključne reči:

grafen, superprovodnost, elektron-fononska interakcija, grafenu slični materijali, DFT, magnezijum-diborid, nisko-dimenzioni materijali, GPU ubrzanje, GPGPU

Naučna oblast: Fizika

Uža naučna oblast: Fizika kondenzovane materije

UDK broj: - 538.9

Information about the thesis

Title of the thesis

”INVESTIGATION OF SUPERCONDUCTIVITY IN GRAPHENE AND RELATED MATERIALS USING AB-INITIO METHODS”

Abstract

The dissertation investigates the superconductivity in doped graphene and magnesium-diboride monolayer as a novel two-dimensional superconducting material. The ab-initio techniques based on the density functional theory were employed for all the studies. It is demonstrated that by application of equibiaxial strain the electron-phonon interaction in graphene doped with Lithium can be tuned and the critical temperature can be significantly enhanced, up to 29K. The extensive focus is devoted to vibrational properties Li and other alkali metal (Ba and Ca) doped graphene in order to get better understanding of electron-phonon coupling and origin of superconductivity in graphene. Furthermore, the study of optical properties of the Li-doped graphene completes the detailed picture of this material.

Inspired with the structural and electronic similarity with graphite and graphene, low-dimensional limit of magnesium-diboride has been investigated. Its electron and phonon properties are thoroughly discussed. It is demonstrated MgB_2 in monolayer is superconducting at 18K and, same as in graphene, the electron-phonon interaction can be tuned by application of the biaxial strain, increasing the critical temperature up to 31K. The results presented in this dissertation not only discuss superconductivity in graphene and related materials but more general issues and perspectives of superconductivity in low-dimensional materials studied with ab-initio methods.

In the dissertation along with ab-initio study of material, the more technical issue of calculations is addressed. The use of hardware acceleration, namely the graphic processors, is tested with the focus on the specificities of low-dimensional materials study.

In addition, the synthesis of two-dimensional materials using micromechanical exfoliation technique is presented in the dissertation. It is also demonstrated how the samples produced this way can be further used in various applications, namely it is

demonstrated how graphene can be used as the protective coating for the organic nanostructures. Samples obtained from micromechanical exfoliation have the highest possible quality and can be used, not only for applications, but for fundamental research (i.e. superconductivity).

Keywords:

graphene, superconductivity, electron-phonon interaction, graphene-related materials, ab-initio, DFT, magnesium-diboride, low-dimensional materials, GPU acceleration, GPGPU

Scientific field: Physics

Subfield: Condensed Matter Physics

UDK number: - 538.9

Contents

Acknowledgements	v
Podaci o doktorskoj disertaciji	vii
Information about the thesis	ix
Table of contents	xi
Preface	1
1. GRAPHENE AND RELATED MATERIALS	3
1.1. Introduction to Graphene	3
1.2. Structure and Electronic Properties of Graphene	4
1.3. Phonons and Electron-Phonon Interaction in Graphene	15
1.4. Other 2D Materials	23
2. SUPERCONDUCTIVITY IN 2D MATERIALS	28
2.1. Brief History of Superconductivity	28
2.2. BCS Theory and Eliashberg Formalism	30
2.2.1. BCS theory	30
2.2.2. The Migdal-Eliashberg Theory, BCS Limit and the Allen-Dynes-McMillan Formula	40
2.3. Superconductivity in 2D Materials	45
2.4. Superconductivity in Graphene and Related Materials	53
2.5. Superconductivity in Magnesium-diboride Family	58
3. AB-INITIO METHODS	61
3.1. Introduction to Ab-initio Methods	61
3.2. The Electronic Structure Problem	61
3.2.1. The Born-Oppenheimer approximation	62

Contents

3.2.2.	The Hartree Theory and Hartree-Fock Equation	64
3.2.3.	The Hohenberg-Kohn Theorems	66
3.2.4.	The Kohn-Sham Scheme	67
3.2.5.	The Exchange-Correlation Functional	69
3.2.6.	Local Density Approximation	70
3.2.7.	Generalized Gradient Approximation	72
3.2.8.	Self-Consistent Calculations	73
3.2.9.	Plane Wave Basis	74
3.2.10.	Pseudopotentials	77
3.2.11.	Hellmann-Feynman Theorem and Density Functional Perturbation Theory	79
3.2.12.	Electron-Phonon Coupling in DFT Framework	82
4.	QUANTUM ESPRESSO AND OTHER COMPUTATIONAL TOOLS	84
5.	RESULTS	93
5.1.	Introduction to Theoretical Results	93
5.2.	Doped Graphene	94
5.2.1.	Li/Ca/Ba doped graphene - phonons and symmetry analysis	98
	Computational details	99
	Results and discussion	99
5.2.2.	LiC ₆ Superconductivity and enhancement	106
	Computational details	107
	Results and discussion	108
5.2.3.	Optical properties of LiC ₆	114
	Computational details	115
	Results and discussion	116
5.3.	Magnesium-diboride monolayer	119
5.3.1.	Computational details	122
5.3.2.	Molecular dynamics study of MgB ₂ -mono	123
5.3.3.	Electrons, phonons, symmetry	125
5.3.4.	Superconductivity and enhancement	128
5.4.	GPU acceleration in 2D materials calculations	133
6.	2D MATERIALS SYNTHESIS	144
6.1.	Micromechanical Exfoliation Technique	144

Contents

6.2. Exfoliation Procedure	148
6.3. Mechanically exfoliated graphene as protective coating for DNA structures	154
7. CONCLUSION	159
Bibliography	162
APPENDICES	198
A. APPENDIX	199
A.1. Graphene	199
A.1.1. Tight-Binding Model	199
A.2. Superconductivity	202
A.2.1. Eliashberg Equations	202
A.3. Numerical Methods	209
A.3.1. Derivation of the Hartree-Fock equations	209
A.3.2. Proof of the first HK Theorem	213
A.3.3. Proof of the second HK Theorem	214
A.3.4. Derivation of the Kohn-Sham equations	215
B. Quantum ESPRESSO inputs	217
B.1. Li-doped graphene	217
CV and list of publications	224

PREFACE

This thesis describes work done on superconductivity in graphene and the graphene related materials using the first principle techniques. However interest of this research is wider, it considers doped monolayer graphene and the magnesium-diboride monolayer in the context of superconducting materials and superconductivity in two-dimensions. Interest in the two-dimensional materials has rapidly accelerated in the past decade, mainly as a result of the discovery of graphene [1] and its remarkable properties. Promptly after the first isolation of graphene interest in superconductivity in it, has grown rapidly. In the world obsessed with miniaturization, low-dimensional superconductors are acquiring great relevance and graphene as an ultimately low-dimensional material earned an important place under the spotlight of modern material science.

Superconductivity and the electron-phonon interaction has been studied, described and discussed for almost a century by plethora of theoretical methods. However, predictive non-empirical technique have become available only during the past two decades, invigorated by the development of computational resources. Today there are broadly accessible techniques to calculate from the first principles many materials properties related to the electron-phonon interaction, including the electron-phonon coupling strength and the critical temperature of conventional superconductors. Some of these techniques have been employed in this dissertation, namely the density functional theory and the density functional perturbation theory (DFT and DPFT, respectively).

The presented research covers study of the superconductivity in the graphene-monolayer doped by alkali-metals and suggests methods for an enhancement of the electron-phonon coupling in order to achieve higher critical temperatures, and proposes new two-dimensional materials, the magnesium-diboride monolayer and investigates its properties. Nonetheless the ultimate goal of this dissertation is in a better understanding of superconductivity in low-dimensional materials and using predictive powers of the ab-initio techniques to find new superconductive materials.

Contents

The dissertation comprises of seven chapters, covering this topic. The first chapter represents an introduction to graphene and its unique properties with an additional focus on other two-dimensional materials that followed discovery of graphene. The second chapter covers basic concepts and theories of superconductivity, concentrating on superconductivity in low-dimensions, especially in graphene and magnesium-diboride. Methodology used in research is presented in the third and fourth chapter. Namely, the theoretical basics of DFT and DPFT in the third chapter and computational tools used for research in the fourth one. The main chapter is the fifth one, it presents the conclusions of the theoretical and computational study, presenting several important results (an enhancement of critical temperature in the Li-doped graphene monolayer and presenting magnesium-diboride as superconducting monolayer material). In this chapter is presented an additional technical study of usage of hardware acceleration in low-dimensional materials study as an integral part of computational science research. The experimental techniques for production of high-quality monolayer samples of graphene and other two-dimensional materials are presented in the sixth chapter. In this chapter is given a brief demonstration of the graphene's remarkable properties and possibilities for application as protective coatings for complex organic nanostructures. The seventh chapter is the conclusion presenting both results and general remarks on using the ab-initio techniques in the study of superconductivity in low-dimensions, and as well as the possible directions for the future work.

1. GRAPHENE AND RELATED MATERIALS

1.1. Introduction to Graphene

The isolation of graphene in 2004, as a true two-dimensional material (2D) opened the way for investigation of a new class of materials in low-dimensional physics. Graphene, a novel nanomaterial, was isolated by K.S. Novoselov, A. Geim [1] and their co-workers at the University of Manchester. Although this was not first isolation of graphene ever, there were several prior reports, such as [5, 6], the discovery of Geim and Novoselov was revolutionary since they were the first to study extraordinary properties of graphene. They were awarded the Nobel prize "for the groundbreaking experiments regarding the two-dimensional material graphene" in 2010. Soon after its discovery, graphene became one of the most studied topics both by the material science and condensed matter physics community. The importance of the graphene arises from its unique physical properties. Graphene is a single atomic layer of graphite, with the carbon atoms arranged in the hexagonal (or honeycomb) lattice. It is considered as a first truly two-dimensional material, with the thickness of only one atomic layer, 3.4\AA . After the discovery of graphene, the new field of two-dimensional materials research has emerged and explored not only graphene but many more Van der Waals' materials, crystal structures where, just like in graphene, cells connected in at least one direction by the Van der Waals' forces [2, 3, 4]

Uniqueness of graphene properties arises from its very simple crystal structure. The hexagonal unit cell consisting of two carbon atoms is the origin for many interesting phenomena that draw an attention both of the scientific community and the industry. The press given name "wonder material" [3] originates in plethora of unique properties. The graphene's incredibly high strength-to-weight ratio and the Young's

1. GRAPHENE AND RELATED MATERIALS

modulus of 1 TPa [7](five times higher than steel) comes from the in-plane σ -bonds between the carbon atoms, while the defect-free lattice structure allows it to be impermeable to all gases, even with a monolayer thickness [8].

The main property that initially made graphene so tempting for research was the high charge carrier mobility [9] achievable in defect-free samples produced through the process of the micro-mechanical exfoliation, reaching the theoretical limit ($\sim 2 \times 10^5 \text{ cm}^2 \text{ V}^{-1} \text{ s}^{-1}$). Due to its unique band structure and dispersion relation, charge carriers in graphene behave as massless Dirac fermions [2], allowing for the first time an experimental insight into new areas of physics previously only confined to theoretical calculations.

The long list of graphene's amazing properties [10, 11, 12, 13] has promoted graphene as a material of the future, and one of the most popular materials for research and development in recent years. Graphene exhibits excellent crystalline uniformity and transport properties which make it a promising material for future nanoelectronic devices and spintronics. Other unique properties (mechanical, thermal) imply it could have a wide array of other practical uses.

1.2. Structure and Electronic Properties of Graphene

Graphene is a member of the carbon allotrope family (Figure 1.2), each with their own dimensionality. Graphite is a three-dimensional form of carbon, while carbon nanotubes are one dimensional and fullerenes are a 0-D carbon allotrope. Although theoretically predicted, it took more than a half of century for its experimental realization. Its stability under ambient conditions [75] was an amazing discovery. According to the Mermin-Wagner theorem [76], whenever an ordering corresponds to a breaking of a continuous symmetry (like crystal lattice), there is no long range order in one-dimensional and two-dimensional cases at any nonzero temperature. This theorem is connected with the Goldstone theorem (which states when there is a broken continuous symmetry at a phase transition, in the ordered state of the system (without the long-range interaction) there should exist a collective mode, an excitation with a gapless energy spectrum, called Goldstone modes.)

In the standard description [77] of the atomic motion in solids it is assumed that amplitudes of atomic vibrations near their equilibrium positions are much smaller than interatomic distances. In a crystal the average vibration amplitude $\langle u^2 \rangle$ is

1. GRAPHENE AND RELATED MATERIALS

$$\begin{aligned}\langle u^2 \rangle &= \sum_k \frac{\hbar}{M\omega_k} \left(\langle b_k^\dagger b_k \rangle + \frac{1}{2} \right) = \sum_k \frac{\hbar}{M\omega_k} \left(n_k + \frac{1}{2} \right) \\ &= \int \frac{d^d k}{(2\pi)^d} \frac{\hbar}{M\omega_k} \left(\frac{1}{e^{\omega_k/T} - 1} + \frac{1}{2} \right)\end{aligned}\tag{1.1}$$

For finite temperatures, $k \rightarrow 0$ is critical. We considered acoustic phonons (s is sound velocity) for the region $\omega_k = sk < T$. This part of the spectrum exists if the spectrum is gapless and in this region:

$$n_k = \frac{1}{e^{\omega_k/T} - 1} \cong \frac{1}{\omega_k/T} = \frac{T}{sk}\tag{1.2}$$

which makes:

$$\langle u^2 \rangle \sim \int \frac{d^d k}{\omega_k} \left(\frac{T}{\omega_k} + \frac{1}{2} \right)\tag{1.3}$$

And in 2D case

$$\langle u^2 \rangle \sim \int \frac{k \cdot dk \cdot T}{\omega_k} \sim T \int \frac{k \cdot dk}{s^2 k^2}\tag{1.4}$$

Namely $\langle u^2 \rangle$ is logarithmically divergent at any finite T . Thus when T is being a finite temperature there is no long range order in 2D systems. In graphene the existence of ripples (that give rise to roughness fluctuations) stabilize structure but play an important role in its electronic properties as well [78]. Another important issue and contribution for thermodynamic instability of graphene (and 2D materials in general) is the role of defects. Finite concentrations of dislocations and disclinations would destroy the long-range translational and the orientational order, respectively. However in graphene and other strongly bonded two-dimensional crystals, density of dislocations in the equilibrium is exponentially small. It is important to emphasize that in the first successful isolation of graphene, Novoselov and Geim started from the stable allotrope of carbon, graphite, and transferred graphene to a substrate, making it stable for a certain amount of time. Graphene in general is considered meta-stable and after a certain amount of time, samples made on substrates begin to wrinkle, break and fold.

The bonding in graphene takes the form of the sp^2 hybridisation, where $2s$, $2p_x$ and $2p_y$ orbitals rearrange themselves to create three equivalent orbitals, separated by 120° in the plane, as shown in Figure 1.3. There is a superposition of $2s$ and two $2p$ -orbitals:

1. GRAPHENE AND RELATED MATERIALS

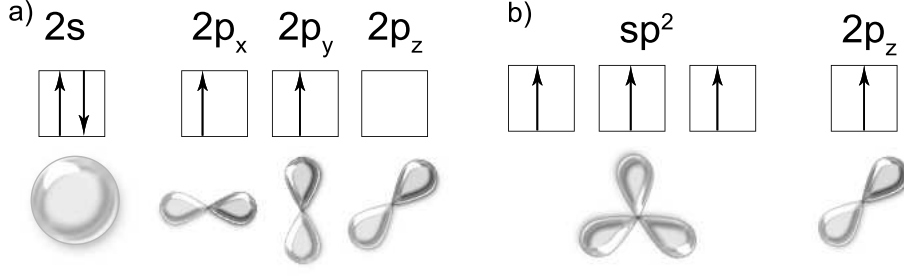


Figure 1.1.: Hybridization of bonds in graphene. Carbon's $2s^2$, p_x , p_y becomes in graphene σ bond from $1s$ p_x p_y and π from p_z filled with one electron.

$$\begin{aligned}
 |sp_1^2\rangle &= \frac{1}{\sqrt{3}}|2s\rangle - \sqrt{\frac{2}{3}}|2p_y\rangle \\
 |sp_2^2\rangle &= \frac{1}{\sqrt{3}}|2s\rangle + \sqrt{\frac{2}{3}}\left(\frac{\sqrt{3}}{2}|2p_x\rangle + \frac{1}{2}|2p_y\rangle\right) \\
 |sp_3^2\rangle &= -\frac{1}{\sqrt{3}}|2s\rangle + \sqrt{\frac{2}{3}}\left(-\frac{\sqrt{3}}{2}|2p_x\rangle + \frac{1}{2}|2p_y\rangle\right)
 \end{aligned} \tag{1.5}$$

This allows each carbon atom to make covalent σ -bonds with three other carbon atoms, forming a honeycomb lattice made out of hexagons. The free $2p_z$ orbital forms out of plane π -bonds, and the π -electrons are mainly responsible for the incredible electronic properties of graphene, and the near-relativistic mobility observed in high quality samples. As each p-orbital contains one electron, the overall π -band is half filled [14]. In graphite, there are no covalent bonds between layers but only in-plane because of the great interlayer distance for orbitals to overlap. π -orbitals are weakly attracted by the Van der Waal's force, binding layers in bulk. In the process of exfoliation these bonds are broken and graphene can be isolated.

We can discuss graphene as a hexagonal Bravais lattice with two atoms per unit cell and we can describe characteristic lattice vectors a_1 and a_2 as function of bond length, which is in graphene $a = 1.42\text{\AA}$.

It is often said that graphene's hexagonal structure consists of two trigonal sublattices each with one carbon atom (blue and black in Figure 1.4), related to each other by inversion symmetry.

The real space unit vectors of the hexagonal lattice are:

$$a_1 = \frac{a}{2} \begin{pmatrix} 3 \\ \sqrt{3} \end{pmatrix}, \quad a_2 = \frac{a}{2} \begin{pmatrix} 3 \\ -\sqrt{3} \end{pmatrix}$$

The three high symmetry points Γ , K and M have the following definitions: Γ is the zone centre, K is the zone corner and M is the centre of the edge of the first

1. GRAPHENE AND RELATED MATERIALS

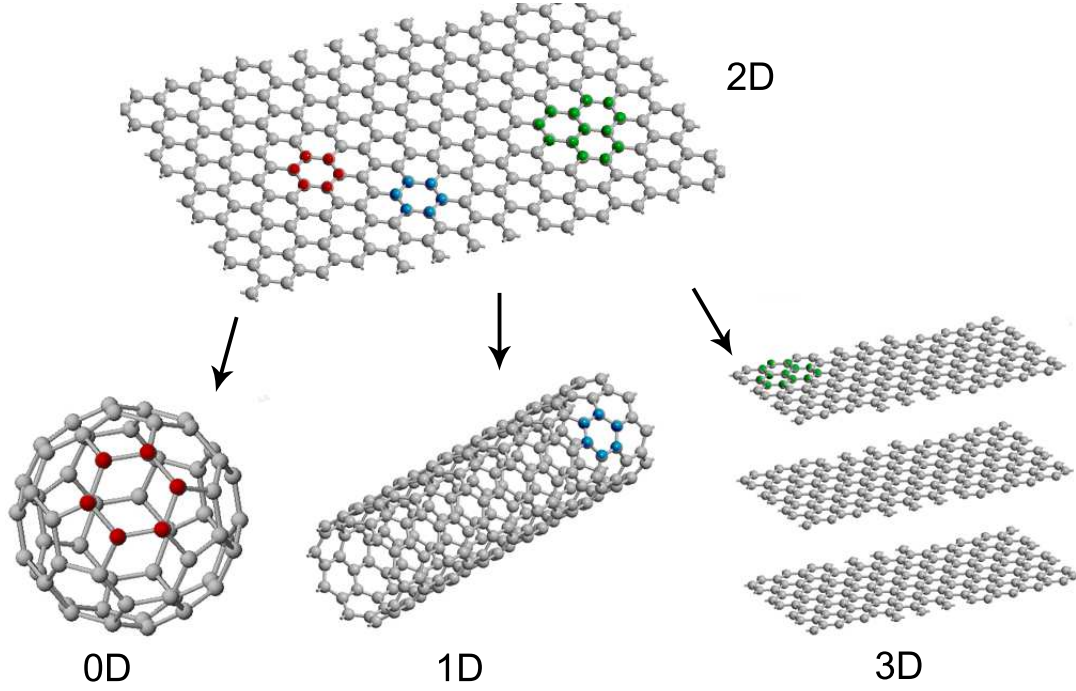


Figure 1.2.: Carbon allotropes. Graphene can be seen as a parent to the other allotropes of carbon with sp^2 hybridisation. From left to right, fullerenes (0-D), nanotubes (1D) and graphite (3D).

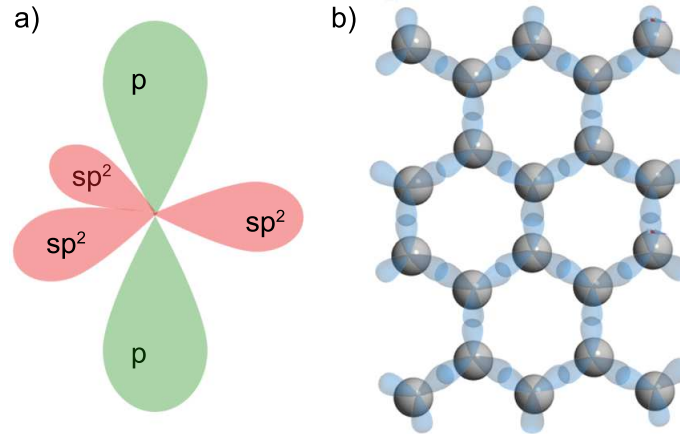


Figure 1.3.: Bonding in graphene. (a) The orbitals of carbon atoms undergoing sp^2 hybridisation, facilitating the formation of the hexagonal lattice (b), present in graphite and graphene.

1. GRAPHENE AND RELATED MATERIALS

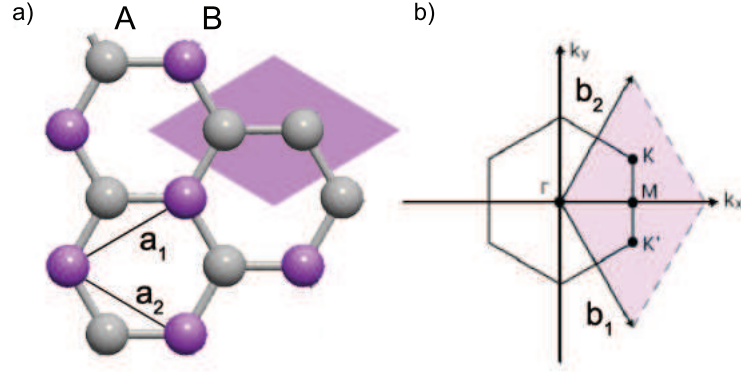


Figure 1.4.: Graphene lattice structure (a) consisting of two overlapping triangular lattices represented by black and blue positions respectively. Each lattice is formed by the vectors a_1 and a_2 (b) Graphene's Brillouin zone plotted in reciprocal space. The high symmetry points Γ , M, K and K' are represented in the first Brillouin zone.

Brillouin zone. The two points, K and K', named "Dirac points", are of particular importance for the physics of graphene are the reciprocal lattice vectors:

$$b_1 = \frac{2\pi}{3a} \begin{pmatrix} 1 \\ \sqrt{3} \end{pmatrix}, \quad b_2 = \frac{2\pi}{3a} \begin{pmatrix} 1 \\ -\sqrt{3} \end{pmatrix}$$

From the reciprocal lattice, the two inequivalent corners of the hexagonal Brillouin Zone are labelled K and K' and positioned in reciprocal space at the points.

$$K = \left(\frac{2\pi}{3a}, \frac{2\pi}{3\sqrt{3}a} \right), \quad K' = \left(\frac{2\pi}{3a}, -\frac{2\pi}{3\sqrt{3}a} \right)$$

It is very important to emphasize that there is no combination of the reciprocal lattice vectors that can connect K and K' points. This means K and K' points are not equivalent, they are chiral, and connected by a reflection operation. This mirror plane lies perpendicular to graphene's plane, in the Γ -M direction.

As discussed above, there are two types of bonds in graphene. The σ -bonds, that are strong and contribute to structural stability of graphene. The electrons in the σ -bonds are very tightly bound and localized. The other type of bonds are delocalized π -bands that cross the Fermi energy and determine the low energy electronic properties of graphene. The band structure of graphene as a single layer of graphite was calculated long before the actual realization of graphene. Wallace [15, 16] in 1946 calculated the band structure of graphene using the tight binding method.

To discuss the band structure, we start from a tight-binding model with nearest-neighbour hopping. The relevant atomic orbital is the carbon π orbital which is left

1. GRAPHENE AND RELATED MATERIALS

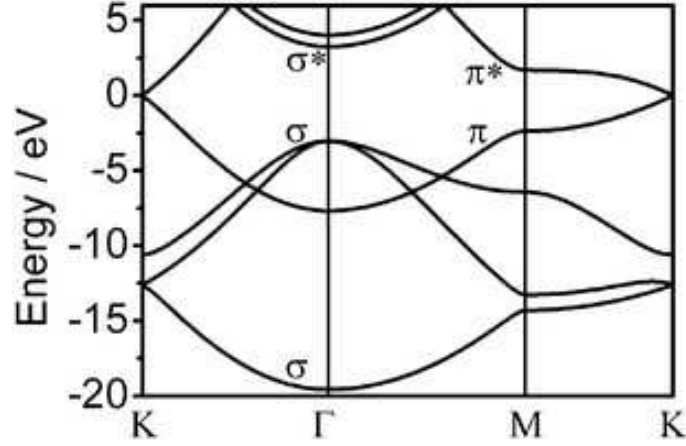


Figure 1.5.: Bands structure of graphene

unfilled by the bonding electrons, and which is oriented normal to the plane of the lattice: as usual, this orbital can accommodate two electrons with spin projection ± 1 . We denote the orbital on atom i with spin σ by (i, σ) , and corresponding creation operator by $a_{i\sigma}^\dagger (b_{i\sigma}^\dagger)$ (H.C. Hermitian conjugate) for an atom on the A (B) sublattice, then the nearest-neighbour tight-binding Hamiltonian has the simple form [15]:

$$\hat{H}_{TB,n.n.} = -t \sum_{ij=n.n.,\sigma} (a_{i\sigma}^\dagger b_{j\sigma} + H.C.) \quad (1.6)$$

The numerical value of the nearest-neighbour hopping matrix element t , which sets the overall scale of the π -derived energy band, is determined to be about 2.8 eV. It is convenient to write the tight-binding (TB) eigenfunctions in the form of a spinor, whose components correspond to the amplitudes on the A and B atoms respectively within the unit cell labelled by a reference point R_i^0 .

For an A-sublattice atom, the three nearest neighbour vectors in real space are given by:

$$\delta_1 = \frac{a}{2} (1, \sqrt{3}), \quad \delta_2 = \frac{a}{2} (1, -\sqrt{3}), \quad \delta_3 = -a(1, 0)$$

While those for the B-sublattice are the same as this one but with a minus sign. Now we chose that A and B are separated by δ_1 (as in the right panel of Figure 1.6) and then the TB eigenfunctions have the form:

$$\begin{pmatrix} \alpha_k \\ \beta_k \end{pmatrix} = \sum_i \exp i k \cdot \mathbf{R}_i^0 \begin{pmatrix} a_i^\dagger e^{-ik \cdot \delta_1/2} \\ b_i^\dagger e^{ik \cdot \delta_1/2} \end{pmatrix} \quad (1.7)$$

1. GRAPHENE AND RELATED MATERIALS

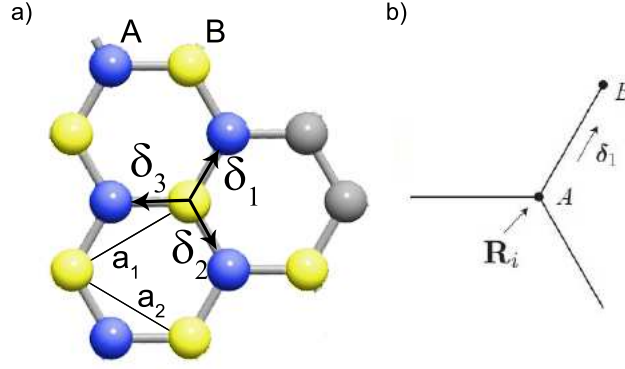


Figure 1.6.: Hexagonal lattice consists of two triangular lattices

Where b_i^\dagger creates an electron on the B atom in cell i . The resulting Hamiltonian in the k -representation is off-diagonal.

$$\hat{H}_k = \begin{pmatrix} 0 & \Delta_k \\ \Delta_k^* & 0 \end{pmatrix} \quad \Delta_k \equiv -t \sum_{l=1}^3 \exp i k \cdot \delta_l \quad (1.8)$$

For explicit values of nearest neighbour vectors δ_l we get:

$$\Delta_k = -t \exp -i k_x a \left(1 + 2 \exp(i \cdot \frac{3k_x a}{2} \cos \frac{\sqrt{3}}{2} k_y a) \right) \quad (1.9)$$

Eigenvalues of H , ϵ_k are given by:

$$\epsilon_k = \pm |\Delta_k| = \pm t \left(1 + 4 \cos \frac{3k_x a}{2} \cos \sqrt{3} \frac{k_y a}{2} + 4 \cos^2 \frac{\sqrt{3}}{2} k_y a \right)^{1/2} \quad (1.10)$$

Here the plus sign applies to the upper (π^*) and the minus sign the lower (π) band. Detailed derivation is presented in the Appendix A.1.1. We are interested in the case for which values of k , Δ_k (hence ϵ_k) is zero. For this to happen, the next condition must be satisfied:

$$\begin{aligned} \frac{3k_x a}{2} &= 2\pi n, & \cos \frac{\sqrt{3}}{2} k_y a &= -\frac{1}{2} \\ \text{or } \frac{3k_x a}{2} &= (2n+1)\pi, & \cos \frac{\sqrt{3}}{2} k_y a &= +\frac{1}{2} \end{aligned} \quad (1.11)$$

The first condition will take k_y outside the first Brillouin zone, but the second (for $n=0$) is satisfied exactly at the points K and K', the Dirac points. Since the energy bands are exactly symmetric about the point $E_k=0$, and this condition is met only

1. GRAPHENE AND RELATED MATERIALS

at the two Dirac points, implying that for exactly half filling of the band, the DOS at the Fermi level is exactly zero. In the absence of doping, graphene has exactly one electron per "spin" per atom (2 per unit cell) so the band is exactly half filled. So, indeed, graphene is a perfect semimetal. Since the two sublattices are physically equivalent, when the state is an energy eigenfunction then (apart possibly from trivial phase factors involved in the precise definition of the a_i and b_i) the behaviour must be either symmetric or antisymmetric with respect to the exchange of A and B.

This dispersion relation is depicted in Figure 1.7. The energy spectrum of this relation results in a large gap in the Brillouin zone (BZ) center which smoothly closes at the corners of the BZ (K and K'). Linear part is described by the $E^\pm = \hbar v_F |k - K|$. As stated above, each carbon atom contributes exactly one electron to the π -bands, each band is exactly half filled with the Fermi energy E_F positioned in the overlap regions of the π and π^* bands, the K points.

Around this point the dispersion relation is defined by two equivalent linear regions, the so-called Dirac cones with its singular overlapping point, the Dirac point. As the Fermi surface in this point is infinitely small, graphene can be defined as a zero band-gap semiconductor. We have two distinguished regions of Fermi surface (Figure 1.7 (c)), low-energy and high-energy region and here they will be briefly discussed.

If we want to discuss the peculiar low energy properties of graphene, we rewrite the Hamiltonian in different basis. We use wave-function amplitudes on the A and B lattice sites near K and K' points $\psi_{K,A}, \psi_{K,B}, \psi_{K',B}, \psi_{K',A}$ [17, 18] and we expand the Hamiltonian for low energies around K-points with $\kappa = k - K$ and the Fermi velocity is $v_F = \frac{3ta}{2\hbar} \approx 0.833 \cdot 10^6 \text{ m/s}$

$$H = \begin{pmatrix} 0 & iv_F |\kappa| e^{-i\Theta} & 0 & 0 \\ -iv_F |\kappa| e^{i\Theta} & 0 & 0 & 0 \\ 0 & 0 & 0 & iv_F |\kappa| e^{i\Theta} \\ 0 & 0 & -iv_F |\kappa| e^{-i\Theta} & 0 \end{pmatrix} = v_F \begin{pmatrix} \hat{\sigma} \cdot \kappa & 0 \\ 0 & -\hat{\sigma} \cdot \kappa \end{pmatrix} \quad (1.12)$$

where $\sigma = (\sigma_x, \sigma_y)$ is the Pauli matrix operator:

$$\sigma_x = \begin{pmatrix} 0 & i \\ -i & 0 \end{pmatrix} \quad \sigma_y = \begin{pmatrix} 0 & 1 \\ 1 & 0 \end{pmatrix} \quad (1.13)$$

1. GRAPHENE AND RELATED MATERIALS

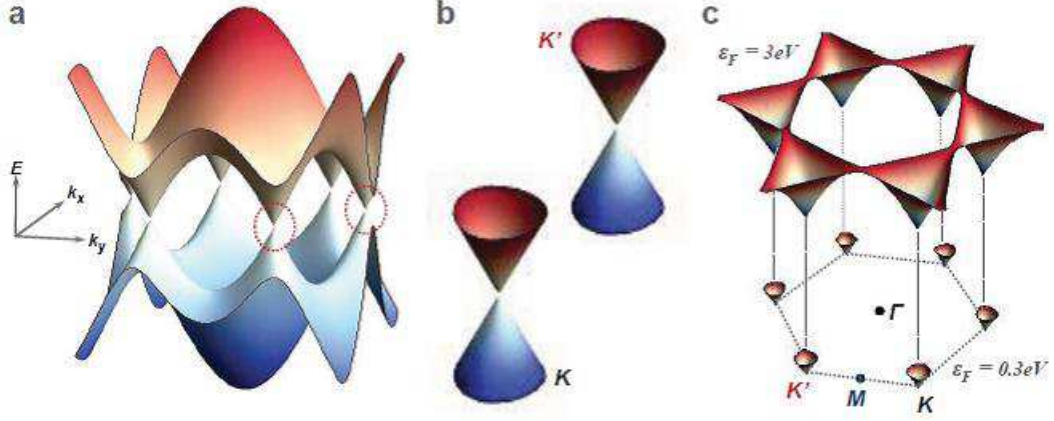


Figure 1.7.: π -bands of graphene from the tight-binding approximation. At zero doping the bands are half-filled with the Fermi energy sitting exactly at the touching points of the Dirac cones, the so-called Dirac points. (b) Low energy spectrum with the two linear Dirac cones in the BZ corner sites K and K'. Hexagonal Brillouin zone of honeycomb lattice, showing intersecting conical electron bands. The linear bands and the two "valleys" at K and K' give unusual electronic properties to graphene. In a pure sample, the lower cones are filled with electrons and the upper cones are empty. (c) Fermi surface for different values of the Fermi energy ϵ_F . At high energies the two separated valleys merge together in the M-point and form a large single Fermi surface. The electronic properties at these energies are no longer defined by the relativistic Dirac equation.

1. GRAPHENE AND RELATED MATERIALS

Two decoupled valleys in the corners of BZ are obtained this way, with each valley having a linear energy dispersion relation:

$$\epsilon(\vec{\kappa}) = \pm v_F |\vec{\kappa}|$$

Hamiltonian equation is identical to the Dirac Hamiltonian of zero-mass relativistic particles (like photons etc.), but speed of light is replaced by the Fermi velocity, hence we have a linear dispersion relation. As shown above, the velocity of electrons in graphene is about three orders of magnitude smaller than speed of light in vacuum. Carriers in graphene do not travel at relativistic speed, but they are described by the Weyl-Dirac equation [19]. Such unique behaviour of graphene carrier enabled several quantum electrodynamics (QED) effects to be observed experimentally. The electron transport in graphene is described by the Weyl-Dirac equation, which made possible to use graphene as an effective medium for experimental testing of relativistic quantum tunnelling described by the Klein paradox [20] and other QED phenomena [21] among which is the half-integer quantum Hall effect [2, 74] which in 2005 initiated an avalanche of graphene research papers. In condensed-matter physics, electrons and phonons are described by separate Schrödinger equations but in graphene, they are interconnected exhibiting properties analogous to the charge-conjugation symmetry in QED.

One of the properties of the Weyl-Dirac equation is that it connects the direction of spin of the particle with its momentum, a concept known as chirality. Two-component wavefunction that describes graphene is very similar to spinor wavefunction in QED but in graphene since we do not have spin index, it is replaced with index that describes belonging to sub-lattice, thus it is usually referred to as a pseudospin σ .

Helicity of a particle is a Hermitian and unitary operator and it is defined as the projection of its pseudospin onto the direction of propagation [22]

$$\eta = \frac{\vec{q} \cdot \vec{\sigma}}{|q|} \text{ and } [\eta, H] = 0$$

where $\vec{\sigma}$ is a spin of the particle. The helicity operator commutes with the Dirac Hamiltonian (due to the absence of the mass term) and represents a good quantum number.

In graphene, we have the same definition for helicity but the Pauli matrices now represent a sublattice pseudo spin. For graphene chirality and helicity are the same. The helicity is a conserved quantum number in elastic scattering processes induced

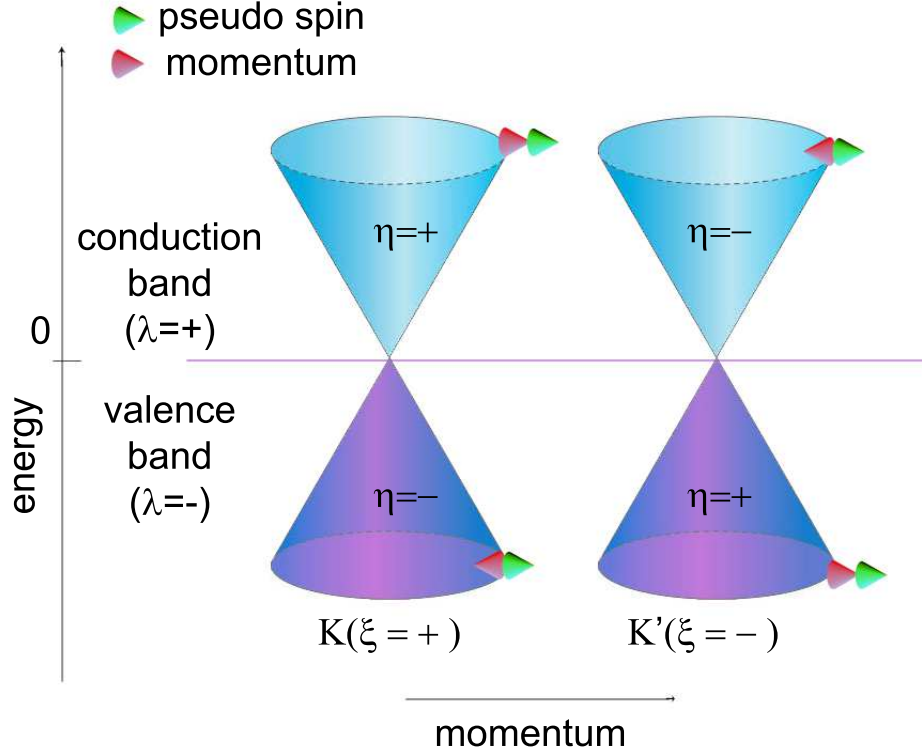


Figure 1.8.: Helicity is a conserved quantum number in elastic scattering on impurity potentials that vary smoothly on the lattice scale

by impurities (when impurity potentials vary smoothly on the lattice scale), causing inter-valley scattering to be suppressed and helicity is conserved. This effect is the origin in ballistic transport in graphene, the Klein tunnelling (transmission probability of a relativistic particle incident on a potential barrier is increasingly higher the higher the barrier becomes, reaching perfect transmission for infinitely high barriers) [22] ergo absence of the backscattering in graphene [23] (Figure 1.8).

At high energies, the Fermi surface alters dramatically from the low energy case as is demonstrated in Figure 1.8. Instead of the two small circular Fermi surfaces around the K and K' points and a linear dispersion relation around them, the two valleys are merged together at around $\epsilon \sim 3$ eV to form a single Fermi surface spanning the entire BZ. The dispersion relation around these energies is not linear and results in flat band regions. In particular in the M-points, the band exhibits a saddle point behaviour with an extremely high density of states (DOS), resulting in the van Hove singularities [24, 26]. In this area, graphene can be better described as a good metal rather than a zero band-gap semiconductor.

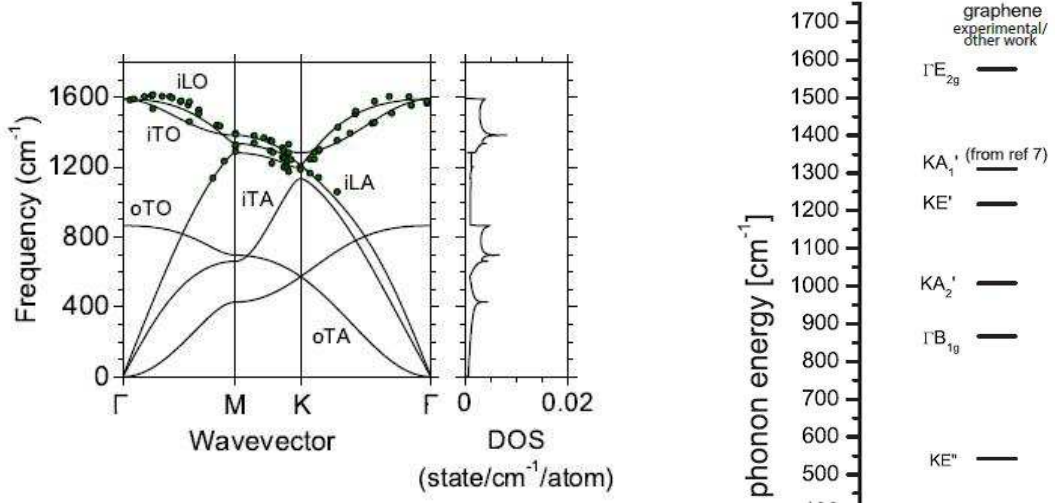


Figure 1.9.: Calculated phonon dispersion relation of graphene. [28] LO, iTO, oTO, LA, iTA and oTO are phonon modes at the Γ point. The green circles are X-ray scattering measurements from Ref. [31]. On the right is the DOS of the phonons.

1.3. Phonons and Electron-Phonon Interaction in Graphene

Since the unit cell of monolayer graphene contains two carbon atoms, A and B, six phonon dispersion bands can be distinguished in phonon spectra [27] (Figure 1.9 of which three are acoustic (A) and other three are optic (O) phonon modes. For one acoustic (A) and one optic (O) phonon branches, the atomic vibrations are perpendicular to the graphene plane, and they correspond to the out-of-plane (o) phonon modes.

For two acoustic and two optic phonon branches, the vibrations are in-plane (i). The directions of the vibrations are considered with respect to the direction of the nearest carbon-carbon atoms so they are classified as longitudinal (L) and transverse (T) according to vibrations parallel or perpendicular, respectively, to the A-B carbon-carbon direction.

In Figure 1.9, phonon dispersion is depicted along the high symmetry Γ M and Γ K directions, and the six phonon dispersion curves are assigned to LO, iTO, oTO, LA, iTA, and oTA phonon modes. The symmetry group of graphene is $D_{6h} = T \wedge D_{6h}$ [29, 30].

At the Γ point, the group of the wave vector is D_{6h} and phonon modes are classified

1. GRAPHENE AND RELATED MATERIALS

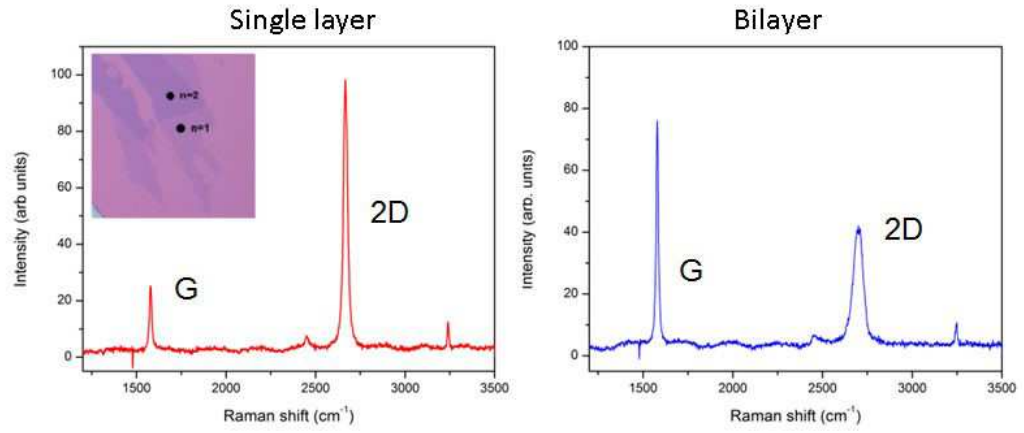


Figure 1.10.: Raman spectra of mechanically exfoliated graphene sample for mono and bilayer graphene (optical image of samples depicted in the inset)

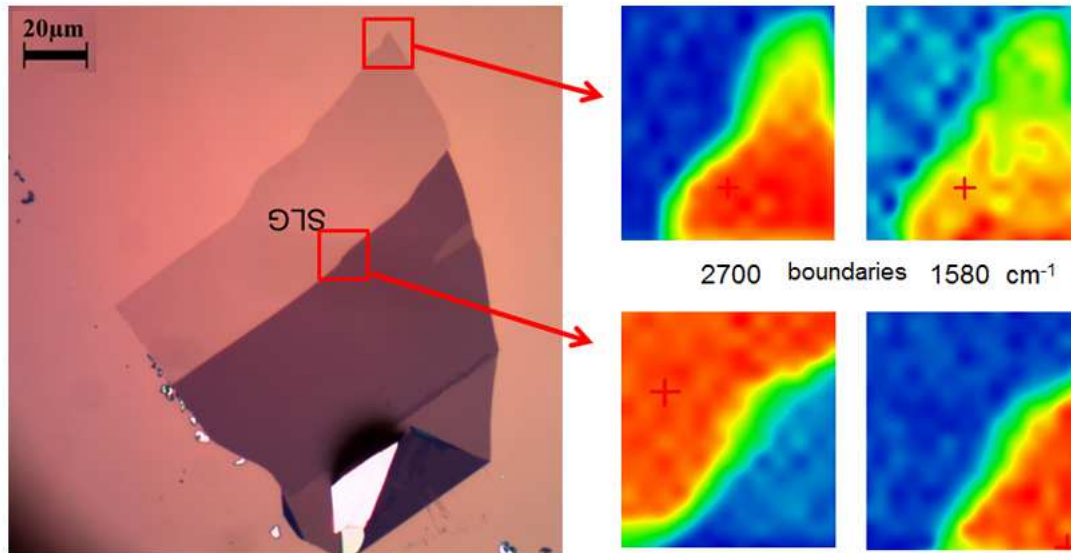


Figure 1.11.: Raman map of mechanically exfoliated graphene sample for mono and the few-layer

1. GRAPHENE AND RELATED MATERIALS

according to [30]:

$$\underbrace{\Gamma B_{1g}}_{\text{out-of-plane}} + \underbrace{\Gamma E_{2g}}_{\text{in-plane}} + \underbrace{\underbrace{\Gamma A_{2u}}_{\text{out-of-plane}} + \underbrace{\Gamma E_{1u}}_{\text{in-plane}}}_{\text{acoustic}} \quad (1.14)$$

For the K point, the group of the wave vector is D_{3h} . Phonon modes at this point are classified as [30]:

$$KA'_1 + KA'_2 + KE' + KE'' \quad (1.15)$$

The in-plane iTO and iLO optic modes correspond to the vibrations of the sublattice A against the sublattice B as shown in Figure 1.12 and these modes are degenerate at the Γ point. According to group theory, the degenerate zone-center iLO and iTO phonon modes belong to the two-dimensional E_{2g} representation. They are Raman active modes [27, 32] and very important for identification of experimental samples. The degeneracy of the iLO and iTO phonons disappears for general points inside the first Brillouin zone of graphene. At the K-point, the phonon which comes from the iTO branch is non-degenerate and belongs to the A'_1 irreducible representation of the point group D_{3h} , and the eigenvectors of all modes are represented in Figure 1.12. The iLO and iLA phonon branches meet each other at the K point giving rise to a double degenerate phonon, with the E' symmetry [31, 33]. This mode is important in identification of graphene samples using Raman spectroscopy. As discussed, there are two optic modes in graphene:

$$\Gamma_{opt} = E_{2g} + B_{2g}$$

E_{2g} is Raman active and B_{2g} is silent mode. There is no infra-red active mode as in graphite where we have:

$$\Gamma_{opt} = A_{2u} + E_{1u} + 2B_{2g} + 2E_{2g}$$

E_{2g} modes are Raman active and A_{2u} and E_{1u} are infra-red active (B_{2g} is also silent).

In graphene, we can see two distinct modes, G (E_{2g} mode) and 2D (E') in the Raman spectra of the graphene. The phonon vibrations for G and 2D mode are presented in Figure 1.13.

Typical Raman spectra for graphene is presented in Figure 1.10. The intensity of peaks is directly connected to the number of layers and the amount of defects in

1. GRAPHENE AND RELATED MATERIALS

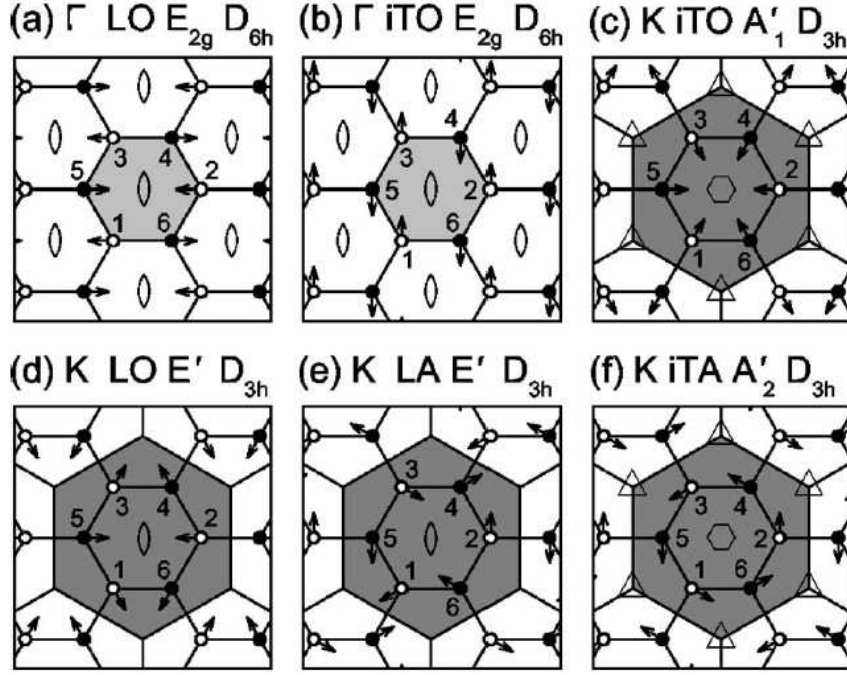


Figure 1.12.: The eigenvectors for the in-plane phonons relevant to the high symmetry Γ point and K points of the Brillouin zone. Each of these twelve modes is labelled and their atomic displacements are indicated. The symbols ellipse, triangle and hexagon, represent the rotation axes C_2 , C_3 and C_6 , respectively, [27]

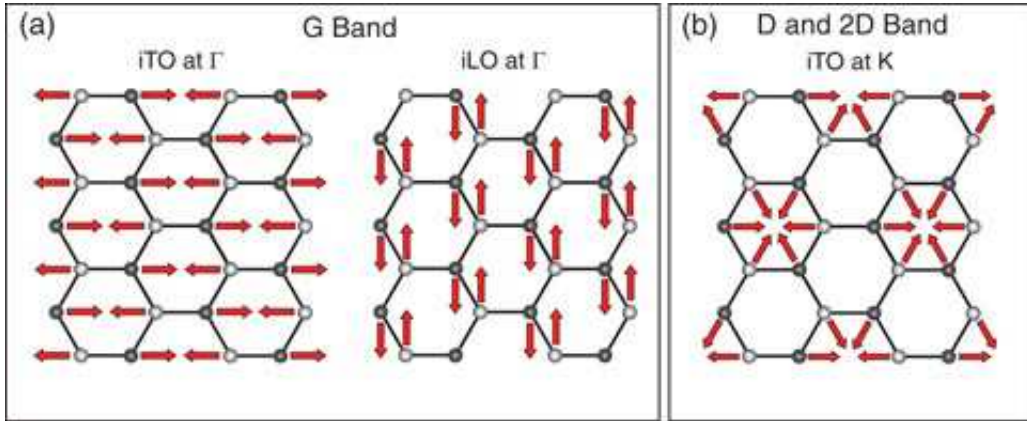


Figure 1.13.: Sketch of the phonon vibrations contributing to the main Raman bands in graphene. a) G band vibration modes for the iTO and iLO phonons at the Γ -point. b) D vibration mode for the iTO phonon at the K-point. Figure taken from [25]

1. GRAPHENE AND RELATED MATERIALS

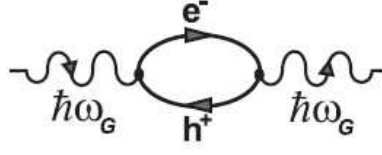


Figure 1.14.: Feynman diagram for the second-order process that changes phonon self-energy. The first node shows the decay of a phonon into an electron-hole pair, and the second node shows the recombination of the electron hole and the emission of a phonon.

the graphene samples. In graphene, electron-phonon interaction is very significant. In the first approximation, the lattice vibrations, phonons, are determined by the vibration of the ions with respect to their equilibrium positions. In graphene, the electronic cloud affects the movement of the ions. When the local density of electrons is increased, an extra kinetic energy should appear due to the exclusion principle, and thus the electronic cloud screens the atomic vibrations [34]. The electron-phonon interaction affects the phonon spectrum and to calculate this change, perturbation theory must be used for the electron-phonon Hamiltonian. The corrected phonon energy due to interaction is:

$$\hbar\omega_q^{(p)} = \hbar\omega_q + \sum_k |M_{kk'}|^2 \frac{2\langle n_k \rangle (\varepsilon_k - \varepsilon_{k'})}{(\varepsilon_k - \varepsilon_{k'})^2 - (\hbar\omega_q)^2} \quad (1.16)$$

where $\langle n_k \rangle$ and $\langle n_q \rangle$ are occupation numbers from electrons and phonons, respectively. k and k' mark the electron before and after scattering and $q=k-k'$ is phonon that is being absorbed. This equation describes the phonon frequency change due to the electron-phonon interaction and in Figure 1.14 it is represented using the Feynman diagrams. An electron in the valence band is first excited to the conduction band by absorbing a phonon, thus creating an electron-hole pair. The electron and hole then recombine, thus emitting a phonon. Both the frequency and lifetime of the phonon are significantly affected by this second-order process [36].

In general, atomic vibrations are partially screened by filled electronic states. In a metal, this screening is determined by the shape of the Fermi surface and can change rapidly from one point to another in the Brillouin zone. The consequent anomalous behavior of the phonon dispersion is called a Kohn anomaly [37]. Kohn anomalies may occur only for phonon wavevectors q such that there are two electronic states k_1 and k_2 on the Fermi surface, where $k_2 = k_1 + q$ [37]. In graphene, the gap between

1. GRAPHENE AND RELATED MATERIALS

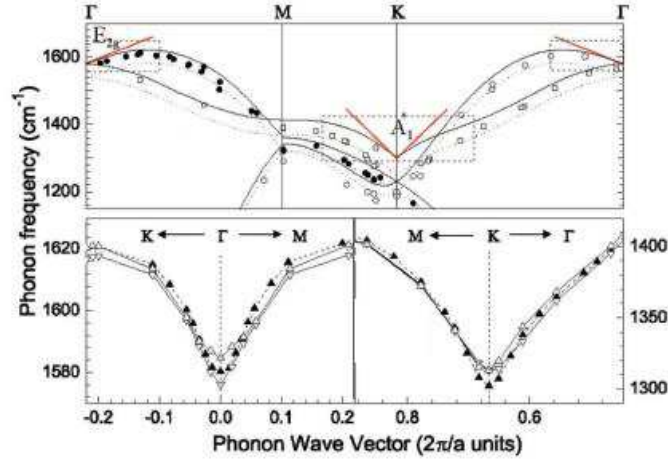


Figure 1.15.: Phonon dispersion of graphene from Ref. [38] showing the Kohn anomaly at the Γ and K points. The lines of the top part of Figure are the theoretical calculated curve and the symbols are the experimental data. The both bottom figures are a close-up of the phonon dispersion near the Γ and K points. The different lines show different parameters for the theoretical calculation done in Ref [38].

occupied and empty electronic states is zero at the six corners of the Brillouin zone, namely K and K' points. These points are connected by a vector of length K. Thus, Kohn anomalies [37] can occur for $q = 0(\Gamma)$ or $q = K$ (Figure 1.15 [38]). For a given value of q , the Kohn anomalies are present only in the highest optical branches. It can be observed as a kink in the phonon spectrum for $q=2k_F$. [39]

In the phononic spectrum of a metal, the Kohn anomaly is a discontinuity in the derivative of the dispersion relation that occurs at certain high symmetry points of the first Brillouin zone, produced by the abrupt change in the screening of lattice vibrations by conduction electrons.

It can be generalized that the Kohn anomaly will happen when $k_1 - k_2 + b = 0$, where k_1 and k_2 are the electron state at the Fermi surface and b is a reciprocal lattice vector, that brings the phonon wavevector q back into the first BZ [37].

Piscanec et al. [38] first reported the Kohn anomaly in graphene. In graphene, the Kohn Anomaly is present at high symmetry points, Γ and K, for certain modes. This is because, as previously discussed, the Fermi surface in graphene corresponds to the K and K' points and Fermi wavevectors k_1 and k_2 are at the corners of the first BZ (K and K' vectors). Picasanes and his co-workers observed divergent characteristic

1. GRAPHENE AND RELATED MATERIALS

of the Kohn anomaly near the Γ point for the iLO mode and at K point for the iTO mode and showed the relation between slopes of the phonon dispersion at Γ and K and the electron-phonon coupling parameter λ_{e-p} [38].

The influence of electron and phonon coupling in graphene is visible in one more important phenomenon. Namely it is the breakdown of Adiabatic Born-Oppenheimer approximation (ABO). In the Section 3.2.1 a detail discussion about the ABO approximation will be presented. Here, we'll just say it assumes that the lighter electrons adjust adiabatically to the motion of the heavier nuclei, remaining in their instantaneous ground states. In graphene this approximation fails and, electrons do not have time to relax their momenta to reach the instantaneous adiabatic ground state. For monolayer graphene we assume the linear electronic dispersion ($E(k) = v_F k$), and then the frequency shift for the phonon at $q = 0$ in units of the electron-phonon coupling as a function of the Fermi energy (E_F) can be calculated in the framework of non-adiabatic second order perturbation theory [35]. Within ABO, the energy of a zone-centre phonon is determined by two contributions: the distortion of the electronic bands, associated with the phonon displacement, and the adiabatic rearrangement of the Fermi surface [41]. In graphene, these two contributions cancel out exactly because of the peculiar rigid motion of the Dirac cones, associated with the E_{2g} phonon. The E_{2g} phonon in graphene consists of an in-plane displacement of the carbon atoms by a vector $\pm 1/\sqrt{2}$ as shown in Figure 1.16. In the presence of such atomic displacements, the bands are still described by a cone with the Dirac point shifted from K by a vector s (Figure 1.16 b) and c))

As shown in Figure 1.16 a) without any distortion, in the perfect crystal the Dirac point is at K, the electronic states are filled up to the Fermi energy ϵ_F and the Fermi surface is a circle centred at K. If we observe bands in the presence of an E_{2g} lattice distortion we can see the Dirac points are displaced from K by $\pm s$. Within ABO, the electrons remain in the instantaneous ground state: the bands are filled up to ϵ_F and the Fermi surface follows the Dirac-point displacement. The total electron energy does not depend on s . However in the non-adiabatic case, the electrons do not have time to relax their momenta (through impurity, electron-electron and electron-phonon scattering) to follow the instantaneous ground state. In the absence of scattering, the electron momentum is conserved and a state with momentum k is occupied if the state with the same k is occupied in the unperturbed case. As a consequence, the Fermi surface is the same as in the unperturbed case and does not follow the Dirac-cone displacement. The total electron energy increases with s^2 ,

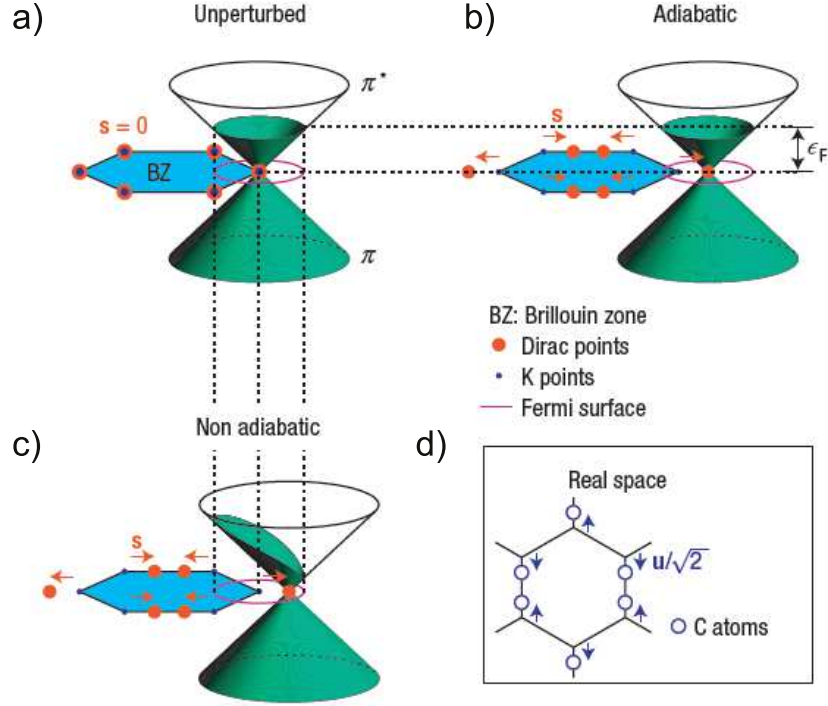


Figure 1.16.: Schematic π band structure of doped graphene near the high-symmetry K point of the Brillouin zone. The filled electronic states are shown in green. a) Electronic bands of the crystal. b) Bands in the presence of E_{2g} lattice distortion within ABO. c) Bands in the presence of E_{2g} lattice distortion in non-adiabatic case. d) Atomic pattern of E_{2g} phonon. Figure taken from [41]

1. GRAPHENE AND RELATED MATERIALS

resulting in the observed E_{2g} -phonon stiffening. [41]

The renormalization of the phonon energy is strongly dependent on the Fermi level position, which can be tuned by doping graphene with electrons or holes. Theoretical models for the phonon self-energy [40, 35, 36] and time-dependent second order perturbation theory have predicted the same logarithmic dependence for the phonon softening on the Fermi level change for graphene. This anomalous phonon behaviour has been experimentally observed by Raman spectroscopy of doped graphene [41, 42, 43].

Existence of strong electron-phonon interaction in graphene can be observed using spectroscopic methods (like infrared and Raman spectroscopy and ellipsometry). Distinct Fano resonant profile is commonly used to parameterize an asymmetrically shaped spectral line that arises from coupling between the band continuum (electron bands) and discrete state (phonons) [44, 45, 46].

1.4. Other 2D Materials

The discovery of graphene changed materials science in many ways, not only by amazing insight into the relativistic effects at table top and variety of applications of the "wonder material" ranging from everyday to almost science-fiction ones, but in the opening of a whole new field of research of other, low-dimensional layered materials with plethora of interesting properties. We call "layered materials" those that are characterized by extended crystalline planar structures held together by strong in-plane covalent bond and the weak out-of-plane Van der Waals forces. Reduction of dimensionality of the system is related to the amazing properties because the reduction of available phase space and decreased screening lead to enhancement of quantum effects and increased correlations. Even before first experimental realization of 2D materials, there was a significant interest in quasi-2D system, including cuprate high-temperature superconductors, whose superconductivity is confined to planar CuO_2 layers and semiconductor interfaces that host the fractional Hall Effect. Soon after graphene, a semi-conductor with zero gap, came other 2D materials (Figure 1.17), insulators like hexagonal boron-nitride, phosphorene, 2D counterpart of black phosphorus which drives its properties out of its inherent in-plane anisotropy [64] and great family of materials ranging from semiconductors to superconductors, known as transitional metal dichalcogenides (TMDs). With common formula, MX_2 , they consist of a one layer of transition metal M, such as molybdenum or wolfram,

1. GRAPHENE AND RELATED MATERIALS

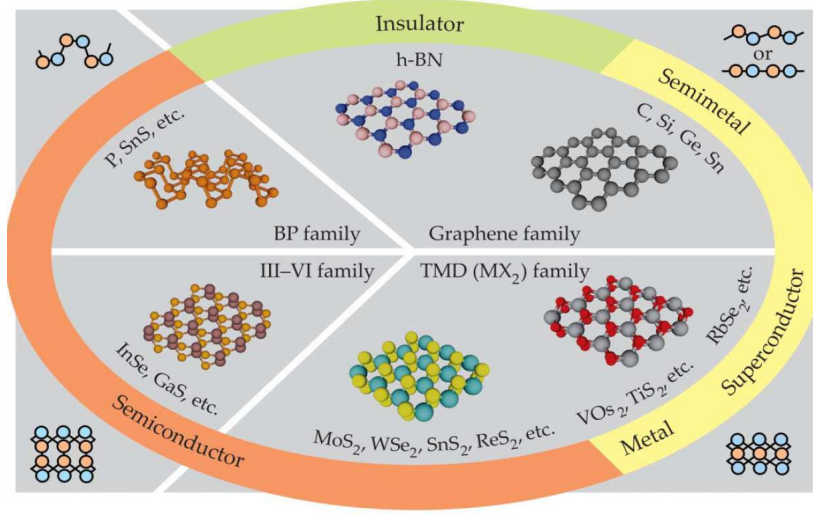


Figure 1.17.: Two-dimensional materials including graphene, its analogues hexagonal boron nitride, black phosphorous, and III-IV family of semiconductors; and transitional-metal dichalcogenides (TMDs)[79]

sandwiched between two layers of chalcogen, such as sulphur, selenium or tellurium X, making its unit cell made out of those three atomic layers, with 6-8 Å thickness [65]. The TMDs do not have an inversion symmetry, they have a variety of physical and electronic properties, non-zero band gap and complicated band structure due to the strong spin-orbit coupling, and very interesting optical properties due to the quantum confinement and the lack of bulk dielectric screening. 2H-NbSe₂ is a conventional superconductor with a critical temperature of 7.2K, highly anisotropic layered TMD and a single crystal can be obtained in the process of mechanical exfoliation [66, 67]. Due to the 2D nature, there is an occurrence of electronic instabilities driven by Fermi surface nesting and this generates the formation of charge density waves (CDW). Although in 2H-NbSe₂ both superconductivity (at 7.2K) and CDW (at 32K) are observed and studied, there is still little agreement on properties and coexistence and competition between these two ground states [68, 69].

The rise of Van der Waals materials opens the possibility of new types of quantum heterostructures [70], consisting of layers of various 2D materials. Stacking of two or more atomic layers of different Van der Waals materials allows designing and creating a novel material system with a rich variety of new properties.

One of the most surprising findings in the world of 2D materials as well as 2D superconductors, is a strong enhancement of critical temperature in one unit cell

1. GRAPHENE AND RELATED MATERIALS

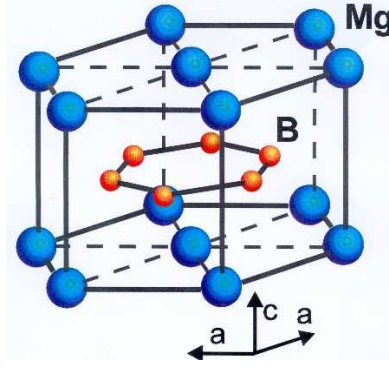


Figure 1.18.: Structure of MgB_2 crystal. Graphene like hexagonal layers of boron atoms alternate with hexagonal layers of magnesium sitting on top of the centre of the boron hexagons.

thick FeSe layer epitaxially grown on SrTiO_3 substrates, reaching 40-100 K [71, 72] which is in great contrast with critical temperature of one unit cell thick FeSe grown on graphene/SiC of 2K [73]. Mechanism of this enhancement is still unknown and under heavy debate but most authors are certain that the effect is based on the atomic-scale film thinning and a strong interaction with a substrate.

Another very interesting material that can easily be placed among "other graphene 2D related materials" is MgB_2 , a metallic superconductor with quasi-two dimensional character. Magnesium diboride MgB_2 (Figure 1.18) has been known for a long time [80, 81] but interest in it grew in 2001 with the discovery of superconductivity with critical temperature ($T_c=39\text{K}$) [82].

MgB_2 has graphene-like hexagonal layers of boron atoms that alternate with hexagonal layers of magnesium atoms sitting on top of the boron hexagons as shown in Figure 1.18. Theoretical studies offered insight in the very interesting nature of this material, proposing that superconductivity originates in the boron p_x, p_y bands [83] and suggesting the possibility of the two-gap superconductivity [84]. Experimental studies by STM tunnelling spectroscopy [87], point-contact spectroscopy [88, 89, 90], specific heat measurement [91] and Raman spectroscopy [92] supported two-band superconductivity. Today we know that there are two distinct superconductivity energy gaps at $\Delta_1=2.3\text{meV}$ and $\Delta_2=7.1\text{meV}$ [93, 94].

The electronic structure of MgB_2 has been studied and discussed in literature thoroughly, especially after 2001 and discovery of superconductivity [82, 95, 96, 97]. In Figure 1.19 a), the band structure of MgB_2 is represented along with high symmetry points of reciprocal hexagonal lattice. The very specific shape of the

1. GRAPHENE AND RELATED MATERIALS

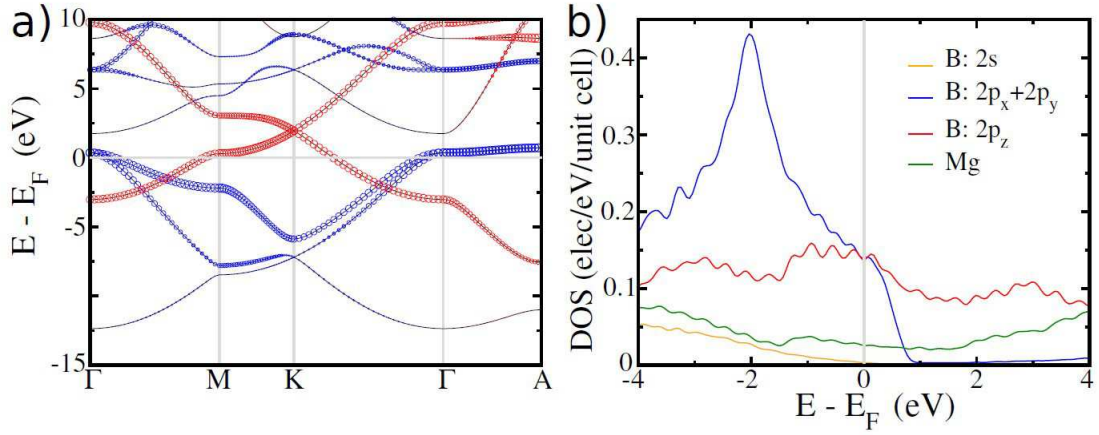


Figure 1.19.: a) band structure of MgB₂, blue circles correspond to boron p_x, p_y character and red to boron p_z character (Γ, M, K, A are high symmetry points of reciprocal hexagonal lattice vectors) b) DOS near the Fermi level, with contributions from boron and magnesium orbitals

Fermi surface (Figure 1.20), consisting of two coaxial cylinders parallel to the c -direction centred around Γ and a complicated tubular three-dimensional structure, is a consequence of specificity of MgB₂ band structure. Namely, as it can be seen in Figure 1.19 a), there are three partially filled bands. Two are based on boron p_x and p_y orbitals (blue circles) and they are associated with the σ bonds of the boron layers. Due to the lack of interaction with magnesium orbitals, they have a two-dimensional character. Other partially filled band (red circles) which is built from the boron p_z orbitals, exhibits dispersion along both the plane of the boron layers (because of their π -type interaction along boron-layers) and the interlayer direction (because of good overlap between the out-of the plane pointing boron p_z and magnesium orbitals).

Having observed the shape of the Fermi surface in Figure 1.20, we can attribute two cylinders to boron p_x and p_y orbitals (namely σ bonding bands) and other structure to boron p_z orbitals (namely, the π bonding and antibonding bands) [98, 344, 328]. It is very interesting to notice that DOS at Fermi level for the boron (p_x, p_y) and boron p_z are almost identical (as depicted in Figure 1.19 b)). Boron s contribution of the Fermi surface cylinder is quite small.

The superconductivity is caused by the E_{2g} phonon mode at 75meV that couples strongly to the two-dimensional σ -bands, and more weakly to the π -bands, leading to two different gaps.

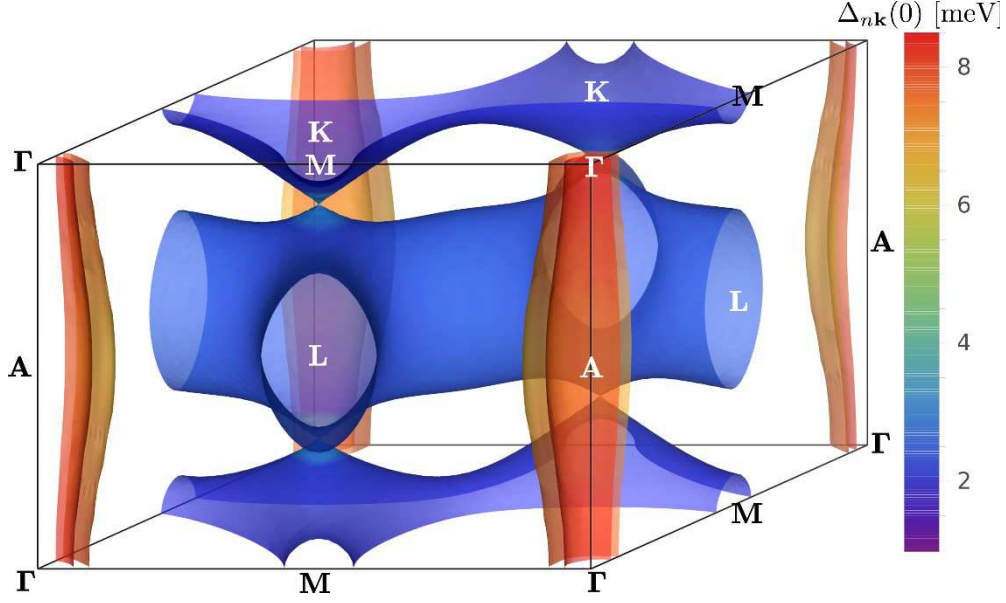


Figure 1.20.: The superconducting energy gap of MgB_2 , calculated at $T \sim 10$ K, mapped on the Fermi surface. The Fermi surface consists of two σ sheets along the Γ - Γ lines, and two π sheets along the K-M and the H-L lines (figure from [98], figure generated by [427])

Significance of discovery of superconductivity is not only in the fact that it is a metallic superconductor with the highest critical temperature, but in the fact that superconductivity originates at quasi two-dimensional boron planes [87, 99] and then extends through magnesium layers forming an anisotropic 3D superconducting state at the material.

In this thesis, the motivation for the study of MgB_2 originates both from the interest for quasi-two dimensionality in this material and effects on superconductivity and from the structural similarity of MgB_2 with the intercalated graphite and all implications coming from it. This will be comprehensively discussed in Chapter 5.

The study of 2D superconductors became one of the most pursued topics of the superconductivity research, promising answers both to fundamental physics and material science. The next chapter of this thesis will briefly discuss superconductivity in general and then in more detail, approach the superconductivity in 2D materials and low dimensions.

2. SUPERCONDUCTIVITY IN 2D MATERIALS

2.1. Brief History of Superconductivity

For the material science, the beginning of the 20th century was an exciting time for many reasons. In the 1908 Kamerlingh Onnes liquefied helium for the first time allowing him to measure the resistance of different materials at low temperatures down to 4.2K. Onnes achieved a big breakthrough in 1911 by discovering superconductivity in mercury at temperature of 4.15 K above absolute zero [102], accidentally while he was trying to measure resistivity at low temperatures. Having discovered that at 4.15 K the resistivity of mercury abruptly drops to zero, he repeated the same measurements for other elements and alloys and noticed the same behavior with several different materials. He concluded that the superconducting behavior of material depends on the nature of the material itself and that critical temperature, when material transitions from normal to superconducting state, is not same for every material but unique for each. Onnes also found that breakdown of SC occurs with very high currents and at high magnetic fields [103].

After Onnes' discovering, numerous theories attempted to explain this zero resistance transition, and an interest in this new behavior of materials upsurged and in 1933 experiments on superconducting materials resulted in one more interesting finding. Walther Meissner and Robert Ochsenfeld discovered that complete expulsion of the magnetic field from the interior of the superconductor occurs at $T < T_c(H)$. In 1953, Fritz and Heinz London published an article that for the first time correctly explained the Meissner effect [104]. Their contribution is not only the development of their equation but in the introduction of characteristic parameter, the London penetration depth λ_L that defines the depth to which a magnetic field is able to penetrate the sample.

2. SUPERCONDUCTIVITY IN 2D MATERIALS

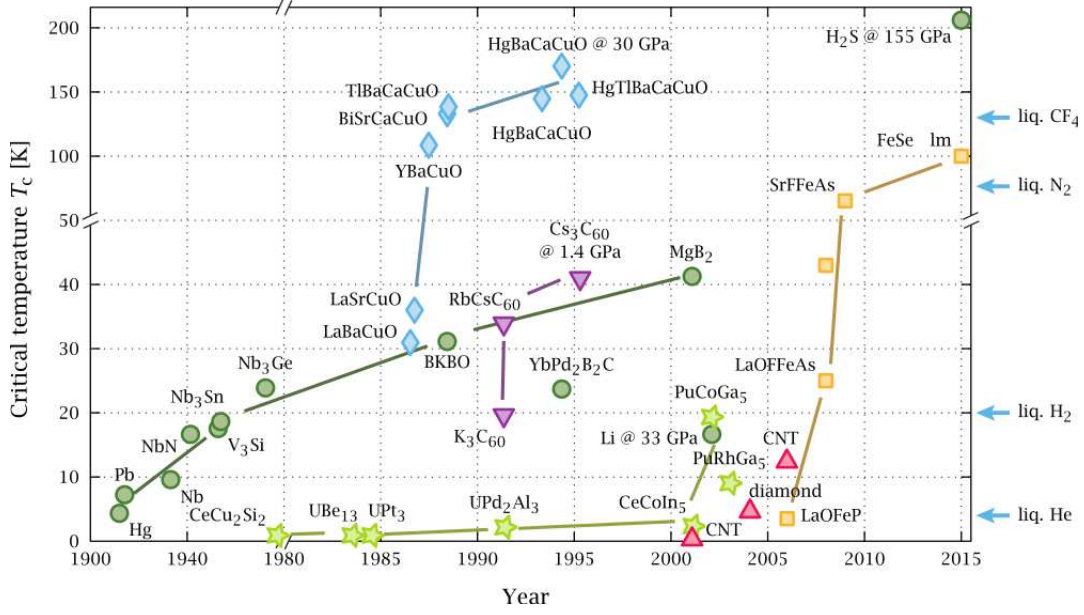


Figure 2.1.: The timeline of discovery of superconducting materials[100]

The milestone in the history of condensed matter physics represented by the work of J. Bardeen, L. Cooper and J.R. Schieffer [85, 86], the new theory from 1957, where they described the mechanism of superconductivity based on Cooper pairing. A discovery that came in a 1962, Josephson effect, introduced the possibility of the flow of Cooper pairs between two superconductors connected by a weak link. The DC Josephson effect is obtained when Cooper pair supercurrent flows in the absence of an applied voltage, while the AC Josephson effect [105] is exhibited when the flow of Cooper pairs occurs with an applied voltage between the two superconductors. Although superconductivity was very fascinating at the time, the limitation of SCs applications concerns their low critical temperatures. In the year 1986, the discovery of high-temperature superconductors (high- T_c) brought a change. Bednorz and Muller [106] published the paper "Possible High T_c Superconductivity in the Ba-La-CuO system" where they discussed the synthesis of a metallic oxygen-deficient compound $\text{Ba}_x\text{La}_{5-x}\text{Cu}_5\text{O}_{5(3-y)}$ with the critical temperature above 30K. This discovery opened a new era in the field and interest in the new group of materials, the so-called cuprates. Next big step was the discovery of superconducting materials with critical temperature well above the boiling point of liquid nitrogen (77 K) enabling condensed matter physicists all over the world to be part of the race. Maeda et al. [107] first reported the existence of superconductivity with a T_c of around 105 K in the BiSrCaCuO system. The highest critical temperature is achieved by

2. SUPERCONDUCTIVITY IN 2D MATERIALS

HgBaCaCuO system [108] with 130K, and after exposure to high-pressure Tc it can be increased up to 150K. In 1991, potassium-doped C₆₀ with T_c of 18 K [109, 110] begun entirely a new area of sc in carbon based materials. A great surprise came in 2001 when sc was discovered in a material that has been known for a long time, MgB₂, with the critical temperature of 39K [84].

A new family of high Tc materials called iron-based pnictides was introduced in 2008 [111]. A pnictide is an element from group V of the periodic table. Oxypnictides generally contain oxygen and rare earth elements and they are layered tetragonal compounds. Oxypnictide materials are similar to high Tc cuprate materials as both of them have conduction layers and spacer layers (charge reservoirs). At the end of 2015 [112], the discovery of superconductivity at 200 K in sulfur hydrides under pressure opened exciting perspectives in the search for new superconducting materials at even higher temperatures streaming toward room-temperature superconductivity.

For little more than a century, some fascinating discoveries took place in the field of condensed matter physics and material science. Enormous progress has been made in most of the physical and engineering aspects of superconductivity and there is still a tremendous scope to do more and try to resolve some of the very intricate unsolved problems. However, great discoveries are yet to happen, paving the way for application of these properties in everyday life.

2.2. BCS Theory and Eliashberg Formalism

2.2.1. BCS theory

In 1957, J. Bardeen, L. Cooper and J.R. Schieffer published the first comprehensive theory of superconductivity [85, 86]. A Nobel Prize was awarded "*for their jointly developed theory of superconductivity, usually called the BCS-theory*" in 1972. BCS theory explains that attraction between electrons leads to an instability of the normal electronic state (namely instability of the Fermi surface) and to the formation of a coherent many-body state. The attractive potential binds two electrons of opposite spin together forming Cooper pairs with zero total spin, that condensate to a single state and form a condensate. In BCS ground state, a fraction of electrons are condensed into a coherent superfluid while the remaining electrons exist in a normal state. As the temperature is raised through the critical temperature, T_c , the fraction of electrons in the superfluid state condensate, and the system, as a whole, undergoes

2. SUPERCONDUCTIVITY IN 2D MATERIALS

a second-order phase transition.

BCS theory ([85, 86, 114] discusses the emerging of this bound state in the presence of many electrons and it is important to emphasize the approximation made in the theory:

1. Pairing interaction is weak
2. The density of state is not varying too fast near the Fermi surface
3. The pairing interaction is constant and independent of momentum ($V_{qk} = V_o$)
4. The pairing interaction occurs within the cut-offs $\pm\hbar\omega_D$ near the Fermi surface, where ω_D is the Debye frequency, and zero otherwise.

The Cooper problem [85] deals with the case of two electrons near the Fermi surface. To begin with, the ground state of a free electron gas corresponds to complete filling of the one-electron energy levels of wavevectors k and energy $\hbar^2 k^2/2m$ up to certain energy $E_F = \hbar^2 k_F^2/2m$ (the Fermi energy). However, in the presence of any attractive interaction, no matter how weak, this state becomes unstable. This is the main setting of Cooper problem [101].

We take two-electron wave function $\Psi(r_1, r_2)$. Expanding Ψ in plane waves:

$$\psi(r_1 - r_2) = \sum_k g(k) e^{ik \cdot (r_1 - r_2)} \quad (2.1)$$

$g(k)$ is the probability amplitude for finding one electron in the plane-wave state of momentum $\hbar k$ and other electron ($-\hbar k$). Since states $k < k_F$ are already occupied, the Pauli exclusion principle imposes: $g(k)=0$ for $k < k_F$, and Schrodinger equation is:

$$-\frac{\hbar}{2m}(\nabla_1^2 + \nabla_2^2)\psi(r_1, r_2) + V(r_1, r_2)\psi = (E + \frac{\hbar^2 k_F^2}{m})\psi \quad (2.2)$$

When we solve this, we find the equation for $g(k)$:

$$\frac{\hbar^2}{m}k^2 g(k) + \sum_{k'} g(k') V_{kk'} = (E + 2E_F)g(k) \quad (2.3)$$

$$V_{kk'} = \frac{1}{L^3} \int V(r) e^{-i(k-k') \cdot r} dr \quad (2.4)$$

$V_{kk'}$ is the matrix element of the interaction between the electronic states k and k' . This equation is known by the name the Bethe-Goldstone equation for two-electron problem. For $E > 0$, it has a continuous spectrum describing collisions of

2. SUPERCONDUCTIVITY IN 2D MATERIALS

two electrons from initial state $(k, -k)$ to final $(k', -k')$ of the same energy. However, if interaction V is attractive, the bound state solution could occur for $E < 2E_F$. We can take the simplified expression for $V_{kk'}$, making interaction attractive and constant in an energy band $\hbar\omega_D$ above the Fermi level:

$$V_{kk'} = \begin{cases} -\frac{V}{L^3}, & \frac{\hbar^2 k_F^2}{2m} < E_F + \hbar\omega_D \quad \text{and} \quad \frac{\hbar^2 k'^2}{2m} < E_F + \hbar\omega_D \\ 0, & \text{otherwise} \end{cases} \quad (2.5)$$

Self-consistency condition is:

$$1 = \frac{V}{L^3} \sum_{k'} \frac{1}{-E + \frac{\hbar^2 k'^2}{m} - 2E_F} \quad (2.6)$$

$$E_F < \frac{\hbar^2 k'^2}{2m} < E_F + \omega_D \quad (2.7)$$

We set:

$$\xi' = \frac{\hbar^2 k'^2}{2m} - E_F \quad (2.8)$$

And introduce the density of states per unit of energy interval:

$$N(\xi') = (2\pi)^{-3} 4\pi k'^2 \frac{dk'}{d\xi'} \quad (2.9)$$

Assuming $\hbar\omega_D \ll E_F$, we can consider DOS constant and replace it with $N(0)$ making the condition after integration:

$$1 = \frac{1}{2} N(0) V \ln \frac{E - 2\hbar\omega_D}{E} \quad (2.10)$$

In limit of weak interaction $N(0)V \ll 1$, energy is:

$$E = -2\hbar\omega_D e^{\frac{2}{N(0)V}} \quad (2.11)$$

So we can conclude that there is a bound state of two-electrons and generalize it to case of many electrons. For present interaction V in free electron gas, electrons will group in pairs and normal state becomes unstable. It is important to emphasize that the instability persists even for very weak V as long as it is attractive (in contrast to 3D systems where attractive interaction has to exceed a certain threshold, for 1D and 2D there is no threshold). Another remark is about binding energy. As shown, binding energy is proportional to $e^{-2/NV}$. The great algebraic difficulty is that it cannot be expanded in powers of V for $V \rightarrow 0$. This represent a general problem in development of theory of superconductivity.

2. SUPERCONDUCTIVITY IN 2D MATERIALS

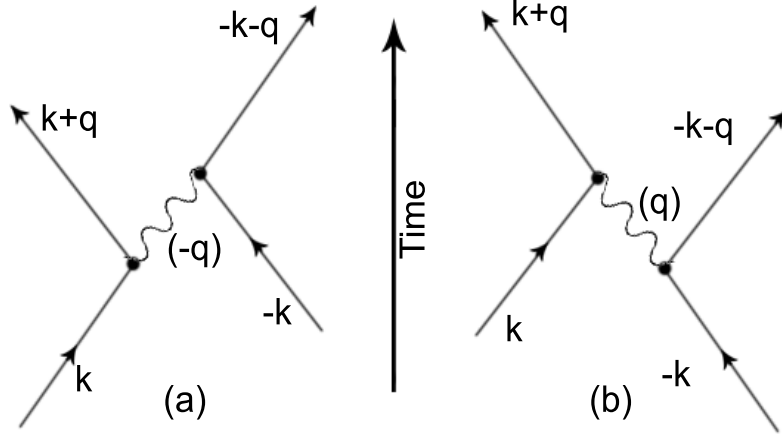


Figure 2.2.: Diagrammatic representation of the effective electron–electron interaction through the exchange of a virtual phonon of momentum $\hbar q$. In process (a) the electron k emits a phonon of wave-vector $-q$. The phonon is absorbed later by the second electron. In process (b) the second electron in state $(-k)$ emits a phonon q , and later it is absorbed by the first electron.

Let's generalize this discussion since simple electron gas (where we only have Coulomb repulsion) is not favourable for the Cooper problem. We need to have an attractive interaction and to obtain matrix element $V_{kk'}$, the electrons interact with one another, exchanging virtual particles.

The mechanism behind the weak attractive force that binds Cooper pairs was first suggested by Fröhlich [113], where he proposed that the electron-phonon interaction leads to superconductivity.

The matrix element $V_{kk'}$ of the electron-electron interaction between initial and final state, $(k, -k)$ and $(k', -k')$ respectively, contains two terms:

1. Coulomb repulsion $U_c(r_1-r_2)$ between two electrons

$$\langle I | \mathcal{H}_c | II \rangle = \int U_c(\rho) d\rho e^{iq\rho} = U_q \quad q = k' - k \quad (2.12)$$

2. One electron may emit a phonon that will be later reabsorbed by the other electron, as shown in Figure 2.2.

The initial state has energy $E_I = 2\xi_k$ and the final state $E_{II} = 2\xi_{k'}$. By the law of momentum conservation, there are two intermediate states with the same energy:

$$E_{i1} = E_{i2} = \xi_{k'} + \xi_k + \hbar\omega_q \quad (2.13)$$

2. SUPERCONDUCTIVITY IN 2D MATERIALS

The second-order matrix element, coupling states I and II, is:

$$\langle I | \mathcal{H}_{indirect} | II \rangle = \sum_i \langle I | \mathcal{H}_{ep} | i \rangle \frac{1}{2} \left(\frac{1}{E_{II} - E_i} + \frac{1}{E_I - E_i} \right) \langle i | \mathcal{H}_{ep} | II \rangle \quad (2.14)$$

Sum is performed over all allowed intermediate states and H_{ep} is electron-phonon coupling. The matrix element of electron-phonon coupling is W_q (for emission or absorption of a phonon of wave vector q):

$$\langle I | \mathcal{H}_{indirect} | II \rangle = \frac{|W_q|^2}{\hbar} \left(\frac{1}{\omega - \omega_q} - \frac{1}{\omega + \omega_q} \right) \quad (2.15)$$

Where we defined ω as:

$$\hbar\omega = \xi_{k'} - \xi_k \quad (2.16)$$

Total matrix element is:

$$\langle I | \mathcal{H} | II \rangle = U_q + \frac{2|W_q|^2}{\hbar} \frac{\omega_q}{\omega^2 - \omega_q^2} \quad (2.17)$$

and we see when $\omega < \omega_q$, the interaction is attractive. But when this interaction is attractive, it is a special issue that has to be analyzed.

In the cas of a bare Coulomb interaction $V(r) = \frac{1}{4\pi\epsilon_0} e^2/r$ and if we look for $V(q)$, we find it is always positive.

$$V(q) = V(k - k') = V_{kk'} = \Omega^{-1} \int V(r) e^{iq \cdot r} dr \quad V(q) = \frac{4\pi e^2}{\Omega q^2} = \frac{4\pi e^2}{q^2} \quad (2.18)$$

If we take into account the dielectric function of a medium, we reduce $V(q)$ for $\epsilon^{-1}(q, \omega)$ factor. This introduces screening effect of conduction electrons and screening length as parameters. Now we have an expression for $V(q)$, where the divergence at $q=0$ is eliminated but $V_{kk'}$ is still positive:

$$V(q) = \frac{4\pi e^2}{q^2 + k_s^2} \quad (2.19)$$

Negative terms come in only when one takes the motion of the ion cores into account [163]. Electron first polarizes the medium by attracting positive ions. The ion attracts the second electron, giving an effective attractive interaction between the electrons. If this attraction is strong enough, it overrides the Coulomb repulsion and it gives rise to a net attractive interaction, as depicted in Figure 2.3.

The Pines [116] was the first to systematically test through the periodic system for superconductive materials. He used "jellium" model (solid is approximated by a fluid of electrons and point ions) and it leads to simplified expression for interaction:

$$V(q, \omega) = \frac{4\pi e^2}{q^2 + k_s^2} + \frac{4\pi e^2}{q^2 + k_s^2} \frac{\omega_q^2}{\omega^2 - \omega_q^2} \quad (2.20)$$

2. SUPERCONDUCTIVITY IN 2D MATERIALS

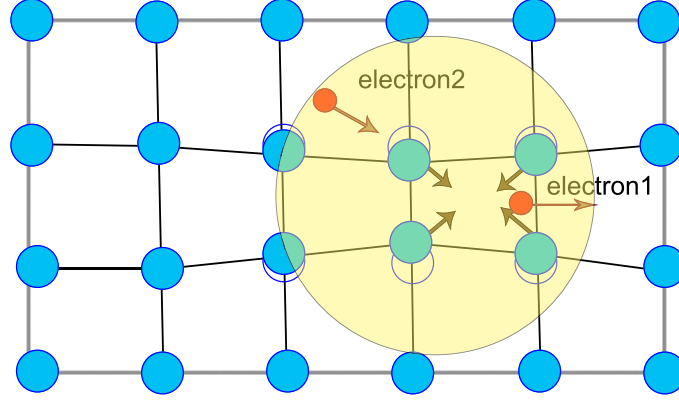


Figure 2.3.: Illustration of the mechanism Cooper pair formation as a result of lattice polarization

The first term is the screened Coulomb repulsion and second is phonon mediated interaction which is attractive for $\omega < \omega_q$. Although this expression is very approximate and it reduces to zero for $\omega=0$ while always being negative for $\omega < \omega_q$, regardless of the properties of material, it is important to illustrate that phonon-mediated interaction is of the same order of magnitude as the direct one.

So we concluded that the Fermi sea is unstable (ie. the Fermi surface is unstable) against the formation of a bound Cooper pair for an attractive interaction and it is expected that pairs will condense until an equilibrium point is reached. To handle this complicated state, a new formalism had to be introduced and it is known by the name, BCS wavefunction. To avoid the problem of handling the antisymmetry of more than two electrons scheme of $N \times N$, the Slater determinant is used to specify N-electron antisymmetrized product functions. In terms of second quantization, the singlet wavefunction is:

$$|\psi_0\rangle = \sum_{k > k_F} g_k c_{k\uparrow}^* c_{-k\downarrow}^* |F\rangle \quad (2.21)$$

, where $|F\rangle$ represents the Fermi sea with all states filled up to k_F and $c_{k\uparrow}^*$ creates an electron of momentum k and spin up and $c_{k\downarrow}$ is an annihilation operator which empties the corresponding state. Then the BCS ground state is set as:

$$|\psi_G\rangle = \prod_{k=k_1 \dots k_M} (u_k + v_k c_{k\uparrow}^* c_{-k\downarrow}^*) |\phi_0\rangle \quad (2.22)$$

where $|u_k|^2 + |v_k|^2 = 1$. This form implies that the probability of the pair $(k\uparrow, -k\downarrow)$ being occupied is $|v_k|^2$ and probability that it is unoccupied is $|u_k|^2 = 1 - |v_k|^2$.

2. SUPERCONDUCTIVITY IN 2D MATERIALS

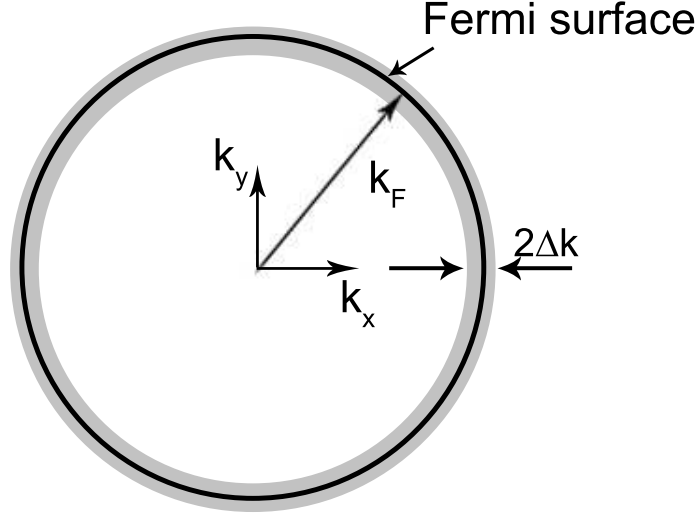


Figure 2.4.: In the BCS picture, only the electrons within the thin layer near the Fermi surface (gray circle) interact via phonons.

The u_k and v_k differ by the phase factor $e^{i\phi}$, where ϕ is independent of k and it is the phase of the macroscopic condensate wavefunction [160].

$$|\psi_\phi\rangle = \prod_k (|u_k| + |v_k|e^{i\phi}c_{k\uparrow}^*c_{-k\downarrow}^*)|\phi_0\rangle \quad (2.23)$$

BCS ground state function can be expressed as sum:

$$|\psi_G\rangle = \sum_N \lambda_N |\psi_N\rangle \quad (2.24)$$

Where members of $|\psi_N\rangle$ term are identified by a common phase factor $e^{iN\phi}$ where $N/2$ is the number of pairs in an N -particle state. (for simpler notation in this part we'll switch from k, k' used in two electron problem to k, l . The cutoff energy $\hbar\omega_C$ of Cooper's attractive matrix element is expected to be of the order of the Debye energy $\hbar\omega_D = k\Theta_D$, which characterizes the cutoff of the phonon spectrum, so although in this part ω_C will be used, ω_D could be equally utilized in description. Using the vibrational method, as in original BCS paper, the explicit values of u_k and v_k are found. Calculations start with the so-called pairing Hamiltonian.

$$\mathcal{H} = \sum_{k\sigma} \epsilon_k n_{k\sigma} + \sum_{kl} V_{kl} c_{k\uparrow}^* c_{-k\downarrow}^* c_{-l\downarrow} c_{l\uparrow} \quad (2.25)$$

To regulate mean number of particles, there has to be an included term $-\mu N_{op}$, where μ is the chemical potential (or Fermi energy) and N_{op} is a particle-number operator.

2. SUPERCONDUCTIVITY IN 2D MATERIALS

Inclusion of this term is mathematically equivalent to taking the zero of kinetic energy to be μ or (E_F)

$$\delta\langle\psi_G|\mathcal{H} - \mu N_{op}|\psi_G\rangle = 0 \quad (2.26)$$

$$\delta\langle\psi_G|\sum_{k\sigma}\xi_k n_{k\sigma} + \sum_{kl}V_{kl}c_{k\uparrow}^*c_{-k\downarrow}^*c_{-l\downarrow}c_{l\uparrow}|\psi_G\rangle = 0 \quad (2.27)$$

, where $\xi_k = \varepsilon_k - \mu$ is a single-particle energy relative to the Fermi energy. Solving above expression we get:

$$\langle\psi_G|\mathcal{H} - \mu N_{op}|\psi_G\rangle = 2\sum_k\xi_k v_k^2 + \sum_{kl}V_{kl}u_k v_k u_l v_l \quad (2.28)$$

We define quantities:

$$\Delta_k = -\sum_l V_{kl}u_l v_l \quad (2.29)$$

$$E_k = (\Delta_k^2 + \xi_k^2)^{1/2} \quad (2.30)$$

E_k is excitation energy of a quasi-particle of momentum $\hbar k$, while Δ_k is minimum excitation energy or energy gap.

By solving the equations we get:

$$\Delta_k = -\frac{1}{2}\sum_l \frac{\Delta_l}{(\Delta_l^2 + \xi_l^2)^{1/2}} V_{kl} \quad (2.31)$$

BCS model states:

$$V_{kl} = \begin{cases} -V & \text{if } |\xi_k| \text{ and } |\xi_l| \leq \hbar\omega_c \\ 0 & \text{otherwise} \end{cases}, \quad (2.32)$$

and we get

$$\Delta_k = \begin{cases} \Delta & \text{for } |\xi_k| < \hbar\omega_c \\ 0 & \text{for } |\xi_k| > \hbar\omega_c \end{cases} \quad (2.33)$$

So, by changing the sum to integral we get:

$$\Delta = \frac{\hbar\omega_c}{\sinh[1/N(0)V]} \approx 2\hbar\omega_c e^{-1/N(0)V} \quad (2.34)$$

This last step is justified in the weak-coupling limit $N(0)V \ll 1$. After Δ is found, u_k and v_k can be easily calculated:

$$v_k^2 = \frac{1}{2}\left(1 - \frac{\xi_k}{E_k}\right) = \frac{1}{2}\left[1 - \frac{\xi_k}{(\Delta^2 + \xi_k^2)^{1/2}}\right] \quad (2.35)$$

2. SUPERCONDUCTIVITY IN 2D MATERIALS

$$u_k^2 = \frac{1}{2} \left(1 + \frac{\xi_k}{E_k} \right) = 1 - v_k^2 \quad (2.36)$$

By outlining the work of Fröhlich [113] and Bardeen and Pinnes [116], we can conclude: E_k is defined as the excitation energy of a fermion quasi-particle and it must be a positive quantity $\geq \Delta$. The probability that is excited in thermal equilibrium is the Fermi function:

$$f(E_k) = (e^{\beta E_k} + 1)^{-1} \quad (2.37)$$

, where $\beta=1/kT$. For $E_k > \Delta$ $f(E_k)$ goes to zero at $T=0$ for all k , including $|k| < k_F$. We can generalize:

$$\Delta_k = - \sum_l V_{kl} \frac{\Delta_l}{2E_l} \tanh \frac{\beta E_l}{2} \quad (2.38)$$

In BCS approximation, $V_{kl}=-V$ and $\Delta_k=\Delta_l=\Delta$ and self-consistency condition becomes:

$$\frac{1}{V} = \frac{1}{2} \sum_k \frac{\tanh(\beta E_k/2)}{E_k} \quad (2.39)$$

This equation determines the temperature dependence of energy gap $\Delta(T)$. For critical temperature T_c , $\Delta(T) \rightarrow 0$ and $E_k=|\xi_k|$ and applying this we get:

$$\frac{1}{N(0)V} = \int_0^{\beta_c \hbar \omega_c / 2} \frac{\tanh x}{x} dx \quad (2.40)$$

Both T_c and Δ depend on material properties such as the phonon spectrum, the electronic structure and the electron-ion coupling strength. However, it is possible to form various thermodynamic ratios, which are independent of material parameters. In the weak coupling we obtain:

$$kT_c = \beta_c^{-1} = 1.13 \hbar \omega_c e^{-1/N(0)V} \quad (2.41)$$

$$\frac{2\Delta}{k_B T_c} = 3.53 \quad (2.42)$$

This ratio is universal and independent of the material. Yet deviations from these universal values (and other similar that can be derived within this theory) imply the need for improved formulation of BCS theory. For example, this ratio of superconducting Pb was closer to 4.5 (this is understood with the Eliasherg theory). Extending BCS theory to the strong coupling limit results again in a universal constant being 4, which is the maximum value attainable within BCS theory [119]. This clearly was not enough to describe certain materials and theory demanded improvement. In the '60s years of 20th century, the first discrepancies between the experimental results and theoretical predictions within BCS became obvious, making

2. SUPERCONDUCTIVITY IN 2D MATERIALS

BCS theory inadequate for superconductors with strong electron-phonon interactions. There is a significant difference in a strong coupling regime, but this is much more than just different equations for SC gap and critical temperature. In strong coupling regime, perturbation theory in the electron-phonon coupling strength no longer holds, and many aspects of physics differ.

Lastly, we can introduce a new parameter $\lambda \equiv N(E_k)V$, the electron-phonon coupling constant. Now we can define the excitation gap and critical temperature: in weak coupling ($\lambda < 1$)

$$\Delta = 2\omega_D \exp(-1/\lambda) \quad (2.43)$$

While in strong coupling ($\lambda \geq 1$):

$$\Delta = 2\omega_D \lambda \quad (2.44)$$

In the weak coupling T_c :

$$T_c = 1.13\omega_D \exp(-1/\lambda) \quad (2.45)$$

And in strong coupling:

$$T_c = \omega_D \lambda / 2 \quad (2.46)$$

(Both of these results at zero temperature [117, 118] are within the range of BCS theory.) We can conclude finally: We have phonon-mediated net attractive interaction between electrons. An electron in a state \mathbf{k}_1 (in momentum space) emits a phonon, and is scattered into a state $\mathbf{k}'_1 = \mathbf{k}_1 - \mathbf{q}$. The electron in a state \mathbf{k}_2 absorbs this phonon, and is scattered into $\mathbf{k}'_2 = \mathbf{k}_2 + \mathbf{q}$. To enable an electron to scatter from the state \mathbf{k}_1 into the state \mathbf{k}'_1 , the latter must be free (in accordance with the Pauli's exclusion principle). This is possible only in the vicinity of the Fermi surface which is represented in momentum space by a sphere of radius k_F , (as shown in Figure 2.4).

Electrons with energies that differ from the Fermi energy by no more than $\hbar\omega_D$ are attracted to each other. In the BCS model, only those electrons that occupy the states within a narrow spherical layer near the Fermi surface experience mutual attraction. The thickness of the layer $2\Delta k$ is determined by the Debye energy as $\Delta(k) \sim \omega_D$. The electron-electron attraction mediated by the background crystal lattice can crudely be pictured as follows; An electron tends to create a slight distortion of the elastic lattice as it moves because of the Coulomb attraction between the negatively charged electron and the positively charged lattice, as illustrated in Figure 2.3. If the distortion persists for a brief time (retardation), a second passing

2. SUPERCONDUCTIVITY IN 2D MATERIALS

electron will feel the distortion and will be affected by it. Under certain circumstances, this can give rise to a weak indirect attractive interaction between the two electrons which may more than compensate their Coulomb repulsion. Thus, as shown in Figure 2.3, the process of electron pairing in conventional superconductors is local in space, but non-local in time.

We can conclude that in BCS, we have pairing in k space i.e. in 2D space on the Fermi surface. Any attractive interaction, no matter how small it is, in 1D and 2D leads to bound state. In 3D case, there is a certain threshold that has to be overcome. Essentially this is one of the reason for 2D systems are favourable for superconductivity.

All the above discussion in this sub-chapter is for superconductors with weak coupling between electrons. For the phonon mechanism, Eliashberg [120] generalized BCS theory to a strong coupling electron-phonon model and later extended by Scalapino, Schieffer and Wilkins [121] into the theory we call today the strong coupling Migdal-Eliashberg theory [120, 122]. The primary restriction for the applicability of the Eliashberg theory is in the fact it is local in space and retarded in time. Also, when the impact of the Coulomb interaction is great, which usually manifests itself in magnetic behaviour, no justifiable theory of superconductivity exists. In this dissertation, all studied systems are strongly within applicability of the Eliashberg theory.

2.2.2. The Migdal-Eliashberg Theory, BCS Limit and the Allen-Dynes-McMillan Formula

As introduction to changes that the Eliashberg theory made, a short digression to first signs of unsuitableness of BCS theory will be made. The instantaneous nature of the BCS interaction did not include enough of the physics of the electron-phonon system. The most prominent example can be seen in specific heat and in a finite lifetime of electron quasi-particle states, namely the electron-phonon interaction which causes a mass enhancement of electron-state near the Fermi level. In many materials these effects are very strong and well-defined quasi-particles no longer exist.

The following important issue was the prediction of superconducting properties such as the critical temperature, superconducting gap etc. and deficiency of the BCS was apparent there. However, starting from it, first-principles Green's function

2. SUPERCONDUCTIVITY IN 2D MATERIALS

method, within Migdal-Eliashberg formalism provided a very accurate description of the superconducting state.

The electron-electron coupling provided by the Eliashberg theory is local in space and retarded in time, reflecting the delay in the development of lattice over-screening. In contrast to instantaneous nature of BCS model interaction, this interaction is attractive for any pair of electrons both within ω_D of the Fermi surface. Another limitation of this theory is that the Eliashberg theory is valid only when $\frac{\lambda\omega_D}{E_F} \left(\cong \sqrt{\frac{m^*}{M}} \right) \ll 1$, where E_F is the Fermi level. This is the range of validity of the Migdal's theorem [123]. It argues that only single phonon scattering terms will contribute to electron self-energy (that comes from the claim that all the vertex corrections are $O(\sqrt{m^*/M})$ (m^* is the electron effective mass and M is an ion mass) compared to bare vertex and they can be ignored.

At the beginning of the 2.2.1 sub-chapter, we demonstrated the Fröhlich Hamiltonian. The Fröhlich interaction can be observed as very similar to the electron-electron interaction via Coulomb forces, so the mutual scattering of two electrons can be explained through the electron-phonon-electron interaction in the same way. However, the problem appears with the phase transition to the superconducting state, which prevents application of the perturbation theory developed for a metal in the normal state. Due to the existence of essential singularity at the function $\exp \frac{1}{\lambda}$. Solution for this problem can be found in the 1960 by Nambu [124] who showed how the formalism used for normal state can be rewritten in such a way that the diagrams used for normal state can be applicable also to the superconducting state. The inclusion of Coulomb interaction causes the electron-phonon interaction to be screened and this causes a significant reduction. Although there is a strong electron-phonon coupling, and phonons' correction to the electron-phonon vertex are small. Moreover, the Coulombic correction is not necessarily small, but constant factors, so they can be included in the coupling constant. Detail derivation of Eliashberg equations is given in the Appendix of this dissertation in section A.2.1. Here discussion will be continued stating that the equilibrium superconducting properties of any material can be derived from the knowledge of the spectral function or the Eliashberg function α^2F [131, 125] where α is the average electronphonon interaction and F is the phonon density of states :

$$\alpha^2 F(\omega) = N(0) \sum_{q,\nu} g_{q,\nu}^2 \delta(\omega - \omega_{q,\nu}) = \frac{1}{N(0)} \sum_{k,k'} \sum_{\nu} |g_{k,k',\nu}|^2 \delta(\varepsilon_{k'}) \delta(\varepsilon_k) \delta(\omega - \omega_{q,\nu}) \quad (2.47)$$

2. SUPERCONDUCTIVITY IN 2D MATERIALS

This function measures the contribution of phonons with frequency ω to scattering processes of electrons at the Fermi level and is related to the dimensionless electronphonon coupling parameter λ :

$$\lambda = 2 \int_0^\omega \frac{\alpha^2 F(\omega)}{\omega} = \sum_{q,\nu} \lambda_{q,\nu} \quad (2.48)$$

Within the Eliashberg theory, the superconducting gap is given by:

$$\Delta = 2\hbar\omega_c \exp\left(\frac{\lambda - \mu^*}{\lambda + 1}\right) \quad (2.49)$$

and

$$T_c = 1.14\hbar\omega_c \exp\left(\frac{\lambda - \mu^*}{\lambda + 1}\right) \quad (2.50)$$

where $\hbar\omega_c$ is a cutoff frequency related to the phonon density of states and μ^* is the Coulomb pseudopotential which is the reduced Coulomb repulsion experienced by a Cooper pair. This equation has essentially summarized all the detailed information contained in the electron-phonon spectral function $\alpha^2 F$ into two parameters, λ and ω_c . However depending on the material, μ^* can have important effect on λ . The Coulomb effects [133] is hidden in the μ^* . Problem with inserting of the repulsive term in the Eliashberg equation is in fact that the Coulomb interaction cannot be introduced with same accuracy of the electron-phonon interaction (there is no natural cut-off to ensure a convergent sum as in the Matsubara's formalism). The electron-electron interaction is large in energy scale and short interaction time, comparing to electron-phonon interaction. The timescale difference is handled by the usage of an energy window ω_C with a renormalized electron-electron interaction called the Morel-Anderson pseudopotential:

$$\mu^* = \frac{\mu}{1 + \mu \ln(E_F/\omega_C)} \quad (2.51)$$

Here μ is an average electron-electron matrix element times the DOS at the Fermi level.

From the presented discussion it is beyond doubt that solving of the Eliashberg equations, even for simple systems is a complex and demanding task. McMillan suggested a simpler approach, that today we know under the name the McMillan formula [135]. It is obtained through a fit of a large set of results obtained considering the spectral function of a lead and solving the Eliashberg equation in a certain range of the parameters ($\lambda < 2$ and $\mu^* < 0.15$).

2. SUPERCONDUCTIVITY IN 2D MATERIALS

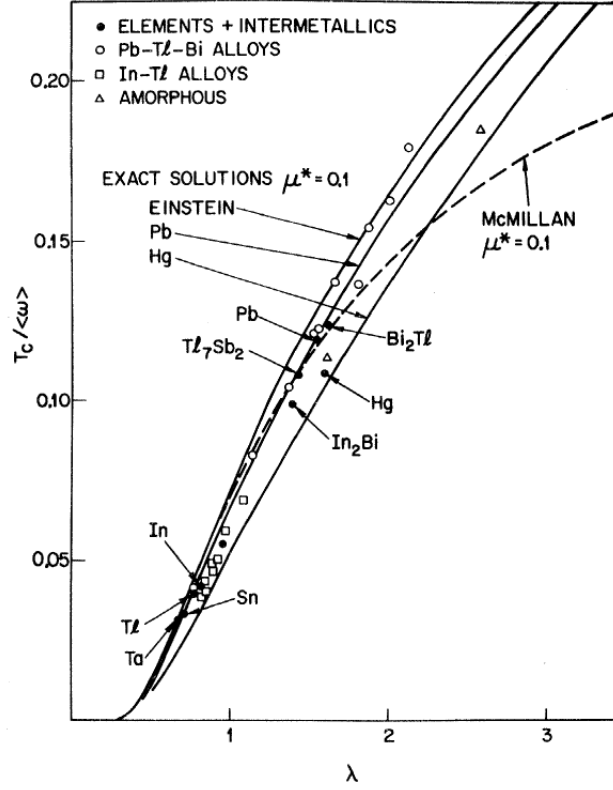


Figure 2.5.: Plotted $T_c / (\langle \omega^2 \rangle)^{1/2}$ vs λ . The solid curves are calculated for the various shapes of $\alpha^2 F$ with $\mu^* = 0.1$, dashed form the McMillan equation with the same μ^* , and experimental results are given as points. (Figure taken from [135])

$$T_c = \frac{\Theta_D}{1.45} \exp \left[-\frac{1.04(1 + \lambda)}{\lambda - \mu^*(1 + 0.62\lambda)} \right] \quad (2.52)$$

θ_D is the Debye temperature and λ is the electron-phonon coupling constant that can be derived from the Eliashberg function.

Allen and Dynes [127] redefined this equation, switching the $\theta_D/1.45$ with $\omega_{log}/1.2$

$$\omega_{log} = \exp \left[\frac{2}{\lambda} \int d\omega \log \Omega \frac{\alpha^2 F(\Omega)}{\Omega} \right] \quad (2.53)$$

Ω_{ln} is weighted on average of the phonon frequencies. Both parameters λ and ω_{ln} are related to the moments of the Eliashberg function $\alpha^2 F$. Although the McMillan formula predicts the upper limit of T_c even for very large λ , this is actually not true. The McMillan equation was not derived analytically, but obtained through numerical calculations in a fixed range of coupling constants so it is not possible to

2. SUPERCONDUCTIVITY IN 2D MATERIALS

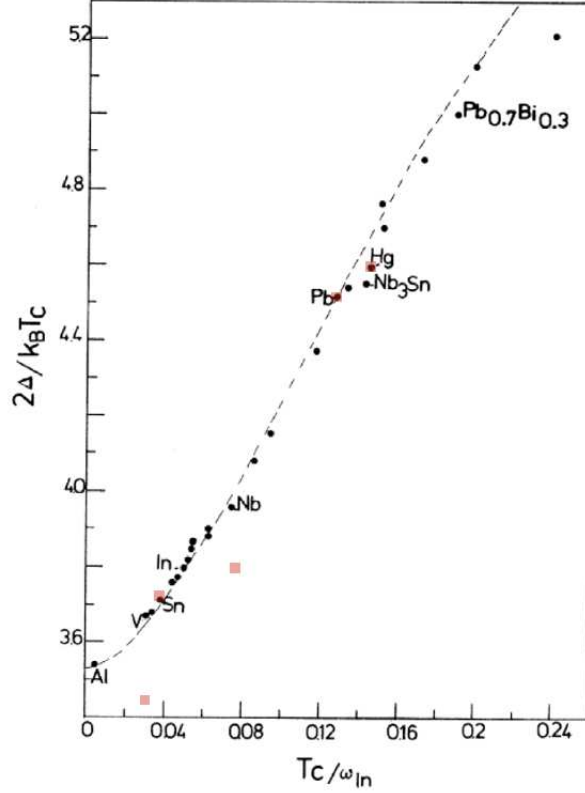


Figure 2.6.: The gap ratio $2\Delta_0/(k_B T_c)$ as a function of $T_c = \omega_I n$. The black circles indicate theoretical calculations, with some of the elements and a couple of binary alloys indicated. The unmarked circles refer various binary alloys. Note the excellent agreement of theory with experiment in the case of Sn, Pb and Hg. Figure taken from [136].

2. SUPERCONDUCTIVITY IN 2D MATERIALS

consider it for $\lambda \rightarrow \infty$. For $\lambda \gg 1$, T_c can be obtained in an analytical way as:

$$T_c = 0.183\omega_D\sqrt{\lambda} \quad (2.54)$$

To conclude, there is no upper limit for the critical temperature in the Eliashberg theory. The McMillan equation for the superconducting critical temperature giving an excellent agreement with the experimental data for λ up to 1.5 [57, 135, 131] (As shown in Figure 2.5 and Figure 2.6)

2.3. Superconductivity in 2D Materials

In the past sub-chapters, the theory of superconductivity was discussed with a brief historical recapitulation and a short introduction to the BCS and the Eliashberg theory. This sub-chapter will be devoted to particularities of the superconductivity in 2D materials. As discussed, the Cooper pair formation leads to a superconducting state and since there is an order-disorder phase transition, the dimensionality of the system can have crucial influence on its characteristics [137, 138, 139]. In low dimensional systems, it appears that phase transition would be more difficult to achieve, due to the fact that interaction between electrons becomes spatially limited and fewer number of particles is available for the interaction with a particular constituent. The question of reduction of dimensionality to its limit to the truly atomic-scale 2D system and its consequences are highly relevant not only to fundamental science but to nanotechnology and it will be crucial for the production of superconducting devices in the future [140, 141, 142]. However, this is not a new issue that appeared with the development of technology. In the 1938, Shalnikov first reported superconductivity in thin Pb and Sn films [143]. After this discovery, many investigated all kinds of thin films made of soft metals and alloys [144, 145, 146, 147]. The improvement of fabrication techniques lead to the production of highly ordered crystalline structures of just a few nm in thickness. The evolution of the thickness of 2D superconductors since 1980 is presented in Figure 2.7.

There are many more questions regarding the 2D superconducting systems. If we exclude the Mermin-Wagner theorem we discussed in the first chapter, several questions emerge: a question of localization of electrons and/or Cooper pairs [148], transition-temperature oscillations caused by quantum size effects [149, 150, 151], excess conductivity originating from superconducting fluctuations [152, 153, 154], Berezinskii-Kosterlitz-Thouless (BKT) transition [155, 156, 157] and quantum phase

2. SUPERCONDUCTIVITY IN 2D MATERIALS

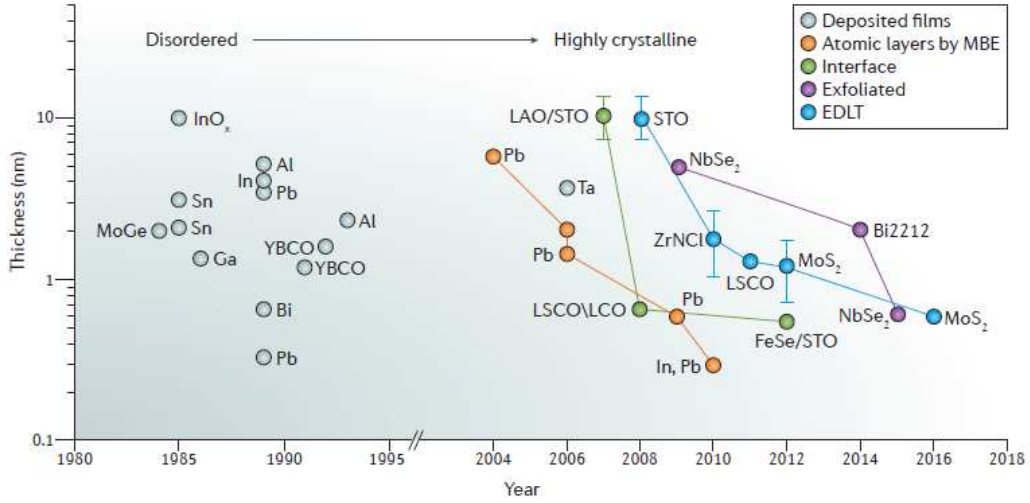


Figure 2.7.: In the past century, most 2D superconductors were fabricated by depositing metallic thin films, which led to strongly disordered, amorphous or granular samples. More recently, atomic layers grown by molecular beam epitaxy (MBE; orange), interfacial superconductors (green), exfoliated atomic layers (purple) and electric double-layer transistors (EDLT; blue) have been fabricated. The deposited films are of three kinds: InO_x, MoGe and Ta are sputtered thin films; Sn, Ga, Al, In, Pb and Bi are MBE-grown thin films; and YBa₂Cu₃O_y (YBCO) was deposited by reactive evaporation. Bi2212, Bi₂Sr₂CaCu₂O₈ + x; LAO, LaAlO₃; LCO, La₂CuO₄; LSCO, La_{2-x}Sr_xCuO₄; STO, SrTiO₃. [194])

2. SUPERCONDUCTIVITY IN 2D MATERIALS

transitions at zero temperature [158, 159] between the superconducting and the insulating phase. The BKT transition occurs in 2D systems and allows the establishment of a quasi-long range correlation of order parameter. Even without the BKT transition, the Cooper pairs can condense at the mean-field level. A system is considered to be superconducting if there exists a certain the order parameter at low temperatures however, the 2D superconductivity is a very fragile state. The introduction of disorder into a 2D superconductor can induce superconductor-insulator transition easily, compared to a 3D material where superconductivity is robust against disorders [161]. Experimental and theoretical studies demonstrated that superconductivity vanishes when the thickness of a metal film approaches 1-2nm and disorder becomes significant [162].

For 2D superconductors, the BKT transition is an important phenomenon. In 2016, A Nobel prize was awarded to John Kosterlitz, David Thouless and Duncan Haldane for "theoretical discoveries of topological phase transitions and topological phases of matter" recognizing the great importance of their work that represents a set of mathematical insights in superfluids and superconductors, but it can be also applied to semiconductors as well. The late Vadim Berezinskii did not get a proper recognition on this occasion, but his name stands equally with names of Kosterlitz and Thouless in acronym BKT showing respect to Soviet scientists who came to the same discovery a year before.

As discussed before, the Mermin-Wagner theory prohibits the emergence of the superconducting phase transition in 2D systems in a strict sense, i.e. the establishment of a long range correlation at a finite temperature. In 2D superconductors, there are phase fluctuations of order parameter Ψ due to the thermally excited free vortices, even if the amplitude of Ψ is well developed below a Cooper pair condensation temperature T_{c0} . Vortex can be defined as an object that exists in a superfluid which has zero atomic density at its centre and a 2π phase winding around it. When these vortices are moved by an external current in the transverse direction, the motion causes a voltage drop in the longitudinal direction, resulting in finite energy dissipation. This inhibits the realization of the true zero-resistance state [163]. However, a vortex in a 2D superconductor can form a bound state with an antivortex (a vortex with the opposite supercurrent circulation) to form a 'neutral' pair. If a vortices interact logarithmically as a function of the distance between them, all vortices and antivortices form pairs below a certain temperature, thus leaving no free vortices. This temperature where transition occurs is denoted as T_{BKT} . For $T > T_{BKT}$ (and

2. SUPERCONDUCTIVITY IN 2D MATERIALS

$T < T_{c0}$), the average separation ξ between free vortices diverges in a following

$$\xi \propto |T - T_{BKT}|^{-1/2} \quad (2.55)$$

as T approaches T_{BKT} and the zero-bias sheet resistance R_{sheet} decreases to zero according to a relation:

$$R_{sheet} \propto \exp \left\{ - \left(\frac{T_{c0} - T}{T - T_{BKT}} \right)^{1/2} \right\} \quad (2.56)$$

Since no free vortices exist for $T < T_{BKT}$, the true zero resistance state can be realized. The vortex-antivortex pair can unbound under the finite external current. This unbinding occurs progressively as the current is increased with a characteristic as

$$V \propto I^a \quad (2.57)$$

As the temperature is lowering, a changes from 1 to 3 at $T = T_{BKT}$ and keeps increasing at lower temperatures. This BKT transition is unique because it does not lead to true long-range order but to rather a quasi-long-range order. The spatial correlation of order decreases as a function of distance with a power-law. [163, 164].

Superconductivity is not just possible in 2D, but we can even say 2D is favourable for superconductivity. The first important reason lies in the density of states. In the previous sub-chapter, we emphasized the necessary prerequisites for superconductivity, and the density of states on the Fermi level was shown to be crucial. In 2D with normal quadratic dispersion, DOS $N(E)$ is a step function near a band edge. This means that even small doping leads to a large, metallic value of $N(0)$, unlike in 3D semimetals, where $N(0)$ increases monotonically with the carrier concentration [203]. Another point is that, due to the 2D character, the Fermi surfaces are closed curves compared to closed surfaces that occur in 3D. Near band edge, these will be circles (or close to circles) making their algebraic description possible and even that of the complex generalized susceptibility $\chi(Q, \omega)$ [180]. Thus the underlying mean-field, static lattice electronic structure and the linear response is straightforward, even simple, to model [203]. In section 2.2.1, it was stated that pairing occurs in k space i.e. in 2D space at the Fermi surface. Therefore there is no threshold for the attractive interaction that forms a bound state.

All these arguments speak in favour of the presence of superconductivity in 2D materials. Contrary to the general belief that superconductivity must be suppressed as a material thickness approaches the atomic-scale limit, many 2D systems exhibited

2. SUPERCONDUCTIVITY IN 2D MATERIALS

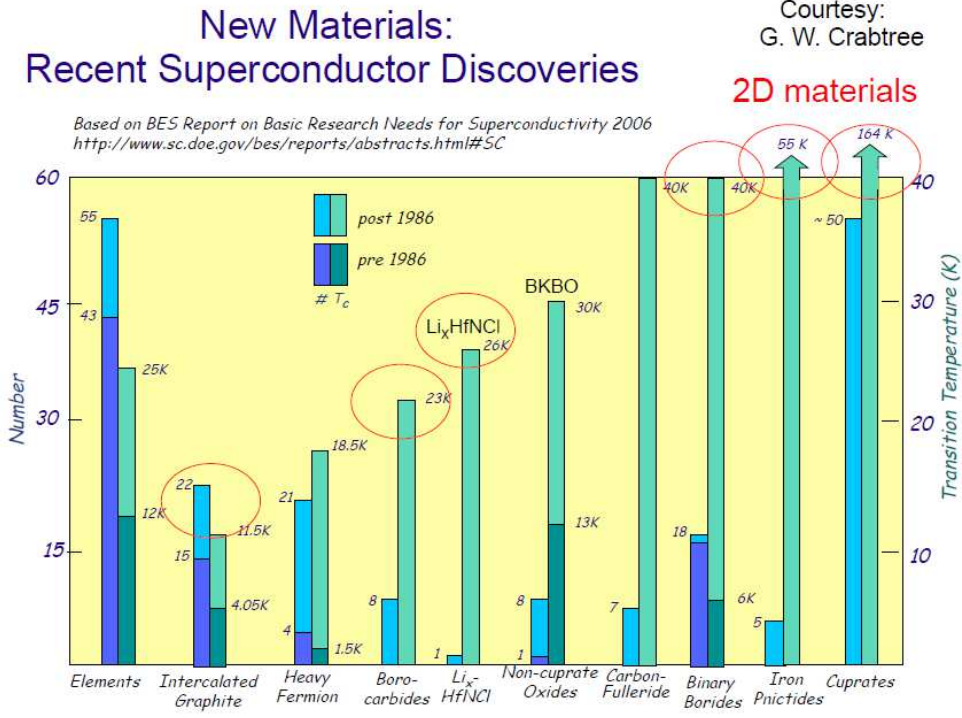


Figure 2.8.: Data relating to the main classes of high temperature superconductors [203]

robust superconductivity at low temperatures as long as the structural and compositional quality of the sample was sufficiently high. And it is not just 2D materials in the sense discussed in the post-graphenic time. An overview of the main classes of superconductors from 2006 is presented in Figure 2.8. Those superconducting materials that exhibit 2D character (2D, quasi-2D and layered materials with 2D character) are marked in red. We can see that most of the classes of HTSCs are quasi-2D. Superconductivity in 2D is not only bound to 2D materials but also to layered materials where superconductivity occurs in narrow space between layers (such in cuprates).

In the past decade, owing to technological advances and new approaches in fabrication, a variety of new 2D superconductor emerged, including interfacial superconductors [165, 166, 167, 168], molecular-beam epitaxy-grown ordered metal atomic layers [169, 170], exfoliated single layers [192, 171, 172], 2D systems showing electric-field-induced superconductivity [173, 174, 175], atomic layers grown by chemical vapour deposition [176, 177] and intercalated graphene [178, 56, 179], to which this dissertation will a specially focus .

A very brief description and examples of several interesting 2D superconducting

2. SUPERCONDUCTIVITY IN 2D MATERIALS

systems that emerged in the past decade will be presented here. Afterwards, as an introduction for main results of this dissertation, more attention will be given to superconductivity in intercalated graphite, and doped graphene and to MgB_2 and the importance of this material for the modern description of superconductivity.

Interfacial superconductivity was realized for the first time in 2007 in a 2D electron system at the $\text{LaAlO}_3/\text{SrTiO}_3(001)$ polarized interface, which was fabricated by pulsed laser deposition [165]. This was a breakthrough in the history of 2D superconductivity, because $\text{LaAlO}_3/\text{SrTiO}_3$ heterostructures show high electron mobility compared with conventional metallic films [181].

The ability to control the superconductor-metal-insulator transition electrostatically using back-gating was demonstrated soon afterwards [182]. The superconducting transition temperature of $\cong 200$ millikelvin at the interface between two insulating dielectric perovskite oxides, LaAlO_3 and SrTiO_3 , inspired the search for other superconductive materials like $\text{La}_{1.55}\text{Sr}_{0.45}\text{CuO}_4$ and La_2CuO_4 . Superconductivity at the interface between a topological insulator and Fe chalcogenide was observed in a $\text{Bi}_2\text{Te}_3/\text{FeTe}$ heterostructure [183]. Transport measurements confirmed that in this system the superconductivity is 2D in nature, realized in a layer with a thickness of ~ 7 nm, but the origin of the superconductive state remains to be understood.

A great surprise came in 2013 when superconductivity at almost 100K was reported in a single layer FeSe grown on Nb doped SrTiO_3 substrates [72] from in-situ measurements. Although bulk FeSe grown was known to be superconductor with a modest T_c of 8 K [71], this increase of the critical temperature was not expected, especially in the low dimensional limit. The ARPES measurements gave some insight but a complete description is still a subject of the heavy debate. From the ARPES measurements we know that there is a single band that crosses the Fermi level. The Fermi surface consists of the electron pockets centred at the zone edges [184] and an annealing process [185] and the suppression of spin-density waves [186] are necessary for the rise of superconductivity. The theories explaining the superconducting mechanism, range from modified BCS and forward scattering peak, to exotic ones [187, 188, 189, 190, 191]. However, leaving the mechanism of this remarkable effect aside, this discovery made important implications that high- T_c superconducting materials should be searched for (or even engineered) in heterostructures of highly crystalline 2D materials.

When discussing high crystallinity, we should definitely mention mechanically exfoliated 2D superconductors. Exfoliation of graphene [1] inspired a search for

2. SUPERCONDUCTIVITY IN 2D MATERIALS

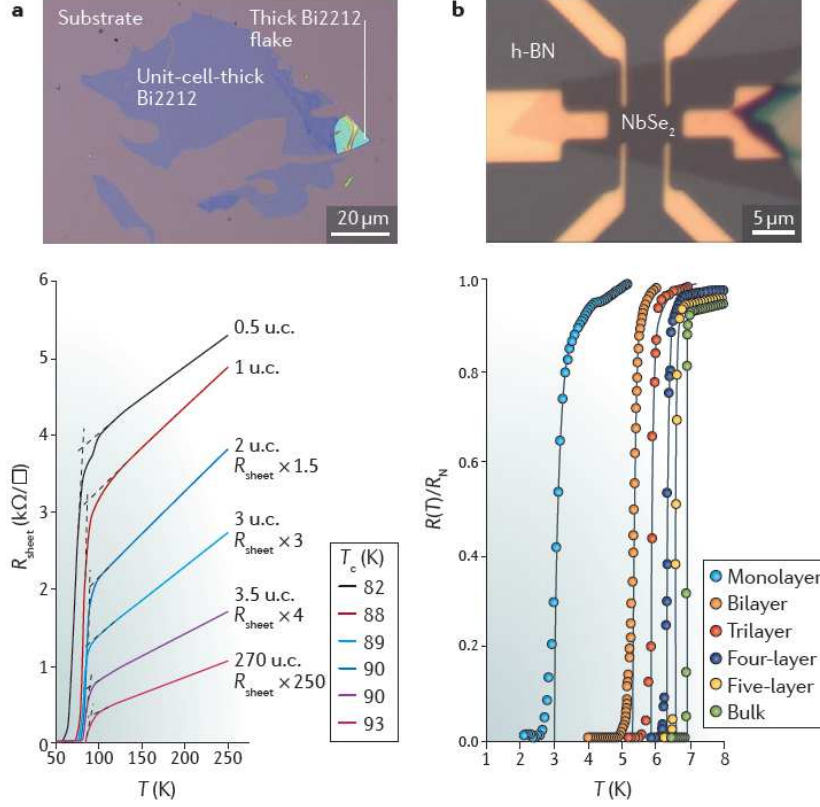


Figure 2.9.: Atomically thin superconductors based on exfoliated 2D crystals. a) Optical microscope image showing Bi₂Sr₂CaCu₂O_{8+x} (Bi2212) flakes (top). Temperature (T)-dependent sheet resistance, R_{sheet} , for Bi2212 samples with various thicknesses, ranging from 270 unit cells to half a unit cell (u.c.; bottom). b) Optical image of a bilayer NbSe₂ device capped by a thin hexagonal boron nitride (h-BN) layer for environmental protection (top). Resistive superconducting transition of NbSe₂ samples with different thicknesses, ranging from atomic thickness to bulk (bottom). R_N , onset resistance; T_c , superconducting transition temperature. Figure from the [194]

2. SUPERCONDUCTIVITY IN 2D MATERIALS

high crystalline 2D superconductors using the process of micromechanical cleavage. The advantage of this method comes from the process of cleavage of single-crystal thin flakes from bulk single (and their transfer to desired substrate) crystal without the need for the complicated process of crystal growth in vacuum chambers. The first cuprate-superconductor produced by exfoliation was a single layer of $\text{Bi}_2\text{Sr}_2\text{CaCu}_2\text{O}_{8+x}$ (Bi2212) [192], Figure 2.9. What seemed interesting was a fact that in the process of cleavage, flakes of different thickness were produced, one to few layers in thickness but also the unit cell was halved in certain flakes, making this a new structure. Due to the sensitivity on external conditions, graphene [192] and hexagonal boron-nitride [193] layers were used as a protection layer. Particularly interesting is the mechanically exfoliated 2D superconductor NbSe_2 [67, 66, 2, 171, 172] (Figure 2.9 b). Its critical temperature is dependent on the number of layers and monolayer is superconducting although it must be protected with a layer of graphene or h-BN.

One important issue in 2D superconductors must be addressed. It is the behaviour of critical temperature with the lowering of dimensionality. As mentioned at the start of this sub-chapter, it was believed that a decrease in thickness causes a decrease in T_c , as in cases of Pb and In. However, in light of new discoveries, this statement no longer represents a rule. Some materials, such as MoS_2 , ZrNCl and Bi2212 exhibit T_c almost the same as their bulk counterparts and FeSe thin films and various interfaces even have a much higher temperature. Even some materials that did not exhibit superconductivity, in 2D limit they become superconductive, such as KTaO_3 [195]. For all these materials, the underlying superconducting mechanism is still elusive but for now it seems to be a material-specific effect [194].

It is worth mentioning that the research of highly crystalline 2D or nanostructured superconductors are well described by the first-principles calculations, which contrasts the conventional 2D superconductors. Their disordered nature usually do not have realistic and precise band structures and are thus described by phenomenological or very general theories. For highly crystalline structures, the realistic calculations can be performed. They will provide a powerful tool for explanation properties and as well in the prediction of new materials.

2.4. Superconductivity in Graphene and Related Materials

Ever since graphene was isolated, the pursuit for superconductivity has been a continuous struggle and myriads of theoretical studies predicted unusual pairing mechanism originating in the chiral Dirac electrons and pseudo-spin [48, 49, 50], and yet none of them got an experimental verification. As many graphene derived materials show superconducting properties [51, 52, 53, 54, 55], it was expected to question if graphene planes in those materials have crucial role in the occurrence of superconductivity and whether the same effect could be observed in low dimensional limit, under the same conditions. Before a discussion on specific case of superconductivity in doped graphene, it will be briefly reviewed why and how could graphene become superconducting.

With a recent experimental verification of superconducting Li-doped graphene based on angle-resolved photoemission spectroscopy (ARPES) measurements of its spectral function 5.10 by the Damascelli group [56], it is safe to assume a conventional electron-phonon interaction mediated superconductivity in a doped graphene.

If we recall the McMillan formula from the previous sub-chapter, Θ_d is the Debye temperature and V_0 the electron-phonon coupling (EPC) potential figure. For graphene, Θ_d is almost an order magnitude larger than in typical metals, which is beneficial. And although V_0 is not negligible (due to the strong electron-phonon coupling term $\lambda=0.2$ [55]), the problem is caused by DOS which is zero in the Dirac point and very small in its vicinity, which makes superconductivity not observable in graphene. Graphite intercalation compounds (GIC) are a well-studied family of materials based on highly oriented pyrolytic graphite (HOPG) with layers of (usually small alkali metal or rare earth) ions arranged between the graphene layers in XC_6 stoichiometry (or sometimes much larger ions in XC_8 stoichiometry) [51]. They are divided by the number of graphene layers intercalated in-between two consecutive ionic layers and named stage 1, 2 (etc. stage 2 corresponds to two graphene planes in-between two ionic planes). Many of GICs exhibit superconductivity which was established and measured several decades ago, researchers study them with undiminished interest and debate whether the graphene derived π -bands have a prominent role or whether it could be solely explained by the 3D spherically symmetric electronic bands derived from the intercalated ions [52, 53, 54, 55]. KC_8

2. SUPERCONDUCTIVITY IN 2D MATERIALS

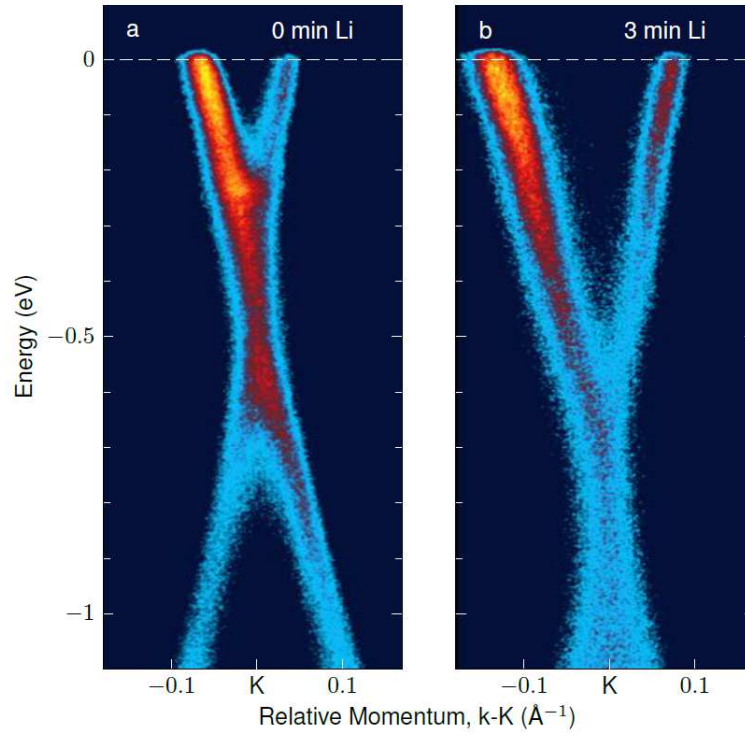


Figure 2.10.: a) Dirac dispersion from 3-minute Li-decorated graphene, exhibiting kink anomalies due to electron-phonon coupling. b) Dirac-cone dispersion measured by ARPES at 8K after 3 minutes of Li-evaporation [56]

2. SUPERCONDUCTIVITY IN 2D MATERIALS

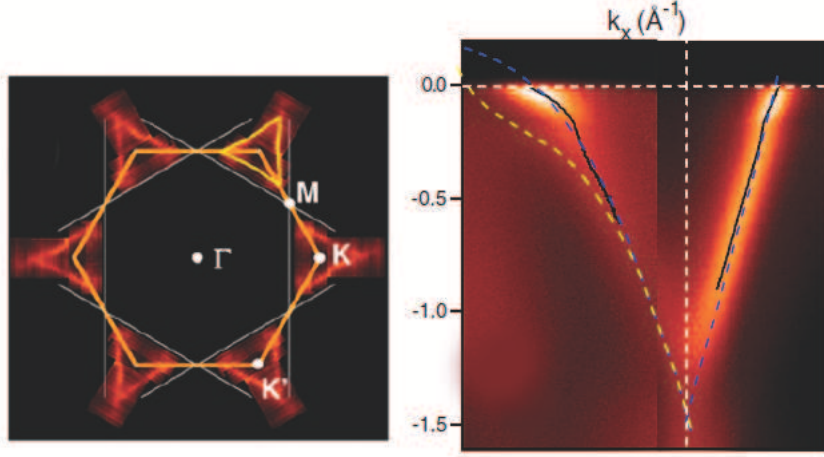


Figure 2.11.: Electronic band-structure of the stage 1 GIC CaC_6 as measured by angle resolved photon emission spectroscopy (ARPES). In contrast to the band-structure of graphite, the dispersion relation of CaC_6 is equivalent to the band-structure of highly doped monolayer graphene. Figure adapted from [55].

($T_c=0.5\text{K}$), YbC_6 ($T_c=6\text{K}$) and CaC_6 ($T_c=11.5\text{K}$) have been found to be superconductors [54, 55]. With development of the experimental techniques, mainly ARPES and STM, these materials were again examined offering an insight that was unavailable several decades ago provided the clues for theories of graphene π -bands' as an origin of superconductivity.

Namely, the band structure of CaC_6 is basically identical to the graphene monolayer's band-structure with the strongly elevated Fermi level (Figure 2.11) and three interesting conclusions about the intercalant layer could be derived from this:

1. The ionic planes increase the interlayer spacing between the graphene sheets, for CaC_6 from 3.35 \AA to 4.52 \AA . This results in their effective electronic decoupling and without a direct electronic hopping between the graphene planes, the band-structure is equivalent to that of a monolayer graphene;
2. The positively charged Ca^{2+} ions dope the graphene planes and elevate their Fermi energy to extremely high values in close proximity to the van Hove singularities in the M-points with their high DOS. Here the charge transfer per ion depends on the ion in various GIC's (highest percentages of $\sim 60 - 70\%$ obtained for CaC_6);

2. SUPERCONDUCTIVITY IN 2D MATERIALS

Intercalation compound	Electron Doping	Interlayer Separation (Å)	Interlayer band occupation	$T_c(K)$
Graphite	0	3.35	No	-
LiC ₆	1/6	3.7	No	-
LiC ₃	1/3	3.7	No	-
LiC ₂	1/2	3.7	Yes	1.9
KC ₁₆	1/16	5.2	No	-
KC ₈	1/8	5.2	Yes	0.14
CaC ₆	1/3	4.6	Yes	11.5
YbC ₆	1/3	4.7	Yes	6.5
BaC ₆	1/3	5.25	Yes	-

Table 2.1.: The relation between the occupation of interlayer states and the observations of superconductivity. Adapted from [63]

3. As the intercalated layers arrange in crystallographic order, they give rise to new phonon branches which in turn can couple to the π -band electrons. ARPES data of CaC₆ [55] confirms that these additional phonons lead to an overall enhancement of the electron-phonon coupling parameter λ from ~ 0.2 in pure graphite to ~ 0.85 in CaC₆.

However, not all GIC's are superconducting. In the superconducting GIC at the Fermi level, an interlayer band has been formed and it enhances the electron-phonon coupling constant λ [58]. Therefore, due to the presence of the interlayer band, the number of carriers is augmented, the coupling to carbon out-of-plane vibrations is enhanced and there is coupling to the intercalant vibrations as well. The electron-phonon coupling constant is proportional to the DOS at the Fermi level and the deformational potential D and inversely proportional to the square of phonon frequency of the mode coupled to electrons.

For the appearance of superconductivity, it is necessary to have the charge transfer to graphene layer, but also the interlayer band must be formed on the Fermi level.

The electron-phonon coupling constant increases with the deformation potential D which depends on the distance between adatoms and the graphene, h . The smaller the distance is, the larger D becomes. The distance h cannot be decreased infinitely, since a too small h will cause a complete charge transfer and an upshift of the inter-

2. SUPERCONDUCTIVITY IN 2D MATERIALS

calant band, which then becomes empty and forms above the Fermi level. Another important prerequisite for the introduction of superconductivity is the existence of coupling between carbon out-of-plane vibrations and electrons (which is essential since the coupling with in-plane vibration is not large enough and λ has a small value). This is achieved by the transitions between the graphene π^* states and the interlayer band.

Not all types of intercalant atoms produce superconductivity or significantly increase T_c . It seems that the charge transfer from the interlayer is crucial. Though charge transfer is necessary, the completion of the charge transfer is deleterious for the enhancement of the superconductivity. In some of GICs, the charge transfer between adatom and graphene layers in GIC is incomplete and they display a superconductivity, on the other hand, like Li-GIC, where the charge transfer is complete resulting in low T_c (0.9 K) [59] (this is still under debate, some authors doubt Li-GIC is superconductive at all [54]). In the Li-GIC, there is a strong confinement for electrons along the z-axis and it prevents the occupation of the interlayer state. After the discovery of graphene, a logical question arose, whether we can use all those experiences and conclusions from GICs to graphene and could monolayer graphene be treated with same conditions to obtain superconductivity. An answer came in 2012 by Profeta and co-workers showing graphene can be superconducting in a manner similar to Li-GIC. In the Li-GIC, a strong confinement for electrons along the z-axis exists and it prevents the occupation of the interlayer state. Because the quantum confinement is removed in monolayer [60, 59], this results in the reduction of charge transfer and it is beneficial for superconductivity. Thus the Li-doped graphene is shown to be superconductive (8.1 K) with much higher T_c than in Ca-doped graphene (1.4 K). This topic will be more thoroughly discussed in Chapter 4 where the study of possibility of enhancement EPC in Li doped graphene will be presented.

Recently metal-doped few layer graphene was reported to be superconductive in variety of experiments. Li-intercalated few-layer graphene was found to have $T_c=7.4$ K from magnetization measurements (yet transport measurements did not show the evidence of resistance drop) [196]. The K-intercalated few-layer graphene produced from liquid solution shown to have $T_c=4.5$ K based on magnetic susceptibility measurements [165]. Ca-intercalated multilayer graphene was produced in UHV environment in process standard for graphite intercalation [198] and both the transport and magnetic measurement showed a superconducting transition at 7 K maximum. The Ca-intercalated bi-layer graphene (C_6CaC_6) was measured using a

2. SUPERCONDUCTIVITY IN 2D MATERIALS

micro four-point probe technique under magnetic fields and revealed $T_c^{(onset)} \approx 4\text{K}$ and $T_{c(zero)} \approx 2\text{K}$ [179].

The analysis by high-energy electron diffraction showed that the intercalated Ca atoms formed a $(\sqrt{3} \times \sqrt{3})E30^\circ$ structure against the $C(1 \times 1)$ surface of the host graphene and that this structural ordering was crucial for having a clear superconducting transition. However what was unforeseen was the result of a similar study on the Li-intercalated bilayer graphene ($C_6\text{LiC}_6$) that did not observe a superconducting transition and the ARPES measurements on the monolayer samples produced similarly indicated emergence of superconductivity at $T_c \sim 5.9\text{K}$ [56], just as the theoretical studies predicted [59].

Superconductivity in graphene laminates was recently studied as well [199]. This is a layered material, similar to bulk graphite but the coupling between layers is weaker due to the presence of the rotational disorder. A laminate with Ca showed a superconducting transition at $\sim 6\text{ K}$ but it was strongly dependent on sample conditions.

Superconductivity with a surprisingly high critical temperature was also suggested to be found in a so-called graphane after significant doping [61]. Graphane is a name for fully hydrogenated graphene with sp^3 carbon bonds [62], making it a two-dimensional analog of the cubic diamond. P-doping of graphane is proposed to be a method for making graphene a high-temperature BCS theory superconductor with a T_c above 90 K [61].

2.5. Superconductivity in Magnesium-diboride Family

Although we discussed about MgB_2 , its structure and properties in the first chapter, here just a very brief look will be given on superconductivity in MgB_2 and implications of its really surprising discovery. Superconductivity in MgB_2 is well described by the Eliashberg theory, within the multiband extension. Plenty of surprises came with its discovery. It is an *sp* metal not *d*, it has strong 2D characteristic and it becomes a HTS superconductor due to extremely strong coupling to extremely few (3%) of the phonons, rather than having the strength spread rather uniformly over the phonon spectrum. A better definition describes MgB_2 not as a metal, but as a self-doped semimetal [203] with crucial σ -bonding band nearly filled. The basic aspects of the electronic structure and pairing is in extremely strong coupling of high frequency B-B stretch modes to the strongly bonding B-B states at the Fermi

2. SUPERCONDUCTIVITY IN 2D MATERIALS

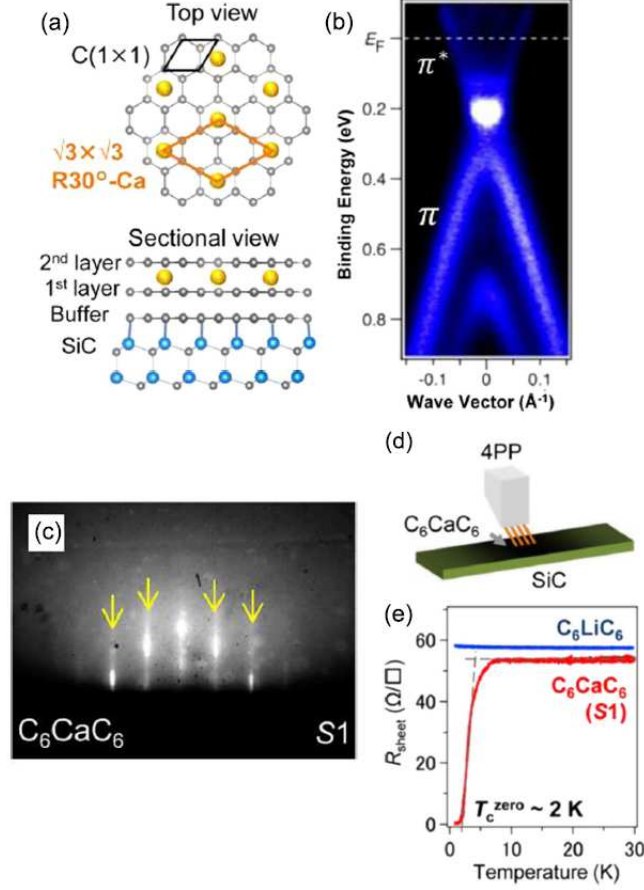


Figure 2.12.: Superconductivity of the Ca-intercalated bilayer graphene. (a) Schematic view of the crystal structure of C_6CaC_6 on SiC. (b) Band dispersions at the K point of pristine bilayer graphene obtained by ARPES. (c) RHEED pattern showing $(\sqrt{3} \times \sqrt{3})E30^\circ$ spots and streaks. (d) Schematic diagram of the four-point-probe measurement setup. (e) Comparison of temperature dependence of sheet resistance R_{sheet} between C_6LiC_6 and C_6CaC_6 . Image from Ichinokura S et al [179]

2. SUPERCONDUCTIVITY IN 2D MATERIALS

surface. This inspired a "recipe" for other materials in the same class that would have much higher T_c . The idea was to change the Fermi surface to make use of coupling to more phonon modes and provide larger electronic density of states, while retaining the structure that gives a very strong bonding [203]. Several MgB_2 -like superconductors were designed in this class. The first proposed was hole-doped LiBC. It has the same structure as MgB_2 (Lithium has one less electron than Magnesium, Carbon has one more electron than Boron) but it is insulating and hole-doping (by partial removal of Li) which were expected to make it superconducting at amazing 75K or even higher [200, 201]. It was expected that the stronger B-C bonding compared to B-B bonding, MgB_2 would give both larger matrix elements and a higher phonon energy scale. However, experimental research proved that this system would be very instable at lower pressures that 60GPa density functional calculations predicted that metallization in this structure would not occur until at least 345 GPa [202]. At the same time, other methods were considered for obtaining MgB_2 -like material. Pickett formulated this as " MgB_2 is, after all, graphite with an extra three dimensional band in the background" [203]. The difference is in the potential barrier between the honeycomb and Mg layer. Bonding σ -bonding band is present in graphene but upper edge is 2eV below the Fermi level, which is determined by the positioning of the π -bonding band at K point of the Brillouin zone. Lowering of the Fermi level was intended to be done by intercalation with highly electronegative ion, fluorine FC_2 [203], however a great degree of charge transfer left Fermi level far from the σ -bonding bands.

Search for superconductivity by MgB_2 model went in two directions, hole-doped ABC and AeB_2C_2 insulators (A stands for alkali and Ae for alkaline earth). Both predicted high critical temperature but unfortunately experimental realization was never successful. Our approach took a different turn. We were also motivated by structural similarity of MgB_2 and intercalated graphene but we went in low dimensional limit where, after the determination of stability, we continued search for superconductivity. Results of this research and our findings and conclusions are presented in Chapter 4.2.

3. AB-INITIO METHODS

3.1. Introduction to Ab-initio Methods

All results presented in this dissertation are based on the "ab-initio" (or first-principles) quantum-mechanical calculations. This means that no empirical parameters are used in order to compute the electronic structure properties of a system, but only the atomic numbers and positions are the inputs to the calculation. The increase in computer power in the last decades has made it possible to perform ab-initio calculations on larger and more realistic systems, achieving a degree of accuracy which enables direct comparison to experiments. However, despite having powerful computational resources and elegant mathematical formalism, the computation of emergent behaviour in complex systems has remained a difficult task. Materials contain a large number of electrons and atomic cores, with plenty of degrees of freedom making it almost impossible to be exactly described. While first-principles calculations performed without any simplifying approximations are still beyond the ability of current computational physics, with the use of a few important physical approximations we are able to arrive at satisfying results to many important problems. The aim of this chapter is to give a brief overview of the theoretical methods used in this thesis.

3.2. The Electronic Structure Problem

All properties of matter are in principle described by the Schrödinger equation.

$$\hat{H}\psi = \epsilon\psi \tag{3.1}$$

Although for one electron this equation has rather simple form, depending on the probability of finding the electron in some point of space, for systems containing more than one electron it become much more complex. A many-body wavefunction

3. AB-INITIO METHODS

Ψ has to be introduced to describe the position of all electrons and nuclei in the system. The Schrödinger equation for many-body system has form

$$\begin{aligned} & \left(-\frac{\hbar^2}{2m_e} \sum_{i=1}^n \nabla_i^2 - \sum_{I=1}^m \frac{\hbar^2}{2M_I} \nabla_I^2 - \sum_{i,j=1}^{n,m} \frac{Z_J e^2}{|R_J - r_i|} + \sum_{i<j}^n \frac{e^2}{|r_i - r_j|} + \right. \\ & \quad \left. \sum_{I<J}^m \frac{Z_I Z_J e^2}{|R_I - R_J|} \right) \Psi = E_{tot} \Psi \end{aligned} \quad (3.2)$$

Any observable can be extracted from the many-body wavefunction Ψ and total energy of the system ϵ . \hat{H} is the Hamiltonian operator and it depends on both electronic and nuclear degrees of freedom. We are dealing with a quantum mechanical problem with a huge number of variables and complex equations that cannot be solved exactly. In the case of condensed matter, the Hamiltonian is given by:

$$\begin{aligned} \hat{H} &= -\frac{\hbar^2}{2m_e} \sum_{i=1}^n \nabla_i^2 - \sum_{I=1}^m \frac{\hbar^2}{2M_I} \nabla_I^2 - \sum_{i,j=1}^{n,m} \frac{Z_J e^2}{|R_J - r_i|} + \\ & \quad \sum_{i<j}^n \frac{e^2}{|r_i - r_j|} + \sum_{I<J}^m \frac{Z_I Z_J e^2}{|R_I - R_J|} + V_{ext} \\ &= \hat{T}_e + \hat{T}_N + \hat{V}_{Ne} + \hat{V}_{ee} + \hat{V}_{NN} + V_{ext} \end{aligned} \quad (3.3)$$

The first two terms represent kinetic energy of the electrons and nuclei, the third term is the interaction between the nuclei and the electrons, the fourth and fifth terms are the electron-electron and nuclei-nuclei interaction, respectively and the final term is any kind of external potential (i.e. from electric/magnetic field). Accordingly, Hamiltonian depends both on electronic and nuclear degrees of freedoms making this very complicated.

3.2.1. The Born-Oppenheimer approximation

The Born-Oppenheimer (ABO) approximation [226] makes great simplification as it allows decoupling of the electronic and nuclear dynamics due to the large difference in their masses, $m_e/M_n \approx 10^{-3} - 10^{-5}$.

$$\Psi(r, R) = \varphi(R) \Phi_i(r, R) \quad (3.4)$$

This implies the motion of electrons to be considerably faster than the nuclear motion. The ABO approximation consists of the two steps, first so-called clamped-nuclei approximation, where nuclei are considered fixed. Though Coulomb repulsion

3. AB-INITIO METHODS

is still present and accounted, kinetic energy of the nuclei is omitted. Now the Schrödinger equation has form:

$$\left[-\frac{\hbar^2}{2m_e} \sum_{i=1}^n \nabla_i^2 - \sum_i V_n(r_i) + \sum_{i<j}^n \frac{e^2}{|r_i - r_j|} \right] \Psi = E\Psi \quad (3.5)$$

The electron problem can be reduced to a N-electron Hamiltonian in which the nuclei are assumed to be fixed in some given position R_I . We consider that the electrons are moving in a static external potential $E_{ext}(\mathbf{r})$ generated by the nuclei. Then the Hamiltonian of the system is reduced to:

$$H = \underbrace{-\frac{\hbar^2}{2m_e} \sum_i \nabla_i^2}_{\hat{T}} - \underbrace{\sum_{i,I} \frac{Z_I e^2}{|R_I - r_i|}}_{\hat{V}_{ext}} + \underbrace{\sum_{i<j} \frac{e^2}{|r_i - r_j|}}_{\hat{V}} \quad (3.6)$$

The second step of ABO approximation introduces the nuclear kinetic energy again and the Schrödinger equation can be solved as:

$$\left[H + \frac{1}{2} \sum_{I \neq J} \frac{Z_I Z_J e^2}{|R_I - R_J|} + E(R) \right] \chi = E_{tot} \chi(R) \quad (3.7)$$

The ABO approximation considerably simplifies many-body problem though there are certain limitation where it can be used. There is well-known issue of ABO approximation failure when electronic and nuclear dynamics are highly intertwined and nuclei motion can not be considered significantly slower than electrons.

Solving electronic Hamiltonian is simpler than total Hamiltonian without ABO approximation accounted but still it represents the fundamental challenge in the theory of electronic structure of matter. Different levels of approximations have been devised in order to solve it. For small molecules, wave-function based methods (minimization of a suitable energy functional within the space of a chosen set of approximations for the real wave-function) are feasible and give satisfying results, but this method is ineffective for larger systems. The many-body perturbation theory is good but extremely expensive numerical method for realistic systems just as a quantum Monte Carlo simulations. The DFT made a different approach and became the basis of the computational many-body physics in past years, offering optimal compromise between accuracy and computational costs. DFT treats the electron charge density instead of wave-function as fundamental variable to solve quantum mechanical many-body problem. The concept of DFT was introduced by Thomas and Fermi [204] in 1927 and in 1964 a firm theoretical foundation was given by the

3. AB-INITIO METHODS

Hohenberg and Kohn [205], who proved that the properties of material are uniquely determined by the ground state electron density. A year later, in 1965, Kohn and Sham [206] devised a simple method for finding the electron density through the use of an auxiliary system of non-interacting electrons, confining the many-body effects in an exchange-correlation energy-functional. Although at the first time, this approximation was crude but later in time it was progressively improved, allowing DFT to reach high accuracy with relatively low computational cost. The Nobel Prize in Chemistry was awarded in 1998 to Walter Kohn for his continual work on development of DFT.

3.2.2. The Hartree Theory and Hartree-Fock Equation

As shown the Born-Oppenheimer approximation simplifies consideration but the many-body problem is a complex one and the Hamiltonian derived in the Born-Oppenheimer is still not suitable for calculations. There are further approximations that must be made to achieve better accuracy and minimize calculation time. There are two distinct approaches, wave-function approach and density functional approach. In this section a very brief description of wave-function approach will be presented before focusing on the DFT approach, main in this dissertation.

Hartree proposed that the total wave function is the direct product of single particle wave functions [214], known as Hartree approximation. Therefore, the many-body wave function can be written as:

$$\Psi(r_1, r_2, \dots, r_N) = \phi_1(r_1)\phi_2(r_2)\dots\phi_N(r_N) \quad (3.8)$$

from which it follows that the electrons are independent, and interact only via the mean-field Coulomb potential. This yields one-electron Schrödinger equations as:

$$\left(-\frac{\hbar^2}{2m}\nabla^2 + V(r)\right)\phi_i(r) = \varepsilon\phi_i(r) \quad (3.9)$$

where $V(r)$ is the potential in which the electron moves, this includes both the nuclear-electron interaction and the mean field arising from the $N-1$ other electrons.

$$V_{nuc}(r) = -\frac{Ze^2}{4\pi\epsilon_0} \sum_R \frac{1}{|r - R|} \quad (3.10)$$

$$V_{ele}(r) = -\frac{e^2}{4\pi\epsilon_0} \int dr' \rho(r') \frac{1}{|r - r'|} \quad (3.11)$$

$$\rho(r) = \sum_i |\phi_i(r)|^2$$

3. AB-INITIO METHODS

However the antisymmetry of the electron wavefunction was not considered in Hartree approximation. The improvement to Hartree's theory and solution to this was introduced by Fock, who including the particle interchange in approximation. According to the Pauli exclusion principle, no two fermions can occupy the same quantum state and the many-body wave function must be anti-symmetric with respect to interchange of any two electrons. For problem of two electrons anti-symmetric wavefunction is:

$$\Psi(r_1, r_2) = \frac{1}{\sqrt{2}}[\phi_1(r_1)\phi_2(r_2) - \phi_1(r_2)\phi_2(r_1)] \quad (3.12)$$

Generalizing to many electron system the antisymmetrised wavefunction is in the form of the determinant (first introduced by Slater [215]):

$$\Psi(r_1, r_2 \dots r_N) = \frac{1}{\sqrt{N!}} \begin{vmatrix} \phi_1(r_1) & \phi_2(r_1) & \dots & \phi_N(r_1) \\ \phi_1(r_2) & \phi_2(r_2) & \dots & \phi_N(r_2) \\ \vdots & \vdots & & \vdots \\ \phi_1(r_N) & \phi_2(r_N) & \dots & \phi_N(r_N) \end{vmatrix} \quad (3.13)$$

This modification adds an extra term to the Hamiltonian which is known as exchange. This is very important term and later the DFT approach it will demonstrate, it requires specific treatment in calculations.

The electronic charge density is given as the sum of probabilities of finding electrons in every occupied state:

$$n(r) = \sum_i |\phi_i(r)|^2 \quad (3.14)$$

This charge density generated electrostatical potential (from the Poisson's equation) is known as the "Hartree potential" and it accounts for the Coulomb repulsion in this system. :

$$V_H(r) = \int dr' \frac{n(r')}{|r - r'|} \quad (3.15)$$

From the Slater determinant a single-particle solution can be found and the single particle Hartree-Fock (HF) equation is then written as:

$$\left\{ -\frac{\hbar}{2m} \nabla^2 + V_{nuc}(r) + V_{el}(r) \right\} \phi_i(r) - \sum_j \int dr' \frac{\phi_j^*(r') \phi_i^*(r') \phi_j(r)}{|r - r'|} = \varepsilon_i \phi_i(r) \quad (3.16)$$

This equation has one extra term compared with the Hartree equation, which is called the exchange term. The Fock exchange potential can be written as:

$$V_x(r', r) = - \sum_j \frac{\phi_j^*(r') \phi_j(r)}{|r - r'|} \quad (3.17)$$

3. AB-INITIO METHODS

The complete derivation of Hartree-Fock equation is given in the appendix A.3.1. The Hartree-Fock calculations have been carried out for the ground state energy of atoms, but for solids these calculations are very complicated. Additionally his scheme neglects screening of the exchange interaction, generally known as the correlation effect which can have significant impact on calculated properties.

3.2.3. The Hohenberg-Kohn Theorems

The two Hohenberg-Kohn (HK) theorems make the core of DFT. They allow the transformation of the many-body problem, in terms of many body wavefunction, to one in terms of the electronic density. These theorems can be applied to any system of interacting particles in an external potential [205]:

First HK Theorem: *The ground state particle density $n_0(r)$ of a system of interacting particles in an external potential $V_{ext}(r)$ uniquely determines the external potential $V_{ext}(r)$, except for a constant.*

In other words, there is a one-to-one mapping between the ground state density $n_0(r)$ and the external potential $V_{ext}(r)$. This means that the ground state particle density determines the full Hamiltonian, except for a constant shift of the energy, and then, at least in principle, ground states of the many-body wavefunctions can be calculated. Therefore, all properties of the system are completely determined given only the ground state density. The proof is given in the appendix A.3.2.

Second HK Theorem: *There exists a universal functional $F[n(r)]$ of the density, independent of the external potential $V_{ext}(r)$, such that the global minimum value of the energy functional*

$$E[n(r)] \equiv \int n(r)V_{ext}(r)dr + F[n(r)] \quad (3.18)$$

is the exact ground state energy of the system and the exact ground state density $n_0(r)$ minimizes this functional.

In other words, the minimum of the total-energy functional $E[n(r)]$ is the ground state energy of the system, and the density which yields its minimum is exactly the single particle ground-state density. The proof is given in the appendix A.3.3.

3.2.4. The Kohn-Sham Scheme

The HK theorems provide the ultimate theoretical foundation of DFT yet they do not propose a simple way to solve the many-body problem. The scheme proposed in [206] states that the ground state density of the original many-body interacting system is equal to the ground state of some fictitious independent particle system where all "problematic" many-body effects are incorporated into a single term. This maps the original interacting system with real potential into a non-interacting system where the electrons move within an effective Kohn-Sham single-particle potential $V_{KS}(r)$. This auxiliary system is described by Hamiltonian:

$$\hat{H}_{KS} = -\frac{1}{2}\nabla^2 + V_{KS}(r) \quad (3.19)$$

(we took $\hbar=1$, $m_e=1$, $e=1$ for simplicity of notation). For system with N independent electrons, we have an N one-electron Schrodinger equations from which we obtain the ground state.

$$\left(\frac{1}{2}\nabla^2 + V_{KS}(r)\right)\psi_i(r) = \varepsilon_i\psi_i(r) \quad (3.20)$$

The density of auxiliary system is:

$$n(r) = \sum_{i=1}^N |\psi_i(r)|^2 \quad \text{with condition} \quad \int n(r)dr = N \quad (3.21)$$

The universal functional $F[n(r)]$ is:

$$F[n(r)] = T_s[n(r)] + E_H[n(r)] + E_{xc}[n(r)] \quad (3.22)$$

$T_s[n(r)]$ is the non-interacting independent-particle kinetic energy, while $E_H[n(r)]$ is the classic electrostatic Hartree energy of electrons:

$$E_H[n(r)] = \frac{1}{2} \int \int \frac{n(r)n(r')}{|r-r'|} dr dr' \quad (3.23)$$

, and $E_{xc}[n(r)]$ is the exchange-correlation energy, which contains all the differences between exact and the non-interacting kinetic energies and also the non-classical contribution to the electron-electron interaction. Energy functional is:

$$E[n(r)] = F[n(r)] + \int n(r)V_{ext}(r)dr \quad (3.24)$$

And we obtain the ground state from its minimization under the constrain of conservation of the number of electrons (μ is chemical potential):

3. AB-INITIO METHODS

$$\delta \left\{ F[n(r)] + \int n(r) V_{ext}(r) dr - \mu[n(r)] - N \right\} = 0 \quad (3.25)$$

$$\mu = \frac{\delta T_s[n(r)]}{\delta n(r)} + V_{KS}(r) \quad (3.26)$$

$$V_{KS}(r) = V_{ext}(r) + V_H(r) + V_{XC}(r) = V_{ext}(r) + \frac{\delta E_H[n(r)]}{\delta n(r)} + \frac{\delta E_{XC}[n(r)]}{\delta n(r)} \quad (3.27)$$

$$V_H(r) = \frac{\delta E_H[n(r)]}{\delta n(r)} = \int \frac{n(r')}{|r - r'|} dr' \quad (3.28)$$

$$V_{XC}(r) = \frac{\delta E_{XC}[n(r)]}{\delta n(r)} \quad (3.29)$$

These equations are known as the Kohn-Sham equations and they have to be solved in self-consistent way (because $V_{KS}(r)$ depends on $n(r)$ through the xc potential). The detailed derivation of the KS equation is given in the appendix A.3.4. The KS energy eigenvalues do not have physical meaning, they cannot be interpreted as one-electron excitation energies of interacting many-body system. However, within the KS theory, the eigenvalues have a well-defined meaning and they are used to construct physical meaningful quantities.

The value and meaning of KS theory can be best depicted by Walter Kohns quote from the Nobel Prize lecture [208]:

"The Kohn-Sham theory may be regarded as the formal exactification of Hartree theory. With the exact E_{XC} and $V_{KS}(r)$ all many-body effects are in principle included. Clearly this directs attention to the functional $E_{XC}[n]$. The practical usefulness of ground-state DFT depends entirely on whether approximations for the functional $E_{XC}[n]$ could be found, which are at the same time sufficiently simple and sufficiently accurate."

In other words, we know that there must be a functional $E_{XC}[n]$ which gives the exact ground-state energy and density however, we do not know what this functional is. Therefore, it is crucial to construct accurate approximations to $E_{XC}[n]$. The most widely used approximation are the local density approximation or LDA and the generalized-gradient approximation or GGA. These two approximations were used in this dissertation and they will be explained in the next sub-chapter in more details.

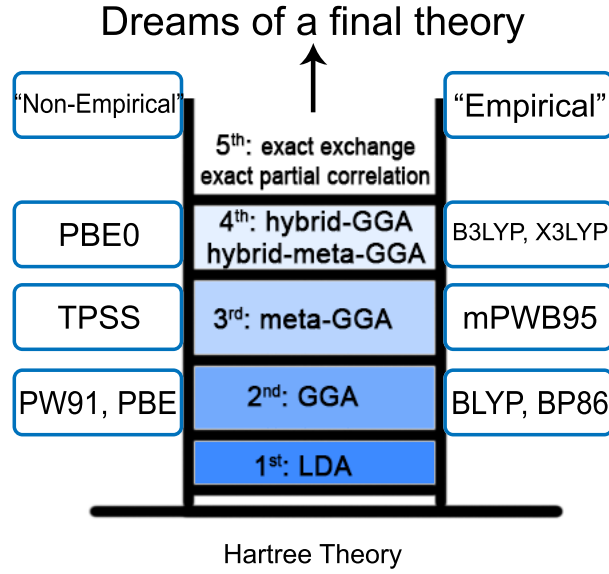


Figure 3.1.: Schematic diagram of the exchange-correlation functionals proposed by J.P. Perdew [209]

3.2.5. The Exchange-Correlation Functional

Ever since the Kohn Sham theory was introduced, there has been significant effort devoted to construct the accurate exchange and correlation functionals. As a result, today there is a great list of approximated functionals with varying levels of complexity. In 2005, Perdew [209] proposed the categorization known as "Jacobs ladder" (presented in Figure 3.1 adapted from [209]).

In this scheme the functionals are grouped according to their complexity, ranging from the Hartree approximation on "earth" to the exact exchange-correlation functional in "heaven". Furthermore, functionals can be categorized into non-empirical (formulated by "first principle") and empirical (made by fitting to experimental result). We have defined the exchange and correlation energy before as the difference between the exact total energy of a system and the classical Hartree energy. Except in very simple cases, it is impossible to treat exchange and correlation exactly and thus an approximation is in order. The quality of a DFT calculation is determined by how close the approximate exchange and correlation comes to the exact value. Before the two main approximations are discussed, we will briefly review what "exchange-correlation" actually stands for. The electron exchange arises from the fact that the system has to satisfy the Pauli Exclusion Principle (as discussed in section 3.2.2). The Slater determinant satisfies the antisymmetric property of the

3. AB-INITIO METHODS

electronic wave function, which is essential because electrons are fermions and obey Pauli exclusion principle and there cannot be two electrons at the same state. The exchange term lowers the energy by keeping the electrons of the same spin away from each other thus reducing the Coulomb repulsion. Which means that for an electron with a certain spin, there will be an area where the density of electrons with the same spin is decreased. This effect is known as the exchange hole. The correlation term is less intuitive. The correlation energy is defined as the difference between the total exact energy and the sum of kinetic and exchange energies. Correlations are a result of the collective behaviour of electrons to screen and decrease the Coulombic interaction. Unlike the exchange term, the correlations become more pronounced for opposite spins since they are more likely to occupy nearby locations. Intuitively, we can explain that due to Coulombic repulsion, the probability of finding an electron somewhere is lower if there is another electron nearby. The correlation energy is typically a small fraction of the total energy. However, it can be a very important contribution to many systems of physical and chemical interest. For the correlation energy even of the electron gas, there is not a simple analytic expression.

3.2.6. Local Density Approximation

Here the simplest functional is described, which goes under the name of Local Density Approximation to density functional theory [210, 211, 212]. In order to introduce such a functional, we study the exchange and correlation energy of a very simple system, the homogeneous electron gas. It is interesting that this is the oldest approximation but nonetheless, still very useful for a great amount of systems. A gas of electrons is constrained within a box and the potential of the nuclei is taken as constant and we consider the Coulomb repulsion between the electrons. For the homogeneous electron gas it is possible to calculate the exchange energy exactly, and it is possible to determine the correlation energy using numerical techniques. At each point in space the exchange-correlation energy is approximated locally by the exchange-correlation energy of a homogeneous electron gas with the same electron density at that point. LDA is based on the local nature of exchange-correlation and the assumption that the density distribution does not vary too rapidly (Figure 3.2).

3. AB-INITIO METHODS

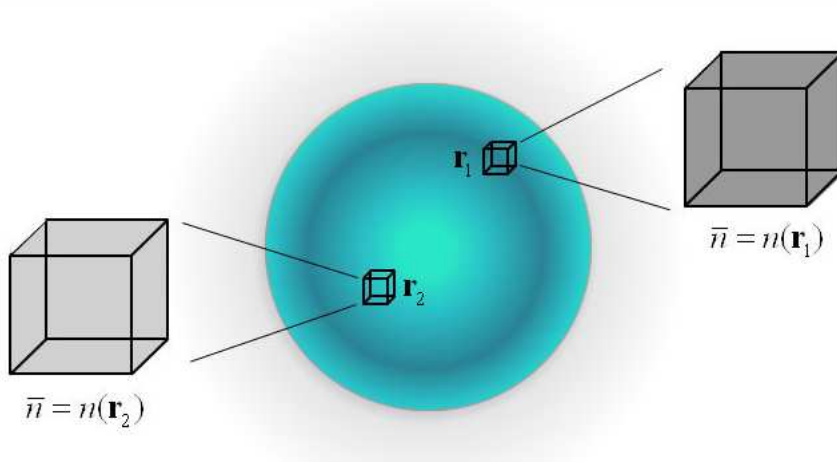


Figure 3.2.: In LDA at each point \mathbf{r} , we can replace the exact xc energy density with that of a uniform homogeneous (hom) electron gas who has same density $n(\mathbf{r})$

$$\begin{aligned}
 V_{LDA}[n(r)] &= \int n(r) \varepsilon_{XC}^{hom}[n(r)] dr \\
 &= \int n(r) \{ \varepsilon_X^{hom}[n(r)] + \varepsilon_C^{hom}[n(r)] \} dr \\
 &= E_X^{hom}[n(r)] + E_C^{hom}[n(r)]
 \end{aligned} \tag{3.30}$$

The exchange energy, E_X , of the electron gas can be obtained from the electron density (in the Hartree units) [213, 215].

$$E_X = -\frac{3}{4} \left(\frac{3}{\pi} \right)^{\frac{1}{3}} n^{\frac{4}{3}} V \tag{3.31}$$

Based on Dirac [213], the exchange functional has a simple analytic form for homogenous electron gas:

$$E_X[n] = -\frac{0.458}{r_s} \tag{3.32}$$

,where r_s is the Wigner-Setz radius radius of a sphere containing one electron. The correlation part is more complicated and, as emphasized in the introduction to exchange correlation functional, there is no analytical form. However, the accurate values for $E_c[n]$ have been determined by Ceperly and Adler in 1980 [216] using Quantum Monte-Carlo techniques. By interpolating these values, Perdew and Zunger provided a simple expression for $E_c[n]$ [217]:

$$\begin{aligned}
 E_C[n] &= A \ln r_s + B + C r_s \ln r_s + D r_s & r_s \leq 1 \\
 &= \gamma / (1 + \beta_1 \sqrt{r_s} + \beta_2 r_s) & r_s > 1
 \end{aligned} \tag{3.33}$$

3. AB-INITIO METHODS

The coefficient A, B, C, D, γ , β_1 and β_2 have been obtained for both the spin-polarized and spin-unpolarised homogeneous electron gas. The correlation energy is consistently an order of magnitude smaller than the exchange energy throughout the range of electron densities and $E_x + E_c$ contribution is comparable in magnitude with kinetic energy and therefore cannot be neglected. Although very old and simplistic, LDA yields good results in geometries of solids, bulk moduli and phonon frequencies, with just few percent errors. Yet it is less accurate in predicting ionization energies and cohesive energies, gap at semiconductors, making an error of 10-20%. It is a well-known fact that LDA fails completely in case of highly correlated systems where electron-electron interaction is dominant [208].

3.2.7. Generalized Gradient Approximation

While LDA depends only on local density $n(r)$, GGA incorporates the density gradient [218, 219, 220]:

$$V_{GGA}[n(r)] = \int n(r) \varepsilon_{XC}^{hom}[n(r), |\nabla n(r)|] dr \quad (3.34)$$

In contrast to LDA, where we had unique $E_{XC}[n(r)]$ available, for GGA several versions exist due to different implementation of density gradient. Also many versions of GGA have free parameters that can be fitted into the experimental data. Commonly used GGA functionals include PW91 proposed by Perdew and Wang [221], and PBE by Perdew, Burke and Ernzerhof[218]. GGA shows an improvement over LDA in predicting bond lengths, atomic energies and binding energies, crystal lattice constants, especially in system where the charge density is rapidly varying. Same as LDA, it performs poorly in materials with localized and strongly correlated electrons, such as transition metal oxides and rare-elements and compounds. There are also many other types of functionals such as the meta-GGA that includes the second derivative of electron density, and hybrid functional which incorporates a portion of the exact exchange component from Hartree-Fock theory, and they show high precisions in particular cases. However, usually the usage of those functionals is computationally very expensive and recommended only if we are certain that effects we are interested in are not good described with LDA/GGA. LDA and GGA provide a good enough description of exchange and correlation energies for large class of materials with moderate computational costs making the DFT the desired technique for exploration of properties of materials.

3.2.8. Self-Consistent Calculations

Using the HK theorems and the Kohn-Sham scheme for solving the KS equations we can, in principle, find the exact density and energy of the ground state of a condensed matter system. If we rewrite the Kohn-Sham equations and each term:

$$\left[-\frac{1}{2}\nabla^2 + V_{tot}(r) \right] \phi_i(r) = \varepsilon \phi_i(r) \quad (3.35)$$

$$V_{tot}(r) = V_n(r) + V_H(r) + V_{xc}(r) \quad (3.36)$$

$$V_n(r) = - \sum_I \frac{Z_I}{|r - R_I|} \quad (3.37)$$

$$\nabla^2 V_H(r) = -4\pi n(r) \quad (3.38)$$

$$V_{xc}(r) = \frac{\delta E_{xc}[n]}{\delta n}(r) \quad (3.39)$$

$$n(r) = \sum_i |\phi_i(r)|^2 \quad (3.40)$$

,we can see that these equations must be solved self-consistently, meaning that all solutions are linked with each other. The "self-consistency" stands for the following concept: if we insert the solutions ϕ_i to calculate the density, determine the corresponding potential V_{tot} , and solve the Schrodinger equation again, then we find, as a solution, the same function ϕ_i from which we started. The self-consistent process starts by us specifying the nuclear coordinates, in such a way that we can calculate the nuclear potential, V_n . We make "an educated guess" of a possible electron density, $n(r)$, in order to determine a preliminary approximation to the Hartree and exchange and correlation potentials. Using the density, we obtain the initial estimates of the Hartree and exchange and correlation potentials, $V_H + V_{xc}$, and from there the total potential, V_{tot} and we can proceed with the numerical solution of the KS equations. By solving the Kohn-Sham equations, we obtain the new wavefunctions, ϕ_i , which can in turn be used to construct a better estimate of the density, n , and the total potential, V_{tot} . If the two quantities differ by a value less than a certain defined tolerance, then the self-consistency has been reached, otherwise a new density has to be defined (usually this value is obtained by mixing the initial and the

3. AB-INITIO METHODS

final electron density) and a new iteration will start with the new electron density. This process continues up until the self-consistency is reached. This procedure is depicted in Figure 3.3.

Having the electron density calculated, various quantities can be obtained: the total energy, forces, stress tensors, eigenvalues, the electron density of states, the band structure and many more. Most demanding part of this cycle is the solving of KS equations. To solve the Kohn-Sham equation, the one-electron wavefunction has to be expanded in a suitable basis set as:

$$\phi_n(r) = \sum_{i=1}^M c_{n,i} \psi_i(r) \quad (3.41)$$

, where ϕ_n is the n^{th} Kohn-Sham orbital and ψ_i is the basis set. The choice of the basis set depends mostly on the type of system studied but as well on the properties we are interested to calculate. In molecular calculations, an atomic basis set is most commonly used. It consists of a finite number of atomic orbitals with Gaussian form $e^{-\alpha r^2}$. For condensed matter, plane-wave basis is the most suitable for description of infinite periodic structures.

3.2.9. Plane Wave Basis

The usage of plane-wave basis set comes with great advantages, but also with certain difficulties. According to the Bloch's theorem, the wavefunction of an electron in a periodic potential can be written as:

$$\phi_{n,k}(r) = e^{ik \cdot r} u_{n,k}(r) \quad (3.42)$$

, where n is the band index, k is the wavevector, and $u_{n,k}(r)$ is a function with the same periodicity of the potential, such that $u_{n,k}(r) = u_{n,k}(r+R)$, with R representing the lattice vector. Consequently $u_{n,k}(r)$ can be expanded in a Fourier series:

$$u_{n,k}(r) = \sum_G c_{n,G}(k) e^{iG \cdot r} \quad (3.43)$$

, where G is the reciprocal lattice vector defined by $G \cdot R = 2\pi m$ (m is an integer). The corresponding electron wavefunction is thus given by:

$$\phi_{n,k}(r) = \sum_G c_{n,k+G} e^{i(k+G) \cdot r} \quad (3.44)$$

3. AB-INITIO METHODS

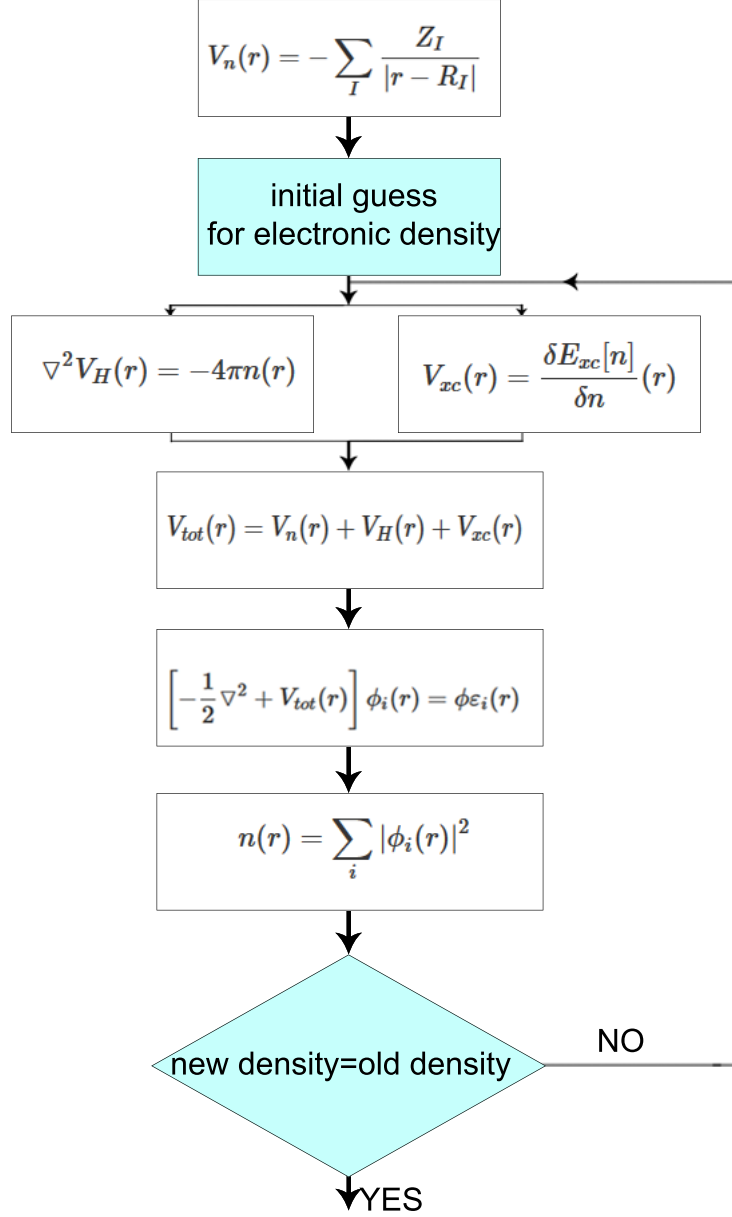


Figure 3.3.: Schematic flow-chart for finding self-consistent solutions of the Kohn-Sham equations. The equality sign in the conditional symbol means that the electron density at this iteration and the density at the previous iteration differ by less than a desired tolerance. While conceptually it makes sense to compare densities in order to check for self-consistency, in practical calculations it is often more convenient simply to compare the total energies at two successive iterations.

3. AB-INITIO METHODS

The Kohn-Sham effective potential has also lattice periodicity and can be represented in the same way. The Kohn-Sham equations can be expanded to a simple plane-wave form:

$$\sum_{G'} \left[\frac{1}{2} |k + G|^2 \delta_{G,G'} + \tilde{v}_{eff}(G - G') \right] c_{n,k+G'} = \epsilon_n c_{n,k+G} \quad (3.45)$$

$$\tilde{v}_{eff} = \tilde{v}_{ext} + \tilde{v}_H + \tilde{v}_{xc} \quad (3.46)$$

Although it looks quite useful, a complete plane-wave basis set is impossible to use in practise. It includes an infinite number of plane waves and we cannot operate with it in a realistic calculation. Instead we apply a set of plane waves which are restricted in a sphere in reciprocal space with a radius related to a cutoff energy E_{cut} , so that (Figure 3.4):

$$\frac{\hbar^2}{2m} |k + G|^2 \leq E_{cut} \quad (3.47)$$

This cutoff value and the volume of the supercell ω determine the number of plane waves N_{PW} that will be used:

$$N_{PW} \sim \Omega_{cut}^{\frac{3}{2}} \quad (3.48)$$

The volume occupied by a single plane wave is:

$$V_{PW} = \frac{2\pi^3}{\Omega} \quad (3.49)$$

A cutoff is chosen individually for each studied system and it has to be varied until the convergence is reached.

A great benefit of the Bloch's theorem is that it allows one to consider only the electrons within a unit cell of solids. Properties such as electron density and total energy are then computed by adding the contributions from in principle an infinite number of k vectors in the Brillouin zone. As wavefunctions vary slowly over small distances in k -space, the integrations can be performed as summations over certain finite and discrete k points. It is very important to appropriately sample the Brillouin zone, and to do that, we must know how fast the integrand changes with respect to k . For metals, the energy dramatically varies in the region where the valence bands cross the Fermi level (this means it requires a dense k mesh for description). For semiconductors and insulators, the electronic bands are relatively flat, and a uniform grid with a small number of k points is generally enough. Concluding this, certain familiarity with studied system is a prerequisite for the correct setup of calculations.

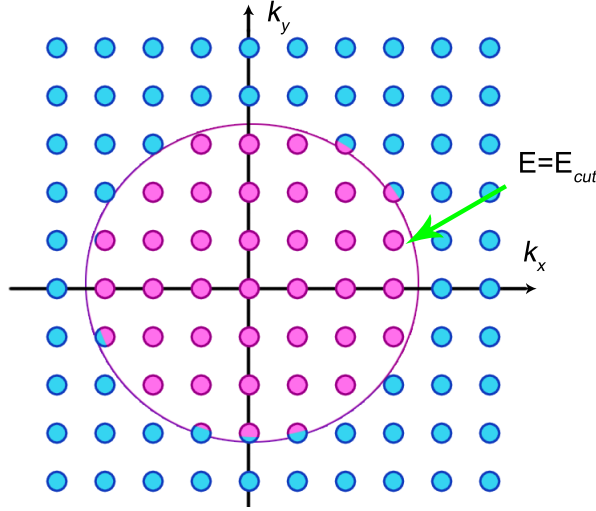


Figure 3.4.: Schematic illustration of the truncating the plane wave expansion - cutoff

3.2.10. Pseudopotentials

There are certain difficulties using the plane wave basis. The main difficulty is in a fact that electron wavefunctions oscillate rapidly in the core region, due to the strong Coulomb interaction. Another complication is in the demand for orthogonality between the core states and valence states. There is a method to overcome these problems, the use of so-called pseudopotentials. We consider the fact that core electrons are tightly bound to nuclei and respond very little to the presence of neighbouring atoms, while the valence electrons strongly interact with the environment and dominate the physical properties of material. When solving the KS equation, we only need valence electrons to treat explicitly. A pseudopotential is an effective potential that valence electrons feel. We view core electrons as frozen and together with nuclei they form a non-polarizable ion cores. They are described by a set of pseudo wavefunctions with no radial nodes in the core region. Outside of the radius cutoff r_c , the pseudopotential and pseudo wavefunctions are identical as the real ones. The smoothness of pseudo wavefunctions near the core dramatically reduce the number of plane waves needed for representation. In Figure 3.5, there is a schematic illustration of wavefunction and pseudopotential.

The main advantage of pseudopotentials is in making calculations more efficient: smoother potentials decrease the number of expansion coefficients for the Kohn-Sham orbitals. However there are some disadvantages: The wavefunctions inside

3. AB-INITIO METHODS

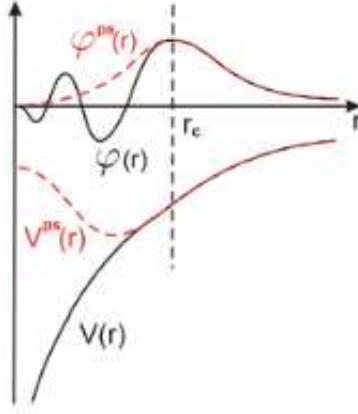


Figure 3.5.: Schematic illustration of the replacement of the true potential $V(r)$ and true electronic wavefunction $\phi(r)$ by a fictitious pseudopotential $V_{ps}(r)$ and pseudo-wavefunction $\phi_{ps}(r)$, respectively. For $r > r_c$, the pseudopotentials and wavefunctions become identical. This is the basic idea of the PP approximation. Figure taken from [224].

the pseudo potential region deviates from the true behaviour. Also there are less degrees of freedom, since the core electrons are frozen into the pseudo potential. There are more than several methods to generate a suitable pseudopotential and accordingly, types of pseudopotentials. The most used are the norm conserving ones [222], which means that the integral of the pseudo charge density will give the same total charge inside the cut-off radius as the true charge. Further development of pseudo potentials was proposed by David Vanderbilt by introducing the concept of ultrasoft pseudo potentials [223]. It allow calculations to be performed with the lowest possible cutoff energy for the plane-wave basis set. In most cases, a high cutoff energy is only required for the plane-wave basis set when there are tightly bound orbitals that have a substantial fraction of their weight inside the core region of the atom. In these situations, the only way to reduce the basis set is to violate the norm-conservation condition by removing the charge associated with these orbitals from the core region. The pseudo wavefunctions are thus allowed to be as soft as possible within the core, yielding a dramatic reduction in the cutoff energy.

3.2.11. Hellmann-Feynman Theorem and Density Functional Perturbation Theory

Lattice vibrations are responsible for many observed phenomena such as the Raman spectra, specific heat, thermal conductivity, thermal expansion, and bear heavily on other phenomena such as conventional phonon-mediated superconductivity we discussed in the previous chapter. Vibrations of ions about their equilibrium positions spread throughout the system and become collective excitations called phonons. Density functional perturbation theory (DFPT) is the state-of-the-art method for calculating lattice dynamics from the first-principles in condensed matter physics. This is a method of applying a linear perturbation theory within DFT. The aim of DFPT is to calculate the derivatives of the total energy within a system based upon a periodic perturbation of the crystal lattice. Possibly the greatest advantage of DFPT over other methods of calculating crystal vibrations such as the frozen-phonon method is that the perturbation may take on any wavevector. This freedom allows one to avoid the need of using computationally-expensive supercells to calculate phonon eigenfrequencies at arbitrary wavevectors. The two main formalisms of DFPT are due to Baroni [227] and Gonze [228]; although the two may be shown to be equivalent, there are differences in the implementation that may result in one method being preferable to another. The Baroni formalism is centred upon obtaining a series of equations that may be solved self-consistently using Green's function methods; the Gonze formalism is based rather upon a perturbative expansion of the Kohn-Sham energy functional, leading to a variational problem for even orders of expansion akin to the zeroth order problem. In this thesis DFPT in Baroni's implementation was used and now it will be briefly discussed [225]. From the lattice dynamics, where the vibrations of nuclei are treated classically, the equations of motion are coupled differential equations. Their solutions are the displacements of the nuclei due to the perturbations. Expanding the force term around the equilibrium positions of the nuclei, the responses to perturbations are higher order coefficients of the expansion. In the harmonic approximation, the second order terms are retained while higher order responses are ignored.

$$C_{I,J} = \frac{\partial^2 E(R)}{\partial R_I \partial R_J} \quad (3.50)$$

In a crystal, the atomic displacements obey the Bloch theorem, allowing for the transformation of the classical equations of motion to be decoupled and expressed

3. AB-INITIO METHODS

in terms of the wave number q . The solutions to the resulting eigenvalue equation are the frequencies of an individual perturbation ω_q [225]. Through DFPT calculations, we obtain the array of derivatives that form a dynamical matrix that can be diagonalized to yield the phonon eigenfrequencies and eigenmodes. For DFPT to be used in materials, the central approximation which enables that is the Born-Oppenheimer approximation [226]. As mentioned above, it allows us to separate the motion of electrons from the atomic cores, making them stationary (from the electrons point). In DFPT the atomic positions are methodically perturbed, the electronic ground state and total energy can be computed as a function of these perturbations. In practice, $E(R)$ is the ground state energy of a system of interacting electrons moving in the field of very slowly moving nuclei (ABO approximation), with Hamiltonian:

$$H_{BO} = -\frac{\hbar^2}{2m_e} \sum_i \nabla_i^2 - \sum_{i,I} \frac{Z_I e^2}{|r_i - R_I|} + \frac{1}{2} \sum_{i \neq j} \frac{e^2}{|r_i - r_j|} + E_N(R) \quad (3.51)$$

$E_N(R)$ is the electrostatic interaction between different nuclei:

$$E_N(R) = \frac{e^2}{2} \sum_{I \neq J} \frac{Z_I Z_J}{|R_I - R_J|} \quad (3.52)$$

The equilibrium geometry of the system is given by the condition that the forces acting on individual nuclei are zero:

$$F_I = -\frac{\partial E(R)}{\partial R_I} = 0 \quad (3.53)$$

The vibrational frequencies ω are determined by the eigenvalues of the Hessian of Born-Oppenheimer energy, scaled by the nuclear masses [227]:

$$\det \left| \frac{1}{\sqrt{M_I M_J}} \frac{\partial^2 E(R)}{\partial R_I \partial R_J} - \omega^2 \right| = 0 \quad (3.54)$$

To calculate the equilibrium geometry and vibrational properties of a system, it is necessary to compute the first and second derivatives of its Born-Oppenheimer energy. The most important tool to achieve this is the Hellmann-Feynman theorem [229, 230] which states that the first derivative of eigenvalues of a Hamiltonian H_λ , which depends of a parameter λ , is given by the expectation value of the derivative of the Hamiltonian:

$$\frac{\partial E_\lambda}{\partial \lambda} = \langle \Psi_\lambda | \frac{\partial H_\lambda}{\partial \lambda} | \Psi_\lambda \rangle \quad (3.55)$$

, where ψ_λ is the eigenfunction of H_λ corresponding to E_λ eigenvalue:

$$H_\lambda \Psi_\lambda = E_\lambda \Psi_\lambda \quad (3.56)$$

3. AB-INITIO METHODS

As discussed before, in Born-Oppenheimer approximation, nuclear coordinates behave as parameters in the electronic Hamiltonian. Then we can calculate forces acting on I nucleus in the electronic ground state as:

$$F_I = -\frac{\partial E(R)}{\partial R_I} = -\langle \Psi(R) | \frac{\partial H_{BO}(R)}{\partial R_I} | \Psi(R) \rangle \quad (3.57)$$

$\Psi(r, R)$ is the electronic ground state wave function of the Born-Oppenheimer Hamiltonian. This Hamiltonian depends on R through the electron-ion interaction that couples to the electronic degrees of freedom only through the electronic charge density. In other words, if we know the ground state electronic density, we can calculate all forces acting upon the system using classic electrostatics only. The Hellman-Feynman theorem states then:

$$F_I = -\int n_R(r) \frac{\partial V_R(r)}{\partial R_I} dr - \frac{\partial E_N(R)}{\partial R_I} \quad (3.58)$$

Where $V_R(r)$ is the electron-nucleus interaction:

$$V_R(r) = -\sum_{iI} \frac{Z_I e^2}{|r_i - R_I|} \quad (3.59)$$

$n_R(r)$ is the ground state electron charge density corresponding to the nuclear configuration R. Now we need to obtain Hessian of the Born-Oppenheimer energy and we do that by differentiating the Hellman-Feynman forces with respect to nuclear coordinates:

$$\frac{\partial^2 E}{\partial R_I \partial R_J} \equiv \frac{\partial F_I}{\partial R_J} = \int \frac{\partial n_R(r)}{\partial R_J} \frac{\partial V_R(r)}{\partial R_I} dr + \int n_R(r) \frac{\partial^2 V_R(r)}{\partial R_I \partial R_J} dr + \frac{\partial^2 E_N(R)}{\partial R_I \partial R_J} dr \quad (3.60)$$

From this equation, we see that for calculation of the Hessian we need to calculate the ground-state electron charge density $n_R(r)$ as well as its linear response to distortion of the nuclear geometry $\frac{\partial n_R(r)}{\partial R_J}$ [231, 232]. This Hessian matrix is known as the matrix of the interatomic force constants (IFC). To obtain the response within the framework of DFT, the KS orbitals are varied according to first order perturbation theory. Following equations are equivalent to the Kohn-Sham equations in a perturbed system. These equations, solved self-consistently, lead to the matrix of force constants known as the dynamical matrix.

$$\Delta n(r) = \sum_n^{N/2} \psi_n^*(r) \Delta \psi_n(r) \quad (3.61)$$

The variation of the KS orbitals $\Delta \psi_n(r)$ is obtained by standard first-order perturbation theory:

$$(H_{SCF} - \epsilon_n) |\Delta \psi_n\rangle = -(\Delta V_{SCF} - \Delta \epsilon_n) |\Delta \psi_n\rangle \quad (3.62)$$

3. AB-INITIO METHODS

, where H_{SCF} is unperturbed KS Hamiltonian:

$$H_{SCF} = -\frac{\hbar^2}{2m} \frac{\partial^2}{\partial r^2} + V_{SCF}(r) \quad (3.63)$$

, $\Delta V_{SCF}(r)$ is the first order correction to the self-consistent potential:

$$\Delta V_{SCF}(r) = \Delta V_{ext}(r) + e^2 \int \frac{\Delta n(r')}{|r - r'|} dr' + \frac{dV_{xc}}{dn(r)} \Delta n(r) dr \quad (3.64)$$

and $\delta\epsilon_n$ is the first order variation of the KS eigenvalue ϵ_n :

$$\Delta\epsilon_n = \langle \psi_n | \Delta V_{SCF} | \psi_n \rangle \quad (3.65)$$

These equations for a set of self-consistent equations for perturbed system and they are analogous to the Kohn-Sham equations in the unperturbed system.

3.2.12. Electron-Phonon Coupling in DFT Framework

Knowing the response of the system to perturbations in a lattice allows calculation of phonon frequencies, energies and enables description of the electron-phonon interaction. As discussed in details in the previous chapter, electron-phonon coupling can be described as the scattering of an electron from a state $|k\rangle$ to a state $|jk \pm q\rangle$ by absorbing or emitting a phonon. The Eliashberg spectral function $\alpha^2 F$ is expressed as a sum over the contributions from scattering processes which connect electrons through phonons on the Fermi surface.

$$\alpha^2 F(\omega) = \frac{1}{N_q} \sum_{q\nu} \delta(\omega - \omega_{q\nu}) \frac{1}{N_F \omega_{q\nu}} \sum_{mn,k} w_k |g_{mn}^\nu(k, q)|^2 \delta(\epsilon_{nk}) \delta(\epsilon_{mk+q}) \quad (3.66)$$

and matrix element for this interaction is:

$$g_{k+q,k}^{(i,j)\nu} = \frac{1}{\sqrt{2M\omega_{\nu,q}}} \langle j, k+q | \delta_\nu^q V_{eff} | i, k \rangle \quad (3.67)$$

In the DFT formalism, this coefficient can be calculated as:

$$g_{q\nu}(k, i, j) = \left(\frac{\hbar}{2M\omega_{q,\nu}} \right) \langle \psi_{i,k} | \frac{dV_{SCF}}{d\hat{u}_{q\nu}} \cdot \hat{\epsilon}_{q,\nu} | \psi_{j,k+q} \rangle \quad (3.68)$$

, while the electron-phonon coupling constant for mode ν at wavevector q is defined as:

$$\lambda_{q\nu} = \frac{\gamma_{q\nu}}{\pi \hbar N(\epsilon_F) \omega_{q\nu}^2} \quad (3.69)$$

3. AB-INITIO METHODS

, where $N(\epsilon_F)$ is a DOS at the Fermi level. Now the spectral function can be defined as:

$$\alpha^2 F(\omega) = \frac{1}{2\pi N(\epsilon_F)} \sum_{q\nu} \delta(\omega - \omega_{q\nu}) \frac{\gamma_{q\nu}}{\hbar\omega_{q\nu}} \quad (3.70)$$

And from knowing spectral function, we can calculate as the first reciprocal momentum of the spectral function:

$$\lambda = \sum_{q\nu} \lambda_{q\nu} = 2 \int \frac{\alpha^2 F(\omega)}{\omega} d\omega \quad (3.71)$$

And using McMillan formula, as shown in the previous chapter, we can calculate the critical temperature.

4. QUANTUM ESPRESSO AND OTHER COMPUTATIONAL TOOLS

Quantum ESPRESSO (230) (opEn-Source Package for Research in Electronic Structure, Simulation, and Optimization) is integrated suite of open-source computer codes for ab initio quantum physics methods for electronic-structure calculation and materials modelling. QE is distributed for free under the GNU General Public License (<http://www.quantum-espresso.org>) and it is based on Density Functional Theory, plane wave basis sets, and pseudopotentials. QE is designed to be a distribution of packages, rather than a tightly integrated single package. It consists of two main packages that share common installation method, input format, pseudopotential format, data output format and large parts of the code:

- PWscf: self-consistent electronic structure and structural relaxation
- CP MD: Car-Parrinello molecular dynamics.

Except these two main packages, there are several more specialized QE originated packages:

- Phonon: DFPT based package that does linear response calculations (phonons, dielectric properties)
- PWneb: energy barriers and reaction pathways through the Nudged Elastic Band (NEB) method
- PostProc: codes and utilities for data postprocessing
- PWcond: ballistic conductance

4. QUANTUM ESPRESSO AND OTHER COMPUTATIONAL TOOLS

- TD-DFPT: spectra from Time-Dependent Density Functional Perturbation Theory
- GWL: GW calculations and solution of the Bethe-Salpeter Equation

and several auxiliary packages:

- Atomic: atomic calculations and pseudopotential generation
- PlotPhon: phonon dispersion plotting utility (to be used in conjunction with PHonon)

QE is strongly interfaced with several other codes that perform various ab initio quantum physics calculations. Here follows a list of just several of them :

- GIPAW (Gauge-Independent Projector Augmented Waves): NMR chemical shifts and EPR g-tensor
- WANNIER90: maximally localized Wannier functions
- WanT: quantum transport properties with Wannier functions
- YAMBO: electronic excitations within Many-Body Perturbation Theory: GW and Bethe-Salpeter equation
- EPW: (calculates properties related to the electron-phonon interaction using Density-Functional Perturbation Theory and Maximally Localized Wannier Functions)

QE is the UNIX environment based code written in C and Fortran languages, optimised for parallel execution using MPI libraries and for massively parallel machines, OpenMP parallelization is supported as well. It uses external libraries:

- BLAS (Basic Linear Algebra Subprograms)
- LAPACK (Linear Algebra Package)
- FFTW (Fastest Fourier Transform in the West)
- MPI libraries

Although it is optimized to use open the source version of those libraries, QE can use any architecture-optimized replacements (such is Intels MKL). As for parallelization, there are two different parallelization paradigms implemented in QE:

4. QUANTUM ESPRESSO AND OTHER COMPUTATIONAL TOOLS

- MPI runs executable on each CPU with its own private set of data, and communicates with other executables only via calls to MPI libraries.
- OpenMP - A single executable spawn subprocesses (threads) that perform in parallel specific tasks. OpenMP can be implemented via compiler directives (explicit OpenMP) or via multithreading libraries (library OpenMP). Library OpenMP is a low-effort parallelization suitable for multicore CPUs. Its effectiveness relies upon the quality of the multithreading libraries and the availability of multithreading FFTs. Explicit OpenMP is a recent addition, still under development, devised to increase scalability on large multicore parallel machines.

In this dissertation most of calculations were performed using Quantum Espresso and its PW and PHonon code (as well as many auxiliary codes). In Figure 4.1, a schematic representation of calculation is presented. All structures were fully relaxed prior to further calculations and all calculations were performed using LDA or GGA. In Figure 4.1, an example of a QE run on certain material, with steps and results of calculations of superconductivity, electric, phonon and optical properties within DFT/DFPT framework is depicted. Major steps of calculation performed with different QE codes (.x stands for QE executable) are in blue squares. Results of calculations are in purple circles. Only some results from calculations are presented here, and there are many more available from the same run (with or without the usage of other post-processing codes). Since most of structures calculated in this dissertation and included papers are 2D materials, a special attention is devoted to modelling of two dimensional material in a three dimensional environment such is a DFT framework. QE (as well as the most other DFT codes) considers periodical systems, where unit cell is "infinitely" repeated in x, y, z direction. To design a 2D material, inclusion of vacuum is necessary in order to avoid interaction between layers.

The unit cell has to include a large empty space in on one direction, i.e. to be elongated in z axis direction, creating a distance between layers, sufficient enough to avoid any interaction between layers. There is no universal recipe for choosing the "amount" of vacuum, it has to be individually tested for every considered system. It ranges from 10 Å up to 25 Å, or even more and it can cause serious influence on time consumption. However, when dealing with such a unit cell, there are tricks that can help reduction of the computational costs. Instead of sampling a whole

4. QUANTUM ESPRESSO AND OTHER COMPUTATIONAL TOOLS

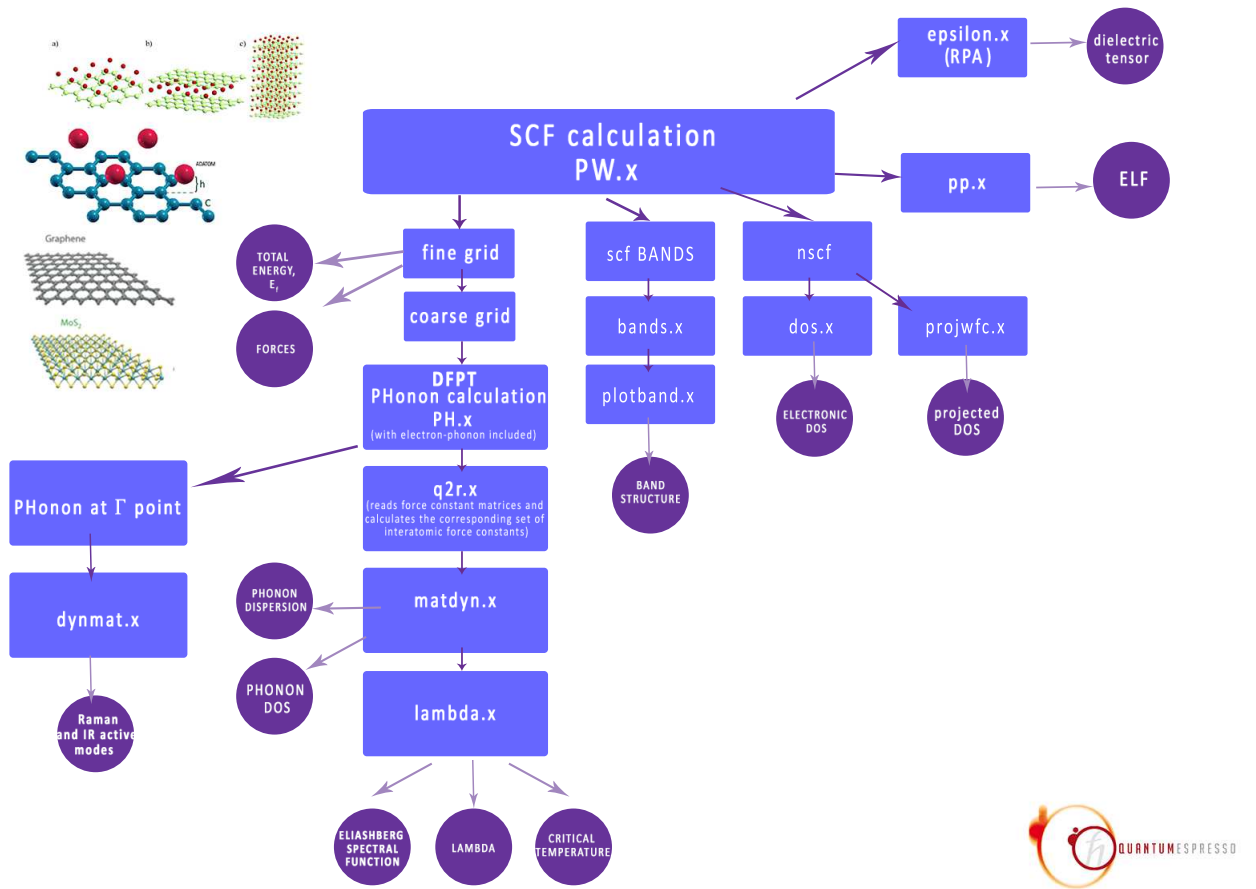


Figure 4.1.: Schematic representation of various calculations performed using QE in the preparation of this dissertation

4. QUANTUM ESPRESSO AND OTHER COMPUTATIONAL TOOLS

unit cell with Monkhorst-Pack grid [234] with same density in every direction, we can take dense grid only in one plane. For example, instead of taking $32 \times 32 \times 32$ grid for a unit cell with 25 Å of vacuum, we can take $32 \times 32 \times 1$ and do not lose anything in accuracy while saving resources. Since this dissertation is focused on investigation of superconductivity in 2D material, an additional attention will be devoted here to the calculations. The input files in QE are structured in a number of namelists and input cards. Namelist (standard input construct in fortran90) allows the specification of the value of an input variable only when it is needed and the defining of the default values for most variables. Variables can be inserted in any order, they are read in a specific order and the one that are not required for certain run are ignored. Input cards are specific in QE. They are used to provide the input data that are necessary, and they require the data in specific order. The input file should contain all information about the system (geometry of the unit cell, number and type of atoms, pseudopotential specification and position of atoms in the unit cell). In Appendix B, some of most important inputs used in calculations in this dissertation are given. It is not only simplifying but also very useful to visualize the crystal structure before conduction any run. Various programs can be used for this. We used XCrysden [235] and Virtual NanoLab [236] for all investigated structures. XCrysDen is a crystalline and molecular structure render program, with additional capabilities of rendering contours, isosurfaces, Wigner-Seitz cells (also Brillouin zone), Fermi surfaces and many more. One of great benefits of using it, is in the fact that it can directly visualize the structure from QE, both inputs and outputs. All structures are advised to be first visualized in XCrysDen to check the input data. In the Figure 4.2, there is screenshot of XCrysDen. VNL stands for Virtual NanoLab, commercial software code (for Linux and Windows both) from Quantum Wise, with free academic licence. It is interfaced with QE and it can be used (partially) as GUI for it. It is a useful tool for visualization of inputs but it can be also used (in Linux) as a working environment for QE (for handling input and output, visualization, submitting job through python scripts, etc.) In the Figure 4.3, the screenshot of VNL is presented.

For EPC and the superconductivity calculations, which are the focal point of this dissertation, workflow of QE will be briefly discussed in following paragraph. The input files are prepared and as stated above, before any further calculations, they are optimized and fully relaxed using BFGS (Broyden-Fletcher-Goldfarb-Shanno) algorithm [238]. BFGS algorithm is an iterative method for solving unconstrained

4. QUANTUM ESPRESSO AND OTHER COMPUTATIONAL TOOLS

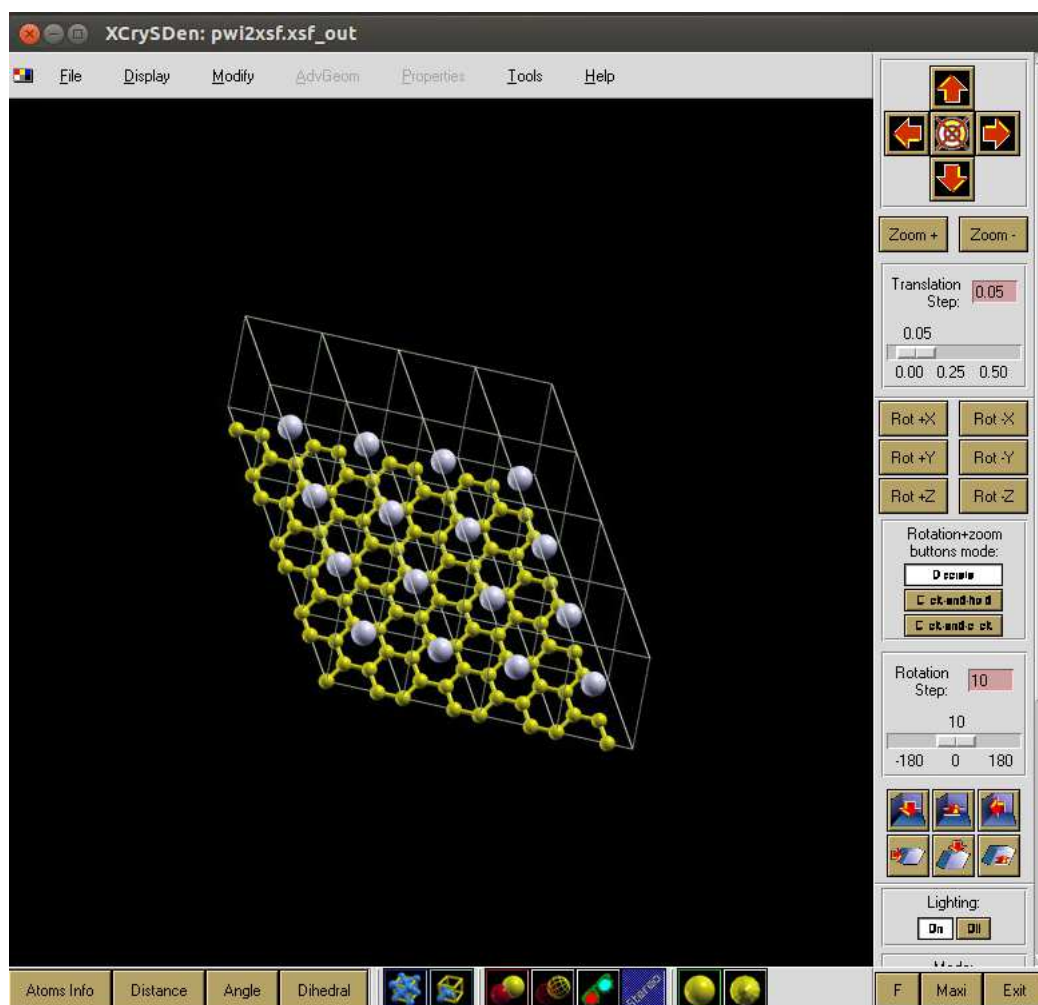


Figure 4.2.: Screenshot of XCrySDen window with the visualization of graphene with lithium adatoms

4. QUANTUM ESPRESSO AND OTHER COMPUTATIONAL TOOLS

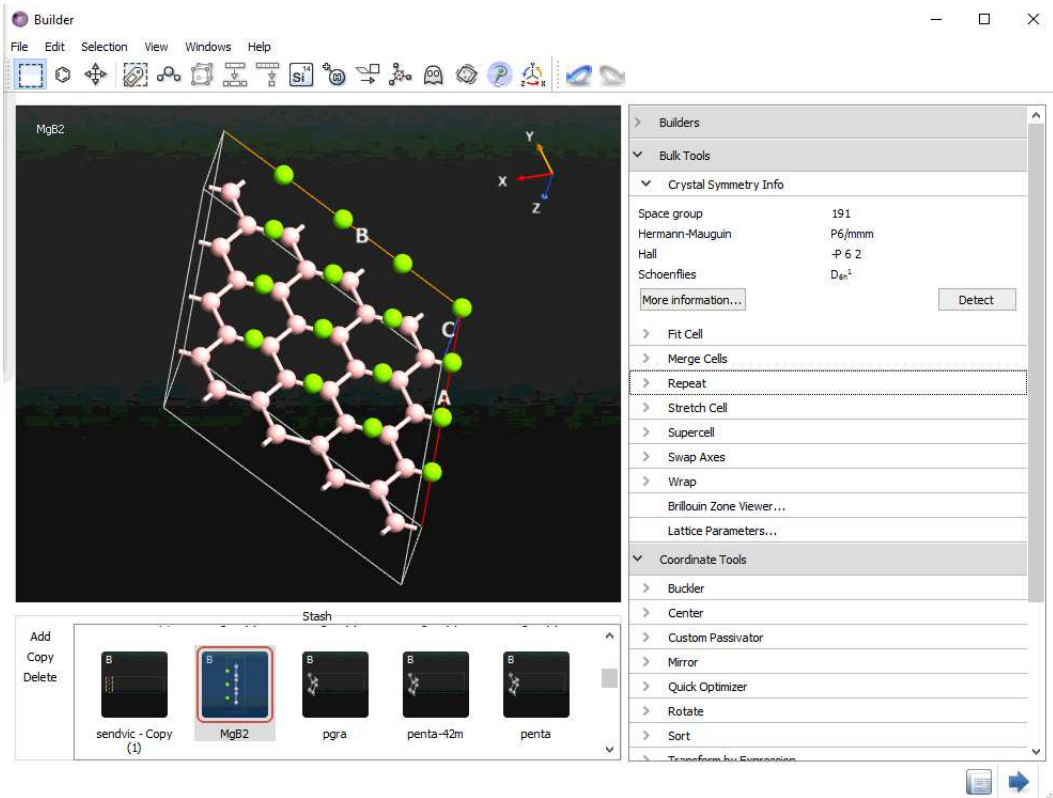


Figure 4.3.: Screenshot of VNL window with the visualization of graphene with magnesium-diboride

4. QUANTUM ESPRESSO AND OTHER COMPUTATIONAL TOOLS

nonlinear optimization problems. The BFGS method approximates the Newton's method, a class of hill-climbing optimization techniques that seeks a stationary point of a (preferably twice continuously differentiable) function. For such problems, a necessary condition for optimality is that the gradient being zero. This algorithm does not require additional variables. Relaxation proceeds until subsequent total energy evaluations differ by less than 1.0d-4 Ry and each force component is less than 1.0d-3 Ry/Bohr. These default values can be changed by defining variables `etot_conv_thr` and `forc_conv_thr`. In our calculations, we usually take 1.0d-6 Ry for total energy and 1.0d-5 Ry/Bohr for forces. The criterion is more stringent than default one because of an extensive use of vacuum in the unit cells. In the relaxation algorithms, some components of the atomic positions can be fixed by adding three integer values (0/1) after the atomic coordinates. A value of 1 means that the corresponding component is left free to vary, while a value of 0 means that the component is fixed. After we made sure that system is in minimum energy, the SCF calculation begins. For EPC calculation, first SCF run is necessary to be on a fine grid. The fine grid must contain all k and $k+q$ grid points used in the subsequent electron-phonon calculation and should be dense enough to produce accurate electron-phonon coefficients. The input for calculation on this dense grid must contain the option `"la2F=.true."` that instructs the code to save data into a file that is subsequently read during the electron-phonon calculation. Fine grid run is followed by the SCF calculation on a coarse grid, containing k points and a value of the gaussian broadening that is suitable for good self-consistency and for the phonon calculation. With this we finished the electronic calculation. We proceed with phonons and electron-phonon calculation. The option `"electron_phonon"` must be specified in input of `ph.x` run as well as the name of a file where the derivative of the potential is stored, `"fldvscf"`. In all calculations we used the option `"electron_phonon= interpolated"` and electron-phonon is calculated by interpolation over the Brillouin Zone as in Wierzbowska, et al [237]. The electron-phonon coefficients are calculated using several values of Gaussian broadening because this quickly shows whether results are converged or not with respect to the k -point grid and Gaussian broadening. Finally, we use `matdyn.x` and `lambda.x` to extract $\alpha^2 F(\omega)$ function, the electron-phonon coefficient λ , and an estimate of the critical temperature T_c using McMillan formula [57]. Usually the EPC calculations are computationally expensive, as they require the large k and q points grids, causing large computational resources consumption. A proper parallelization is essential for this calculation. Although it might look like a minor

4. QUANTUM ESPRESSO AND OTHER COMPUTATIONAL TOOLS

technical point, it is in fact a topic for itself. The details about enhancement of speed of calculations, used techniques and results will be discussed as a last part of the next chapter with a special focus on using of GPU acceleration in DFT calculations of low-dimensional materials. In that sub-chapter, another DFT code will be discussed. That is BigDFT [239], a massively parallel electronic structure code that uses a wavelet basis set. It is distributed under GPL licence as well. BigDFT implements DFT by solving the Kohn-Sham equations describing the electrons in a material, expanded in a Daubechies wavelet basis set and using a self-consistent direct minimization or Davidson diagonalisation methods to determine the energy minimum. Computational efficiency is achieved through the use of fast short convolutions and pseudopotentials to. It calculates the total energy, forces and stresses and geometry optimizations and ab initio molecular dynamics may be carried out. The greatest advantage of BigDFT is in the basis of Daubechies wavelets [240]. The Daubechies wavelet basis sets are an orthogonal systematic basis set, just as plane wave basis set of QE, but it has the great advantage of allowing the adaptation of mesh with different levels of resolutions (two levels in BigDFT). Also wavelets enable that the Hamiltonian can be done locally [241] which permits to have a linear scaling in function of the number of atoms instead of a cubic scaling for traditional DFT software. This provides great efficiency to BigDFT. However, although this method is very efficient, it demands translating whole DFT paradigm to language of wavelets, which is very far from elementary. An interest in BigDFT comes from the fact it is among the first massively parallel density functional theory codes which benefited from graphics processing units (GPU) on hybrid CPU/GPU systems [241] using CUDA and then OpenCL languages. Just as in QE, the effects of hardware accelerations have been studied and specificity of GPU-enabled runs for two-dimension materials were discussed.

5. RESULTS

5.1. Introduction to Theoretical Results

The fifth chapter of the dissertation presents a study of an electron-phonon coupling and superconductivity, the electronic and phononic properties of graphene and related materials performed within DFT and DFPT formalism. Specifically, doped graphene and magnesium-diboride have been studied in the low-dimensional limit, as single layer. In the previous chapters graphene properties, superconductivity in GICs and relations to graphene have been briefly discussed and theoretical framework for ab-initio study have been presented. The studies described here are fully related to the dissertation and resulted in the following articles [242, 243, 244, 245, 246, 247]. This chapter opens with an introduction to the doped graphene 5.2. The first section 5.2.1 gives the ab-initio description and the symmetry analysis of the phonons in graphene doped with lithium, calcium and barium [242] It continues with the detail ab-initio analysis of lithium doped monolayer in 5.2.2 section. This concerns the LiC₆-mono's electron and phonon properties and continues with the engineering of superconductivity by an application of biaxial strain in order to enhance EPC [243]. The critical temperature of 29K is obtained in the case of a tensile biaxial strain. In section 5.2.3 the optical properties are discussed for LiC₆-mono using RPA framework [244]. The third subchapter discusses properties of the thinnest limit of magnesium-diboride superconductor (5.3). In the section 5.3.2 stability of MgB₂-monolayer is established. Its electronic and vibrational properties were determined and the symmetry analysis of phonon modes at the Γ point is performed. After proving that MgB₂ monolayer is superconducting, we proceed with an engineering its properties, i.e. adjusting the electron-phonon interaction in order to enhance the critical temperature (section 5.3.4). The paper based on the results reported in this subchapter is submitted to a journal and is currently in press [246]. The final part of this chapter discusses the more technical issues about application of GPU acceleration in DFT calculations with a target on study of low-dimensional materi-

5. RESULTS

als and specificity of such calculations. Two papers are related to this topic, [245] and [247] which is currently in press. Two different DFT codes have been tested on hybrid architecture CPU/GPU for various low-dimensional materials. Different paradigms of both programs demand different approach to implementation of GPU and here they are tested in order to understand the particularities of calculation of a low-dimensional material.

5.2. Doped Graphene

In Chapter 2 section 2.4 the superconductivity in graphene and related materials have been discussed. Under the term "related" there are considered GICs and their relationship to doped graphene. When considering how to make graphene superconducting, it was clear that the rigid-band doping of the carbon π -states (in order to increase number of carriers) was not proper way to achieve that. Not only the π -DOS grows very slowly with doping, but even if achieved two problems could interfere. The first, even if the deformation potential related to the coupling of the π -bands and the in-plane phonon vibrations are large, these vibrations are highly energetic and EPC is small, owing to the ω_{ph}^2 factor in the denominator of the Hopfield formula. Second, the symmetry forbids the coupling between the π -states and the softer out-of-planes vibrations [59]. Taking all this into account, it is then necessary to promote the new electronic states at the Fermi level as in GICs. As stated before, GICs are the family of layered carbon materials, first synthesized in 1861 [248] and systematically studied for the first time in 1930s. Today under the term GIC there are more than hundred compounds [51] with various properties.

The first discovered GIC superconductors were the alkali compounds [249] (C_8A with $A = K, Rb, Cs$ with $T_c < 1$ K), than it continued with GICs with a large concentration of metals ($T(C_2Na)=5K$) [250], rare-earth GICs ($T_c(C_6Yb)=6.5K$) [251]. C_6Ca was discovered [251] in a graphite sample intercalated with Ca only on the surface layers and YbC_6 and CaC_6 hold record of the highest temperature in GIC family. The electron-phonon coupling mechanism has been shown to be responsible for the occurrence of the superconductivity in GICs [52] where an intercalant atom plays a crucial role. The simple doping of the π -bands in graphite does not lead to a sizable electron phonon coupling and in order to stabilize a superconducting state, it is necessary to have an electronic states of the intercalants on the Fermi surface. However, it is not only necessary to have an adatom but the intercalant

5. RESULTS

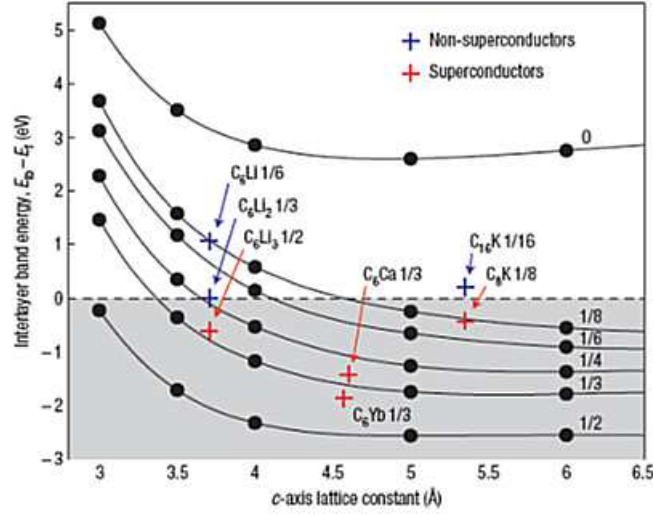


Figure 5.1.: The dependence of the interlayer band energy (at the Γ point) of the empty graphite system with changing c-axis spacing for different electron dopings. The interlayer band is occupied in the systems that fall into the shaded area. Figure taken from [254].

band needs to be partially occupied, i.e., the intercalant is not fully ionized [52, 252]. In superconducting GICs, an intercalant band (interlayer state) occurs at the Fermi level [52, 252] and its role is multiple [253, 63]. Not only the number of carriers is enhanced; but as well the coupling to the carbon out-of-plane vibrations is promoted. The coupling to the intercalant vibrations occurs with a corresponding enhancement of the deformation potential and a reduction of the effective atomic mass and phonon frequency term in the Hopfield relation.

$$\lambda = \frac{N(0)D^2}{M \omega_{ph}^2} \quad (5.1)$$

In section 2.4 the two important conclusions were made: Not all types of intercalant can lead to the superconductivity due to the charge transfer from the interlayer state; and second: the interlayer distance between the intercalant atom and the graphite plane should be smaller due to an increase of the deformation potential of an intercalant and the carbon out-of-plane modes [253, 254]. However, the distance should not be too small since the quantum confinement of the interlayer state. If it is too narrow, this could result in an upshift of the intercalant band well above the Fermi energy (as shown in Figure 5.1). With respects to all these conclusions regarding GICs, the exploration of the superconductivity in graphene

5. RESULTS

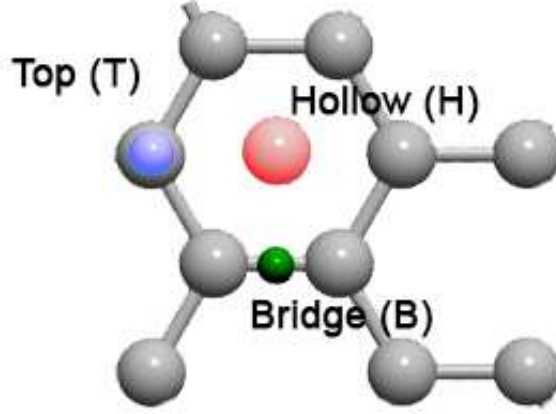


Figure 5.2.: Possible positions for the adatoms in doped graphene. Bridge is between two C atoms, top is above the carbon atom and h stands for the hollow center of the graphene hexagon

in a similar manner, gave some very interesting results but as well a completely a new way of studying the superconductivity in 2D materials . Namely, similarly to GIC, graphene can adsorb atoms in the three possible positions at the surface: B (Bridge), T (Top) and H (Hollow) (Figure 5.2).

The detail DFT analysis [255] show the most elements prefer a hollow site, and so does lithium, calcium and barium that have been studied in this chapter. Just as in GICs, in doped graphene the presence of the interlayer is of the vital importance and especially interesting in the case of the Li-doped graphene. Comparing the LiC_6 -mono and the CaC_6 -mono with their bulk counterparts, two scenarios occur, as described briefly in section 2.4 The critical temperature is lowered for the CaC_6 -mono and enhanced for the LiC_6 -mono (comparing to the bulk) all because of the particularity of their corresponding interlayers.

As explained by Profeta et al [59] in the bulk LiC_6 , the interlayer state is completely empty due to the strong confinement along the z direction that prevents its occupation. Comparing the LiC_6 bulk to the LiC_6 -mono, the removal of the quantum confinement along the c direction brings the interlayer to the Fermi level. Figure 5.3 compares the planar averages of the interlayer charge density for the Li-doped and Ca-doped graphene and graphite. In the CaC_6 -mono, the interlayer charge density spills out in the vacuum region, whereas in the bulk case, it is much more confined between the graphene and adatom layers (it has a period of $2h$). And the lower

5. RESULTS

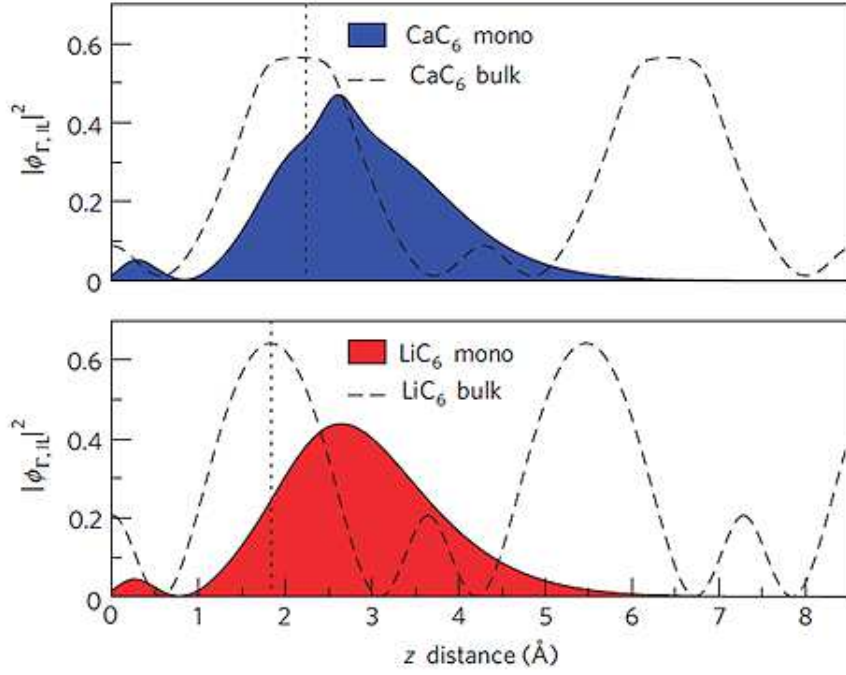


Figure 5.3.: The Interlayer-state wavefunction. Planar (in the xy direction) average of $|\Phi_{\Gamma}, IL|^2$ along the perpendicular (with respect to the graphene layer) direction (z). IL stands for interlayer. The vertical dotted lines represent the z position of the calcium and lithium adatoms in the monolayer (Image taken from the reference [59])

box shows that the spatial extension of the interlayer for lithium is the same as for calcium, but as the interlayer is strongly localized around the adatom and closer to the graphene layer, causing the enhancement of the total electron-phonon coupling.

Bringing the interlayer state to the Fermi energy and to localize it as close as possible to the graphene plane is beneficial for superconductivity. For the LiC_6 -mono, the presence of the interlayer state triggers the electron-phonon coupling of the carbon modes along the z direction that is inactive in the bulk, and increases the contribution of the intercalant modes, making it superconductive. An important conclusion arises from this discussion. A graphene layer-adatom distance is deciding parameter and proper engineering could be beneficial and increase of EPC. This can be achieved by application of strain [243] but before focusing on enhancement of EPC and the superconductivity a detail analysis of the phonons and symmetry in lithium, calcium and barium doped graphene should be given.

5.2.1. Li/Ca/Ba doped graphene - phonons and symmetry analysis

The mutual influence of electrons and phonons in graphene is a highly debated topic and the origin of some very interesting phenomena. The semi-metallic character of its electronic structure is an important issue in understanding the behavior of phonons. The atomic vibrations are partially screened by electrons but in metal this screening can change rapidly for vibrations associated with certain q points which are determined by the shape of the Fermi surface [38]. As mentioned before, graphene is a material where the adiabatic Bohr-Openheimer approximation [226, 41] is no longer valid, which means electrons relax non-adiabatically to the lattice motion and that leads to the softening of phonon. It may occur only for q such that there are two electron states, k_1 and $k_2 = k_1 + q$, both on the Fermi surface [37]. For graphene, the electronic gap is zero only at two Brillouin zone points K and K' = 2K so we know that the Kohn anomaly occurs at $q = G$ and $q' = K$. The opto-electronic properties of graphene and graphite are directly affected by their environmental conditions and adatoms in graphene.

In this section, we used DFT to calculate vibrational frequencies and normal coordinates at the Γ point for the Li, Ca and Ba-doped graphene (the LiC₆-mono, CaC₆-mono and BaC₆- mono, respectively). These materials have been studied for their superconducting properties [60, 59, 243, 63, 257]. For the understanding of the electron-phonon coupling and the appearance of superconductivity in the doped graphene monolayer it is of great importance to have insight in phononic properties of the material. As explained in the previous section, the dopant-related vibrations are crucial for achieving superconductivity [258] and phonon softening is shown to be an indication of a strong electron-phonon coupling enhancing superconductivity [243]. A detailed description, as presented here, is meant also to be used as a practical guide for an experimental research, namely IR and Raman spectra, identifying and characterizing these materials, as well as a theoretical ground for further research. The recent experimental and theoretical studies of the electron-phonon coupling and superconductivity in single layer iron-selenides [72, 259] strengthen the need for a thorough analysis of phonons in the monolayer superconducting structures, like the doped monolayer graphene. Due to the fact that DFT and DFPT [225] (used for this work) are based on the adiabatic ABO approximation, which is not sufficient for the study of the Kohn anomaly necessary analytical corrections are required for certain

5. RESULTS

modes. The group theory methods are additionally used to support the calculation. Finally, the ab-initio results are compared to experimental data for graphene.

Computational details

All results reported here are obtained from the DFT calculations in the LDA, using the QE. The ionic positions in the cell are fully relaxed, in all calculations, to their minimum energy configuration using the BFGS algorithm. The hexagonal cell parameter c was set to $c = 12.5 \text{ \AA}$ in order to simulate a two-dimensional system. The norm-conserving pseudopotential [260] and the plane wave cutoff energy of 65-75 Ry are used in the calculation, accordingly convergence is achieved with an error less than 1% for all calculated frequencies, by varying values of the plane wave energy cutoff. The unit cell for the H-site doped monolayer was modeled in the $\sqrt{3} \times \sqrt{3}$ R60° in-plane unit cell (seven atoms per unit cell, with adatom in every other hollow spot), consisting of one adatom placed above the center of the carbon hexagon. This configuration has been theoretically studied as an optimal structure [59, 60] and experimentally realized for the Li-doped monolayer [56] and Ca-doped bi-layer graphene [261]. The adatom-graphene distance for the LiC₆-mono is $h = 1.8 \text{ \AA}$, for the CaC₆-mono $h = 2.04 \text{ \AA}$, for the BaC₆-mono $h = 2.17 \text{ \AA}$. The phonon frequencies are determined by the DFPT for evaluating the effects of the adatoms on the phonon spectrum. All calculations are performed at the Γ point of the Brillouin zone. The symmetry groups of these structures are $Dg80 = TD_{6h}$ for pristine graphene and $Dg77 = TC_{6v}$ for graphene doped at the H-site [262, 263]. All groups are diperiodic (i.e. Dg) and represented as a semi-direct product of the translational subgroup T and a point group. Translational subgroups of these symmetry groups need not to be mutually identical.

Results and discussion

The total energies for all considered structures and graphene are calculated and, as expected, graphene doped at the H-site has a higher total energy than the graphene. This does not represent an obstacle for the stability. If the provided reservoir of adatoms is large enough, adatoms will be adsorbed in graphene, because the thermodynamical potential is a grand-canonical one and then becomes minimized:

$$-k_B T \ln \mathcal{Z} = \Phi_G = \langle E \rangle - TS - \mu \langle N \rangle \quad (5.2)$$

5. RESULTS

The transfer of the adatoms on the graphene will reduce Z , even if μ is small. We begin with the group theory discussion and the symmetry assignment of the modes. The symmetry group $Dg77 = TC_{6v}$ of the H-site adatom doped graphene is a subgroup of the diperiodic group $Dg80 = TD_{6h}$, a symmetry group of graphene. In order to find which of the phonon modes of the H-site adatom doped graphene monolayer corresponds to a certain phonon mode of the graphene, it was necessary to reduce the corresponding irreducible representation of group $Dg80$ to its subgroup $Dg77$. For the modes belonging to the Γ point:

$$\begin{aligned}\Gamma E_{2g}(Dg80) \downarrow Dg77 &= \Gamma E_2 \\ \Gamma B_{1g}(Dg80) \downarrow Dg77 &= \Gamma B_1\end{aligned}\tag{5.3}$$

(\downarrow is the notation for the subduction operation). Since the translational subgroup of these diperiodic groups is represented by the number one in irreducible representations belonging to the Γ point, the upper formulae are obtained using the point group character tables (see, e.g., [264]). For the modes belonging to the K point, the characters of $Dg80$ for irreducible representations at this point [29] are necessary. The reduction procedure gives

$$\begin{aligned}KA'_1(Dg80) \downarrow Dg77 &= \Gamma A_1 + \Gamma B_2, \\ KA'_2(Dg80) \downarrow Dg77 &= \Gamma A_2 + \Gamma B_1, \\ KE'(Dg80) \downarrow Dg77 &= KE''(Dg80) \downarrow Dg77 = \\ &\Gamma E_1 + \Gamma E_2.\end{aligned}\tag{5.4}$$

ΓB_{1g} , ΓE_{2g} , KA'_1 , KA'_2 , KE' , KE'' of graphene correspond to the mode B_1 , E_2 , A_1 and B_2 , A_2 and B_1 , E_1 and E_2 , E_1 and E_2 for the graphene doped at H-site, respectively. There is a perfect agreement with the irreducible representation shown in Figures 5.4, 5.6, 5.5, . T' is a translational subgroup of $Dg77$ while T is translational subgroup of $Dg80$. T' is a subgroup of T such that for all elements of T' the phase factor $\cos(\vec{k}_K \cdot \vec{R})$ is equal to one. This factor appears in the characters of irreducible representations of $Dg80$ for the K point [29]. The vibrational frequencies and normal coordinates for the LiC_6 -mono, CaC_6 -mono, BaC_6 -mono are shown in Figure 5.4, 5.5, 5.6 respectively. For all compounds, true acoustic mode (with $\omega = 0$ at the Γ point) are not represented. Also, modes where Kohn anomaly is present are not depicted. For all H-site doped graphene, the two lowest modes can be related to three acoustic modes of graphene. Therefore, their frequencies are the lowest. The remaining modes have normal coordinates similar to graphene phonons at the Γ and K points.

5. RESULTS

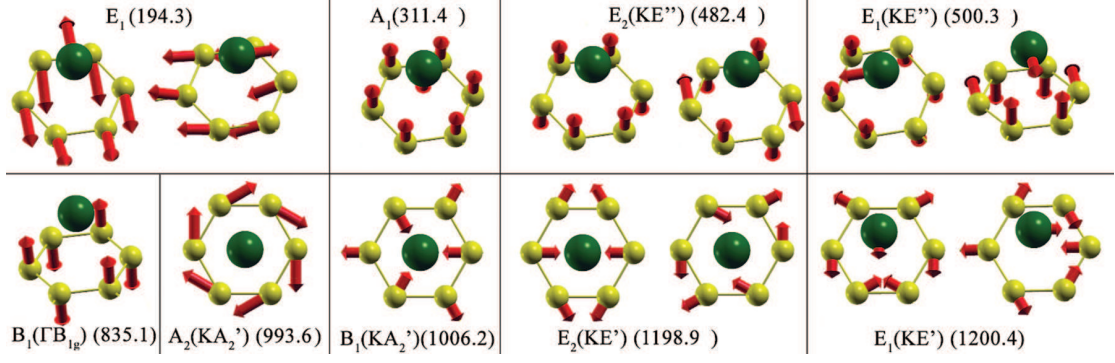


Figure 5.4.: Vibrational frequencies (in wave numbers) and normal coordinates for the monolayer $\text{LiC}_6\text{-mono}$. The modes of graphene with a similar displacement pattern are denoted in parentheses.

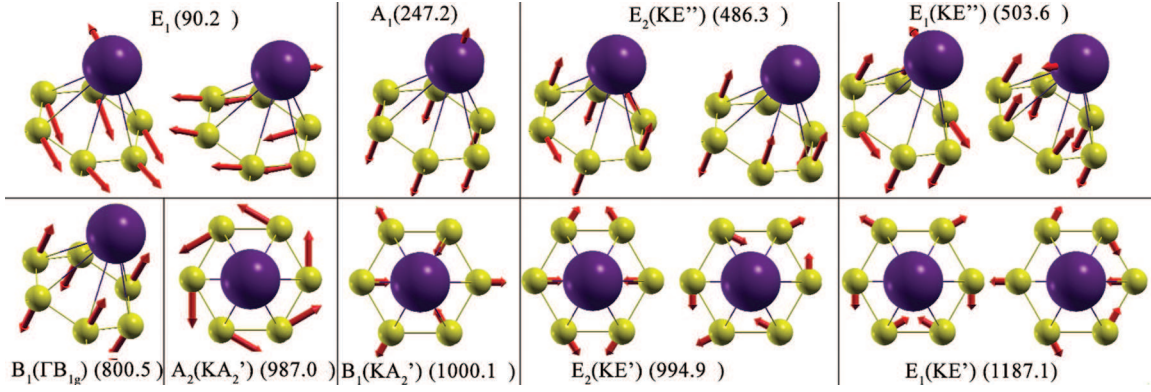


Figure 5.5.: Vibrational frequencies (in wave numbers) and normal coordinates for the monolayer $\text{CaC}_6\text{-mono}$. The modes of graphene with a similar displacement pattern are denoted in parentheses.

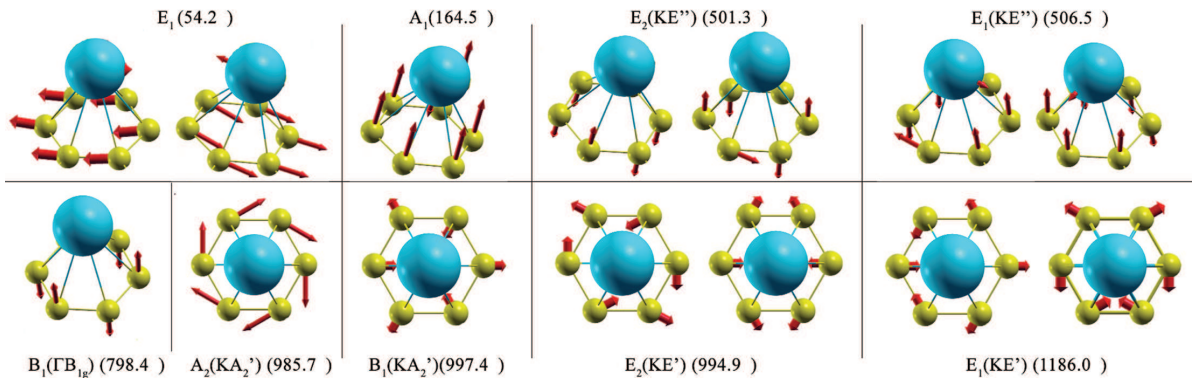


Figure 5.6.: Vibrational frequencies (in wave numbers) and normal coordinates for the monolayer $\text{BaC}_6\text{-mono}$. The modes of graphene with a similar displacement pattern are denoted in parentheses.

5. RESULTS

This is indicated in Figure 5.7 (the Kohn anomaly is marked with red) and it is a consequence of the Brillouin zone folding. The K point of graphene becomes equivalent to the Γ point of H-site doped graphene, due to the reduction of the basis vectors length in the reciprocal space [58]. This reduction is caused by an increase in the size of the primitive cell in direct space, as depicted in Figure 5.8. The K point of the Brillouin zone (BZ) of graphene is folded to the Γ point of the reconstructed BZ in the H-site doped graphene and the phonon bands at the Γ and K points in graphene are ascribed to the folded superstructure, as shown in Figure 5.7. The Γ point is the same for both structures. The normal coordinates of phonons at high symmetry points of the BZ of monolayer graphene can be determined solely by the symmetry arguments [265, 266, 30]. For the complete system of eigenvectors of the honeycomb lattice at the Γ and K points, see ref. [30]. There are several reports on the experimental realization of doped graphene [258, 267, 268, 269]. None of them contains Raman or infra-red spectra of these structures. Therefore, we compared our results with inelastic X-ray scattering experiments on graphite [270]. In this paper graphite is considered as a system of weakly interacting graphene sheets. The bonds between the two carbon atoms in the plane are much stronger than the weak van der Waals interactions between the layers. The graphite phonon modes correspond approximately to the in-phase and out-of-phase vibrations of the two graphene planes. Most of the phonon branches in graphite are almost the same as in graphene [38, 270]. The group of wave vectors for all H-site doped graphene at the Γ point is C_{6v} . The modes of E_2 symmetry are Raman active while those of the A_1 and E_1 symmetries are both Raman and infra-red active. According to ref. [270], the experimentally determined values for phonon frequencies are 542 cm^{-1} , 867 cm^{-1} , 1007 cm^{-1} , 1218 cm^{-1} , 1576 cm^{-1} , for KE'' , ΓB_{1g} , KA'_2 , KE' , ΓE_{2g} , respectively, while the KA_1 mode is unresolved (its value is known from other ab initio calculations, and it is 1310 cm^{-1} [38]).

If we compare our calculated modes with experimental data [251], small discrepancies exist due to the presence of the adatoms. Significant discrepancies can be seen for modes related to the Kohn anomaly. In graphene, the Kohn anomaly exists in E_{2g} and KA'_1 modes due to the strong electron-phonon coupling. The fact that the Kohn anomaly can be observed in a two-dimensional system is quite remarkable since this phenomenon is more pronounced for one-dimensional systems the Kohn anomaly can be observed and measured using Raman spectroscopy [38]. As mentioned before, the zone folding effects in graphene occur because the graphenes unit

5. RESULTS

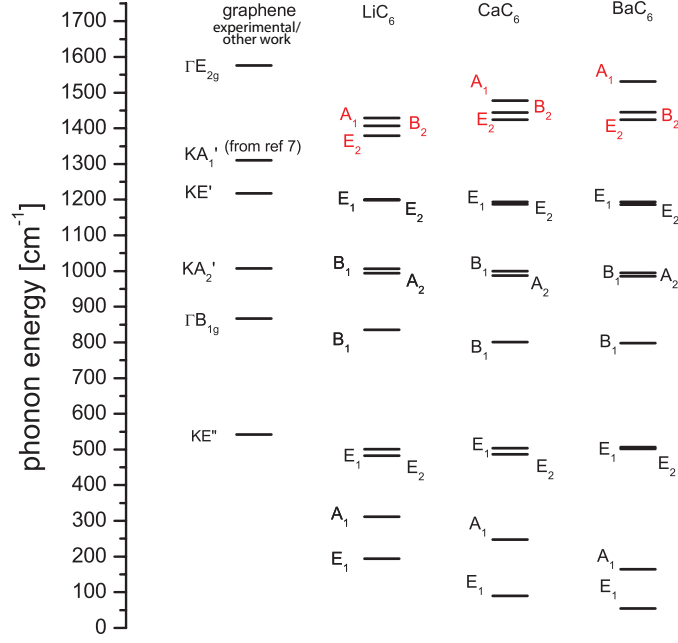


Figure 5.7.: Comparison of calculated vibration frequencies for various stacking and experimental data. The modes which require non-adiabatic are marked in red. The experimental values are taken from ref. [270].

cell consists of two carbon atoms, where the presence of an additional adatom enlarges the unit cell. This affects the electron [261] and phonon configuration as well. Comparing the phonon dispersion relations of the pristine and doped graphene, the phonon bands along the Γ -K direction in graphene correspond to the ones at the H-site doped graphene along the $\Gamma M \Gamma'$ direction. A small shift in energies can be observed due to the adatom presence.

In the phonon dispersion relations of doped graphene one can distinguish three regions: the low-energy region (0-400 cm⁻¹) with the adatom-related modes, the mid-energy region (400-900 cm⁻¹) can be associated with the C_z and the high-energy

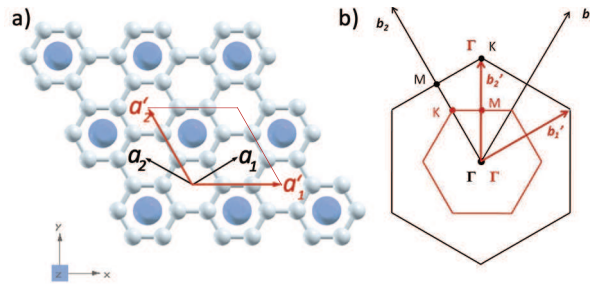


Figure 5.8.: a) Unit cell of pristine graphene (black) and H-site doped graphene (red); b) corresponding BZ.

5. RESULTS

region consisting of the carbon-carbon stretching modes [59]. Comparing the phonon dispersion bands, like in Figure 5.9 for graphene and the LiC₆-mono, one can see how, due to the zone folding, graphene's Γ and K point modes correspond to the Γ modes of the H-site doped graphene with small discrepancies which originate due to the presence of an adatom. For the graphenes out-of-plane optical phonon (Γ at 867 cm⁻¹ [270]) and the corresponding H-site doped graphenes mode there is a discrepancy in energies which depends on the type of adatom (different shifts appear for the Li, Ba and Ca doping). A similar behaviour appears for the two optical in-plane modes of graphene and its corresponding H-site doped ones. Due to the zone folding, it is also expected that the Kohn anomaly will be also present in modes which are related to these two. All frequencies are computed by the static perturbation theory of the DFT energy, from the linearized forces acting on the atoms due to the static displacement of the other atoms from their equilibrium positions. As stated, this DFT approach is based on the adiabatic ABO approximation, which is broken for graphene so the modes where the Kohn anomaly seems to require a dynamic approach, i.e. time-dependent perturbation theory. As a conclusion, our calculated frequencies, for modes where the Kohn anomaly does not exist, are in a satisfying agreement with those reported in [270]. There is a discrepancy around 10% (10-90 cm⁻¹ depending on the mode) between experimental results for graphene presented in [270] and calculated energies of graphene-related modes, which we can attribute to the presence of the adatom in H-site doped graphene. The occurrence of non-adiabatic effects in the GIC is observed and studied [271] thoroughly. In Li, Ca and Ba GIC, for modes with present Kohn anomaly, non-adiabatic correction is less than 20%. ($\Delta\omega$ for E_{2g} mode in Li GIC is 218 cm⁻¹, Ca GIC is 83cm⁻¹ and for Ba GIC is 59cm⁻¹ [271].)

It is expected that the doped graphene has the same correction since we considered graphite as a system of weakly interacting graphene sheets. In all cases, the vibrational frequencies for modes with displacement pattern similar to the corresponding phonon in monolayer graphene are almost the same.

The frequency splitting is due to the presence of the adatoms. The Raman tensors and optical modes [272] for all considered structures are summarized in table 5.1. In summary, by using DFT, we have calculated the vibration frequencies and normal coordinates of the Γ point phonons for monolayer graphene doped with lithium, calcium and barium. We found that they have a similar displacement pattern as those for graphene at the Γ and K points. The group theoretical analysis that

5. RESULTS

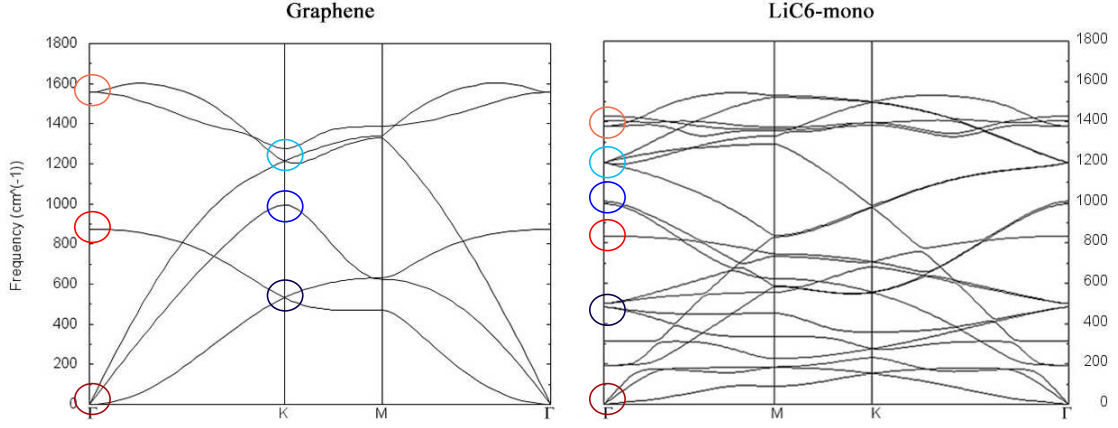


Figure 5.9.: Phonon dispersion for graphene and the LiC₆-mono. Red circles mark modes in the Γ point and blue circles at the K point. Due to the zone folding, graphene modes from the Γ and K points fold to modes in the Γ point at the LiC₆-mono.

Table 5.1.: Raman tensors and symmetry classification of optical modes for doped monolayer graphene

		<i>Raman tensors</i>					
graphene		A_{1g}	E_{1g}	E_{1g}	E_{2g}	E_{2g}	
$Dg80=TD_{6h}$		$\begin{pmatrix} a & 0 & 0 \\ 0 & a & 0 \\ 0 & 0 & b \end{pmatrix}$	$\begin{pmatrix} 0 & 0 & 0 \\ 0 & 0 & c \\ 0 & c & 0 \end{pmatrix}$	$\begin{pmatrix} 0 & 0 & -c \\ 0 & 0 & 0 \\ -c & 0 & 0 \end{pmatrix}$	$\begin{pmatrix} d & 0 & 0 \\ 0 & -d & 0 \\ 0 & 0 & 0 \end{pmatrix}$	$\begin{pmatrix} 0 & -d & 0 \\ -d & 0 & 0 \\ 0 & 0 & 0 \end{pmatrix}$	
$O_z \parallel C_6$							
$O_x \parallel C'_2$							
Aα		A_1	E_1	E_1	E_2	E_2	
$Dg77=TC_{6v}$		$\begin{pmatrix} a & 0 & 0 \\ 0 & a & 0 \\ 0 & 0 & b \end{pmatrix}$	$\begin{pmatrix} 0 & 0 & c \\ 0 & 0 & 0 \\ c & 0 & 0 \end{pmatrix}$	$\begin{pmatrix} 0 & 0 & 0 \\ 0 & 0 & c \\ 0 & c & 0 \end{pmatrix}$	$\begin{pmatrix} d & 0 & 0 \\ 0 & -d & 0 \\ 0 & 0 & 0 \end{pmatrix}$	$\begin{pmatrix} 0 & -d & 0 \\ -d & 0 & 0 \\ 0 & 0 & 0 \end{pmatrix}$	
$O_z \parallel C_6$							
$O_x \parallel \sigma_v$							
		<i>Optical modes</i>					
$A\alpha$		$\Gamma_{opt} = 2A_1 + A_2 + 2B_1 + B_2 + 3E_1 + 3E_2$					

5. RESULTS

demonstrates the correspondence between phonon modes of graphene and the H-site doped graphene. A satisfying agreement with experimental data [270] additionally supports these calculations. The results provided in this work are important for the characterization of those structures and their further investigation and application.

5.2.2. LiC_6 Superconductivity and enhancement

Results of Damascelli group [56] in 2015 indubitably shown that graphene can become superconductive and the ARPES measurements on their monolayer graphene doped with lithium, just as predicted with DFT, have an electron-phonon pairing mechanism. However much before an experimental realization, almost right after the superconductivity in the Li-intercalated graphene has been suggested by Profeta, the considerable attention has been devoted to the study of its enhancement [257, 273, 274, 275]. From the previous GIC research as well as a graphene study, a conclusion is drawn. Beside the Li doping, an increase of electron-phonon pairing potential is necessary to enhance EPC. And in order to increase λ , the phonon frequencies must be softened. In the bulk material such effect would not be easy to accomplish. Nonetheless, the low-dimensional materials offer great possibility for manipulation and engineering, especially with techniques that are not available in bulk materials. Application of homogenous strain would be practically impossible outside of the theoretical discussion, and in low-dimensional material it is rather simple. Based on this concept, we study the effects of the tensile equibiaxial strain on the Li-intercalated graphene. Application of the strain is an intensively studied topic, both in theory and experiment [276, 277, 278, 7]. Namely, an application of strain on graphene can induce changes of the vibrational properties [279, 280], in the electronic band gaps [281, 282] and significant changes in conductivity both at local and macroscopic level [283, 284, 285]. The type of the strain is a very important feature, since the graphene lattice symmetry determines its band structure. The breaking of the hexagonal symmetry will modify the band structure of graphene [286, 287], causing the opening of the band gap and many other effects [288, 289]. Since our intention is to soften modes, without drastically modifying the structure, the tensile equibiaxial strain is employed in the calculations on the LiC_6 -mono (Figure 5.10 b)). Here it is shown that such strain causes softening of the phonons, in particular, the in-plane phonons will be dramatically softened, whereas the out-of-plane ones will be less affected [289]. This causes a wanted outcome and greatly

5. RESULTS

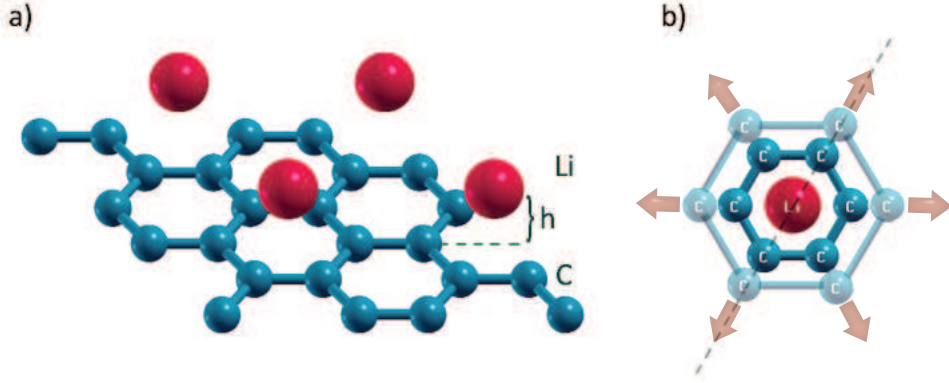


Figure 5.10.: a) Lithium-intercalated graphene, h is the adatom graphene distance.
b) Schematic description of biaxial tensile strain.

affects λ . We investigate the enhancement of the electron-phonon interaction in the LiC_6 -mono using the DFT calculation in the LDA [260] and based on the prior discussion, we find that λ is sensitive to the tensile equibiaxial strain, therefore producing a higher T_c . For instance, the strain of 10% makes a T_c increase of almost 300%!

Computational details

The ionic positions in the cell are fully relaxed, in all calculations, to their minimum energy configuration using the BFGS algorithm. The hexagonal cell parameter c was set to $c = 12.5$ in order to simulate a two-dimensional system. The norm-conserving pseudopotential and the plane wave cutoff energy of 65 Ry were used in the calculation. Although DFT with LDA may have problems in application in certain situations where electronic correlations are strong, for graphene, with large electronic bands, it is quite a suitable assumption [289, 290]. As stated before, there is pronounced Kohn anomaly in certain modes. Although DFT is known to underestimate the electron-exchange correlation energy in the presence of the Kohn anomaly [291], the application of DFT here is justified. The differences appear only in a small portion of the first Brillouin zone (as thoroughly discussed in previous section) and do not lead to significant inconsistencies when the electron interaction with entire phonon system is observed [292]. The unit cell for the LiC_6 -mono was modeled in the in-plane unit cell, with an adatom-graphene distance $h = 1.8 \text{ \AA}$. (Figure 5.10).

5. RESULTS

Table 5.2.: Physical properties of graphene under different values of tensile equibiaxial strain

<i>Strain</i> %	<i>h distance</i> (\AA)	<i>C-C bond</i> <i>length</i> (\AA)	λ	ω_{log}	T_c
0%	1.80	1.42	0.61	278.88	8.1
3%	1.69	1.46	0.47	876.17	6.42
5%	1.64	1.49	0.49	976.20	9.43
7%	1.61	1.52	0.55	1009.05	14.73
10%	1.54	1.57	0.73	827.09	28.72

λ was calculated with the electron momentum k-mesh up to $40 \times 40 \times 1$ and the phonon q-mesh $20 \times 20 \times 1$. The superconducting critical temperature was estimated using the Allen-Dynes formula with $\mu^* = 0.112$ [135]

Results and discussion

In order to strain the LiC₆-mono and increase the lattice constant, the in-plane distance between C atoms is increased leaving the hexagonal symmetry preserved. The Li adatom is placed above the H site in graphene (the center of hexagon) (Figure 5.10). The modification of the lattice constant does not interfere with the Li adatom position which remains fixed in the center of the hexagon, leaving the symmetry unbroken. Due to the expansion of the carbon atom distances and the invariance of the hexagonal symmetry, the Li adatom shifts only along the z-axis. The effects of several values of the strain, which increase the lattice constant by 3%, 5%, 7%, and 10%, are studied. Larger strains are not applied due to the instabilities that occur after the attempt of geometrical optimization and relaxation.

Table 5.2 presents the physical parameters of the Li-doped graphene under the various strains. The distance between the Li adatom and graphene decreases with the strain, as the Li adatom moves down deeper towards graphene. When the strain is applied, the distance between neighboring C atoms increases and the graphene π bonds less repulse the Li adatom, which then moves down along the z-axis. In Figure 5.11, the electronic DOS is shown (values are normed to the Fermi level).

The small shift of the Fermi level can be observed with the strain. Here it is worth mentioning that in graphene, a truly 2D system with low electron density, the long-range Coulomb force is weakly screened and the electron-electron interaction cannot

5. RESULTS

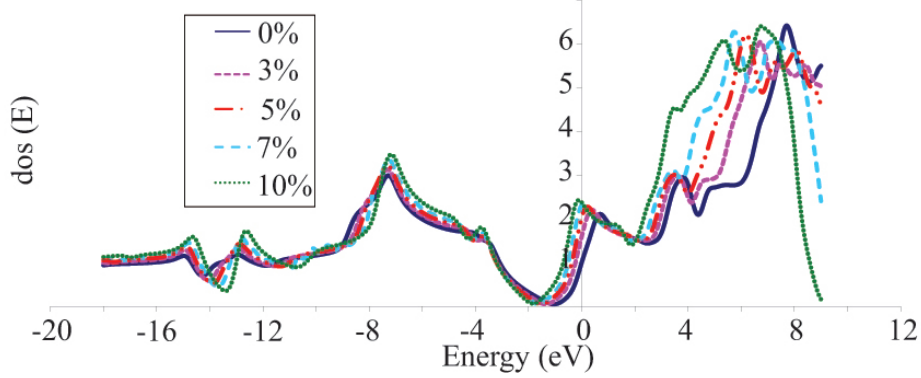


Figure 5.11.: Electron density of states for the LiC_6 -mono under a tensile equibiaxial strain

be neglected. The two-dimensionality in graphene can cause enhanced excitonic effects, like the M-point exciton [44, 293] or the charge density waves (CDWs) formation (the Peierls transition) as a result of the Fermi nesting. Especially an interplay between superconductivity and CDWs seems to be important [294, 295]. Namely, CDWs make a pre-existing environment for superconductivity [296]. Various strains in graphene have been studied as a method for the introduction of different broken symmetry phases. CDWs in graphene have been thoroughly investigated both theoretically [297, 298, 299] and experimentally [298] showing interesting results. For instance, the presence of axial magnetic field caused by a buckle strain can lead to realization of CDWs [297]. Also, in CaC_6 the electron-electron repulsion is dominant within graphene sheets [298] producing the CDW stripes. In the case of strained the LiC_6 -mono, DOS near the Dirac point gets enhanced (Figure 5.11), hence the question about interplay of electron-electron and electron-phonon interaction can be imposed. The problem of CDW in graphene, doped and strained, is discussed comprehensively and its very existence in LiC_6 -mono is not in conflict with our discussion and results. Moreover, CDW and superconductivity appear together in different systems like high- T_c superconductors or intercalated graphite [299, 300, 301] and can be even used as a criterion for high-temperature superconductivity.

Contrary to electronic image, where there is no significant adjustments, consid-

5. RESULTS

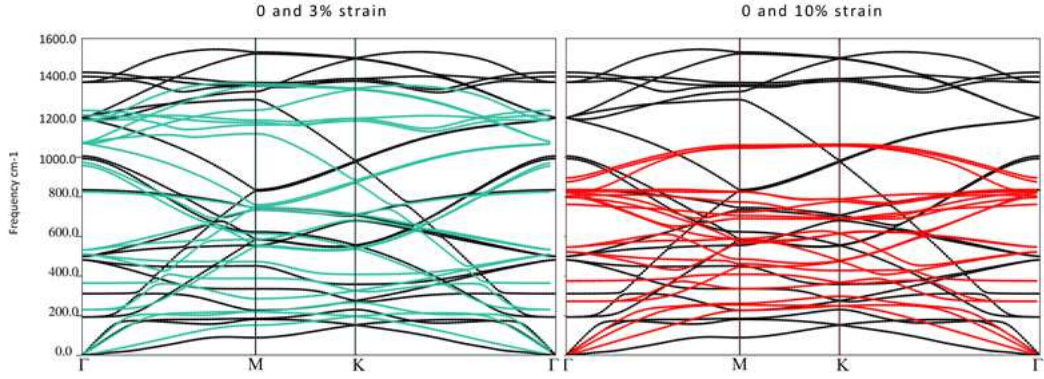


Figure 5.12.: Phonon dispersion for the LiC₆-mono, black lines as for the non-strained the LiC₆-mono and green and red for the 3% and 10% tensile biaxial strain, respectively.

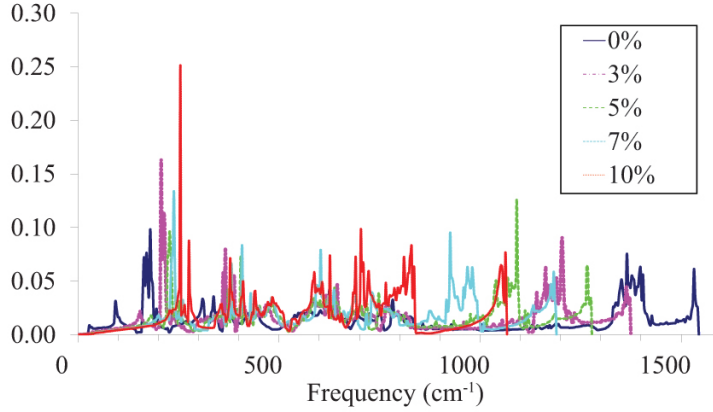


Figure 5.13.: Comparison of phonon DOS for various strains

erable changes are present for the phonons. In the phonon dispersion spectrum the three regions can be distinguished: the adatom-related modes are associated with low-energy regions ($0-400 \text{ cm}^{-1}$), where $300-400 \text{ cm}^{-1}$ are Li modes mixed with the out-of-plane carbon modes (Cz), the mid-region ($400-900 \text{ cm}^{-1}$) can be associated with Cz modes and the high-energy region with carbon-carbon stretching modes [59]. The main contributions to λ come from the low-energy lithium modes and the carbon vibrations along the z-axis, with an additional contribution from the C-C stretching modes (in agreement with [59] and [60]).

As shown in Figure 5.12 significant softening of phonons occurs with the application of strain. In green phonon dispersion is depicted for the 3% strained LiC₆-

5. RESULTS

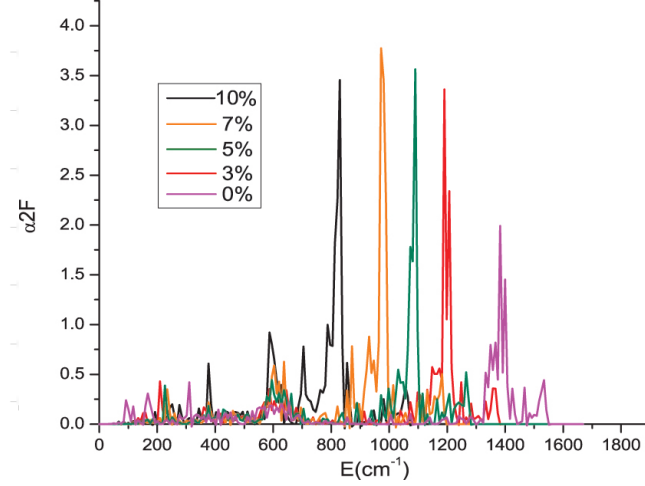


Figure 5.14.: Comparison of Eliashberg function for equibiaxial strain.

mono and in red for 10%. The softening of the high-energy C-C stretching modes is strongly present with a larger strain. In addition, the consequent increase of the phonon DOS in the low energy region occurs as well. The phonon density of states (PhDOS) as a function of strain is depicted in Figure 5.13. Although the low-energy modes slightly move upwards in energy, the main effect on the electron-phonon coupling is the softening of graphene high energy C-C stretching modes.

The Eliashberg spectral function (Figure 5.14) describes which phonon modes couple with the electrons on the Fermi level. The intensity of the Eliashberg function is greatly increased in the area of the C-C stretching modes, with the strain. This results in a great increase of λ and T_c . For the 10% tensile equibiaxial strain we get $\lambda = 0.73$ and $T_c = 29$ K. λ is presented as function of strain in Figure 5.15. It is worth mentioning that there is a reduction in λ for small values of strain (0-3%) (Figure 5.15). Particularly, with strain, the C-C bonds expand, causing a decrease of the Coulomb repulsion between the p orbitals and the Li adatom. That allows the Li adatom to descend toward the center on the graphene hexagon. As emphasized before, a too small intercalant-graphite layer distance in the GIC is destructive for superconductivity. On the other hand, this effect vanishes for larger strains, while an increase in T_c , even up to three times larger than the value reported for non-strained LiC_6 -mono, can be observed. This effect is associated to an overlap of the carbon π and the Li orbitals. For the small strain, the Li adatom drops down toward the center of hexagon and its orbitals overlap more with the carbon π orbitals. That causes an increase in charge transfer and emptying of the interlayer band, which reduces λ . When more strain is applied, the carbon bonds

5. RESULTS

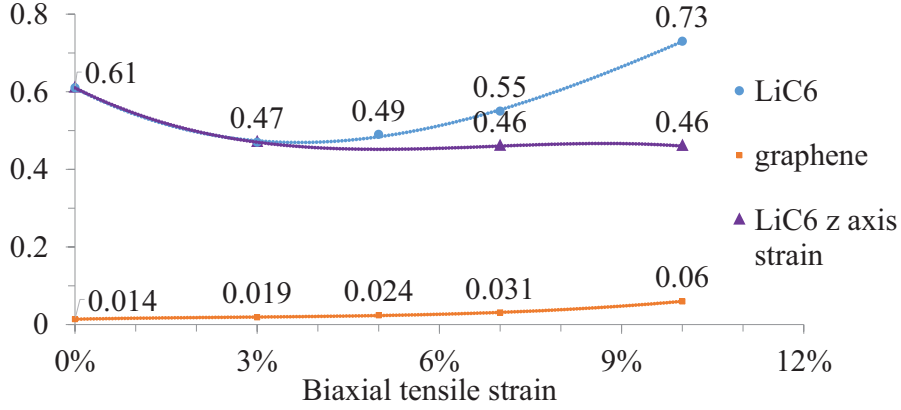


Figure 5.15.: Electron-phonon coupling constant behavior with tensile equibiaxial strain.

are elongated and the n orbitals move away, both from each other and the center of the hexagon. The orbital overlap is reduced, and after the certain critical value, λ increases, following the strain (circles in Figure 5.15). In order to corroborate this interpretation, we perform two additional calculations: the calculation on non-strained graphene, where the Li adatom position is shifted along the z -axis; and the second one with the strained pristine graphene.

Here it is proven that an increase of λ is a mutual effect of strain and doping. For the first calculation, the π orbitals remain fixed in their positions (since there is no strain). As the overlap with the lithium orbital and carbon π orbitals increases and one can clearly see that λ is decreased (violet triangles in Figure 5.15) due to an approach to the charge transfer completion and emptying of the interlayer band. The effects of the strain on the pristine graphene λ are also depicted in Figure 5.15 (orange squares). Graphene has a very small λ which is increased with strain almost four times, but effect of this enhancement is negligible ($\lambda = 0.06$). On the other hand, Figure 5.16 presents the effects of the different strain on electronic localization function (ELF). The significant changes for the large strain are presented, proving the above-described effects. For ELF at 10% of the strain, the electron localization region is greatly lowered as graphene and adatom separate one from another and as a C-C bond are elongated. As expected, the strain alone will not boost the λ considerably, nor the doping itself. A complex mechanism of the enhancement is a mutual effect of the mechanical effects with the presence of the interlayer level, all owing to the unique structure of graphene. For the notable enhancement of λ the

5. RESULTS

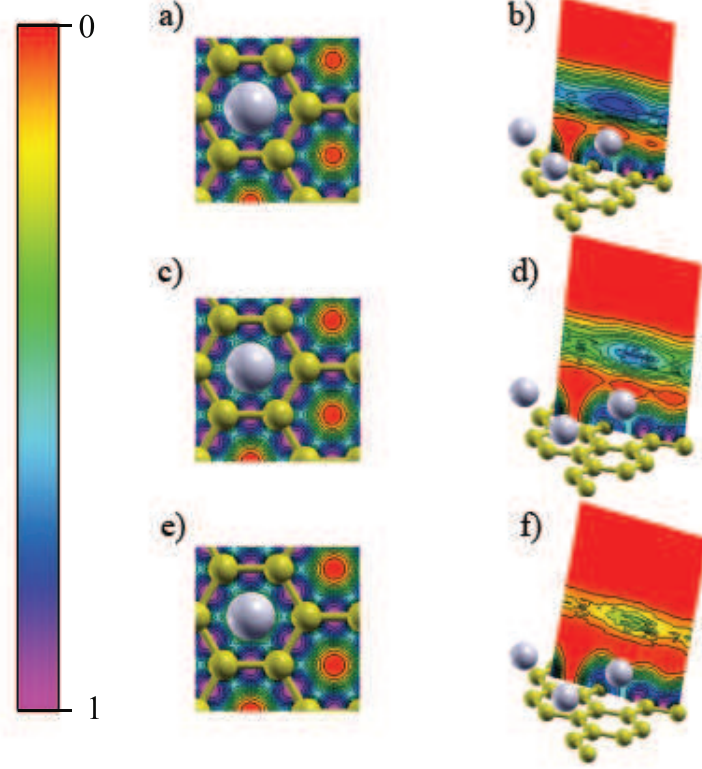


Figure 5.16.: ELF (electron localization function) for the LiC_6 -mono with strain: (a) ELF for the LiC_6 -mono without strain on the xy plane; (b) ELF for the LiC_6 -mono without strain on the xz plane; (c) ELF for the LiC_6 -mono for the 5% strain on the xy plane; (d) ELF for LiC_6 -mono for the 5% strain on the xz plane; (e) ELF for LiC_6 -mono for the 10% strain on the xy plane; (f) ELF for LiC_6 -mono for the 10% strain on the xz plane. In panels (a), (c) and (e) we can see slight changes in ELF projected on the xy plane, localization region at Li adatom is enlarged. In panels (b), (d) and (f) are shown effects of strain, projected on the xz plane. Notable change is present for the 10% of strain, where the electron localization region is significantly lowered due to the described effects.

5. RESULTS

presence of both the adatom and the strain is essential. In summary of this section, we can conclude tensile biaxial strain enhances EPC for the LiC₆-mono. Since no symmetry is broken, there are no major changes in the electronic structure of the system. On the other hand, the strain softens the phonon modes significantly. The critical temperature is enhanced by the strain, up to $T_c = 29$ K where the EPC constant is 0.73. Further we conclude that both the presence of the adatom and the strain are necessary for an enhancement of λ . It is important to stress that this increase in T_c , achieved by the described mechanism, can be experimentally realized. A pristine graphene is experimentally confirmed to be elastically stretchable up to 25% [7] making here considered strains feasible.

5.2.3. Optical properties of LiC₆

The graphene's specific electronic structure and unique combination of the optical electronic properties have inspired numerous investigations of its optoelectronic properties and possible applications in photonics, energy applications and detectors. For optical properties as well, intercalation can induces interesting new properties. Great example is that optical transmittance of graphite increases upon metallization by intercalation with e.g caesium [302]. This unusual property results from the unique band structure of the graphene layer; intercalation heavily dopes ultrathin graphite, shifting the Fermi level upward more than any other band engineering method [303, 304, 305, 306] suppressing interband optical transitions due to Pauli blocking thus increasing transmittance of light in the visible range. Li doped graphitic materials are studied for optical properties, mostly in form of the ultrathin films (3-60 layers) [307]. In this section we continue investigation of the LiC₆-mono by studying optical properties using only DFT techniques. This computationally inexpensive method though very crude can gives us a surprisingly good qualitative image. Since there are no prior calculations of the LiC₆-mono optical properties in literature to compare our results with, a test on a known material is necessary to check the sufficiency of applied method. The calculations on MoS₂ using the same DFT method were made and the results were compared with the literature proving the satisfactory correspondence.

The MoS₂ monolayer is a member of transitional metal dichalcogenides 2D materials family, and it has a hexagonal structure, like graphene, with the monoatomic Mo plane placed between two monoatomic S planes, and it displays some interesting

5. RESULTS

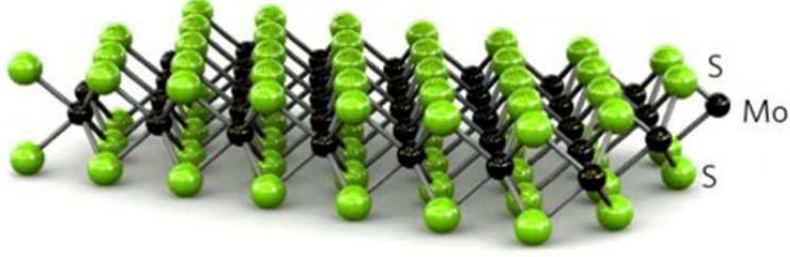


Figure 5.17.: Atomic model of single layer MoS₂

electronic and photocatalytic properties [308, 309]. Unlike the graphene, which does not have a band gap, a property essential for many optical applications, MoS₂ is direct-gap semiconductor [310] which opens possibilities for many optical applications. In this section we study optical properties of graphene doped with lithium and MoS₂ (as shown in Figure 5.17), in particular we discuss the imaginary part of dielectric function, using approaches based on DFT, implemented in the QE. In QE the dielectric constant computed by phonon package is the static (high-frequency) dielectric constant of the system (also referred as ϵ_∞ in the literature). It is a ground state property and its computation is exact (as much as exchange-correlation functional is). In QE implementation of the RPA frequency dependence is computed from an explicit summation of dipole matrix elements and transition energies. [428] We are interested in the study of the optical properties of this two materials using DFT as a computational inexpensive method for the qualitative description. First, we study MoS₂ and compare it with existing studies in order to approve this technique as sufficient for study and then we investigate graphene doped with Li and compare it with pristine graphene.

Computational details

The ionic positions in the cell are fully relaxed, to their minimum energy configuration using the BFGS algorithm. The hexagonal cell parameter c was set to $c = 12.5$ Å in order to simulate a two-dimensional system. The norm-conserving pseudopotential [260] and the plane wave kinetic energy cutoff of 65 Ry were used in the calculation of the LiC₆-mono. The uniform k -point grid was composed of

5. RESULTS

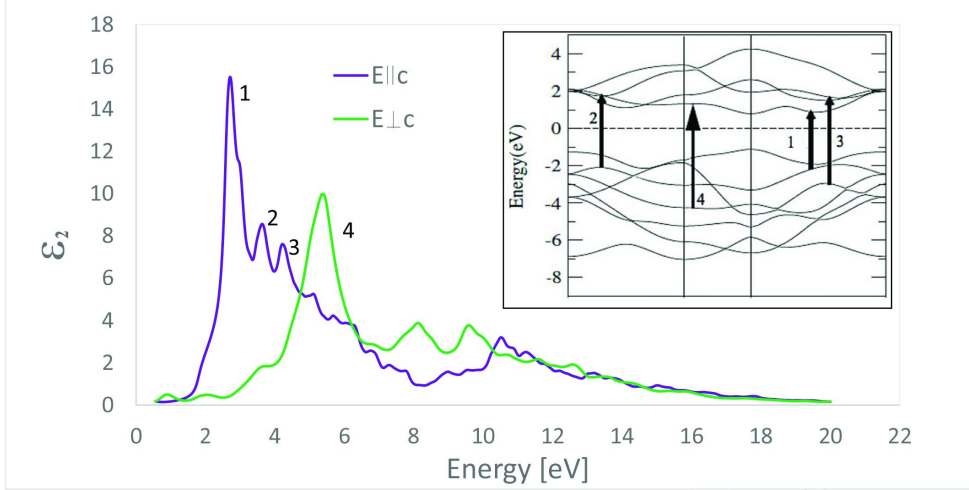


Figure 5.18.: The calculated imaginary part of the dielectric function for MoS₂

4096 points in the first Brillouin zone. For MoS₂, the GGA exchange-correlation functional, Perdew-Burke-Ernzerhof (PBE) [311] was used for the relaxation of the system. Also, similar as in graphene, to avoid periodicity effects, 20 Å vacuum between layers was added. The plane wave kinetic energy cutoff of 50 Ry was used and the uniform k-point grid was composed of 4096 points in the first Brillouin zone. Dielectric function $\epsilon(\omega)$ was calculated, in the range 1-20 eV, within the framework of the RPA [312] based on the DFT ground-state calculations, starting from eigenvectors and eigenvalues, implemented in the QE code as epsilon.x post-processing utility. Matrix elements were accounted only for interband transitions that can cause an inaccuracy $\epsilon(\omega)$. RPA does not include the nonlocal part of the pseudopotential and it is not able to include in the calculation the non-local field effects and excitonic effects. We are interested in the study of the optical properties of this two materials using DFT as a computational inexpensive method for the qualitative description. For a more precise and detailed approach the many-body theory and its methods are required (Bethe-Salpeter equation (BSE) and GW approximation).

Results and discussion

The imaginary part of the dielectric function of the MoS₂, pristine graphene and the LiC₆-mono is calculated. From the imaginary part of dielectric function an absorption spectra can be derived. The dielectric function have been calculated in the energy range from 1 to 20 eV.

The imaginary part of the dielectric function of MoS₂ for the E vector perpendicular to the c axis is presented in the green color and E parallel to the c axis is

5. RESULTS

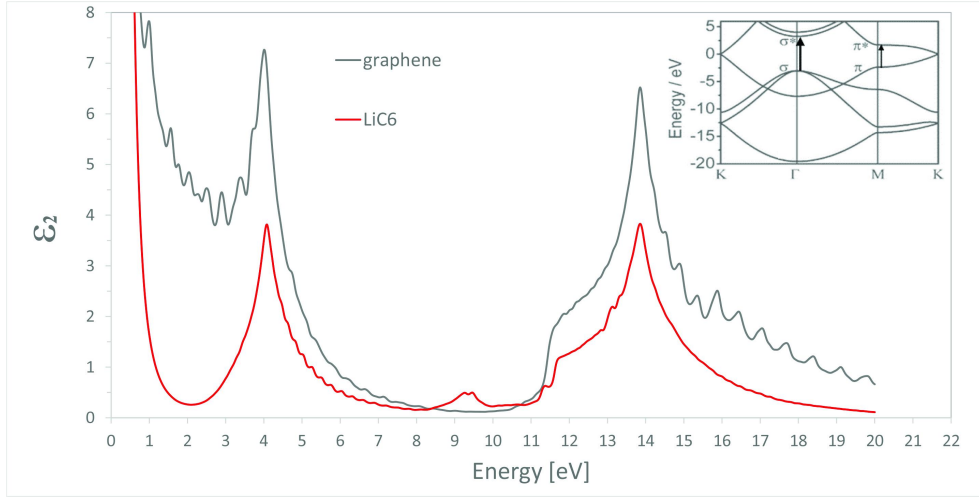


Figure 5.19.: The calculated imaginary part of the dielectric function for the pristine and intercalated graphene for the E vector perpendicular to the c axis

presented in the violet on Figure 5.18. Four distinct structures on Figure 5.18 , 1 (2.7 eV), 2 (3.7 eV), 3 (4.2 eV) and 4 (5.3 eV) can be connected to the interband transitions, marked on the inset of the electronic band structure, with 1, 2, 3 and 4 as well. All interband transitions depicted here, are mainly due to the transition from the p valence bands of s to the d conduction bands of the Mo [313]. The peak 1 is determined by the interband transitions from the valence bands I, II below the Fermi energy to the conduction bands I, II and III above the Fermi energy along the Γ M and $K\Gamma$ direction. The peak 2 is due the interband transitions from the valence bands II below the Fermi energy to the conduction bands II and III above the Fermi energy along Γ M direction and near the M. The peak 3 exists due to the interband transitions from the valence bands III below the Fermi energy to the conduction bands II and III above the Fermi energy along $K\Gamma$ direction. Peak 4 is determined by the interband transitions from the valence bands IV below the Fermi energy to the conduction band I above the Fermi energy in the vicinity of the M high symmetry point. Our calculations are in agreement with the other similar DFT studies [313] and experimental research as well [314] but for the more precise results an advance approach is needed (BSE). By concluding this, we proceed to the imaginary part of the dielectric function of the pristine and intercalated graphene. Results are presented in Figure 5.19.

For the pristine graphene, there is a significant peak at small frequencies at 4 eV and another peak at 14 eV. The origin of these peak structures is $\pi^* \rightarrow \pi$ and $\sigma^* \rightarrow \sigma$ interband transition [315], respectively. The ellipsometry measurements

5. RESULTS

show that the first peak is at 4.6 eV [293, 316, 317] and it is connected with the van Hove singularity in graphenes DOS (the M point). The lower value compared to one derived from the experiment, could be due to neglecting of the interaction between graphene and substrate and many-body interactions within the RPA calculation [318, 319]. There is also present singularity at zero frequency (due to metallic property of studied system). The intercalation did not introduce the band gap so peaks are not shifted as it can be seen on the Figure 5.19. The intensity of peaks obtained in this study cannot be discussed in a proper way due to approximative nature of the used method. The variation in peak heights for the same material, can be observed in calculations based on various models [320]. We can discuss qualitatively, for the peak at 4 eV, it is expected that, analogues to bulk graphite and the bulk LiC_6 , due to the up-shift of the Fermi level, part of the π^* -like final bands in graphite fall below the Fermi level in LiC_6 and lead to a reduction of the peak height [321]. Similar is expected to happen in graphene and the LiC_6 -mono. Similar effect is discussed in graphene monolayer doped with various amounts of B and N [322]. Continuing analogy with LiC_6 bulk, for other peak a 14 eV, this structure also corresponds to transitions at graphite, however, due to zone folding, they correspond to contributions from different regions in the LiC_6 Brillouin zone [321, 323]. In this section we made a brief study of the optical properties i.e. the dielectric function of the LiC_6 -mono using DFT techniques. To ensure quality of our approximate method first was performed calculation of MoS_2 and compared to literature where it was proven that the used method gives satisfactory results. Afterwards, graphene and the LiC_6 -mono calculations were made and we concluded that the Li intercalation in monolayer graphene does not significantly affects the imaginary part of the dielectric function and hence the absorption spectra. Because of the similarity in their properties, in the Li doped and pristine graphene, we can expect that they can be used in similar optic applications. Experimental data for comparison are not yet available for LiC_6 but parallels with graphene and the bulk LiC_6 can be drawn and discussed. Although used technique qualitatively well describes MoS_2 and LiC_6 , effects present in those materials due to the excitonic effects and interband transitions, demand a detail and advanced approach (but computationally significantly more expensive, time-demanding and resource-consuming). In technical aspect, we can conclude that DFT techniques can be used for study of the optical properties of these and similar 2D materials, and they provide the reliable and computationally non-expensive solution (even available for calculating on personal computer) for the

5. RESULTS

satisfactory qualitative description.

5.3. Magnesium-diboride monolayer

Magnesium diboride is an inter-metallic compound superconductor with a quasi-two dimensional character [82] and a critical temperature of $T_c=39\text{K}$. Although first synthesized and its structure confirmed in 1953 [80] interest in its properties grew since 2001 when it is discovered that MgB_2 exhibits the highest superconducting transition temperature T_c of all metallic superconductors. Peculiar properties of MgB_2 just begin with high T_c . The presence of unexpected phenomenon of the two-band superconductivity draw even more attention and debate. Because the limit of T_c in metallic superconductors had been believe to be 30 K in the framework of the BCS theory, the discovery of surprisingly high- T_c superconductivity in this simple binary inter-metallic compound has triggered enormous interests in the community. MgB_2 is the first and one of few materials where the presence of intrinsic multiple gaps has been experimentally established. There were additional surprises, MgB_2 is an sp not d metal, it has strong two-dimensional character and it becomes a superconducting with a high critical temperature due to extremely strong coupling to just few (3%) phonons, rather than having the strength spread rather uniformly over the phonon spectrum. Better definition describes MgB_2 not as a metal but as a self-doped semimetal with crucial a-bonding band nearly filled [203]. The light mass of B in MgB_2 certainly enhance the phonon frequency and therefore the critical temperature. There are some features considered to produces such a high T_c : (1) hole doping of the covalent s bands, achieved through the ionic, layered character of MgB_2 , (2) 2D character of the σ band density of states, making small doping concentrations n_h give large effects on DOS on the Fermi level, independent of n_h and [96] a very strong deformation potential of the σ bands from the bond-stretching E_{2g} modes [84]. The basic aspects of the electronic structure and pairing is in a rather strong coupling of the high frequency B-B stretch modes to the strongly bonding electronic B-B states at the Fermi surface. The phonon mediated mechanism with different coupling strengths between a particular phonon mode and selected electronic bands, boron σ and π -bands [96, 84, 87, 325, 326, 327, 328, 332, 333] results in the presence of two superconducting gaps at Fermi level. Moreover, its high T_c , simple crystal structure, large coherence length, high critical current density, high critical field, transparency of grain boundaries to current and low normal state re-

5. RESULTS

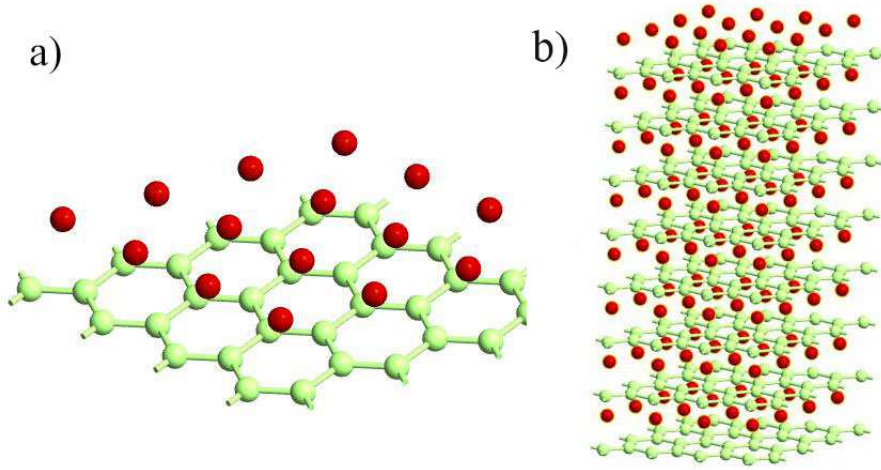


Figure 5.20.: Crystal structure of the monolayer MgB₂ (a) and the bulk MgB₂ (b), with hexagonal unit cell. Green (red) spheres represent Boron (Magnesium) atoms.

sistivity promise that MgB₂ will be a good candidate material for both large scale applications and electronic devices. MgB₂ has already been fabricated in the form of bulk, single crystal, thin film and shows potential for practical applications.

MgB₂ has layered structure where boron atoms form a honeycomb layer and magnesium atoms are located above center of the hexagons, between every boron plane. The boron layers alternate with a triangular lattice of magnesium layers. Theoretical studies offered insight in very interesting nature of this material, proposing that superconductivity originates in the boron p_x , p_y bands [83] and suggesting the two-band and even a new type-1,5 superconductivity [84, 329, 330, 331]. Experimental studies by STM tunnelling spectroscopy [87], point-contact spectroscopy [88, 89, 90], specific heat measurement [91] and Raman spectroscopy [92] supported two-band superconductivity. Today we know that there are two distinct superconductivity energy gaps of $\Delta_1 = 2.3\text{meV}$ and $\Delta_2 = 7.1\text{meV}$ [93, 94]. The Fermi surface consists of several parts, it is very anisotropic [326] and EPC is dominated by the in-plane B-B stretching modes (E_{2g}) [87, 326, 335] which have a large anharmonicity [87, 328, 335]. The σ -bonding states are confined in the boron planes but the charge distribution of these states is not symmetrical with respect to the in-plane positions of the boron atoms, due to their coupling. As boron atoms vibrate in-plane, shortening and elongating bonds, shortened bonds become attractive to electrons and elongated bonds became repulsive, this means σ -bonding states couple strongly to the vibrational

5. RESULTS

mode [333] and this pairing is a principal mechanism responsible for superconductivity. Also, three-dimensional π -bands couple weakly to phonons generating second superconducting gap. Measurement of B-isotope effect on T_c , tunneling, transport, thermodynamic properties and phonon density of states confirm that MgB_2 is most likely an electron-phonon mediated σ -wave superconductor with an intermediate or strong coupling [325, 59]. There is noticeable structural similarity of MgB_2 to GIC some of which also exhibit superconductivity. Furthermore, similarity to graphite exists as well as in electronic structure. The peculiar and unique property of MgB_2 is the incomplete filling of two σ bands corresponding to strongly covalent, sp^2 -hybrid bonding within the graphite-like boron layers [334]. The band structure of MgB_2 was studied and determined in detail, long time before discovery of superconductivity [336, 337]. Charge carriers in MgB_2 can be divided in two distinctive groups: π -electrons similar to those in graphite and σ -electrons which represent highly specific case of covalent bands crossing Fermi level that demonstrate anomalously strong interaction with only two phonons with sufficiently small wave vector [334]. Various approaches have been thoroughly studied in search for enhancement of critical temperature in MgB_2 . The pressure effects and doping on the electron-phonon coupling and superconductivity in MgB_2 are well investigated [338, 339, 340]. Inspired with doped-graphene and similarity to MgB_2 , we continue study of superconductivity in low-dimensional materials and theoretically consider the two-dimensional limit of MgB_2 and a possibility of enhancement of the electron-phonon coupling. Although some theoretical studies already exist on bilayer [343] MgB_2 and thin films and nanosheets [352, 353, 354] here is presented for the first time a comprehensive study of the lowest limit of MgB_2 , a single monolayer MgB_2 -mono, studying its electron-phonon interaction and an enhancement of electron-phonon coupling strength by affecting the interdopant distance and softening phonons applying a tensile and compressive strain. The electron-phonon coupling was studied using the Eliashberg formalism. For simplicity, we do not study multiband and anisotropy effects and use an isotropic Eliashberg function [61]. The comprehensive molecular dynamics study was performed prior to all other calculations to establish stability of material in broad range of temperatures. Combining results from DFPT with group theory we analyze phonons in MgB_2 -mono.

5. RESULTS

5.3.1. Computational details

MgB₂ has a hexagonal unit cell and consists of graphite-like B₂ layers stacked on-top, with the Mg atom between layers, as shown in Figure 5.20. The first principle calculations have been performed within DFT formalism in GGA to calculate the electronic structure. For all electronic, phonon structure and electron-phonon interaction, QE is used with the ultra-soft pseudopotentials and plane-wave cutoff energy of 30 Ry. All calculated structures are relaxed to their minimum energy configuration following the internal force on atoms and stress tensor of the unit cell. We used the Monkhorst-Pack $48 \times 48 \times 48$ and $40 \times 40 \times 1$ k-mesh, for calculations of the electronic structure of the MgB₂ bulk and the MgB₂-mono, respectively. Phonon frequencies are calculated using DFPT on the $12 \times 12 \times 12$ and $20 \times 20 \times 1$ phonon wave vector mesh for bulk and monolayer structures, respectively. The crystal structure of the MgB₂ and MgB₂-mono are presented in Figure 5.20. The lattice parameters for the MgB₂ bulk are in agreement with the experimental results, $a=3.083$ Å and $c/a=1.142$ [325]. In order to simulate 2D material, an artificial vacuum layer was set to be 25 Å. When the monolayer is modeled, the structure is geometrically optimized, allowing atoms to reach points of minimum energy. The bond length between neighboring atoms remained 1.78 Å but the Mg atoms distance from the boron layer changed from $h=1.76$ Å to $h=1.60$ Å. The results of geometrical optimization are summarized in Table 5.4. For the molecular dynamics (MD) study the Siesta code is utilized [345]. The super-cell is built by repeating the unit cell 3 times in both in-plane directions whereas the lattice vector in the perpendicular direction is 15 Å providing a large enough vacuum space between the 2D material. The lattice parameters and the geometry of the unit cell are initially optimized using the conjugate gradient method. The Perdew-Burke-Ernzerhof form of the exchange-correlation functional [311], double-zeta polarized basis set and Troulier-Martins pseudopotentials [346] were used in all MD calculations. To estimate electron-phonon coupling, the Eliashberg function was calculated within QE with the electron momentum k -mesh up to $80 \times 80 \times 1$ for a fine grid and $40 \times 40 \times 1$ for a coarse one, and the phonon q -mesh $20 \times 20 \times 1$ for the monolayer ($48 \times 48 \times 48$ fine grid, $24 \times 24 \times 24$ coarse grid and $12 \times 12 \times 12$ q mesh, for the MgB₂ bulk). To estimate the strength of the electron-phonon coupling, the Eliashberg function $\alpha^2 F(\omega)$ is calculated.

5. RESULTS

5.3.2. Molecular dynamics study of MgB₂-mono

In order to determine the stability of a single layer of MgB₂ in monolayer we perform the MD simulations based on DFT and the super-cell approach. Besides the system with optimized (pristine) lattice parameters, we also consider the biaxially stretched system up to 3% of tensile strain and the biaxially compressed system up to 5% of compressive strain. The MD simulations are conducted in the range of temperatures between 50K and 300K in steps of 50K using the Nose-Hoover thermostat [347]. Figure 5.21 a) shows the average distance between the Mg and B atomic layers as evolved during time of 1 ps. Throughout the simulation time there is no further evolution of the z-coordinate and the Mg atoms show only an oscillatory movement around the equilibrium positions (as it is shown in Figure 5.21) Importantly the separation indicates that the Mg atoms do not leave surface of the MgB₂ crystal. The plane where the Mg atoms reside shifts away from the plane of the B atoms in average by 0.09Å in the compressed crystal while the distance between the planes decreases in average by 0.42 Å in the stretched system. This relatively larger shift in the latter case can be understood by analyzing the details of the MgB₂ atomic structure. When the crystal is biaxially stretched its bond lengths increase, effectively destabilizing the lattice. The interaction between Mg and B is especially affected since each Mg atom is at the hollow sites of the B sublattice and builds six bonds with its neighboring B atoms. This destabilization is partially compensated by nesting the Mg atoms closer in the B sub-lattice. This support a phonon spectrum which will be analyzed later in the text. There are no negative phonon modes present indicating a stable system. As a result of this MD calculation one can conclude that the MgB₂ monolayer is a stable structure.

Figure 5.21 b) presents the dependence of the global Lindemann index on temperature. It is calculated for the pristine crystal, with a compressive strain of 5% and a tensile one of 3% from the local Lindemann indices from formula

$$q_i = \frac{1}{N-1} \sum_{j \neq i} \frac{\sqrt{\langle r_{ij}^2 \rangle - \langle r_{ij} \rangle^2}}{\langle r_{ij} \rangle}$$

by averaging over all atoms. Here q_i is the local Lindemann index of atom i , N is the number of atoms, r_{ij} is a separation between i and j atoms while the angle brackets denote averaging over time, i.e. the MD steps [327]. The linear behavior of the Lindemann indices indicate that systems are stable at least up to the room

5. RESULTS

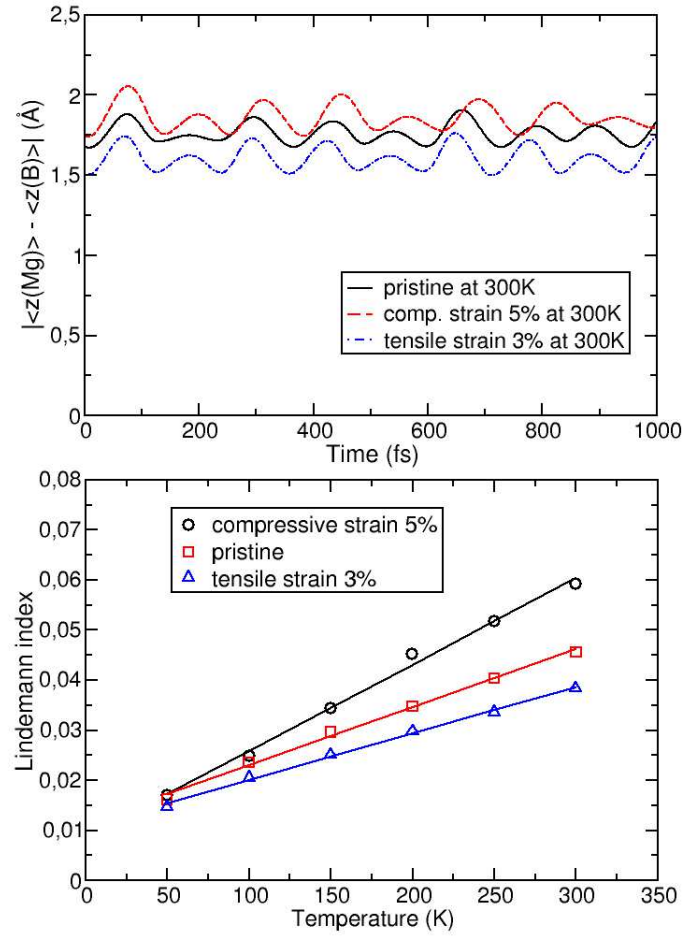


Figure 5.21.: a) An average distance between the Mg and B atomic layers
b) dependence of the global Lindemann index on temperature.

5. RESULTS

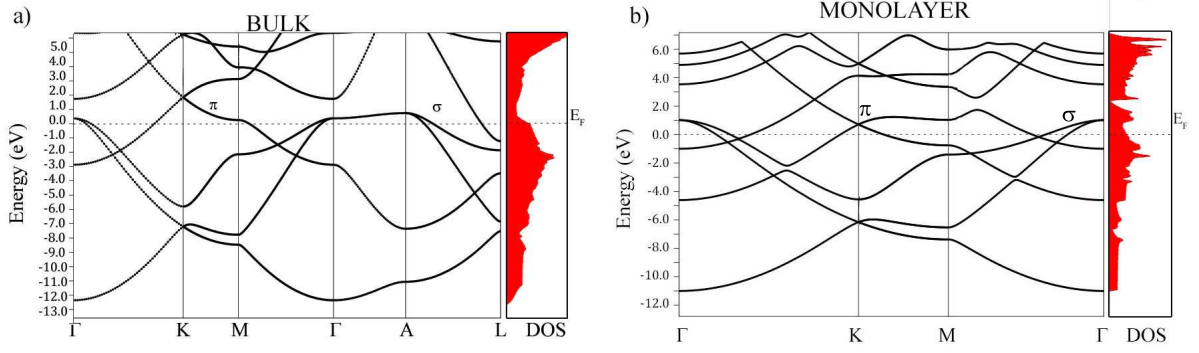


Figure 5.22.: The Electronic band structure and the total density of states of the MgB_2 bulk and the monolayer.

temperature.

5.3.3. Electrons, phonons, symmetry

In Figure 5.22 the electronic structure of the MgB_2 mono and the bulk is presented. The band structures for the bulk along the high-symmetry points Γ -K-M- Γ -A-L and for the monolayer along Γ -K-M- Γ were calculated. The Fermi level is set to zero. The band structure of the bulk is in a full agreement with the previous studies [338, 326, 344, 98]. The two bands crossing the Fermi level play a crucial role for the electronic properties of MgB_2 . The density of states around E_f are predominantly related to the B atoms and its p-orbitals whereas the Mg atom contribution is negligible in this region. The previous studies described that Mg is fully ionized in this material and the electrons donated to the system are not localized on the anion, but rather are distributed over the whole crystal [96]. A similarity to graphite can be observed, with three σ bands corresponding to the in-plane $sp_x sp_y$ (sp^2) hybridization in boron layer and two π -bands of boron p_z orbitals. [334]. Boron $p_{x(y)}$ and p_z orbitals contribute as σ and π states. Analyzing PDOS one concludes that the σ states are considerably involved to the total density of states at the Fermi level, while the π states have only a partial contribution. It is worth emphasizing that the bulk bands of this material at the K-point above the Fermi level present a formation similar to the Diracs cones of graphene. In the monolayer there is an increase of the total density of states on the Fermi level from $N(E_f)_{\text{bulk}}=0.72$ states/eV to $N(E_f)_{\text{mono}}=0.97$ states/eV, which is beneficial for an enhancement of superconductivity. In the same manner as in the bulk, the monolayer Mg atoms negligibly contribute to the DOS at the Fermi level and the main contribution comes from the B p-orbitals. The characteristic

5. RESULTS

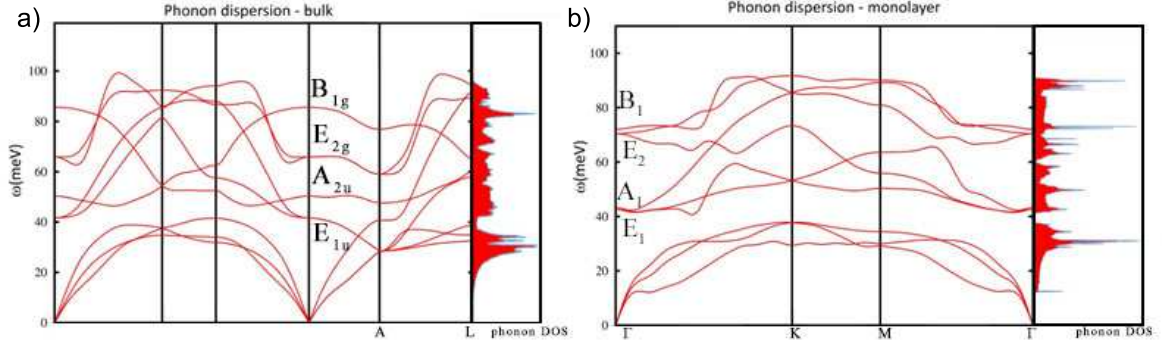


Figure 5.23.: The phonon dispersion and the phonon density of states for the MgB_2 bulk and the monolayer.

Diracs cone-like structure is still present and closer to the Fermi level. Dg77 as the symmetry group of the MgB_2 -mono hosts a Dirac-like dispersion in the vicinity of the K-point in the hexagonal BZ, if the orbital wave functions belong to the 2D representation E of the C_{3v} point group of the wave vector [349, 350]. In the tight-binding case, the p_x and p_y orbitals of two boron ions give rise to the two E - representations, while s - orbitals form a basis for one E - representation. This explains the presence of the Dirac cones at the K-point in the band structure of the MgB_2 monolayer (shown in Figure 5.22 b)).

Figure 5.23 shows the phonon dispersions for the bulk and monolayer. For the bulk, in Figure 5.23 up, there are four optical modes at the Γ point. Due to a light atomic mass of the B atoms and the strong B-B coupling the two high-frequency modes almost have a pure boron character. The in-plane stretching mode E_{2g} and the out-of-plane mode (where atoms move in opposite directions B_{1g}) are the boron atom modes. E_{2g} is a doubly degenerate Raman mode and the experimental studies [96, 84, 203, 87, 325] show this mode is very sensitive to structural changes and it has a strong electron-phonon coupling. The low-frequency modes, A_{2u} and double degenerate E_{1u} , are infrared active and they do not involve changes on in-plane bonds. In Figure 5.23 right the phonon dispersion of the MgB_2 monolayer is presented. In the phonon spectrum there are no imaginary frequency which confirms once again the dynamical stability of the system also demonstrated earlier by the MD calculations.

At the Γ point there are three acoustic and four optical modes. The optical modes A_1 , B_1 , E_1 and E_2 are related to the optical modes of the parent material. Two significant differences between the bulk and monolayer spectrum can be observed. There

5. RESULTS

Table 5.3.: Raman tensors and symmetry classification of optical modes for MgB₂-mono

		<i>Raman tensors</i>				
MgB₂-mono <i>Dg</i> $\gamma\gamma = TC_{6v}$ $O_z \parallel C_6$ $O_x \parallel \sigma_v$	A_1	E_1	E_1	E_2	E_2	
	$\begin{pmatrix} a & 0 & 0 \\ 0 & a & 0 \\ 0 & 0 & b \end{pmatrix}$	$\begin{pmatrix} 0 & 0 & c \\ 0 & 0 & 0 \\ c & 0 & 0 \end{pmatrix}$	$\begin{pmatrix} 0 & 0 & 0 \\ 0 & 0 & c \\ 0 & c & 0 \end{pmatrix}$	$\begin{pmatrix} d & 0 & 0 \\ 0 & -d & 0 \\ 0 & 0 & 0 \end{pmatrix}$	$\begin{pmatrix} 0 & -d & 0 \\ -d & 0 & 0 \\ 0 & 0 & 0 \end{pmatrix}$	
		<i>Optical modes</i>				
<i>MgB₂</i>	$\Gamma_{opt} = A_1 + B_1 + 2E_1 + 2E_2$					

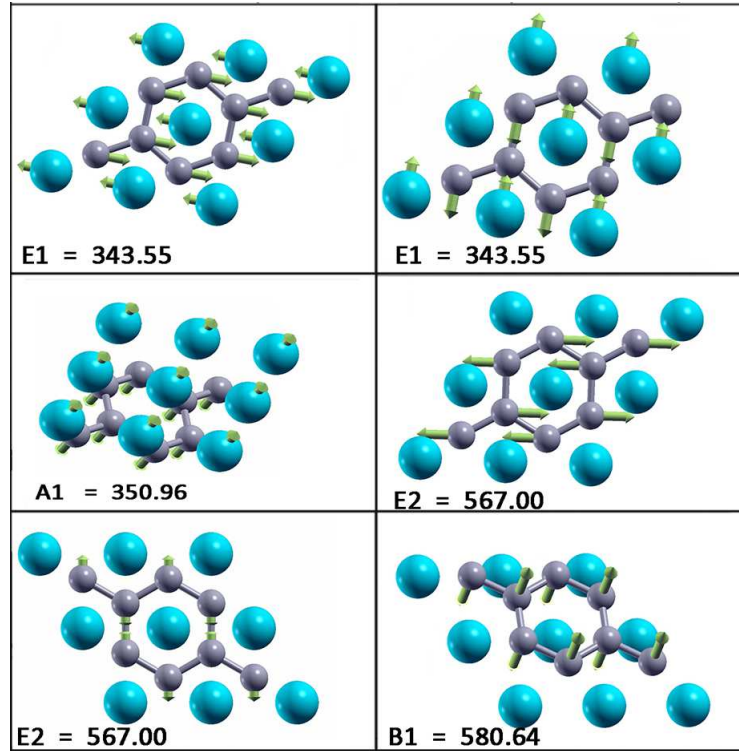


Figure 5.24.: Vibrational frequencies (in wave numbers) and the normal coordinates for the MgB₂-mono.

5. RESULTS

is a slight softening (hardening) of a mode which leads to nearly equal frequencies, this opens a gap in phonon DOS between the acoustic and optical modes. More significant effect concerns the softening of the B_1 mode and hardening of the E_2 mode. As in the bulk E_{2g} mode, the monolayer E_2 mode is strongly coupled to electrons causing the superconductivity in the monolayer in a similar fashion as in the bulk. At this point, it is important to make another comparison to graphite and graphene. Similar to the intercalated graphite and graphene in MgB_2 [351] there is a presence of the Kohn anomaly [273]. As mentioned above, there is a strong electron phonon coupling of the E_{2g} mode, which results both in a large phonon linewidth and, in the neighborhood of $2k_F$, an abrupt change in the phonon mode frequency with a phonon momentum - essentially the Kohn anomaly [351]. From previous studies of graphene [243], we are aware that DFPT approach is not a proper tool for a treatment of the Kohn anomaly and that some discrepancies with experimental results can exist for specific modes when the Kohn anomaly is present, but also it is shown [56, 59] that this does not affect total assessment of the electron-phonon coupling and the Eliashberg function. In Figure 5.24 the vibrational frequencies and normal coordinates for the MgB_2 -mono are presented. The symmetry group is C_{6v} and the acoustic modes are A_1 and E_1 . The optical modes at Γ point are: A_1, B_1, E_1, E_2 where the infrared active ones are A_1 and E_1 , The Raman active modes are A_1, E_1, E_2 and B_1 is silent. In Table 5.3 the Raman tensor for the MgB_2 -mono is presented. Similar to graphene, the phonon eigenvectors and the normal coordinates at the Γ -point are determined by symmetry rules and therefore are a model independent.

5.3.4. Superconductivity and enhancement

To investigate the strength of the electron-phonon coupling we calculate the Eliashberg function and the electron-phonon coupling constant λ for the bulk and the monolayer. In Figure 5.26 the corresponding Eliashberg function is presented. In the bulk material one can observe a large contribution close to 60 meV which comes from the coupling of the E_{2g} mode to the holes at the top of the a bands [59].

There is also smaller contribution from the coupling of the out-of-plane boron B_{1g} mode at 90 meV and a very small influence of the low frequency modes. The calculated values are $\lambda=0.72$ and $T_c=39.5$ K. There are different results for monolayer materials. Our calculations show a decrease of the λ to be $\lambda=0.55$ and $T_c=18.2$ K. The Eliashberg spectral function for the MgB_2 -mono changes its appearance

5. RESULTS

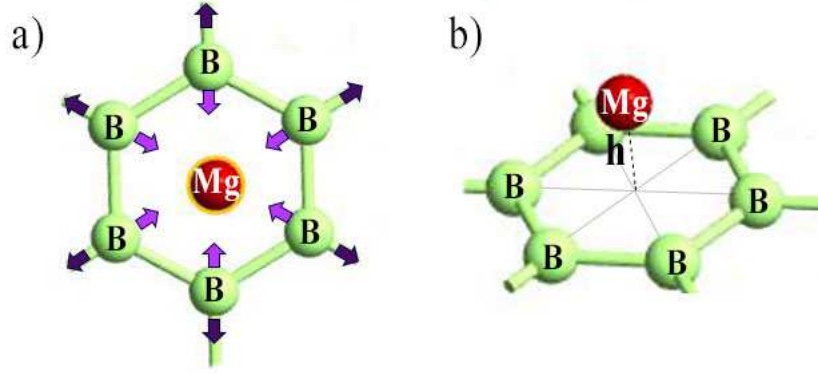


Figure 5.25.: a) Schematic description of MgB_2 under a tensile (dark arrows) and a compressive (light) strain. b) MgB_2 -mono, h is the distance between the Mg and B layer

comparing to the bulk. The coupling of the high-frequency modes (which are soft comparing to the bulk) is still present but with a lesser intensity, which is the adverse for superconductivity and eventually causes lowering of the critical temperature. In the area of low-frequency modes there is a certain enhancement associated to the softening of the A_1 mode. Nonetheless, low-dimensional materials are favorable for enhancement of electron-phonon coupling comparing to bulk materials. Increasing of the DOS at the Fermi level and softening of the modes are both beneficial for EPC. In principle both effects can be achieved rather easily in low-dimensional systems. Since we proved that the MgB_2 -monolayer is stable and superconducting a potential superconductivity enhancement can be studied. Therefore, we apply a biaxial strain to the MgB_2 -mono (Figure 5.25). Both a tensile and compressive strain were applied and a certain enhancement from the both approaches was observed. The Eliashberg spectral functions for all tested structures are summarized in Figure 5.27 and results for the electron phonon coupling constant, critical temperature and cell parameters are presented in Table 5.4.

When a biaxial strain is applied several mechanical effects happen which affect the electron and phonon dispersions. The application of the biaxial strain leaves the symmetry of the system unchanged, yet a tensile (compressive) strain moves B atoms further (closer) from (to) each other in the same proximity, allowing the Mg atom to move along the z-axis (As it is described by the h parameter in Table 5.4, h is distance of the Mg atom from the boron layer). This causes a change in the charge transfer from the magnesium atoms to the boron plane increasing (decreasing) DOS

5. RESULTS

Table 5.4.: The cell parameters, electron phonon coupling constant and critical temperature for the MgB₂-mono biaxial tensile and compressive strains

<i>Mono-layer</i>	<i>a</i> (Å)	<i>h</i>(Å)	%	λ	T_c (K)
<i>No-strain</i>	3.083	1.60038	No strain	0.55	18.2
<i>Compressive_1%</i>	3.0574	1.63555	-1%	0.58	20.6
<i>Compressive_3%</i>	2.99051	1.69576	-3%	0.65	24.0
<i>Compressive_5%</i>	2.92885	1.74098	-5%	1.04	31.0
<i>Tensile_1%</i>	3.11383	1.58069	1%	0.56	19.1
<i>Tensile_3%</i>	3.17549	1.50779	3%	0.62	22.3
<i>Tensile_5%</i>	3.23715	1.43748	5%	0.70	25.3
<i>Tensile_7%</i>	3.29881	1.36789	7%	0.85	27.9

on the Fermi level. Other effects concern the softening (hardening) of modes of the boron atoms due to an elongation (compression) of the B-B bonds. Generally based on the Hopfield formula [359] softening of phonons favors an increase in λ and consequently also the critical temperature (as shown by the Hopfield formula). Together these effects enhance the electron-phonon coupling but not enough to achieve values of λ and T_c of bulk MgB₂. Once again, we can make a comparison with an intercalated graphene where it is known that not all types of intercalant atoms produce superconductivity or significantly increase T_c . This discovery was in contradiction expected phenomenon of decreasing of the T_c and λ with the reducing dimensions of a material (as we have here).

As shown in previous section an application of the tensile biaxial strain in the LiC₆-mono enhances EPC and increases the critical temperature dramatically [243]. Inspired with it and structural similarity of materials same procedure is repeated here. In the MgB₂-monolayer an application of the strain enhances EPC as well, the 5% compressive strain raises the critical temperature almost 60% but it is negligible to the critical temperature of the bulk MgB₂. In Figure 5.27 the Eliashberg spectral functions are compared for the MgB₂ bulk, monolayer and biaxially strained structures, tensile 1%, 3%, 5%, 7% and compressive strains 1%, 3%, 5%. For higher values of the strain structural instabilities occur in material and they are excluded from further analysis. The Coulomb pseudopotential (μ) is included in the Eliashberg theory as a parameter obtained experimental values of critical temperature [339]. In the multiband case it (μ^*) becomes a matrix which can be treated in

5. RESULTS

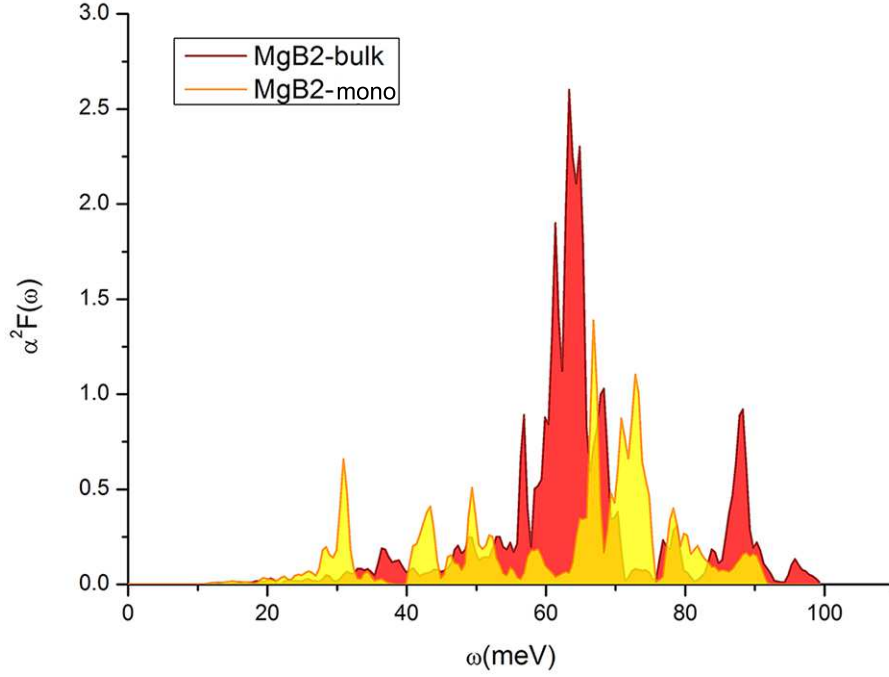


Figure 5.26.: The Eliashberg function $\alpha^2 F$ for the MgB_2 bulk and monolayer

various approximations [328, 334]. In anisotropic treatment μ^* is determined to be 0.12 for critical temperature of 39K. Uniqueness of MgB_2 and its anisotropy and anharmonicity (present in the B-B stretching modes [87, 335]) demand the fully anisotropic Eliashberg equations [328]. However, due to the interlayer interaction the system should have only one transition temperature and other common properties [331] which justifies use of the isotropic Eliashberg equation in our calculations.

In this section the electronic band structure, density of states, phonon dispersion and phonon DOS have been calculated for the MgB_2 -mono and compared to the bulk material, using first principle calculation. We calculated the Eliashberg function and determined the electron-phonon coupling constant for the MgB_2 -mono and concluded that it is superconducting while EPC strength is weaker than in bulk material. To enhance it, we applied the biaxial strain and achieved an increase for both tensile and compressive strain, due to increase of DOS at the Fermi level and softening of the modes, but not enough to reach values for the MgB_2 bulk. We showed that the low-frequency vibrations contribute more in low-dimensional structures however not to overcome a decrease of coupling in high-frequency region. Our further calculations on enhancement of EPC suggest that adding one more layer of boron (i.e. making of MgB_2 thin sheet) is beneficial and critical temperature will be

5. RESULTS

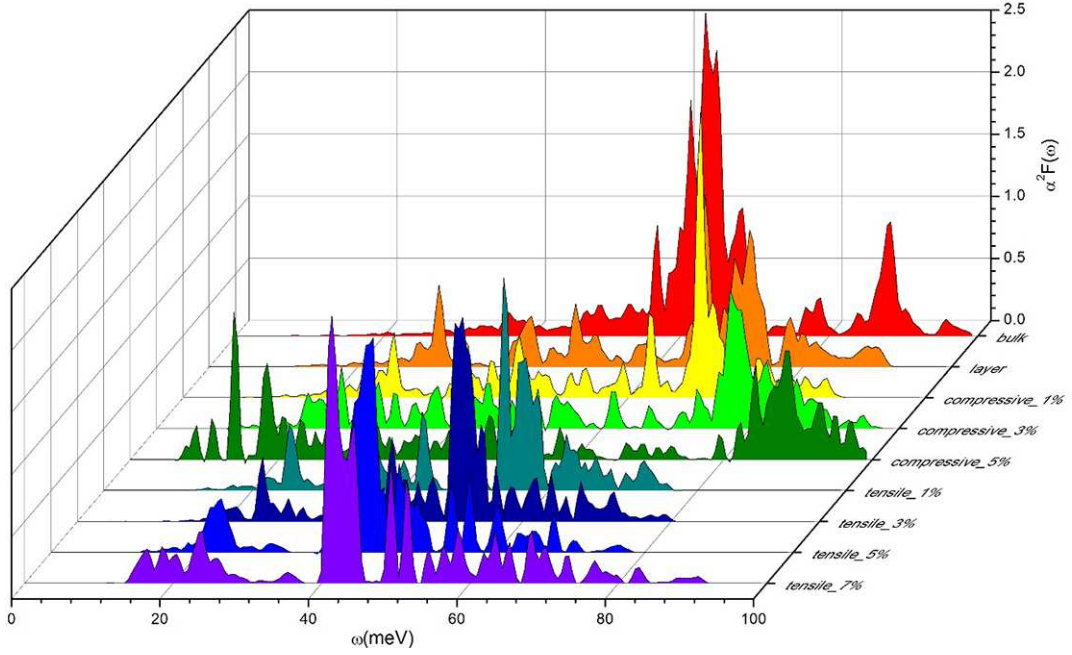


Figure 5.27.: The Eliashberg function $\alpha^2 F(\omega)$ for the MgB_2 bulk, monolayer and the biaxial tensile and compressive strains

enhanced. This statement is in agreement with previous study [343]. To enhance even further EPC in the MgB_2 -mono, increasing of DOS at the Fermi level is needed. This could be achieved by adsorption of suitable adatoms. The approach used in this research does not include the anisotropy effects. For more precise description of the superconductivity in 2D MgB_2 an anisotropic approach is suggested (for example using electron-phonon approach based on Wannier functions, which showed remarkable accurate description of MgB_2 -bulk [344, 98]). However the isotropic Eliashberg theory gives overall description of the superconducting properties of the thinnest limit of magnesium-diboride. Establishing its stability and offering insight in this new 2D material, we focus on effects of ultimate lowering of the dimensionality. The question of reduction of dimensionality to its limit to the truly atomic-scale 2D system and the consequence of this [352, 353, 354, 355, 356, 357, 358, 359, 360] are highly relevant not only to fundamental science but to nanotechnology and it will be crucial for production of superconducting devices in future. The thin films with nanometer thickness and nanosheets of MgB_2 have been studied and shown to be superconductive [352, 353, 354] however best to our knowledge this is the first study of the thinnest limit of MgB_2 . Importance of the insight in MgB_2 -mono is both for fundamental research in the low-dimensional superconductivity and in the

5. RESULTS

field of applications e.g. through production of low-dimensional superconductive heterostructures. Another important implication of our research reflects in opening a possibility to revisiting of ideas of constructing MgB₂-inspired high-temperature superconductors [203], but now in the new context of two-dimensional materials and all benefits offered by such systems.

5.4. GPU acceleration in 2D materials calculations

In the third chapter it was shown that DFT provides an excellent balance between computational accuracy and cost for quantum mechanical calculations. The approximate nature of DFT lowers computational cost drastically, comparing to other calculation methods, but the resources demand becomes still very high for systems with few hundred atoms. For such a systems with a large number of atoms, the computational demand is still a serious limitation for the considered system size.

In recent years, GPGPU (General Purpose Graphics Processing Unit) accelerators have raised the interest for massively parallel computing in the field of scientific calculations. GPGPUs were specifically designed to target high performance computation (HPC) applications incorporating additional features into GPUs, such as caching technology, and support for double-precision arithmetic. This technology has rapidly evolved from graphics processing to programmable parallel streaming processing. GPU accelerators are specialized for highly parallel and for computationally intensive computations. The GPU computing model uses a Central Processing Unit (CPU) and GPU together in a heterogeneous co-processing computing model.

Term "parallel computation" simply can be described as performing many calculations, or the execution of processes, simultaneously. Certain large problems can be divided into smaller ones, which can then be solved at the same time. For expressing parallel CPU code the two most widely used application programming interfaces (APIs) are MPI (Message Passing Interface) [361] and OpenMP (Open Multi-Processing) [362]. MPI is a library called upon from existing CPU code and it is language-independent. This means it can be called from code written in any compatible programming language, that is, C, C++, or Fortran. MPI is primarily designed for use with a distributed memory system and it enables point-to-point and collective communication between processors in a system. OpenMP is primarily a set of compiler directives that can be called from within C/C++ and Fortran

5. RESULTS

code. OpenMP is designed primarily for shared memory programming. OpenMP is considered a higher level parallel programming API than MPI.

Benefit of GPU accelerators are in potentially several times faster calculations than the CPUs (Central Processing Units) in data-parallel applications. Nonetheless the architectures of GPUs are more focused to data processing rather than to instruction control and data caching. Due to the excellent price to performance ratio and the low energy consumption per FLOP, it is tempting to use GPGPU to accelerate highly data parallel scientific computations [365]. However, these GPU accelerators have some special characteristics which makes this rather complex task. Often they are optimized in such a way that the performance has the higher priority rather than numerical accuracy. Most of the GPUs are only support single precision floating point numbers with very high performance and only single precision accuracy is not sufficient in the quantum physics simulations. Response of one of the biggest GPU manufacturer NVIDIA, comes in as a series of GPU cards, Tesla, dedicated only to computation [363]. The Tesla products target the HPC market due to their high computational power and the lack of ability to output images to a display. This made the main difference between Tesla products and rest of NVIDIA's commercial (GeForce) and professional (Quadro) cards [363]. However Quadro cards have double precision floating point numbers accuracy and can be used as computational accelerator although then is necessary to use additional card for video output.

In scientific computing, in order to achieve high performance from GPU accelerators, the application needs to be very fine divided with highly parallel algorithms, where each thread can do the calculations using the resources allocated for it. Applications with high arithmetic intensity are particularly well suited for GPU accelerators. A lot of quantum calculations application have been ported to the GPU [372]. Thus there is an opportunity for high-throughput GPUs to play an active role on DFT calculations.

The greatest benefit of introducing GPU in the scientific calculations is the fact that performance of the supercomputers was brought to the desktop. The idea behind the usage of GPGPU for the scientific computing is to offload the demanding parts of calculations to GPUs while the remaining parts of the code will run on CPUs (as shown in Figure 5.28). The advantage of GPGPUs massively parallel architecture lies in the thousands of cores specially designed to handle multiple tasks parallelly. Although the core clock of GPUs is slower, the number of cores inside provides more

5. RESULTS

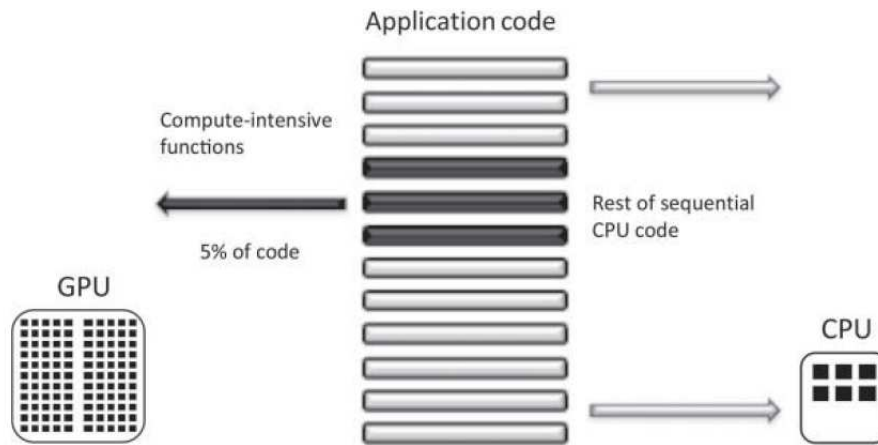


Figure 5.28.: Illustration of a GPU working in conjunction with a CPU as work is offloaded and computed on a GPU concurrently with CPU execution [367]

computational power. A great advantage of the GPU technology it is not limited to the supercomputers but is increasingly found in desktop, laptop computers and high-end workstations. Multiple GPUs can be plugged into desktop machines as well as the supercomputer nodes for an increased performance. There are three main vendors for the GPGPUs, Nvidia, Intel and ATI/AMD and they are actively developing computing technology on GPUs.

Designing code suitable for massive parallel system such are GPUs demand careful approach. When parallelizing computer code, it is important to know that not all parallel processing elements have access to all the data in memory. As GPUs were originally designed for applications involving graphics rendering, the lack of sophisticated hardware limited the number of applications suitable for acceleration using the historical GPU hardware design. The first programmers had difficult task to represent their calculations in terms of graphics primitives, triangles and polygons, when attempting to execute general-purpose applications on a GPU. As GPUs were made exclusively for computer graphics, the input was a list of geometric primitives, typically triangles, in a 3-D world coordinate system. With development of GPGPU and the need for executing non-geometrical problems, APIs were designed for general-purpose scientific computing. It significantly reduced the complexity of general purpose usage of GPUs, that an extensive range of scientific problems is making use of its acceleration in an economically efficient manner. At present there are two main APIs available to program GPUs: OpenCL and CUDA ("Compute

5. RESULTS

United Device Architecture” or CUDA is a parallel computing platform and API created by Nvidia). Although modern GPU hardware design (along with usage of dedicated APIs) has become more accepting to the general-purpose application, it is still necessary to ensure that an algorithm is suited to the hardware.

Today the GPU computing model is known as the heterogeneous CPU - GPU programming model. In this model, the sequential parts of an application are running on CPU, whereas the data parallel, computationally expensive, parts are running on the GPU. There are two major commercial standards for GPGPU development. One is ATI’s StreamSDK and the other is the Nvidia’s CUDA.

To discuss performance of GPU acceleration term ”speedup”, has to be defined.

$$S(n) = \frac{T(1)}{T(n)} \quad (5.5)$$

,where $T(1)$ is the execution time of the original algorithm and $T(n)$ is the execution time of the new algorithm on n processors/cores/threads. Amdahl’s and Gustafson’s laws provide a guideline for speedup after parallelizing code. These laws show that the serial portion of a parallel program is always the limiting factor in speedup. Amdahl presumes a fixed problem size, whereas Gustafson presumes increasing problem size with increasing numbers of processors. Amdahl’s Law [368], was introduced in 1967 and is defined by:

$$T(n) = T(1) \left(\beta_A + \frac{1}{n} (1 - \beta_A) \right),$$

$$S(n) = \frac{T(1)}{T(1) \left(\beta_A + \frac{1}{n} (1 - \beta_A) \right)} = \frac{1}{\beta_A + \frac{1}{n} (1 - \beta_A)},$$

where β_A is the fraction of the algorithm that is non-parallelizable, that is, the fraction of the total run time $T(1)$ that the serial program spends in the non-parallelizable part. It can be seen from Amdahls equation, as the number n of processors increases, the speedup becomes limited by the serial code fraction β_A . Amdahl’s Law is rather simplistic, as it makes many assumptions: the number of processes used throughout the parallel portions of the code is a constant; the parallel portion achieves linear speedup, and the parallel portion scales perfectly. Gustafson [369] attempted to remedy this shortcoming by defining parallel speedup by a new equation:

5. RESULTS

$$\beta_A = \frac{1}{1 + \frac{(1-\beta_G)^n}{\beta_G}}$$

where β_G is again the non-parallelizable fraction, but now defined as the fraction of the total time $T(n)$ that the parallel program spends in serial sections if run on n processors and β_A as defined at Amdahl's law. What Gustafson's law says is that the true parallel power of a large multiprocessor system is only achievable when a large parallel problem is applied. Both from Amdahl and Gustafson's law it is clean that, the serial code will ultimately become the bottleneck as the core count increases. So this means that even if there is only 10% of serial code (and in DFT calculations there is much more) time consumption is significantly increased.

Except fundamental limitations shown above, there are certain technical limitations when it comes to application of GPU acceleration in scientific calculations. When porting a code from the CPU to GPU, certain changes must be made in algorithms to suit the GPU strongly parallel environment [366]. The communication between hardware parts, since the speed is limited by the PCIe bus which connects GPU and CPU is well known issue. Practically, this means there has to be a good amount of computing on GPU to compensate for the bottleneck in the communications. Specially, in the material science there are parts of the code that are suitable for parallelization (like matrix calculations, FFTs...) and they greatly benefit from usage of the GPU, but also there are serial parts of the calculation that cannot be parallelized for GPU.

In porting DFT codes to GPU the main focus is in finding a computationally most expensive parts and reimplementing them with GPUs. The most demanding parts are usually matrix elements (i.e. integrals), vector operations and FFTs [366]. Although there are already GPU versions of the standard computational libraries (e.g. BLAS for GPU is CUBLAS) there is so much more than simple replacement of libraries with their GPU equivalents. A satisfying speedup demands minimizing of the slow transfer between GPU and CPU, in addition to porting of other routines to GPU.

When it comes to 2D materials calculations, as discussed in the Chapter 3 it is very misleading to think about 2D system calculations as simpler due to existence of the system in x-y plane. Most of existing DFT codes do not recognize 2D systems as such and there are necessity for modification in description and in input files

5. RESULTS

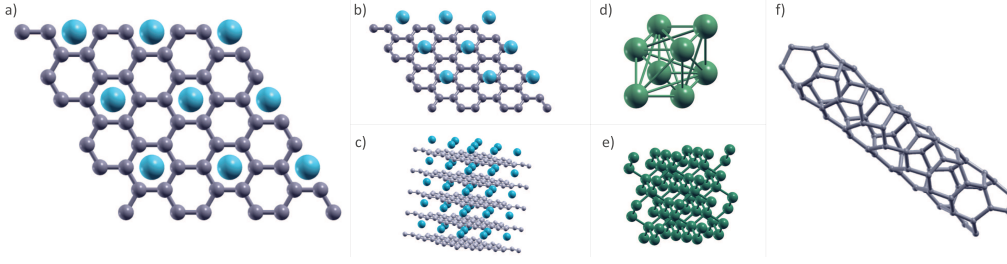


Figure 5.29.: Structures used for testing of the GPU acceleration. a) the LiC_6 bulk, carbon and lithium atoms are presented with gray and blue color, respectively, b) the LiC_6 -mono c) bulk, the Li-intercalated graphite d) and e) silicon atoms in 8 and 64 atoms per unit cell configuration, f) the single-wall zig-zag carbon nanotube

to avoid periodicity in the z plane. In this section the two codes (available under GPL license) that benefit from the usage of GPU are compared on various low-dimensional systems. It is important to emphasize these two codes, although they are based on the same DFT formalism, are very different from each other and vary in the approach on many subjects. The worlds first complete DFT code with GPU-enabled calculations, BigDFT[238] is discussed and tested. The BigDFT reported a speedup for the factor 6 for the whole hybrid code (and 20 for GPU routines). The other code is Quantum Espresso [233] used throughout this dissertation. Porting of QE to GPU is ongoing process [370, 371] and for version used for research presented in this chapter (QE v5.2) it reports speedups for the factor 3-5.

The hardware used for all calculation has configuration: Intel Core i7-3930K at 3.7 GHz empowered with Nvidia Tesla K20c. Tesla K20c is GPU card with dual slot, it has Kepler architecture, 2496 processor cores with 5GB GDDR5 memory on the card, connected using 320-bit memory interface [363]. The GPU is operating at a frequency of 706 MHz, memory is running at 1300 MHz.

For demonstration of GPU acceleration in DFT codes we employed several low dimensional materials and its bulk counterparts, as presented in Figure 5.29. For the first test we used LiC_6 -mono.

The BigDFT [238] is a massively parallel electronic structure code that uses wavelets as a basis set and GTH [373] and HGH [374] pseudopotentials. BigDFT is distributed as stand-alone code but as well as part of Abinit DFT program [375]. The performance was tested for 8 different system configurations (1,2,4 and 6 mpi processes, with and without GPU) for the monolayer (Figure 5.29 (b)) and bulk

5. RESULTS

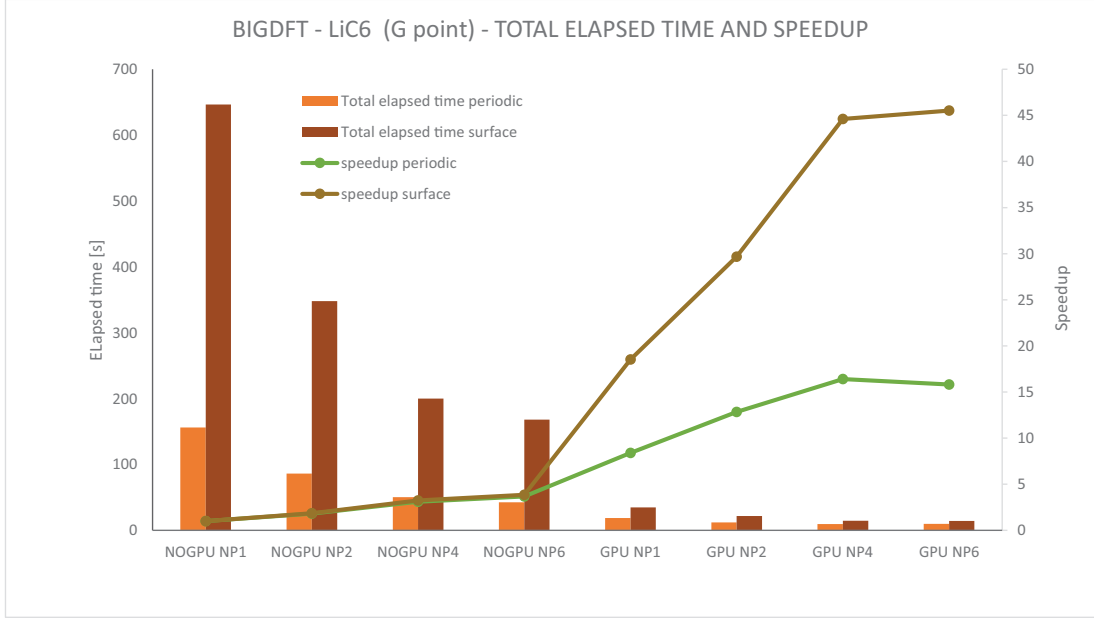


Figure 5.30.: Elapsed time and speedup for LiC₆-mono using BigDFT

(Figure 5.29 (c)) LiC₆ and results are presented in Figure 5.30. This test was performed to observe difference of boundary conditions. All the other properties are exactly the same except the boundary conditions, which distinguish monolayer from bulk. We can observe the slightly decreased wall-times for periodic structures, but at the same time better speedup for the monolayer. Here GPU acceleration is more efficient because the size of the simulation domain (i.e. the number of degrees of freedom) is bigger for monolayer system. This is also a reason for the longer run. The tests where GPU calculations were employed, show significantly better results that can be eminently enhanced with the joined use of the MPI parallelization and GPU together. It is worth emphasizing that the size of the problem is one of important prerequisites that dictate efficiency of the usage of the computing resources. As a result, we can confirm the fact that, for best speedups it is very important to adjust computational resources to specific problem. Best result is achieved for the GPU run with 6 processes (for monolayer) and 4 mpi processes (for bulk) and achieved speedup, compared to non-paralleled and non-accelerated system is up to 16 times for periodic (bulk) and even 45 for the surface (monolayer) configuration. When we compare parallel run with and without benefits of GPU, the speedup of 4 to 5 times can be observed for both configuration. To show difference that number of atoms makes in effectiveness of GPU acceleration we employed two simple examples. Silicium bulk systems with 8 and 64 atoms, common example in BigDFT, is used

5. RESULTS

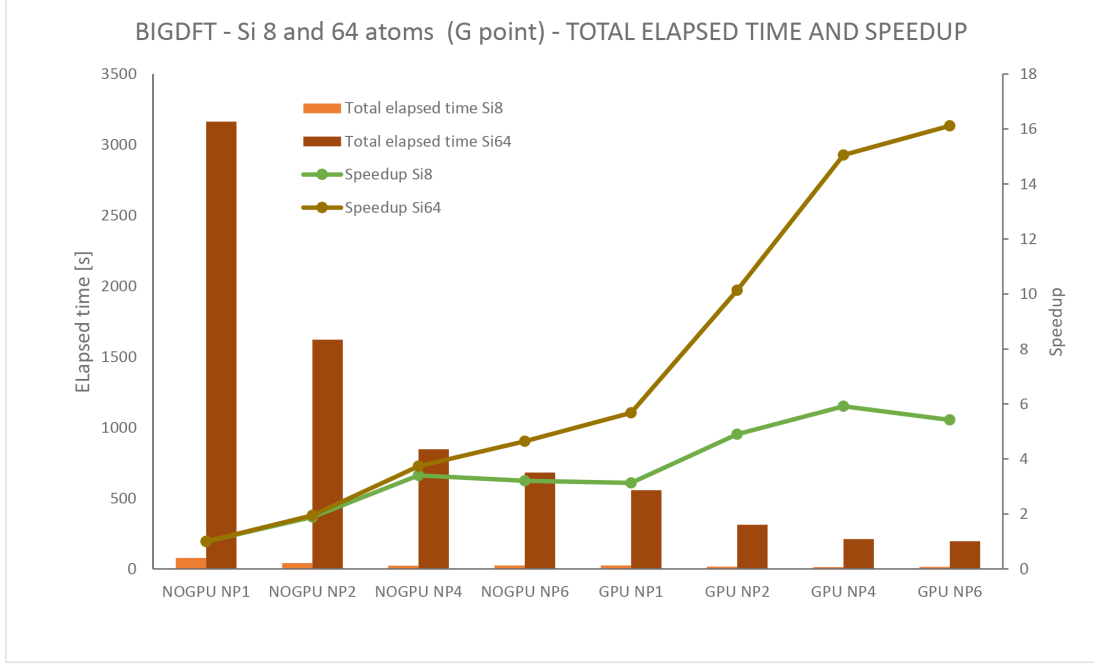


Figure 5.31.: Elapsed time and speedup for bulk Si with 8 and 64 atoms per unit cell using BigDFT

(Figure 5.29 (d) and (e)), to demonstrate effects of size of system on speedup. Results of this tests are presented in Figure 5.31. It is clear, better speedups are visible on the larger systems, due to the fact that larger system can be better parallelized.

Other tested code with the GPU implementations is QE [233]. As BigDFT, it is freely available and distributed as an open-source software under the terms of the GNU General Public License (GPL). One of the important differences between this two programs is in the basis set (as described in details in the Chapter 4). The plane waves basis is easy to use on any atomic type. It uses FFT and has many more advantages but is computationally expensive and requires large number of basis functions. This was discussed thoroughly in the Section 4.

Introduction of GPU acceleration in the QE is an ongoing process [371, 370], where main focus is on accelerating core modules first. The PWscf module is main part of QE distribution involves the calculation of the Kohn-Sham orbitals and energies [206] for the isolated or extended/periodic systems and the complete structural optimizations of the microscopic (atomic coordinates) and macroscopic (unit cell) degrees of freedom and it is the first part of the QE distribution that is fully ported for hybrid CPU-GPU configuration. The special library PhiGEMM [370] was de-

5. RESULTS

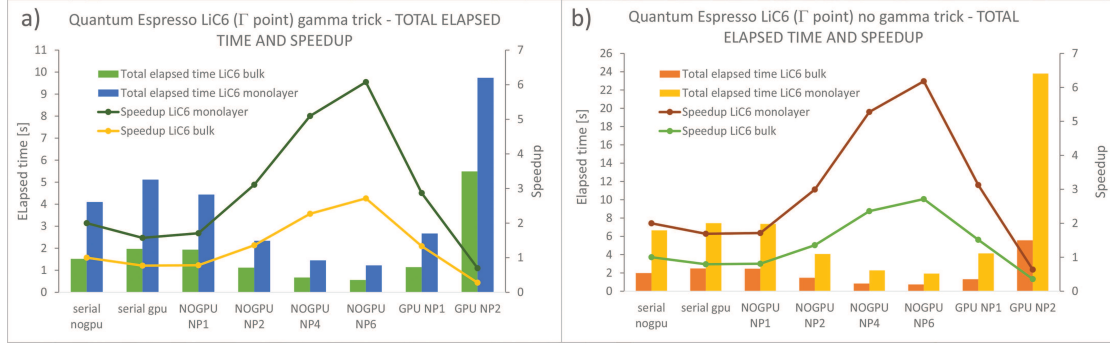


Figure 5.32.: Elapsed time and speedup for bulk and monolayer LiC_6 using Quantum Espresso, a) with gamma trick b) without gamma trick usage

signed to makes use of the CUDA features to provide a matrix multiplication that concurrently utilizes multiple GPUs and the host processor. As a result, usage of phiGEMM with QE benefits in speedups of 8.9-times [370]. An important feature of QE-GPU is fact the package is configured to run concurrently on one the single GPU and multi-core host processor, but greater speedups are achieved when it runs on multiple GPUs.

We perform test on the same system as for BigDFT. QE can be compiled in two different configuration, serial and parallel. In the parallel run, because of the unique configuration of QE GPU, unlike in BigDFT, it is required for every MPI process to have assigned one GPU. Otherwise, calculation would be cluttered and unnecessary weighted by the GPU-CPU communication. Since, our calculations have only employed one GPU, the calculation in the parallel configuration for more than 2 mpi processes are pointless with GPU acceleration. They are unnecessarily prolonged and we did not include such cases in our study. The performance was tested for several different system configurations (serial with and without GPU and parallel for 1,2,4 and 6 mpi processes) and results are presented on Figure 5.32. All calculations are performed at the Γ point. In QE, a special algorithm is implemented, called "Gamma trick" which enables significantly faster calculations for the Γ point only. For the Γ point ($k=0$), the Kohn-Sham orbitals are chosen to be real functions in real space and this allows only half of Fourier components to be stored. Two real FFTs can be performed as a single complex FFT with introduction of the auxiliary complex function. We performed our tests with and without the usage of the "gamma trick". As it can be seen in Figure 5.32, usage of the "gamma trick" reduces the total elapsed time in half but do not affect the achieved speedups. There

5. RESULTS

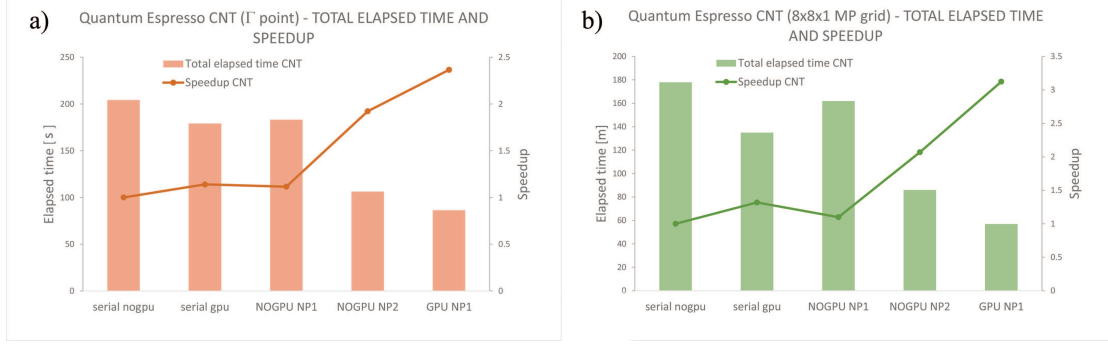


Figure 5.33.: Elapsed time and speedup for CNT using Quantum Espresso, a) in Γ point b) on the 8x8x1 Monkhorst-Pack grid

is some speedup when comparing GPU run and non-GPU run, but not significant. We can see that in parallel run, effects of the GPU acceleration can be observed but better speedups are present for no-GPU run with multiple mpi processes. This is consequence of the fact we have quite small system.

In systems with small number of atoms communication between CPU and GPU (which is known as largest drawback) happens too often and time saved on parts of calculations performed on GPU disipate on this communication. For the large systems, there is significant difference. One of illustrious examples of large systems is AUSURF112 (system of 112 atoms of Au with one surface) used for benchmarks, where the true benefit of GPU-QE can be seen [370].

To show the effects of the GPU acceleration on the low-dimensional system with large number on atoms in the unit cells we choose a one-dimensional system, a single-wall zigzag carbon nanotube (CNT) (Figure 5.29 (f)). The system with 76 carbon atoms was modeled, and the calculations with and without the GPU on the serial and parallel configurations were performed in the Γ point (using "gamma-trick") and on the 8x8x1 Monkhorst-Pack grid [234]. On Figure 5.33 are presented results of these calculations. As explained above, the larger systems can show higher benefit from usage of GPU technologies and this example demonstrates that fact. The result speedups are 2-3 times with usage of GPU acceleration, depending on configuration of the system. We showed that use of GPU and single mpi process is better than usage of the multiple mpi processes (up to 4), for the same system.

It is demonstrated that, depending on the method of the GPU implementation and properties of studied system various acceleration can be achieved. The fundamental difference in two different approaches to DFT implementation (like in BigDFT and

5. RESULTS

QE) makes it impossible to compare their speedups to each other. Furthermore important conclusion imposes, GPU technologies have become an important part of the high performance computing and their implementation is improving with an every new program version. A goal of this study is to asses the effects of GPU usage in low dimensional material DFT calculations, that has its own peculiarities and tricks. Significant speedups can be observed in various DFT approaches (varying from 2 to 45 times) but it is important to emphasise, that this is work in progress and some problems are still present. There is always present dilemma of porting vs writing new code from the scratch. At the same time almost everyday new technologies and new solutions are appearing opening possibilities for new ways and paradigms. The biggest advantage of GPU technologies introduced in scientific calculations is in fact that performance of supercomputer was brought to the desktop computers and high-end computational resources are available to everyone. Newer generations of GPUs, that may provide more computational resources, are showing up in an amazing speed. The next generation of NVidias TESLA GPUs is already announced. Named Tesla V100 (using Volta architecture) it promises 5120 cores and 7.5 TFLOPS in double precision [376]. We can conclude that although results and benchmarks are promising, the golden age of GPU accelerated DFT is yet to come and many more exciting improvements are yet to be seen. Results presented in this section are formed in two papers [245, 247] where second paper is currently in process of preparation for submission to relevant journal.

6. 2D MATERIALS SYNTHESIS

6.1. Micromechanical Exfoliation Technique

In the first chapter it was described how did Novoselov and Geim, synthesized graphene by a micromechanical fabrication technique [1]. This techniques gives the best sample quality, truly monolayer flakes of graphene, with ideally flat surface but of the micrometer size. Samples made by micromechanical exfoliation are mostly used in fundamental research or for proof-of-concept devices. Although samples are of the highest quality, it is very difficult, or even impossible to scale up the production of graphene via this route. Being aware of the great potential that discovery of graphene opened, a significant part of the research in the field for first few years was devoted to solving a problem of a mass synthesis of graphene. Dozens of various techniques were proposed resulting with a large spectra of sample properties (as presented in Figure 6.1. The number of layers and control over the number of layers also differs for different production approaches. Although the final product is called graphene it can happen that most of the properties that pristine graphene has are not present in obtained sample.

The technique of micromechanical exfoliation did not appear with graphene and two-dimensional materials although it did made them very recognizable both to scientific wider community. It is based on a well known method in mineralogy called cleavage. It exploits the tendency of crystalline materials to split along definite crystallographic structural planes [378]. It is not required that material has the Van der Waals forces in the direction perpendicular to the cleavage plane. Sometimes relative weakness of bond between the planes is result of the regular location of atoms and ions in the crystal (example will be presented in this section). The cleavage techniques include not only peeling or exfoliation, but also cutting and controlled breaking (as with Si wafers). The cleavage parallel to the crystallographic (001) plane is the most common one and all of the two-dimensional the Van der Waals materials have their unit cells connected by Van der Waals forces in a direction

6. 2D MATERIALS SYNTHESIS

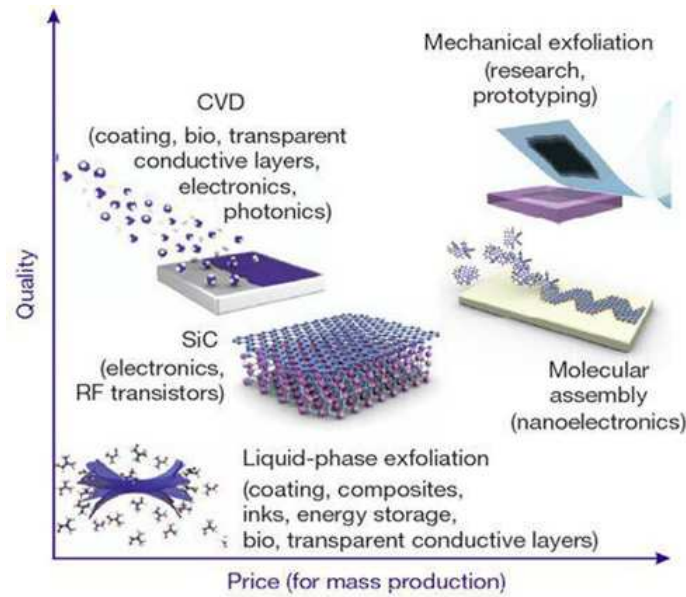


Figure 6.1.: Several most commonly used fabrication methods of graphene (Figure taken from [377]). Methods position in the chart illustrates the sample quality versus mass-production costs; potential applications are also noted for each method.

perpendicular to the basal 001 plane. In material science, long before graphene, the cleavage technique was used to obtain near perfectly flat surfaces of highly oriented pyrolytic graphite (HOPG), or mica group materials and others. This was very important in scanning microscopy techniques (scanning electron, scanning tunneling microscopy, atomic force microscopy), since these materials have been used as substrates, because after cleavage they have almost perfectly flat surfaces. These surfaces are perfect for the analysis where a substrate imperfections would affect measurements of nanoscopic structures.

After the cleavage along well defined crystallographic plane, the surface is almost perfectly flat. The micromechanical exfoliation is based on cleavage but with one additional requirement. There should be no material left under the surface produced by cleavage, i.e. cleavage should give only one atomic layer of the material (which is not mandatory after the cleavage).

Micromechanical exfoliation if done properly should produce surfaces of only one atomic layer with relatively high yield. In graphene production it exploits weak the Van der Waals forces existing in crystal graphite making perfect monoatomic samples. However an exfoliated graphene cannot be free-standing and it needs to be

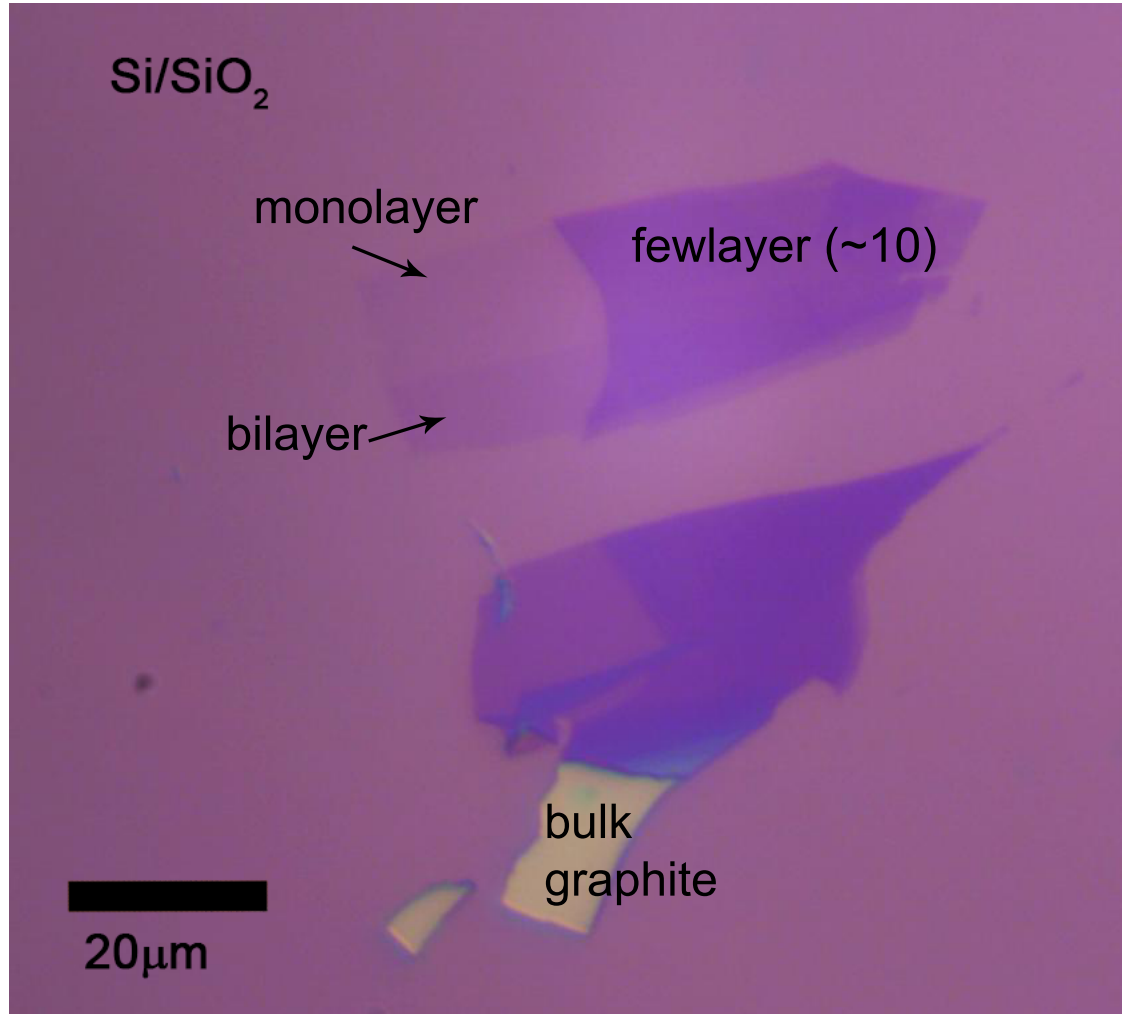


Figure 6.2.: Optical image of the mechanically exfoliated graphene sample on Si/SiO₂ substrate (SiO₂ 300nm dry oxide)

supported (or at least partly supported) by a substrate. The substrate preparation is one of the most crucial steps for the deposition of atomically thin samples. In most cases graphene and other atomically thin materials do not chemically bond to a supporting substrate, and are only held on by the Van der Waals forces. In practise this means, any microscopic dirt, chemical residue, or high enough surface roughness will reduce a binding of sample to surface and deposition of graphene will not be possible over such substrates. Having a systematic way of substrate preparation (cutting, cleaning etc) therefore it is of great importance for successful and controllable deposition of graphene. The success of micromechanical exfoliation technique lies in the fact that the Van der Waals forces between the cleaved surface of graphite (i.e. the surface layer) and the substrate are stronger than the forces

6. 2D MATERIALS SYNTHESIS

between each graphene layer in graphite. So if we would have a flat substrate surface with a graphite flake firmly attached to it by the Van der Waals forces, an additional cleavage of that surface would remove all the graphite but the last layer which remains on the substrate. This technique is not only recipe for graphene samples preparation but for many other the Van der Waals materials as MoS_2 , WS_2 , WSe_2 [3, 4], FeSe [72], NbSe [66] and even some layered cuprates (Bi2212) [192].

Although it is a completely manual technique, properties of the exfoliated graphene are unparalleled. Exfoliated samples are always single crystals, usually with well defined crystal edges. Due to the unique process the resulting graphene layer is not exposed to anything but other graphite layers, substrate and the ambient making it perfectly clean. Any number of layers could be produced by this method, although there is no direct control over the number of layers, flakes size, shape and position on the substrate. It is considered that thinner structures are more favorable, and "graphene" is considered to be graphene up to 10-15 layers. The starting material (natural crystalline graphite) has almost perfect structure and very low amount of defects, obtained graphene samples have almost no defects in their crystal structure.

With all this benefits however there are several major drawbacks of this method. For industry and application of graphene in it the biggest one is that it would be almost impossible to scale up the production of exfoliated graphene and especially to make it cost-effective. For this reason an exfoliated graphene is used in fundamental research mainly and in proof-of-concept devices. It could be extended to very small series of highly sophisticated devices. For fundamental research quality of samples is of greatest importance so making large number of samples and using those that were best suited for the planned experiment is way to overcome issues. Depending on the requirements, the yield is usually one-tenth or even one-hundredth of the prepared samples.

The mechanically exfoliated graphene can be used in various nano-electronic devices, due to its excellent electrical conductivity, and as protective coating due to its unequaled mechanical properties, originating in strong carbon-carbon bonds. The Young's modulus of graphene is about five times greater than of the bulk steel [7, 379]. Not only strong but graphene is elastic and at the same time it can be folded by 180° over less than one nanometer in length, without breaking its in-plane carbon-carbon bonds. Another important point is in the fact the crystal lattice of graphene is so densely packed that it is impermeable to any gases, even H_2 [8]. One of the most important application is graphene-based proton ex-

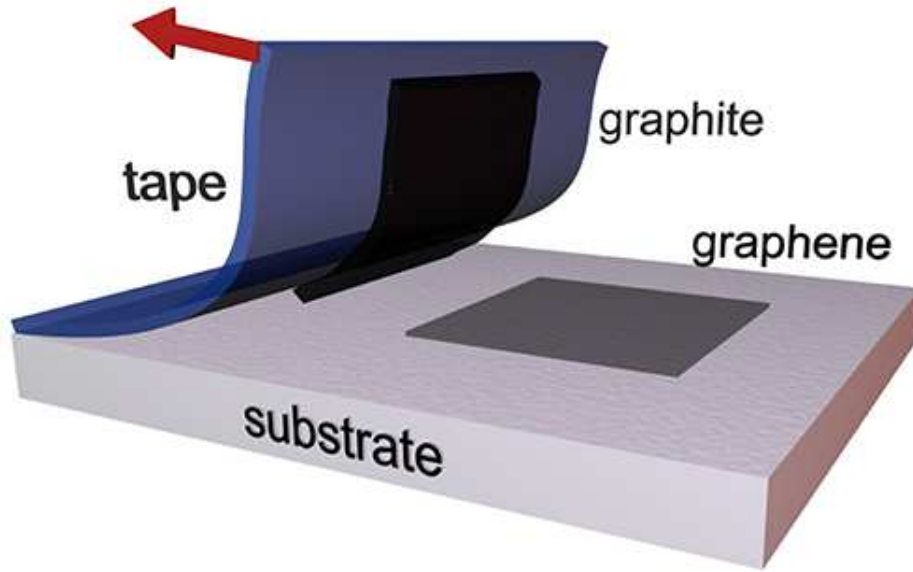


Figure 6.3.: Schematic diagram of the mechanical exfoliation. Figure used with permission of the author [425].

change membrane. Also, graphene has low friction coefficient [380], and has been employed as a protective coating for friction reduction [381, 382, 383, 384, 385], wear protection [386, 387] and as corrosion barriers [388]. Recently, graphene has been employed to encapsulate objects such as single yeast cells [389], bacteria [390], water molecules [391, 392, 393, 394, 395, 396, 397, 398, 399, 400], fluorescent films [401], single-stranded DNA and DNA nanostructures [402, 403]. It was demonstrated that graphene replicates the topography of the DNA molecules [402, 403].

In the next two sections detail procedure of exfoliation will be described 6.2, and afterwards its application as protective coating for DNA structures will be briefly discussed 6.3.

6.2. Exfoliation Procedure

As emphasized before, the proper substrate preparation is one of the most important prerequisite for successful isolation of high-quality micromechanically exfoliated graphene samples. In this section several substrate preparation procedures that have been used in the dissertation are presented. These techniques together with many others are commonly used in the Si-based industry, nanotechnology, and surface

6. 2D MATERIALS SYNTHESIS

science. For successful substrate preparation usually several steps of cleaning are combined. [404] As discussed above, graphene samples require a substrate to be placed onto. Silicon substrates covered with 80 nm or 300 nm thick dry thermal oxide (SiO_2/Si) are most commonly used. Since graphene absorbs about 2.3 % of the incident light, it should not be visible on any surface and it would be very hard to locate flakes on substrate surface. However due to the interference of the light within the oxide layer, the optical contrast of the graphene is enhanced and enables a good visibility of graphene using optical microscopy, which is essential for the identification [422]. If the thickness of the oxide layer is increased by only 5 % (315 nm), the contrast is significantly reduced [422]. Cleaning process for SiO_2/Si substrates begins with a mechanical cleaning, followed by thermal annealing. Mechanical cleaning starts with removing visible dirt and residue with q-tips specialized for cleaning optical components, either dry or soaked with acetone. To remove acetone residue substrates should be dried with an air or argon gun. Gas flow should be 15 - 30 l/min with a nozzle diameter of ~ 1 mm. If mechanical cleaning is not sufficient chemical cleaning should follow. The chemical cleaning begins in sonication acetone for 5 minutes, followed by another repeated sonication for 5 minutes more in fresh acetone. Afterwards substrates should be removed from the acetone and, without drying, should be transferred to be sonicated again in isopropyl alcohol for 5 minutes. After sonication in isopropyl alcohol it is necessary to quickly be dried with an air gun, preferably using argon gas. Gas flow should be over 15 l/min with a nozzle diameter of ~ 1 mm. When samples are cleaned from mechanical and/or chemical residue, thermal annealing proceeds. Samples heat for about 30 minutes, at temperatures between 200°C and 250°C . This temperature is suitable for SiO_2/Si , quartz, sapphire and similar substrates. Higher temperature would increase surface roughness which is adverse. However with other substrates like thin metallic films, or organic layers, or predefined micro- or nano-structures, such high temperature could cause substrate degradation. Heating is ended with a quick cooldown. Substrates should be cooled to room temperature quickly, e.g. by removing them from the heater and placing them onto a metallic surface (at room temperature). A substrate should be inspected by an optical microscope in dark field for any residue or dirt. If there are any substrate contaminations, a chemical cleaning followed again by thermal annealing should be carried out. A final step should be plasma or ozone cleaning, to remove any organic residue. In preparation of samples Novascan UV 8 system was employed. Process of ozone cleaning consists

6. 2D MATERIALS SYNTHESIS

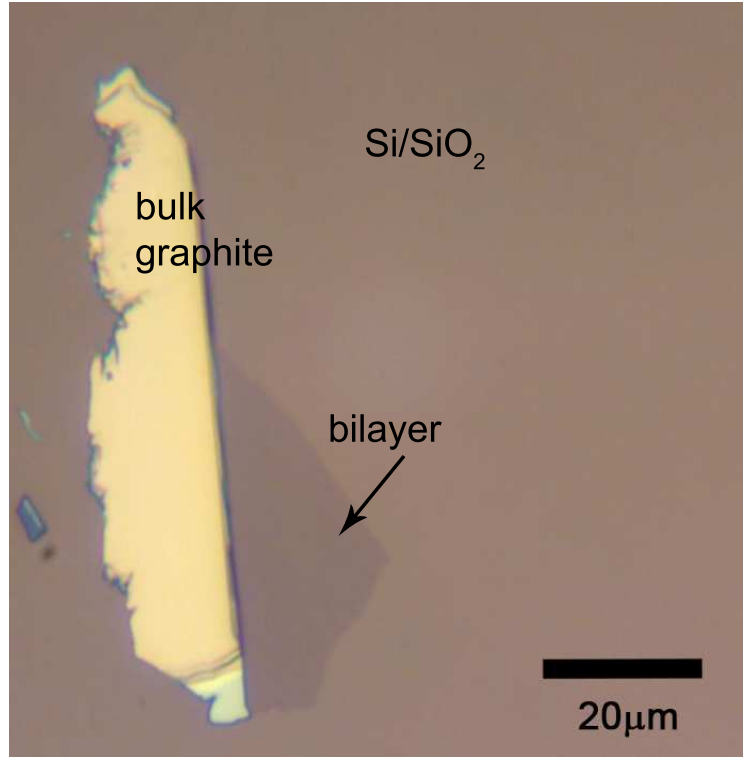


Figure 6.4.: Optical image of the mechanically exfoliated graphene sample on Si/SiO₂ substrate (SiO₂ 85 nm dry oxide)

of several steps. It begins with an exposure to ozone (UV light) for time duration of 10 minutes, at temperature between 100°C and 200°C. It is followed by the ozone incubation period (with a lamp turned off) for 10 minutes, at the temperature between 25°C and 60°C. After time is elapsed ozone is purged (evacuation system on) for 5 - 10 minutes, at temperature between 25°C and 60°C. Ozone is hazard for human health and before opening of cleaning chamber it must be completely evacuated. When chamber is opened substrates should be used in next several minutes (up to 15 minutes), or the entire ozone cleaning procedure should be repeated. For glass substrates (glass, quartz, SiO₂/Si, etc.) ozone cleaning is not only proper way to clean from any organic residue but it will further break any silanol bonds (Si-OH) that are formed on the surface due to water contamination. As a result a substrate should be highly hydrophilic. These broken Si-OH bonds will reform in ambient conditions in the matter of several minutes hence graphene deposition should follow immediately after ozone cleaning. After substrates were prepared micromechanical exfoliation procedure can be performed. Procedure consists is a two-step process, consisting of chemical and mechanical exfoliation steps. This procedure results with

6. 2D MATERIALS SYNTHESIS

very large samples and yield of about 50% (with samples greater than $10 \times 10 \mu\text{m}^2$) and also it minimizes any sample contamination, since graphene layers comes in contact only with a clean substrate and ambient environment. The sample itself is never exposed to any kind of chemicals, tape or tape residue, however surrounding substrate will have both chemical and tape residue. Exfoliation procedure begins with tape preparation process. A small flake (less than 10 mm in diameter) of Kish graphite (preferably: NGS Naturgraphit GmbH) is placed between two pieces of a sticky tape (preferably: NITTO ELP BT150ECM tape). Two pieces of tapes are peeled off, exfoliating a graphite flake in two pieces, one piece on each side of the tape. The process is repeated several times depending on the thickness of the starting flake. Once graphite flakes on the tape are thin enough (there should be several regions of graphite that are semi transparent, grayish in color, and non transparent regions should be thin enough so their thickness should not be visible by the naked eye), less than 100 nm tape is considered prepared. Prepared tape should be gently placed over a clean substrate, just removed from ozone cleaner. After placement of the tape, there should be no air bubbles left, and the tape should not be stretched nor strained. Excess tape (the part not supported by the substrate) should be cut away, to about 1 mm from the substrate edge with sharp scalpel. The sample with the tape on is then placed in Methyl-isobutyl ketone (MIBK), and kept at about 40°C until the tape comes off. This commonly lasts from 45 minutes up to 2 hours, for a substrate size of $1 \times 1 \text{ cm}^2$. MIBK dissolves the adhesive, leaving exfoliated graphene on surface of substrate. After the tape falls off, samples should be rinsed in acetone, followed by iso-propyl alcohol, and quickly dried with an air gun. With this, the first, chemical, exfoliation is over and as a result of the surface of the substrate should be covered with large (about 1 mm in diameter) graphite flakes that are not thicker than several hundred nanometers. There is still not graphene at the surface. Second, mechanical, exfoliation continues. Samples should be slowly (approximately 5 minutes) heated from room temperature (RT) to 150°C and kept at elevated temperature for about 30 minutes. After 30 minutes they should be slowly cooled down back to RT in order to enhance the contact between flakes and substrate. After cooled down samples should be covered with another tape (NITTO ELP BT150ECM), again with no air bubbles nor strain. Procedure of mechanical exfoliation occurs when the tape is pulled off as depicted at Figure 6.3. The rate of the pulling will determine the amount of graphite and graphene that remains on the sample surface. For example a slower pulling (about 1 mm per minute) will result

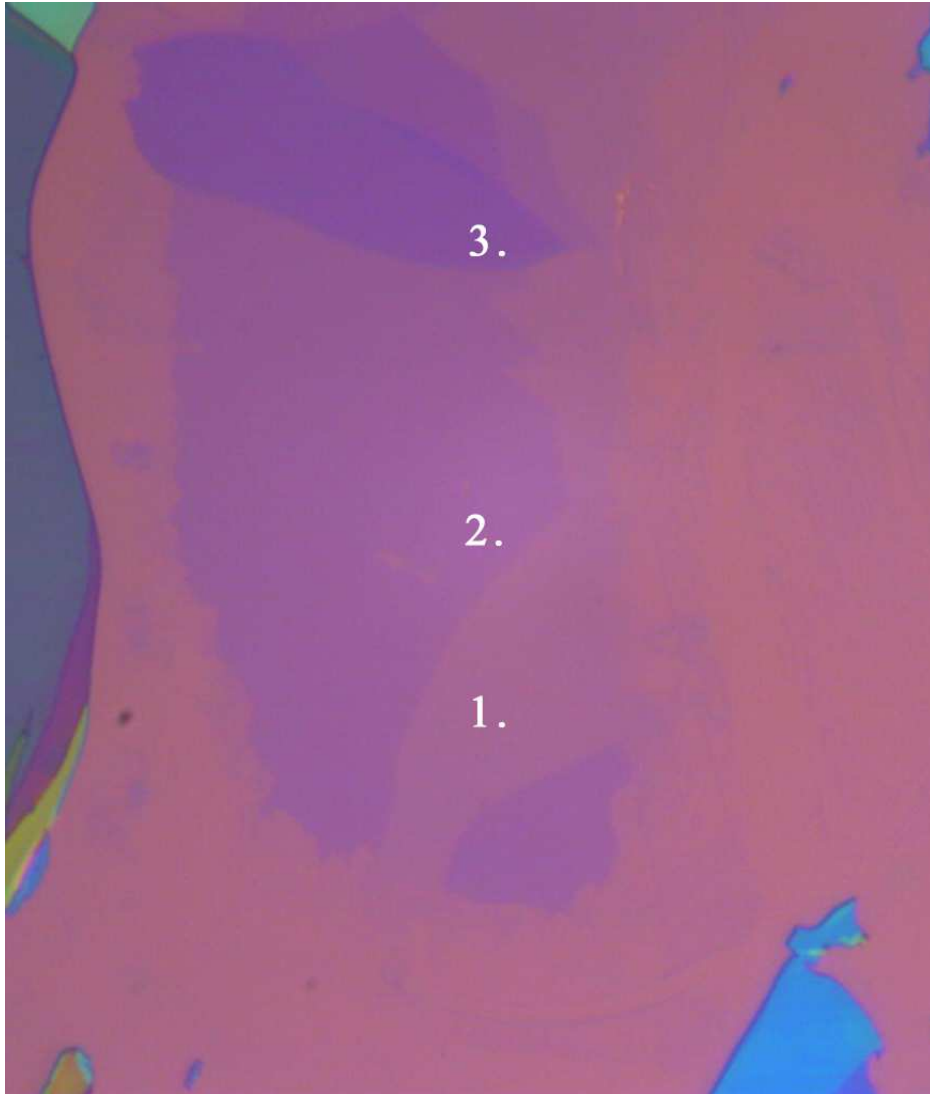


Figure 6.5.: Image obtained by the optical microscopy of the mechanically exfoliated Bi2212. In the area marked by 1, in the lightest violet, the half unit cell of Bi2212 is present. In area 2 is single unit cell region and in the area marked by number 3 is Bi2212 with few unit cells thickness. Inhomogeneity of the area 1 is due to the degradation of material in the interaction with oxygen from the air [192]. After the period of 12 hours, the half unit cell samples were almost completely degraded. To further study this way obtained samples, coating with the layer of graphene or hexagonal boron-nitride is necessary

6. 2D MATERIALS SYNTHESIS

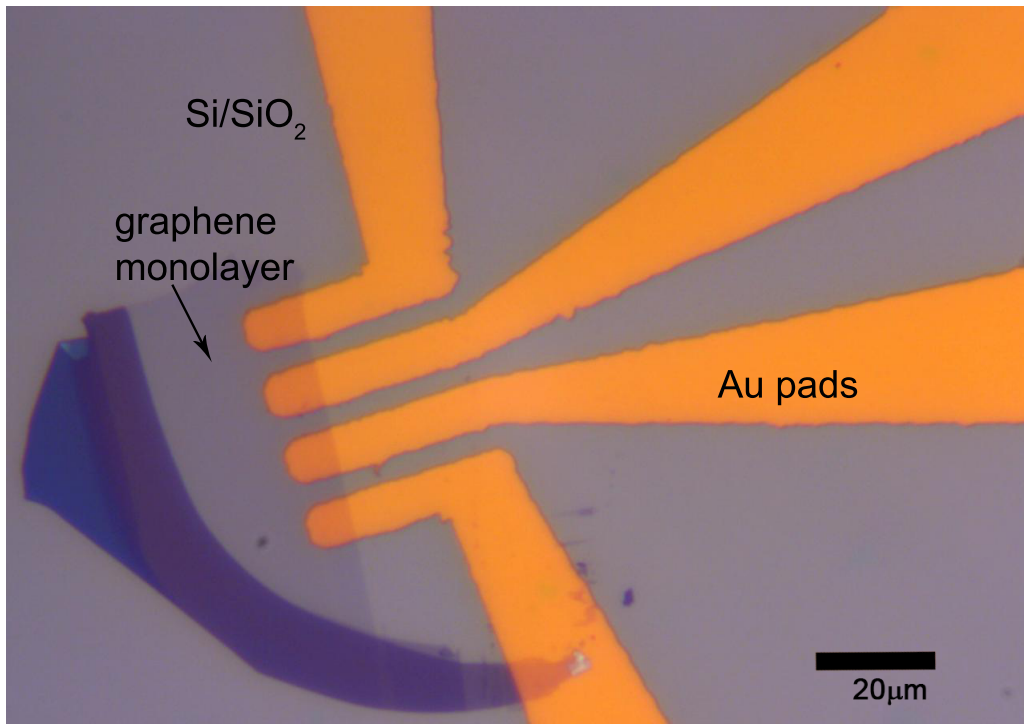


Figure 6.6.: Graphene monolayer on 85 nm dry oxide Si/SiO₂ substrate with golden contact in four point probe configuration made by UV photolithography. Figure used with permission of author [426]

6. 2D MATERIALS SYNTHESIS

with larger flakes but also with a more residual graphite. Quick pulling could strip the wanted graphene from the surface. The resulting sample should be inspected under optical microscope, where potential atomically thin flakes should be located. It can occur that there is no graphene samples on a substrate but a still significant amount of graphite. Then second exfoliation can be repeated even several times if needed. After the samples are obtained and thickness and number of layers is optically estimated comparing contrast of different layers (as shown in the first chapter, and in Figures 6.2 and 6.4), they can be submitted to Raman spectroscopy where exact number of layers can be determined, as described in the first chapter of this dissertation (but only up to 5 layers). This way prepared samples, defect-free and clean can be used for micro-electronic devices. Metallic contacts can be placed on the surface, as presented in Figure 6.6. The above described procedure is suitable not only for exfoliation of graphene but as well for other 2D materials, as well as certain layered non-van der Waals materials. In Figure 6.5, 6.7 the mechanically exfoliated $\text{Bi}_2\text{Sr}_2\text{CuO}_2$ (Bi2212), a high-Tc cuprate superconductor, using same technique as for graphene.

6.3. Mechanically exfoliated graphene as protective coating for DNA structures

In this section it is demonstrated how mechanically exfoliated graphene can be used as a protective layer for organic nanostructures. Results presented in this section are presented in two papers [423, 424]. They are not directly related to the subject of this thesis but they present part of experimental research of the candidate.

Manipulation of the artificial deoxyribonucleic acid (DNA) macromolecules can be used for highly controllable process of bottom-up fabrication of various nanostructures. The wide variety of structures and patterns and many 2D and 3D DNA origami nanostructures were fabricated [405, 406, 407] using the technique of DNA folding. Application for these structures are various. Spectra ranges from simple usage as substrates [408], offering a solution-based self-assembly with nanometer precision geometries, over usage as scaffolds for assembly of metallic nanoparticles [409, 410, 411], for routing polymers [412], surface-enhanced Raman scattering [413], as positive and negative masks for DNA nano-lithography [414, 415, 416, 417], and even graphene patterning [418]. However a mechanical wear or solution phase

6. 2D MATERIALS SYNTHESIS

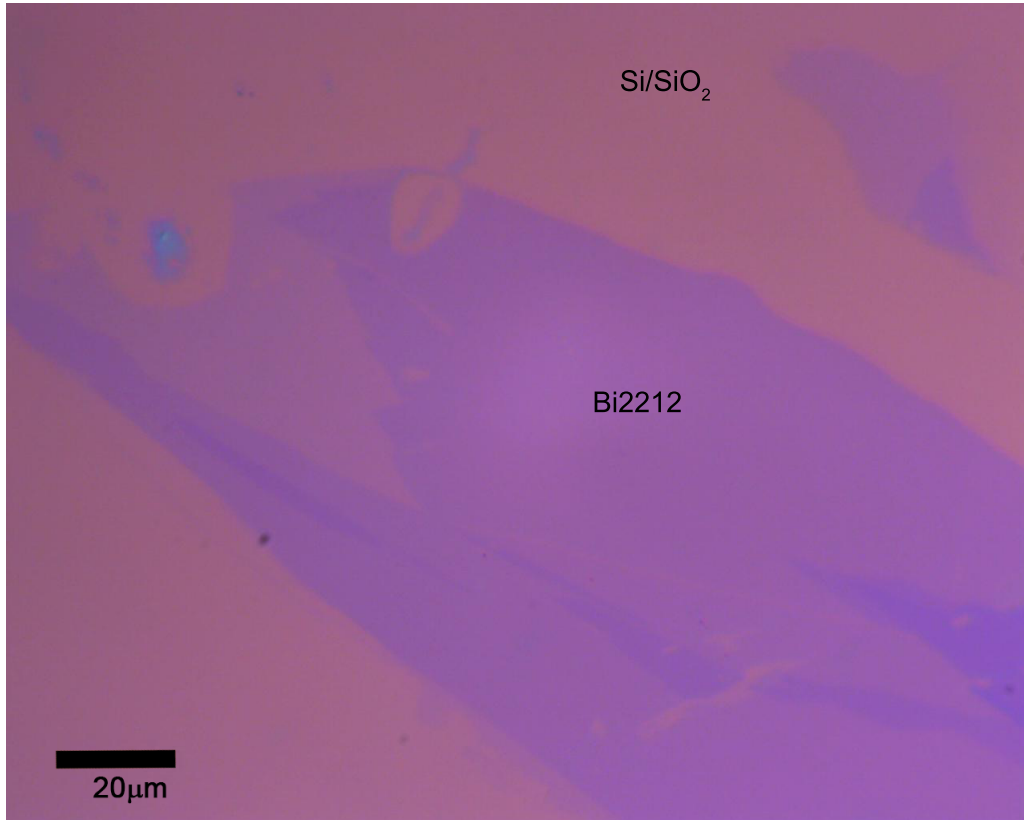


Figure 6.7.: Image obtained by the optical microscopy of the mechanically exfoliated Bi2212 on Si/SiO₂ substrate (300nm dry oxide). Large scale samples right after exfoliation procedure (deterioration process did not start yet).

6. 2D MATERIALS SYNTHESIS

processing could damage these nanostructures [410, 420, 421] due to their delicate nature and limits their applicability in bottom-up fabrication.

Excellent mechanical properties of graphene offer possibility on enhancing the structural stability of the DNA origami nanostructures by encapsulation. For this purpose triangular the DNA origami nanostructures are deposited onto silicon substrates and encapsulated by single layer exfoliated graphene. The procedure of mechanical exfoliation is slightly modified due to the sensitive nature of the DNA origami. As emphasized in the previous section, prior to any other procedure, the substrates were cleaned and prepared by 5 min treatment in Novascans ozone cleaner. Subsequently, drops of 0.5 μl of DNA origami solution were deposited on each substrate and covered with 10 μl of 10TAE with 10 mM of MgCl_2 . After one hour of the incubation period in the water-saturated environment, the samples were rinsed in 1:1 water-ethanol solution to clean excess of material and dried with an argon gun (flow 10 l min^{-1}). The DNA origami nanostructures covered the entire substrates with an averaged density of twenty triangular nanostructures per square micrometer and substrates were prepared for deposition. After this point, there were no any further cleaning or treating of substrates. Quickly after cleaning the graphene was deposited over the DNA origami structures using, above described, micromechanical exfoliation. The tapes were prepared and deposited on the substrates with the DNA origami nanostructures. In order to avoid damaging the DNA origami nanostructures (since their sensitivity on heat), the entire micromechanical exfoliation was carried out at room temperature, without any heating. This made process of chemical exfoliation in MIBK much longer, almost 4 hours. After the deposition the individual flakes were detected using optical microscopy and single atomic layer samples were chosen by the optical contrast, and confirmed by the Raman spectroscopy and AFM. Schematic representation of the encapsulation by graphene is shown in Figure 6.8

The morphology of DNA origami nanostructures is very well transferred to the graphene, having even the inner triangle clearly resolved by atomic force microscopy (AFM) (as shown in Figure 6.9). The samples are tested for their structural stability using AFM based manipulation and aqueous solution exposure. The forces required to damage bare and graphene encapsulated nanostructures are compared, and the effects of cumulative damage introduced by successive manipulations are investigated. In addition, the stability of the graphene encapsulated DNA origami nanostructures is tested against prolonged exposure to deionized water (DIH_2O).

6. 2D MATERIALS SYNTHESIS

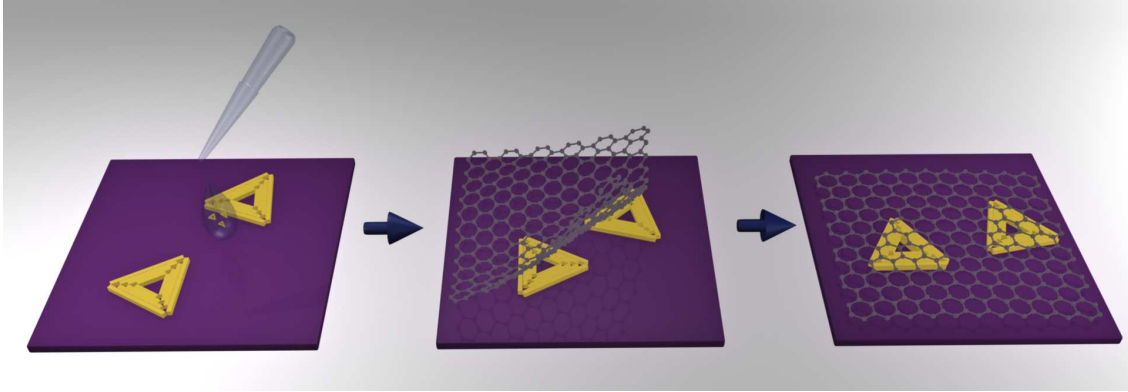


Figure 6.8.: Schematic diagram of the DNA origami deposition and encapsulation by the exfoliated graphene.

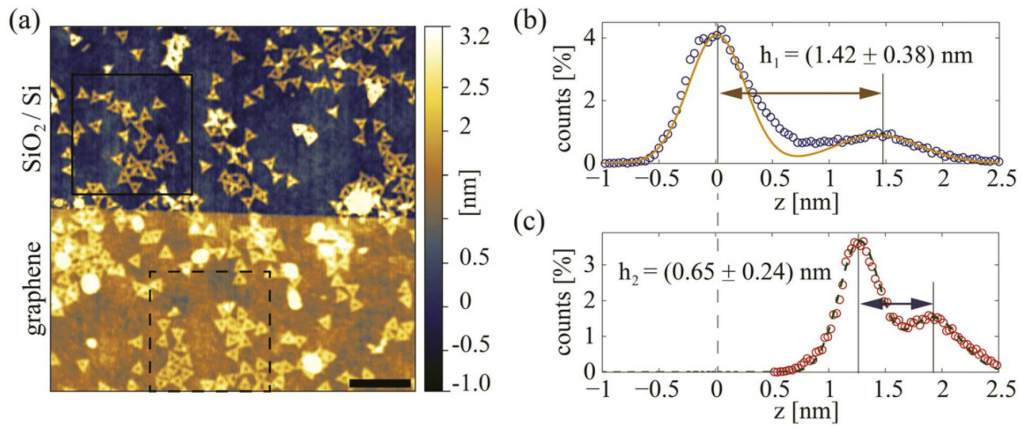


Figure 6.9.: (a) TAFM topography of a step edge of graphene covering a substrate with DNA origami nanostructures. Scale bar is 500 nm. (b) and (c) histograms (circles) and Gaussian fits (solid and dashed lines) of the selected areas in (a), corresponding to the bare and graphene encapsulated nanostructures. h_1 and h_2 stand for the height of the bare and graphene encapsulated structures, and are estimated as a peak-to-peak distance within the corresponding histograms. Figure taken from [423]

6. 2D MATERIALS SYNTHESIS

It was demonstrated that a single layer exfoliated graphene can be used as a protective layer for the DNAorigami nanostructures. The threshold for the normal force that induces structural damage to the graphene encapsulated DNA origami nanostructures was found to be about 60 nN. The graphene provides wear protection against multiple manipulations if the applied normal force is below the damage threshold. Also graphene encapsulated nanostructures remain intact even after 30 min of the exposure to the deionized water, while the bare structures are significantly damaged in the matter of seconds. The limits of graphene protection against deionized water exposure arise from wrinkling of the graphene layer itself. It is expected that other liquids will act in the similar manner as long as they do not damage graphene, and will only take different amount of time to damage the bare DNA origami nanostructures. This extends the use of the DNA origami scaffolds in many fabrication processes, as various lithography steps or wet transfer of 2D materials.

However this is not only application of graphene with DNA origami nanostructures. The unique electronic, mechanical, and thermal properties of graphene are combined with the plasmonic properties of the gold nanoparticle (AuNP) dimers, which are assembled using the DNA origami nanostructures [424]. A strong interactions between graphene and AuNPs result in superior SERS performance of the hybrid structure compared to their individual components. Furthermore, an improved photostability due to graphene encapsulation resulting in significantly lower photobleaching rates. This is attributed to the efficient protection of the dye molecules from reactions with the ambient oxygen by graphene and heat dissipation from the SERS hot spots [424].

7. CONCLUSION

In the conclusion, the dissertation and publications directly related to it [242, 243, 244, 245, 246, 247] address the topic of superconductivity in the graphene and related materials and study it using the ab-initio methods.

Research of 2D materials, as a field is born with the discovery of graphene, and it is growing at a fast pace with each new atomically thin material that is isolated or synthesised. The thin films have been studied for the second half of the 20th century but their micron thickness still made them bulk materials. Graphene and its thickness of only one atom showed completely new physics in a truly lowest limit.

In this dissertation the alkali doped graphene have been studied using DFT and DPFT with an extensive focus on the vibrational properties [242]. A detail description and understanding of the phonons in the doped graphene is of the utter importance for the comprehension of the electron-phonon coupling and the appearance of superconductivity thus making it necessary prerequisite for any further study. The vibration frequencies and normal coordinates of the Γ point phonons for monolayer graphene doped with lithium, calcium and barium have been studied and compared it with ones in the pristine graphene. In addition, using the group theory methods, the correspondence between phonon modes of the graphene and phonon modes of the variety of doped graphene possessing C_{6v} symmetry have been demonstrated. A satisfying agreement with experimental data [270] additionally supports these calculations. Not only the results provided in this study give important information for further analysis of superconductivity but as well are relevant for the characterization of those structures and their further investigation and application. To complete the description, the optical properties of Li doped graphene have been studied within DFT formalism [244]

Ever since superconductivity in graphene have been suggested, a tireless struggle for its enhancement have begun, suggesting plethora of methods how to make "the wonder material" even better superconductor [257, 275, 273]. The method for the engineering of superconductivity in graphene by application of tensile biaxial strain,

7. CONCLUSION

suggested in this dissertation and including paper [243] proposes an experimentally available and plausible method [7] for the augmentation of the electron-phonon coupling. The biaxial tensile stain can greatly enhance the eph coupling by softening the optical phonon modes without breaking symmetry, resulting in a significant increase of the critical temperature, up to 29K.

The experimental realisation of the Li-doped monolayer graphene [56] and successive ARPES measurements shown, just as previous theoretical studies suggested [59], that Li deposited on graphene strongly modifies the phonon density of states, leading to superconductivity. This is not the only experimental realization of superconductive graphene, there are several others, as the Ca-doped graphene bilayer [261], graphene laminates [199] and the potassium-doped few layer graphene [178]. However, this was the first experimental proof of superconductivity in the Li-doped monolayer graphene and it gave the strong evidence for the electron-phonon coupling mechanism. This makes the ab-initio approach (DFT, DPFT, calculation of the Eliashberg function and the McMillan formula) used in this dissertation, completely justified. Also since the electronic correlations are not strong in graphene, usage of DFT and LDA is quite a suitable assumption [289, 290] ensuring the correctness of presented approach.

Conclusions drawn from the superconducting graphene not only have the fundamental importance for the understanding of superconductivity in the low dimension but, as well, for search for other 2D superconductors and engineering of EPC in them. This concerns the fundamental problem of the existence of superconductivity in 2D limit. In general a 2D crystal structure and its phonon dispersion can be easily modified which can be beneficial for superconductivity. A low density of states in a 2D system might be unfavorable to superconductivity but it can be easily increased since a doping of one or few atomic layers is much simpler task than the bulk system. The 2D systems not only give new properties but as well present a great possibility for the manipulation and engineering, and artificially producing of the new materials by stacking them, as heterostructures, that exhibit different (sometimes dramatically [72]) properties than its building components.

Inspired with the structural similarity between intercalated graphite and graphene, and magnesium-diboride, research is continued on 2D limit of magnesium-diboride. After proving its stability, a comprehensive analysis was performed including the ab-initio methods and group theory study [246] showing that monolayer of magnesium-diboride is superconductive with the critical temperature of 18 K. Calculating the

7. CONCLUSION

Eliashberg function and the electron-phonon coupling constant, it is concluded that EPC strength is weaker in comparison to the bulk. The low-frequency vibrations contribute more in the low-dimensional structure however not enough to overcome a decrease of the coupling in the high-frequency region occurred after the removal of the other layers. Transferring conclusions made for the doped graphene and enhancement of EPC by engineering biaxial strain to, not only structurally but electronically similar, magnesium-diboride monolayer expected increase of EPC and critical temperature was achieved. Modifying the of DOS at the Fermi level and softening of the modes are beneficial for EPC resulting in the critical temperature of 31 K. Value of this study not only lies in discovery of the new superconducting 2D material but more importantly in this new perspective given to the "old" material. It is opening a possibility to revisiting of ideas of constructing MgB₂-inspired high-temperature superconductors but as the 2D materials. It demonstrates opportunity to review known superconducting materials in context of the low-dimensional systems.

It is important to emphasize that low-dimensional systems open new possibilities but as well as challenges and effects. The quantum confinement effects, sample surface effects, BKT transition and many more become a factors [359]. Although some of those are not included in ab-initio techniques, results obtained this way still have remarkable value. The purpose of ab-initio calculation is not only in interpretation of the experimental results but more importantly, in giving predictions for the further research and improvements. Also, the ab-initio methods are ever-growing part of science and new techniques are constantly being developed, approximations are improving, including more effects and specificities. This is all followed by the fascinating development of computational resource that become inescapable part of theoretical research and almost the science for itself. As presented in this dissertation [245, 247], the usage of various hardware and software accelerations can make significant difference. Technological development of the computational resources skyrocketed in the past decade enabling more complex and extensive problems to be conquered. The new computational methods together with the constantly-improving ab-initio methods are on synergic road to exact description of the reality.

Bibliography

- [1] K. S. Novoselov, A. K. Geim, S. V. Morozov, D. Jiang, Y. Zhang, S. V. Dubonos, I. V. Grigorieva, and A. A. Firsov, "Electric field effect in atomically thin carbon films", *Science*, **306**, 666–669, 2004.
- [2] K. S. Novoselov, A. K. Geim, S. V. Morozov, D. Jiang, M. I. Katsnelson, I. V. Grigorieva, S. V. Dubonos, and A. A. Firsov, "Two-dimensional gas of massless dirac fermions in graphene", *Nature*, **438**, 197–200, 2005.
- [3] A. K. Geim, "Graphene: Status and prospects", *Science*, **324**, 1530–1534, 2009.
- [4] K. S. Novoselov, "Nobel lecture: Graphene: Materials in the flatland", *Rev. Mod. Phys.*, **83**, 837, 2011.
- [5] Von H.P. Boehm, A. Clauss, G.O. Fischer and U. Hofmann, "Dnnste Kohlenstoff-Folien", *Naturforschg*, **17b**, 150-153, 1962.
- [6] X. Lu, M. Yu, H. Huang and R. S Ruoff "Tailoring graphite with the goal of achieving single sheets", *Nanotechnology*, **10**, 269-272, 1999.
- [7] Lee, C., Wei, X., Kysar, J. & Hone, J. "Measurement of the elastic properties and intrinsic strength of monolayer graphene", *Science*, **321**, 385–388, 2008.
- [8] J. S. Bunch, S. S. Verbridge, J. S. Alden, A. M. van der Zande, J. M. Parpia, H. G. Craighead and P. L. McEuen, "Impermeable atomic membranes from graphene sheets" *Nano Lett.*, **8**, 245862, 2008.
- [9] Mayorov, A., Gorbachev, R. & Morozov, S. "Micrometer-scale ballistic transport in encapsulated graphene at room temperature", *Nano Letters*, **11**, 2396–2399, 2011.
- [10] Balandin, A. A. "Thermal properties of graphene and nanostructured carbon materials", *Nature Materials*, **10**, 569–81, 2011.

Bibliography

- [11] Nair, R. R., Blake, P. & Grigorenko, A. "Fine structure constant defines visual transparency of graphene", *Science*, **320**, 1308, 2008.
- [12] Nair, R. R. et al. "Fluorographene: a two-dimensional counterpart of Teflon", *Small*, **6**, 2877–84, 2010.
- [13] Hu, S. et al. "Proton transport through one-atom-thick crystals", *Nature*, **516**, 227–230, 2014.
- [14] Castro Neto, A. H., Peres, N. M. R., Novoselov, K. S. & Geim, A. K. "The electronic properties of graphene", *Reviews of Modern Physics*, **81**, 109–162, 2009.
- [15] P. R. Wallace, "The band theory of graphite", *Phys. Rev.*, **71**, 622–634, 1946.
- [16] G. W. Semenoff, "Condensed-Matter Simulation of a Three-Dimensional Anomaly", *Phys. Rev. Lett.*, **53**, 2449, 1984.
- [17] S. Das Sarma, S. Adam, E. H. Hwang, and E. Rossi. "Electronic transport in twodimensional graphene" *Reviews of Modern Physics*, **83**, 2, 2011.
- [18] S. V. Morozov, K. S. Novoselov, and A. K. Geim. "Electron transport in graphene", *Physics-Uspekhi*, **51**, 7, 2008.
- [19] P. A. M. Dirac. "The quantum theory of the electron", *Proc. Royal Soc. Of London. Series A*, **117**, 610–624, 1928.
- [20] O. Klein, "Die reflexion von elektronen an einem potentialsprung nach der relativistischen dynamik von Dirac", *Zeitschrift fur Physik*, **53**, 157–165, 1929.
- [21] M. I. Katsnelson, K. S. Novoselov, and A. K. Geim, "Chiral tunnelling and the klein paradox in graphene", *Nature Phys.*, **2**, 620–625, 2006.
- [22] M. O. Goerbig, "Electronic properties of graphene in a strong magnetic field", *Rev. Mod. Phy.*, **83**, 1193, 2011.
- [23] N. Hong Shon and T. Ando, "Quantum transport in two-dimensional graphite system", *Jour. Phys. Soc. Jap.*, **67**, 2421–2429, 1998.
- [24] M. S. Dresselhaus. "Solid state physics - part II - optical properties of solids", *MIT Solid State Physics Course*, 2011.

Bibliography

- [25] Jorio A, Dresselhaus M S, Saito R and Dresselhaus G "Raman Spectroscopy in Graphene Related System" *Weinheim: Wiley*, 1st edn, 2011.
- [26] P. Y. Yu and M. Cardona. "Fundamentals of semiconductors - physics and materials properties", *Springer Science & Business Media*, 2010.
- [27] G. Dresselhaus R. Saito and M. S. Dresselhaus. "Physical Properties of Carbon Nanotubes". *Imperial College Press*, London, 1998.
- [28] Ge. G. Samsonidze, E. B. Barros, R. Saito, J. Jiang, G. Dresselhaus, and M. S. Dresselhaus, "Electron-phonon coupling mechanism in two-dimensional graphite and single-wall carbon nanotubes", *Phys. Rev. B* **75**, 155420, 2007.
- [29] V. Damjanović, R. Kostić, R. Gajić, "Characters of graphene's symmetry group D_{6h} ", *Phys. Scr.*, **T162**, 014022, 2014.
- [30] V Damjanović and R Gajić, "Phonon eigenvectors of graphene at high-symmetry points of the Brillouin zone", *Phys. Scr.*, **T149**, (2012) 014067.
- [31] J. Maultzsch, S. Reich, C. Thomsen, H. Requardt, and P. Ordejón. "Phonon Dispersion in Graphite", *Phys. Rev. Lett.*, **92**, 075501, 2004.
- [32] K. A. Wang, A. M. Rao, P. C. Eklund, M. S. Dresselhaus, and G. Dresselhaus. "Observation of higher-order infrared modes in solid C_{60} films", *Phys. Rev. B*, **48**, 11375, 1993.
- [33] J. Jiang, R. Saito, Ge. G. Samsonidze, S. G. Chou, A. Jorio, G. Dresselhaus, and M. S. Dresselhaus. "Electron-phonon matrix elements in single-wall carbon nanotubes", *Phys. Rev. B*, **72**:235408, 2005.
- [34] P. L. Taylor and O. Heinonen. "Quantum approach to condensed matter physics", *Cambridge University Press*, 2002.
- [35] T. Ando. "Screening Effect and Impurity Scattering in Monolayer Graphene" *J. Phys. Soc. Jpn.*, **75**, 024707, 2006.
- [36] A. H. Castro Neto and F. Guinea, "Electron-phonon coupling and Raman spectroscopy in graphene", *Phys. Rev. B*, **75**, 045404, 2007.
- [37] W. Kohn. "Image of the Fermi Surface in the Vibration Spectrum of a Metal", *Phys. Rev. Lett.*, **2**, 393, 1959.

Bibliography

- [38] S. Piscanec, M. Lazzeri, M. Mauri, A. C. Ferrari, and J. Robertson. "Kohn Anomalies and Electron-Phonon Interactions in Graphite", *Phys. Rev. Lett.*, **93**, 185503, 2004.
- [39] I. Milošević, N. Kepčija, E. Dobardžić, M. Damnjanović, M. Mohr, J. Maultzsch, C. Thomsen, "Kohn anomaly in graphene", *Mat. Sci. and Eng. B*, **176**, 6, 15 , 2011
- [40] M. Lazzeri, S. Piscanec, Francesco Mauri, A. C. Ferrari, and J. Robertson, "Phonon linewidths and electron-phonon coupling in graphite and nanotubes" *Phys. Rev. B*, **73**, 155426, 2006.
- [41] S. Pisana, M. Lazzeri, C. Casiraghi, K. S. Novoselov, A. K. Geim, A. C. Ferrari and F. Mauri. "Breakdown of the adiabatic Born-Oppenheimer approximation in graphene" *Nature Mater.*, **6**, 198, 2007.
- [42] J. Yan, Y. Zhang, P. Kim and A. Pinczuk. "Electric field effect tuning of electron-phonon coupling in graphene", *Phys. Rev. Lett.*, **98**, 166802, 2007.
- [43] A. Das, S. Pisana, B. Chakraborty, S. Piscanec, S. K. Saha, U. V. Waghmare, K. S. Novoselov, H. R. Krishnamurthy, A. K. Geim, A. C. Ferrari and A. K. Sood. "Electrochemically Top Gated Graphene: Monitoring Dopants by Raman Scattering" *Nature Nanotech.*, **3**, 210, 2008.
- [44] A. Matković, U. Ralević, G. Isić, M. M. Jakovljević, B. Vasić, I. Milošević, D. Marković, R. Gajić, "Spectroscopic ellipsometry and the Fano resonance modeling of graphene optical parameters", *Phys. Scr.* 2012, **T149**, 014069, 2012.
- [45] A. Matković, A. Beltaos, M. Milićević, U. Ralević, B. Vasić, D. Jovanović, R. Gajić, "Spectroscopic imaging ellipsometry and Fano resonance modeling of graphene", *J. Appl. Phys.*, **112**, 123523, 2012.
- [46] A. Matković, U. Ralević, M. Chhikara, M. M. Jakovljević, Dj. Jovanović, G. Bratina, R. Gajić, "Influence of transfer residue on the optical properties of chemical vapor deposited graphene investigated through spectroscopic ellipsometry", *J. Appl. Phys.* **114**, 093505, 2013.
- [47] L. Yang et.al., "Excitonic effects on the optical response of graphene and bilayer graphene" *Phys. Rev. Lett.* **103**, 186802, 2009.

Bibliography

- [48] N. B. Kopnin and E. B. Sonin. "BCS superconductivity of Dirac electrons in graphene layers". *Phys. Rev. Lett.*, **100**, 24, 2008.
- [49] J. L. McChesney, A. Bostwick, T. Ohta, T. Seyller, K. Horn, J. Gonzalez, and E. Rotenberg. "Extended van Hove singularity and superconducting instability in doped graphene". *Phys. Rev. Lett.*, **104** 13, 2010.
- [50] R. Nandkishore, L. S. Levitov, and A. V. Chubukov. "Chiral superconductivity from repulsive interactions in doped graphene". *Nature Physics*, **8**, 2, 2012.
- [51] M. S. Dresselhaus and G. Dresselhaus. "Intercalation compounds of graphite". *Advances in Physics*, 2002.
- [52] M. Calandra and F. Mauri. "Theoretical explanation of superconductivity in CaC_6 ". *Phys. Rev. Lett.*, **95**, 23, 2005.
- [53] N. Emery, C. Herold, M. d'Astuto, V. Garcia, Ch. Bellin, J. F. Mareche, P. Lagrange, and G. Loupiau. "Superconductivity of bulk CaC_6 ". *Phys. Rev. Lett.*, **95**, 8, 2005.
- [54] Z. H. Pan, J. Camacho, M. H. Upton, A. V. Fedorov, C. A. Howard, M. Ellerby, and T. Valla. "Electronic structure of superconducting KC_8 and nonsuperconducting LiC_6 graphite intercalation compounds : Evidence for a graphene-sheet-driven superconducting state". *Phys. Rev. Lett.*, **106**, (18), 2011.
- [55] T. Valla, J. Camacho, Z. H. Pan, A. V. Fedorov, A. C. Walters, C. A. Howard, and M. Ellerby. "Anisotropic electron-phonon coupling and dynamical nesting on the graphene sheets in superconducting CaC_6 using angle-resolved photoemission spectroscopy." *Phys. Rev. Lett.*, **102** 10, 2009.
- [56] B. M. Ludbrook, G. Levy, P. Nigge, M. Zonno, M. Schneider, D. J. Dvorak, C. N. Veenstra, S. Zhdanovich, D. Wong, P. Dosanjh, C. Stra er, A. St hr, S. Forti, C. R. Ast, U. Starke, and A. Damascelli, "Evidence for superconductivity in Li-decorated monolayer graphene", *PNAS* **112**, 38, 11795-11799, 2015.
- [57] W.L. McMillan, "Transition Temperature of Strong-Coupled Superconductors, *Phys. Rev.* **167**, 331, 1968.
- [58] Dresselhaus M., Dresselhaus G., Eklund P. and Chung D., "Lattice vibrations in graphite and intercalation compounds" *Mater. Sci. Eng.*, **31** ,141, 1977.

Bibliography

- [59] Profeta G., Calandra M. and Mauri F., "Phonon-mediated superconductivity in graphene by lithium deposition" *Nat. Phys.*, **8**, 131, 2012.
- [60] Calandra M., Profeta G. and Mauri F., "Superconductivity in metal-coated graphene", *Phys. Status Solidi B*, **12**, 2544, 2012.
- [61] G. Savini, A. C. Ferrari, and F. Giustino, "First-Principles Prediction of Doped Graphane as a High-Temperature Electron-Phonon Superconductor", *Phys. Rev. Lett.* **105**, 037002, 2010.
- [62] Marcel H. F. Sluiter and Yoshiyuki Kawazoe, "Cluster expansion method for adsorption: Application to hydrogen chemisorption on graphene", *Phys. Rev. B* **68**, 085410, 2003.
- [63] Csányi, G., Littlewood, P. B., Nevidomskyy, A. H., Pickard, C. J. & Simons, B. D. "The role of the interlayer state in the electronic structure of superconducting graphite intercalated compounds", *Nature Physics* **1**, 42–45, 2005.
- [64] Xu, M., Lian, T., Shi, M. & Chen, H. "Graphene-like two-dimensional materials" *Chem. Rev.* **113**, 3766–3798, 2013.
- [65] Han Liu, Adam T. Neal, Zhen Zhu, Zhe Luo, Xianfan Xu, David Tománek, and Peide D. Ye, "Phosphorene: An Unexplored 2D Semiconductor with a High Hole Mobility", *ACS Nano* **8** 4, 4033-4041, 2014.
- [66] Staley, N.E., et al., "Electric field effect on superconductivity in atomically thin flakes of NbSe₂". *Phys. Rev. B*, **80**, 18, 2009.
- [67] Frindt, R.F., "Superconductivity in Ultrathin NbSe₂ layers". *Phys. Rev. Lett.*, **28** 5, 299-301, 1972.
- [68] Borisenko, S.V., et al., "Pseudogap and charge density waves in two dimensions". *Phys. Rev. Lett.*, **100**, 19, 2008.
- [69] Calandra, M., I. Mazin, and F. Mauri, "Effect of dimensionality on the charge density wave in few-layer 2H-NbSe₂". *Phys. Rev. B*, **80**, 24, 241108, 2009.
- [70] A.K. Geim, I.V. Grigorieva, "Van der Waals heterostructures", *Nature*, **499**, 419–425, 2013.

Bibliography

- [71] Wang Q-Y et al. "Interface-induced high-temperature superconductivity in single unit-cell FeSe films on SrTiO₃" *Chin. Phys. Lett.*, **29**, 037402, 2012
- [72] Ge J-F, Liu Z-L, Liu C, Gao C-L, Qian D, Xue Q-K, Liu Y and Jia J-F "Superconductivity above 100 K in single-layer FeSe films on doped SrTiO₃" *Nat. Mater.*, **14**, 285–9, 2015.
- [73] C.-L. Song, H.-M. Zhang, Y. Zhong, X.-P. Hu, S.-H. Ji, L. Wang, K. He, X.-C. Ma, and Q.-K. Xue "Observation of Double-Dome Superconductivity in Potassium-Doped FeSe Thin Films" *Phys. Rev. B*, **84**, 020503, 2011.
- [74] Zhang, Y., Y.-W. Tan, H. L. Stormer, and P. Kim, "Experimental observation of the quantum Hall effect and Berry's phase in graphene", *Nature*, **438**, 201, 2005.
- [75] Mermin, N. D., "Crystalline Order in Two Dimensions" *Phys. Rev.*, **176**, 250, 1968.
- [76] Novoselov, K. S., et al., "Two-dimensional atomic crystals" *Proc. Natl. Acad. Sci. USA*, **102**, 10451, 2005.
- [77] Born, M., and Huang, K., "Dynamical Theory of Crystal Lattices", *Oxford University Press*, Oxford, UK 1998.
- [78] S.V. Morozov, K.S. Novoselov, M.I. Katsnelson, F. Schedin, L.A. Ponomarenko, D. Jiang and A.K. Geim "Strong suppression of weak (anti)localization in graphene", *Phys. Rev. Lett.*, **97**, 016801, 2006.
- [79] P.Ajayan, P. Kim and K Banerjee "Two-dimensional van der Waals materials" *Phys. Today*, **69**, 9, 2016.
- [80] M.E. Jones, R. E. Marsh, "The preparation and structure of magnesium diboride MgB₂", *Journal of the American Chemical Society*, **76**, 1434, 1954.
- [81] V. Russell, R. Hirst, F.A. Kanda, A. J. King, "An X-ray study of the magnesium borides", *Acta Crystallographica*, **6**, 870, 1953.
- [82] J. Nagamatsu, N. Nakagawa, T. Muranaka, Y Zentani, J. Akimitsu, "Superconductivity at 39K in magnesium diboride", *Nature* **410**, 63, 2001.

Bibliography

- [83] W.B. Pearson "Crystal Chemistry and Physics of Metals and Alloys", *Wiley*, 1956.
- [84] J.M. An, W.E. Pickett, "Superconductivity of MgB_2 : Covalent bonds driven metallic", *Phys. Rev. Lett.* **86**, 4366, 2001.
- [85] J. Bardeen, L. N. Cooper, and J. R. Schrieffer, "Microscopic Theory of Superconductivity", *Phys. Rev.* **106**, 162- 64, 1957.
- [86] J. Bardeen, L. N. Cooper, and J. R. Schrieffer, "Theory of Superconductivity", *Phys. Rev.* **108**, 1175, 1957.
- [87] A.Y. Liu, I.I. Mazin, J. Kortus, "Beyond Eliashberg superconductivity in MgB_2 : Anharmonicity, two-phonon scattering and multiple gaps". *Phys. Rev. Lett.* **87**, 087005, 2001.
- [88] F. Guibileo, D. Roditchev, W. Sacks, R. Lamy, D.X. Thanh, J. Klein, S. Miraglia, D. Fruchart, J. Marcus, P.Monod, "Two-gap state density in MgB_2 : A true bulk property or a proximity effect?" *Phys. Rev. Lett.*, **87**, 177008, 2001.
- [89] H. Schmidt, J.F. Zasadzinski, K.E. Gray, D. G. Hinks, "Evidence for two-band superconductivity from break-junction tunneling on MgB_2 ", *Phys. Rev. Lett.* **88**, 127002, 2002.
- [90] P. Szabo, P.Samuely, J. Kacmarcik, T. Klein, J. Marcus, D. Fruchrt, S. Miraglia, C. Marcenat, A.G.M. Jansen, "Evidence for two superconducting energy gaps in MgB_2 by point-contact spectroscopy", *Phys. Rev. Lett.* **87**, 137005, 2001.
- [91] R.S. Gonnelli, D. Daghero, G.A. Ummarino, V.A. Stepanov, J.Jun, S. M. Kazakov, J. Karpinski, "Direct evidence for two-band superconductivity in MgB_2 single srystals from directional point-contact spectroscopy in magnetc fields", *Phys. Rev. Lett.*, **89**, 247004, 2002.
- [92] F. Bouquet, R.A. Fisher, N.E. Phillips, D.G. Hinks, J.D. Jorgsen, "Specific heat of MgB_2 : Evidence for a second energy gap", *Phys. Rev. Lett.*, **87**, 047001, 2001.
- [93] X. K. Chen, M. J. Konstantinović, J. C. Irwin, D. D. Lawrie, and J. P. Franck, "Evidence for Two Superconducting Gaps in MgB_2 ", *Phys. Rev. Lett.*, **87**, 157002, 2001.

Bibliography

- [94] D. Roditchev, F. Giubileo, F. Bobba, R. Lamy, E.M Choi, H.J. Kim, W.N. Kang, S.Miraglia, J. Marcus, W.Sacks, J. Klein, A. M. Cucolo, S.I. Lee, D. Fruchart, "Two-gap interplay in MgB_2 : a tunneling spectroscopy study", *Physica C: Superconductivity*, 408-410, **768**, 2004.
- [95] Z. Li, J. Yang, J. G. Hou, Q. Zhu, "First-principle study of MgB_2 (0001) surfaces", *Phys Rev, B*, **65**, 100507, 2002.
- [96] J. Kortus, I.I. Mazin, K.D. Belashchenko, V.P. Anropov, L. L. Boyer, "Superconductivity of metallic boron in MgB_2 ", *Phys. Rev. Lett.* **86**, 4656, 2001.
- [97] G. Satta, G. Profeta, F. Bernardini, A. Continenza, S. Massidda, "Electronic and structural properties of superconducting MgB_2 , CaSi_2 and related compounds", *Phys. Rev. B*, **64**, 104507, 2001.
- [98] E. R. Margine and F. Giustino, "Anisotropic Migdal-Eliashberg theory using Wannier functions", *Phys. Rev. B* **87**, 024505, 2013.
- [99] W.E. Pickett, J.M. An, H. Rosner, S.Y. Savrasov, "Role of two dimensionality in MgB_2 ", *Physica C* **387**, 117-121, 2003.
- [100] Pia Jensen Ray. Figure 2.4 in Master's thesis, "Structural investigation of $\text{La}_{(2-x)}\text{Sr}_{(x)}\text{CuO}_{(4+y)}$ - Following staging as a function of temperature". Niels Bohr Institute, Faculty of Science, University of Copenhagen. Copenhagen, Denmark
- [101] P.G. de Gennes "Superconductivity of Metals and Alloy" Westview Press, 1999
- [102] Onnes, H.K. "Further experiments with liquid helium. C. On the change of electric resistance of pure metals at very low temperatures etc. IV. The resistance of pure mercury at helium temperatures." *KNAW, Proceedings* 1911.
- [103] Onnes, H.K., "Communications from the Physical Laboratory of the University of Leiden Supplement" **34**, 64-71, 1913.
- [104] London, F. and H. London, "The Electromagnetic Equations of the Supraconductor" *Proceedings of the Royal Society of London. Series A, Mathematical and Physical Sciences*, **149**, 71-88, 1935.

Bibliography

- [105] Josephson, B.D., "Possible new effects in superconductive tunnelling", *Physics Letters*, **1**, 251-253, 1962.
- [106] Bednorz, J.G. and K.A. Müller, "Possible highTc superconductivity in the Ba–La–Cu–O system. *Zeitschrift für Physik B Condensed Matter*, **64**, 189-193, 1986.
- [107] Maeda, H., et al., "A new high-Tc oxide superconductor without a rare-earth element", *Japanese Journal of Applied Physics Part 2-Letters*, **27**, L209-L210, 1988.
- [108] Schilling, A., et al., "Superconductivity above 130 K in the Hg-Ba-Ca-Cu-O system", *Nature*, **363**, 56-58, 1993.
- [109] Hebard, A.F., "Superconductivity in doped Fullerenes", *Physics Today*, **45**, 26-32, 1992.
- [110] Hebard, A.F., "C₆₀: Buckminsterfullerene", *Annual Review of Materials Science*, **23**, 159-191, 1993.
- [111] Takahashi, H., et al., "Superconductivity at 43 K in an iron-based layered compound LaO_{1-x}F_xFeAs". *Nature*, **453**, 376-378, 2008.
- [112] A. P. Drozdov, M. I. Erements, I. A. Troyan, V. Ksenofontov and S. I. Shylin "Conventional superconductivity at 203 Kelvin at high pressures in the sulfur hydride system", *Nature*, **525**, 73-76, 2015.
- [113] H. Fröhlich, "Theory of the Superconducting State. I. The Ground State at the Absolute Zero of Temperature", *Phys. Rev.* **79**, 845, 1950.
- [114] J Bardeen, *Physics* **7**, 54, 1972.
- [115] J.R. Schrieffer, "Theory of Superconductivity" (Benjamin/Cummings, Don Mills, 1964.
- [116] J. Bardeen and D. Pinnes, "Electron-Phonon Interaction in Metals" *Phys. Rev.* **99**, 1140, 1955.
- [117] A.J. Leggett, *J. de Physique*, C7, 41, 19 (1980); A.J. Leggett, in "Modern Trends in the Theory of Condensed Matter", edited by S. Pekalski and J. Przys-tawa (Springer, Berlin, 1980)

Bibliography

- [118] P. Nozieres and S. Schmitt-Rink, *J. Low Temp. Phys.* **59**, 195 (1985).
- [119] J.C. Swihart, *IBM J. Research Develop.* **6** 14 (1962); *Phys. Rev.* **131** 73 (1963).
- [120] G. M. Eliashberg, *Zh. Eksperim. Teor. Fiz.* **38**, 966 (1960) [English transl.: *Soviet Phys. JETP* **11**, 696, 1960.
- [121] D. J. Scalapino, J. R. Schrieffer, and J. W. Wilkins, *Phys. Rev.* **148**, 263, 1966.
- [122] G. Eliashberg, "Temperature Green's function for electrons in a superconductor," *Sov. Phys JETP*, **12**, 1000, 1961.
- [123] A. Migdal, "Interaction between electrons and lattice vibrations in a normal metal," *Sov. Phys. JETP*, **7**, 6, 996-1001, 1958.
- [124] Y. Nambu, "Quasi-particles and gauge invariance in the theory of superconductivity," *Physical Review*, **117**, no. 3, p. 648, 1960
- [125] G. Ummarino, "Eliashberg Theory", *Chapter 13, Emergent Phenomena in Correlated Matter* edited by Eva Pavarini, Erik Koch, Ulrich Schollwöck, 2013.
- [126] W. Jones and N. H. March, "Theoretical solid state physics: Perfect lattices in equilibrium", vol. **1**, Courier Dover Publications, 1973.
- [127] V. Ambegaokar, "The Green's function method," *Parks RD*, New York, Marcel Dekker, pp. 259-319, 1969
- [128] T. Matsubara "A New Approach to Quantum-Statistical Mechanics", *Prog. Theor. Phys.*, **14**, 351, 1955.
- [129] P. B. Allen and B. Mitrovic, "Theory of superconducting T_c ," *Solid State Physics*, **37**, 1-92, 1983.
- [130] D. J. Scalapino, "The electron-phonon interaction and strong-coupling superconductors," *Superconductivity*, (RD Parks, ed.), **1**, 449-560, 1969.
- [131] J. Carbotte, "Properties of boson-exchange superconductors," *Reviews of Modern Physics*, **62**, 1027, 1990.
- [132] F. Marsiglio and J. Carbotte, "Electron-phonon superconductivity," *Superconductivity*, 73-162, Springer, 2008.

Bibliography

- [133] F. Marsiglio, "Eliashberg theory of the critical temperature and isotope effect. Dependence on bandwidth, band-filling, and direct Coulomb repulsion," *Journal of low temperature physics*, **87**, 659-682, 1992.
- [134] V. Kresin, H. Morawitz, and S. A. Wolf, "Mechanisms of conventional and high Tc superconductivity". *Oxford Univ. Press*, 1993.
- [135] P. B. Allen and R. Dynes, "Transition temperature of strong-coupled superconductors reanalysed," *Phys. Rev. B*, **12**, 905, 1975.
- [136] G.W. Webb, F. Marsiglio and J.E. Hirsch "Superconductivity in the elements, alloys and simple compounds," *Physica C*, **54**, 17, 2015.
- [137] Cardy J., *Scaling and Renormalization in Statistical Physics* (Cambridge: Cambridge University Press, 1996.
- [138] Rice T M "Superconductivity in one and two dimensions", *Phys. Rev.* **140**, A1889–91, 1965.
- [139] Hohenberg P C 1967 "Existence of long-range order in one and two dimensions", *Phys. Rev.* **158**, 383, 1967.
- [140] Likharev K K and Semenov V K "RSFQ logic/memory family: a new Josephson-junction technology for subterahertz- clock-frequency digital systems", *IEEE Trans. Appl. Supercond.* **1**, 3-28, 1991.
- [141] Yazdani A "Lean and mean superconductivity *Nat. Phys.*, **2**, 151, 2006.
- [142] Seidel P (ed) "Applied Superconductivity: Handbook on Devices and Applications" vol **2** (New York: Wiley) Ch. 9 & 10, 2015.
- [143] Shalnikov, A. "Superconducting thin films", *Nature*, **142**, 74 1938.
- [144] Buckel, W. & Hilsch, R. "Einfluss der Kondensation bei tiefen Temperaturen auf den elektrischen Widerstand und die Supraleitung für verschiedene Metalle". *Z. Phys.*, **138**, 109–120, (in German) (1954).
- [145] Hilsh, R. *Non-crystalline Solids* (ed. Frechette, V. D.) (Wiley, 1958).
- [146] Ginsberg, D. M. & Shier, J. S. *Basic Problems in Thin Films Physics* (eds Niedermayer, R. & Mayer, H.), 543, (Vandenhoeck and Ruprecht, 1966).

Bibliography

- [147] Strongin, M. & Kammerer, O. F. "Superconductive phenomena in ultrathin films", *J. Appl. Phys.* **39**, 2509–2514, 1968.
- [148] Mooij, J. E. in Percolation, *Localization and Superconductivity* (eds Goldman, A. M. & Wolf, S. A.), 325–370, (Plenum, 1984).
- [149] Guo, Y. et al. "Superconductivity modulated by quantum size effects". *Science*, **306**, 1915–1918, 2004.
- [150] Blatt, J. M. & Thompson, C. J. "Shape resonances in superconducting thin films". *Phys. Rev. Lett.*, **10**, 332–334, 1963.
- [151] Orr, B. G., Jaeger, H. M. & Goldman, A. M. "Transition temperature oscillations in thin superconducting films". *Phys. Rev. Lett.*, **53**, 2046–2049, 1984.
- [152] Aslamasov, L. G. & Larkin, A. I. "The influence of fluctuation pairing of electrons on the conductivity of normal metal". *Phys. Lett. A*, **26**, 238–239, 1968.
- [153] Maki, K. "The critical fluctuation of the order parameter in type-II superconductors". *Prog. Theor. Phys.*, **39**, 897–906, 1968.
- [154] Thompson, R. "Microwave, flux flow, and fluctuation resistance of dirty type-II superconductors". *Phys. Rev. B*, **1**, 327–333, 1970.
- [155] Berezinskii, V. L. "Destruction of long-range order in one-dimensional and two-dimensional systems having a continuous symmetry group. I. Classical systems". *Sov. Phys. JETP*, **32**, 493–500, 1971.
- [156] "Berezinskii, V. L. "Destruction of long-range order in one-dimensional and two-dimensional systems possessing a continuous symmetry group. II. Quantum systems". *Sov. Phys. JETP*, **34**, 610–616, 1972.
- [157] Kosterlitz, J. M. & Thouless, D. J. "Long range order and metastability in two dimensional solids and superfluids. (Application of dislocation theory)". *Sov. J. Phys. C Solid State Phys.*, **5**, 124–126, 1972.
- [158] Fisher, M. P. A. "Quantum phase transitions in disordered two-dimensional superconductors". *Phys. Rev. Lett.* **65**, 923–927, 1990.

Bibliography

- [159] Goldman, A. M. "Superconductor–insulator transitions", *Int. J. Mod. Phys. B* **24**, 4081–4101, 2010.
- [160] Anderson P.W., Edited by C.J. Gorter *Progress in Low Temp Phys*, **5**, 5, 1967.
- [161] Anderson P. W. "Theory of dirty superconductors", *J. Phys. Chem. Solids*, **11**, 26–30, 1959.
- [162] Strongin M, Thompson R S, Kammerer O F and Crow J E, "Destruction of superconductivity in disordered nearmonolayer films" *Phys. Rev. B*, **1**, 1078–91, 1970.
- [163] Tinkham M, "*Introduction to Superconductivity* (New York: McGraw-Hill), 1996.
- [164] Uchiashi T., "Two-dimensional superconductors with atomic-scale thickness", *Supercond. Sci. Technol.* **30**, 013022, 2017.
- [165] Reyren, N. et al. "Superconducting interfaces between insulating oxides". *Science*, **317**, 1196–1199, 2007.
- [166] Gozar, A. et al. "High-temperature interface superconductivity between metallic and insulating copper oxides". *Nature*, **455**, 782–785, 2008.
- [167] Gariglio, S. & Triscone, J. M. "Oxide interface superconductivity". *C. R. Phys.*, **12**, 591–599, 2011.
- [168] Gariglio, S., Gabay, M., Mannhart, J. & Triscone, J.-M. "Interface superconductivity". *Phys. C* **514**, 189–198, 2015.
- [169] Qin, S., Kim, J., Niu, Q. & Shih, C.-K. "Superconductivity at the two-dimensional limit", *Science*, **324**, 1314–1317, 2009.
- [170] Zhang, T. et al. "Superconductivity in one-atomic-layer metal films grown on Si(111)", *Nat. Phys.*, **6**, 104–108, 2010.
- [171] Cao, Y. et al. "Quality heterostructures from twodimensional crystals unstable in air by their assembly in inert atmosphere" *Nano Lett.*, **15**, 4914–4921, 2015.
- [172] Xi, X. et al. "Strongly enhanced charge-density-wave order in monolayer NbSe₂", *Nat. Nanotechnol.*, **10**, 765–769, 2015.

Bibliography

- [173] Ueno, K. et al. "Electric-field-induced superconductivity in an insulator", *Nat. Mater.*, **7**, 855–858, 2008.
- [174] Ye, J. T. et al. "Liquid-gated interface superconductivity on an atomically flat film", *Nat. Mater.*, **9**, 125–128, 2010.
- [175] Ueno, K. et al. "Field-induced superconductivity in electric double layer transistors", *J. Phys. Soc. Jpn*, **83**, 32001, 2014.
- [176] Xu, C. et al. "Large-area high-quality 2D ultrathin Mo₂C superconducting crystals", *Nat. Mater.*, **14**, 1135–1141, 2015.
- [177] Wang, L. et al. "Magnetotransport properties in high-quality ultrathin two-dimensional superconducting Mo₂C crystals", *ACS Nano* **10**, 4504–4510, 2016.
- [178] Xue M, Chen G, Yang H, Zhu Y, Wang D, He J and Cao T., "Superconductivity in potassium-doped few-layer graphene", *J. Am. Chem. Soc.* **134**, 6536–6539, 2012.
- [179] Ichinokura, S., Sugawara, K., Takayama, A., Takahashi, T. & Hasegawa, S. "Superconducting calcium intercalated bilayer graphene", *ACS Nano*, **10**, 2761–2765, 2016.
- [180] W.E. Pickett, "The next breakthrough in phonon-mediated superconductivity", *Physica C*, **468**, 126, 2008.
- [181] Ohtomo, A. & Hwang, H. Y. "A high-mobility electron gas at the LaAlO₃/SrTiO₃" . *Nature*, **427**, 423–426, 2004.
- [182] Caviglia, A. D. et al., "Electric field control of the LaAlO₃/ SrTiO₃ interface ground state", *Nature*, **456**, 624–627, 2008.
- [183] He, Q. L. et al. "Two-dimensional superconductivity at the interface of a Bi₂Te₃ /FeTe heterostructure". *Nat. Commun.* **5**, 4247, 2014.
- [184] Lee, J. J. et al. "Interfacial mode coupling as the origin of the enhancement of T_c in FeSe films on SrTiO₃", *Nature*, **515**, 245–248, 2014.
- [185] He, S. et al. "Phase diagram and electronic indication of high-temperature superconductivity at 65 K in single layer FeSe films", *Nat. Mater.*, **12**, 605–61, 2013.

Bibliography

- [186] Tan, S. et al. "Interface-induced superconductivity and strain-dependent spin density waves in FeSe/SrTiO₃ thin films." *Nat. Mater.*, **12**, 634–640, 2013.
- [187] Shen, S. et al. "Observation of quantum Griffiths singularity and ferromagnetism at superconducting LaAlO₃/SrTiO₃(110) interface", *Phys. Rev. B*, **94**, 144517, 2016.
- [188] M. L. Kulić and O.V. Dolgov, "The electron-phonon interaction with forward scattering peak is dominant in high T_c superconductors of FeSe films on SrTiO₃(TiO₂)", *New J. Phys.*, **19**, 013020, 2017.
- [189] Q. Fan, W. H. Zhang, X. Liu, Y. J. Yan, M. Q. Ren, R. Peng, H. C. Xu, B. P. Xie, J. P. Hu, T. Zhang & D. L. Feng "Plain s-wave superconductivity in single-layer FeSe on SrTiO₃ probed by scanning tunnelling microscopy", *Nature Physics*, **11**, 946–952, 2015.
- [190] S. Coh, M. L. Cohen and S. G. Louie, "Large electron-phonon interactions from FeSe phonons in a monolayer", *New Journal of Physics*, **17**, 073027, 2015.
- [191] Ziqiao Wang et al, "High-temperature superconductivity in one-unit-cell FeSe films", *Journal of Physics: Condensed Matter*, **29**, 153001, 2017.
- [192] Jiang, D. et al. "High-T_c superconductivity in ultrathin Bi₂Sr₂CaCu₂O_{8+x} down to half-unit-cell thickness by protection with graphene". *Nat. Commun.*, **5**, 5708, 2014.
- [193] Dean, C. R. et al. "Boron nitride substrates for high-quality graphene electronics", *Nat. Nanotechnol.* **5**, 722–726, 2010.
- [194] Yu Saito, Tsutomu Nojima and Yoshihiro Iwasa, "Highly crystalline 2D superconductors", *Nature Reviews Materials*, **2**, 16094, 2016.
- [195] Ueno, K. et al. "Discovery of superconductivity in KTaO₃ by electrostatic carrier doping", *Nat. Nanotechnol.*, **6**, 408–412, 2011.
- [196] Tiwari A P, Shin S, Hwang E, Jung S-G, Park T and Lee H, "Superconductivity at 7.4 K in few layer graphene by Li-intercalation" *arXiv: 1508.06360*, 2015.
- [197] Reyren, N. et al. "Superconducting interfaces between insulating oxides", *Science*, **317**, 1196–1199, 2007.

Bibliography

- [198] Li K et al., "Superconductivity in Ca-intercalated epitaxial graphene on silicon carbide", *Appl. Phys. Lett.*, **103**, 062601, 2013.
- [199] Chapman J, Su Y, Howard C A, Kundys D, Grigorenko A N, Guinea F, Geim A K, Grigorieva I V and Nair R R, "Superconductivity in Ca-doped graphene laminates", *Sci. Rep.*, **6**, 23254, 2016.
- [200] H. Rosner, A. Kitaigorodsky, and W. E. Pickett, "Prediction of High Tc Superconductivity in Hole-doped LiBC" *Phys. Rev. Lett.* **88**, 127001, 2002.
- [201] J. M. An, S. Y. Savrasov, H. Rosner, and W. E. Pickett, "Extreme Electron-Phonon Coupling in Boron-based Layered Superconductors", *Phys. Rev. B* **66**, 220502, 2002.
- [202] A. Lazicki, C. S. Yoo, H. Cynn, W. J. Evans, W. E. Pickett, J. Olamit, K. Liu, and Y. Ohishi, "Search for superconductivity in LiBC at high pressure: Diamond anvil cell experiments and first-principles calculations", *Phys. Rev. B*, **75**, 054507, 2007.
- [203] W. Pickett, "Superconductivity: 2D Physics, Unknown Mechanisms, Current Puzzles, Emergent Phenomena in Correlated Matter: Autumn School Organized by the Forschungszentrum Jülich and the German Research School for Simulation Sciences at Forschungszentrum Jülich 23-27 September 2013" ; *Lecture Notes of the Autumn School Correlated Electrons*, 2013.
- [204] Thomas, L. H., "The calculation of atomic fields," *Proc. Cambridge Phil. Soc.*, **23**, 542548, 1927.
- [205] Hohenberg, P. and Kohn, W., "Inhomogeneous electron gas", *Phys. Rev.*, **136**, 864870, 1964.
- [206] Kohn, W. and Sham, L. J., "Self-consistent equations including exchange and correlation effects", *Phys. Rev.* **140**, pp. 11331138, 1965.
- [207] F. Giustino "Materials Modelling Using Density Functional Theory: Properties and Predictions" *Oxford University Press*, 2014.
- [208] Kohn, W., "Nobel Lecture: Electronic structure of matter wave functions and density functionals," *Reviews of Modern Physics*, **71**, 12531266, 1999.

Bibliography

- [209] John P. Perdew, Adrienn Ruzsinszky, Jianmin Tao, Viktor N. Staroverov, Gustavo E. Scuseria et al, "Prescription for the design and selection of density functional approximations: More constraint satisfaction with fewer fits", *J. Chem. Phys.* **123**, 062201, 2005.
- [210] U. von Barth and L. Hedin, "A local exchange-correlation potential for the spin polarized case", *J. of Phys. C: Solid State Physics* **5**, 1629, 1972.
- [211] J. P. Perdew, "Density-functional approximation for the correlation energy of the inhomogeneous electron gas," *Phys. Rev. B*, **33**, 8822, 1986.
- [212] J. P. Perdew and Y. Wang, "Accurate and simple analytic representation of the electron-gas correlation energy," *Phys. Rev. B*, **45**, 13244, 1992.
- [213] Dirac, P. A. M. "Note on exchange phenomena in the Thomas-Fermi atom". *Proc. Cambridge Phil. Roy. Soc.*, **26**, 376385, 1930.
- [214] D. R. Hartree, "The Wave Mechanics of an Atom with a Non-Coulomb Central Field. Part I. Theory and Methods", *Proc. Cam. Phil. Soc.*, **24**, 89, 1928.
- [215] J.C. Slater, "A simplification of the hartree-fock method", *Phys.Rev.*, **81**, 385390, 1951.
- [216] D. M. Ceperley and B. J. Alder "Ground State of the Electron Gas by a Stochastic Method". *Phys. Rev. Lett.* **45**, 566569, 1980.
- [217] J. P. Perdew and A. Zunger "Self-interaction correction to density-functional approximations for many-electron systems". *Phys. Rev. B*. **23**, 5048, 1981.
- [218] J. P. Perdew, K. Burke, and M. Ernzerhof, "Generalized gradient approximation made simple," *Phys. Rev. Lett.*, **77**, 3865, 1996.
- [219] A. Zupan, J. P. Perdew, K. Burke, and M. Ernzerhof, "Distributions and averages of electron density parameters: Explaining the effects of gradient corrections" *J. Chem. Phys*, **106**, 184, 1997.
- [220] J. P. Perdew, A. Ruzsinszky, G. I. Csonka, O. A. Vydrov, G. E. Scuseria, L. A. Constantin, X. Zhou, and K. Burke, "Restoring the density-gradient expansion for exchange in solids and surfaces," *Physical Review Letters*, **100**, 136406, 2008.

Bibliography

- [221] J. P. Perdew K. Burke and Y. Wang "Generalized gradient approximation for the exchange-correlation hole of a many-electron system". *Phys. Rev. B* **54**, 23, 1996.
- [222] D. R. Hamann, M. Schluter and C. Chiang. "Norm-conserving pseudopotentials", *Phys. Rev. Lett.*, **43**, 1494, 1979.
- [223] D. Vanderbilt. "Soft self-consistent pseudopotentials in a generalized eigenvalue formalism", *Phys. Rev. Lett.*, **41**, 7892, 1990.
- [224] W.E. Pickett. "Pseudopotential methods in condensed matter applications", *Comp. Phys. Rep.*, **9**, 115, 1989.
- [225] Stefano Baroni, Stefano de Gironcoli, Andrea Dal Corso, and Paolo Giannozzi. "Phonons and related crystal properties from density-functional perturbation theory", *Rev. of Mod. Phys.*, **73**, 515, 2001.
- [226] M. Born and R. Oppenheimer. "Zur Quantentheorie der Molekeln" *Ann. D. Phys.*, **84**, 457, 1927.
- [227] S. Baroni, P. Giannozzi and A. Testa, "Greens-function approach to linear response in solids", *Phys. Rev. Lett.* **58**, 1861, 1987.
- [228] X. Gonze, "Adiabatic density-functional perturbation theory", *Phys. Rev. A* **52**, 1086, 1995.
- [229] Hellmann, "H Einfhrgung in die Quantenchemie". Leipzig: Franz Deuticke. **285**, 1937.
- [230] Feynman, R. P. "Forces in Molecules". *Phys. Rev.* **56**, 340, 1939.
- [231] P. D. DeCicco, F. A. Johnson, "The Quantum Theory of Lattice Dynamics. IV", *Proc. R. Soc. Lond. A* 1969, **310**, 111-119, 1969.
- [232] Robert M. Pick, Morrel H. Cohen, and Richard M. Martin, "Microscopic Theory of Force Constants in the Adiabatic Approximation", *Phys. Rev. B* **1**, 910, 1970.
- [233] Paolo Giannozzi, Stefano Baroni, Nicola Bonini, Matteo Calandra, Roberto Car, Carlo Cavazzoni, Davide Ceresoli, Guido L Chiarotti, Matteo Cococcioni, Ismaila Dabo, Andrea Dal Corso, Stefano de Gironcoli, Stefano Fabris, Guido

Bibliography

- Fratesi, Ralph Gebauer, Uwe Gerstmann, Christos Gougoussis, Anton Kokalj, Michele Lazzeri, Layla Martin-Samos, Nicola Marzari, Francesco Mauri, Riccardo Mazzarello, Stefano Paolini, Alfredo Pasquarello, Lorenzo Paulatto, Carlo Sbraccia, Sandro Scandolo, Gabriele Sclauszero, Ari P Seitsonen, Alexander Smogunov, Paolo Umari, and Renata M Wentzcovitch. "QUANTUM ESPRESSO: a modular and open-source software project for quantum simulations of materials". *Journal of Physics: Condensed Matter*, **21**, 395502, 2009.
- [234] H. J. Monkhorst and J. D. Pack, "Special points for Brillouin-zone integration", *Phys. Rev. B*, 13, 5188, 1979.
- [235] A. Kokalj, "Computer graphics and graphical user interfaces as tools in simulations of matter at the atomic scale", *Comp. Mater. Sci.*, 28, 155168, 2003.
- [236] "Atomistix ToolKit version 2016.0, QuantumWise A/S" (www.quantumwise.com)
- [237] M. Wierzbowska, S. de Gironcoli and P. Giannozzi "Origins of low and high pressure discontinuities of Tc in niobium" *Arxiv condmat* **0504077**, 2005.
- [238] L. Genovese, A. Neelov, S. Goedecker, T. Deutsch, S. A. Ghasemi, A. Willand, D. Caliste, O. Zilberberg, M. Rayson, A. Bergman, R. Schneider, "Daubechies wavelets as a basis set for density functional pseudopotential calculations", *Journal of Chemical Physics*, **129**, 014109, 2008.
- [239] S. Mohr, L. E. Ratcliff, P. Boulanger, L. Genovese, D. Caliste, T. Deutsch, and S. Goedecker, "Daubechies wavelets for linear scaling density functional theory", *Journal of Chemical Physics*, **140**, 204110, 2014.
- [240] I. Daubechies, "Ten Lectures on Wavelets", *SIAM*, **194**, 1992.
- [241] L. Genovese, M. Ospici, T. Deutsch, J.-F. Mhaut, A. Neelov, S. Goedecker, "Density Functional Theory calculation on many-cores hybrid CPU-GPU architectures in hybrid architecture", *Journal of Chemical Physics*, **131**, 034103, 2009.
- [242] Pešić J., Damljanić V., Gajić R., Hingerl K. and Belić M., "Density functional theory study of phonons in graphene doped with Li, Ca and Ba" *Europhys. Lett.*, **112**, 67006, 2015.

Bibliography

- [243] . Pešić J. , Gajić R., Hingerl K. and Belić M., "Strain-enhanced superconductivity in Li-doped graphene", *Europhys. Lett.*, **108**, 67005, 2014.
- [244] Pešić J. and Gajić R., "Ab-initio study of the optical properties of the Li-intercalated graphene and MoS₂", *Opt Quant Electron*, **48**, 368, 2016.
- [245] Pešić J., and R. Gajić. "Advantages of GPU technology in DFT calculations of intercalated graphene" *Phys. Scr.*, **T162**, 014027, 2014.
- [246] Pešić J., Popov I., Damjanović V., Gajić R., Hingerl K. and Belić M., "Ab-Initio Study of Superconductivity in Magnesium-Diboride Monolayer, *in press*, 2017.
- [247] Pešić J. and Gajić R., "GPU accelerations in DFT codes in 2D-materials research" *in press*, 2017.
- [248] P. Schaffautl, *J. Prakt. Chem.*, **21**, 155, 1861.
- [249] N. B. Hannay, T.H. Geballe, B. T. Matthias, K. Andres, P. Schmidt, and D. MacNair, "Superconductivity in Graphitic Compounds" *Phys. Rev. Lett.*, **14**, 225, 1965.
- [250] I. T. Belash, O.V. Zharikov, and A.V. Palnichenko, "Synthesis, stability and structure of GIC with Li, Na, K" *Synth. Met.*, **34**, 455 1990.
- [251] Weller, T. E., Ellerby, M., Saxena, S. S., Smith, R. P. and Skipper, N. T., "Superconductivity in the intercalated graphite compounds C₆Yb and C₆Ca" *Nature Phys.*, **1**, 39 2005.
- [252] R. A. Jishi and M. S. Dresselhaus, "Superconductivity in graphite intercalation compounds" *Phys. Rev. B* **45**, **12**, 465, 1992.
- [253] M. Calandra and F. Mauri, "Possibility of superconductivity in graphite intercalated with alkaline earths investigated with density functional theory", *Phys.Rev. B*, **74**, 094507, 2006.
- [254] Boeri, L. et al. "Electron-phonon interaction in graphite intercalation compounds". *Phys. Rev. B*, **76**, 064510, 2007.
- [255] K. Nakada and A. Ishii, "DFT Calculation for Adatom Adsorption on Graphene", *Graphene Simulation*, Prof. Jian Gong Ed., 2011.

Bibliography

- [256] Chacn-Torres J. C., Wirtz L. and Pichler T., "Manifestation of charged and strained graphene layers in the Raman response of graphite intercalation compounds", *Phys. Status Solidi. B*, **251**, 2337, 2014.
- [257] Kaloni T. P., Balatsky A. V. and Schwingenschlgl U., "Substrate enhanced superconductivity in Li-decorated graphene" *Europhys. Lett.*, **104**, 47013, 2013.
- [258] Fedorov A. V., Verbitskiy N. I., Haberer D., Struzzi C., Petaccia L., Usachov D., Vilkov O. Y., Vyalikh D. V., Fink J., Knupfer M., Bchner B. and Gruneis A., "Observation of a universal donor-dependent vibrational mode in graphene", *Nat. Commun.*, **5**, 3257 2014.
- [259] Koufos A. P. and Papaconstantopoulos D. A., "First-principles study of the electronic structure of iron-selenium: Implications for electron-phonon superconductivity" *Phys. Rev. B*, **89**, 035150, 2014.
- [260] Perdew J. P. and Zunger Alex, "Self-interaction correction to density-functional approximations for many-electron systems" *Phys. Rev. B*, **23**, 5048, 1981.
- [261] Kanetani K., Sugawara K., Sato T., Shimizu R., Iwaya K., Hitosugi T. and Takahashi T., "Ca intercalated bilayer graphene as a thinnest limit of superconducting C_6Ca " *Proc. Natl. Acad. Sci. U.S.A.*, **109**, 19610, 2012.
- [262] Milošević I., Nikolić B., Damnjanović M. and Krčmar M., "Irreducible representations of diperiodic groups" *J. Phys. A: Math. Gen.*, **31**, 3625, 1988.
- [263] Wood A., "The 80 Diperiodic Groups In Three Dimensions", *Bell Syst. Tech. J.*, **43**, 541, 1964.
- [264] Altmann S. L. and Herzig P., "Point-Group Theory Tables" *Clarendon Press, Oxford; Oxford University Press, New York*, 1994.
- [265] Damljanić V., Kostić R. and Gajić R., "M-point phonon eigenvectors of graphene obtained by group projectors" *Rom. Rep. Phys.*, **65**, 193, 2013.
- [266] Mapelli C., Castiglioni C., Zerbi G. and Mllen K., "Common force field for graphite and polycyclic aromatic hydrocarbons" *Phys. Rev. B*, **60**, 12710, 1999.
- [267] Sugawara K., Kanetani K., Sato T. and Takahashi T., "Fabrication of Li-intercalated bilayer graphene" *AIP Adv.*, **1**, 022103, 2011.

Bibliography

- [268] Virojanadara C., Watcharinyanon S., Zakharov A. A. and Johansson L. I., "Epitaxial graphene on 6H-SiC and Li intercalation" *Phys. Rev. B*, **82**, 205402, 2010.
- [269] Kumar A., Leela A., Reddy M., Mukherjee A., Dubey M., Zhan X., Singh N., Ci L., Billups W. E., Nagurny J., Mital g. and Ajayan P. M., "Direct synthesis of lithium-intercalated graphene for electrochemical energy storage application." *ACS Nano*, **5**, 4345, 2011.
- [270] Mohr M., Maultzsch J., Dobardžic E., Reich S., Milošević I., Damnjanovic M., Bosak A., Krisch M. and Thomsen C., "Phonon dispersion of graphite by inelastic x-ray scattering" *Phys. Rev. B*, **76**, 035439, 2007.
- [271] Marco Saitta A., Lazzeri M., Calandra M. and Mauri F., "Giant non-adiabatic effects in layer metals: Raman spectra of intercalated graphite explained" *Phys. Rev. Lett.*, **100**, 226401, 2008.
- [272] Poulet H. and Mathieu J. P., "Vibration Spectra and Symmetry of Crystals" *Gordon and Breach, New York, London, Paris*, 1976.
- [273] Szczniak D., Durajski A. P. and Szczniak R., "Influence of lithium doping on the thermodynamic properties of graphene based superconductors" *J. Phys.: Condens. Matter*, **26**, 255701, 2014.
- [274] C. Si, Z. Sun, and F. Liu, "Strain engineering of graphene: a review" *Nanoscale*, **8**, 3207, 2016.
- [275] Guzman D. M., Alyahyaei H. M. and Jishi R. A., "Superconductivity in graphene-lithium" *2D Mater.*, **1**, 021005, 2014.
- [276] Ni Z. H., Yu T., Lu Y. H., Wang Y. Y., Feng Y. P. and Shen Z. X., "Uniaxial strain on graphene: Raman spectroscopy study and band-gap opening", *ACS Nano*, **11**, 2301, 2008.
- [277] Huang M., Yan H., Chen C., Song D., Heinz T. F. and Hone J., "Phonon softening and crystallographic orientation of strained graphene studied by Raman spectroscopy" *Proc. Natl. Acad. Sci. U.S.A.*, **106**, 7304, 2009.
- [278] Pereira V. M., Castro Neto A. H. and Peres N. M. R., "A tight-binding approach to uniaxial strain in graphene" *Phys. Rev. B*, **80**, 045401, 2009.

Bibliography

- [279] Ding F., Ji H., Chen Y., Herklotz A., Dorr K., Mei Y., Rastelli A. and Schmidt O. G., "Stretchable graphene: a close look at fundamental parameters through biaxial straining" *Nano Lett.*, **10**, 3453, 2010.
- [280] T. M. G. Mohiuddin, A. Lombardo, R. R. Nair, A. Bonetti, G. Savini, R. Jalil, N. Bonini, D. M. Basko, C. Galiotis, N. Marzari, K. S. Novoselov, A. K. Geim, and A. C. Ferrari, "Uniaxial strain in graphene by Raman spectroscopy: G peak splitting, Grneisen parameters, and sample orientation" *Phys. Rev. B*, **79**, 205433, 2009.
- [281] Levy N., Burke S. A., Meaker K., Panlasigui M. L., Zettl A., Guinea F., Neto A. H. C. and Crommie M. F., "Strain-induced pseudo-magnetic fields greater than 300 Tesla in graphene nanobubbles", *Science*, **329**, 544 2010.
- [282] Guinea F., Katsnelson M. I. and Geim A. K., "Energy gaps and a zero-field quantum Hall effect in graphene by strain engineering", *Nat. Phys.*, **6**, 30 2009.
- [283] Teague M. L., Lai A. P., Velasco J., Hughes C. R., Beyer A. D., Bockrath M. W., Lau C. N. and Yeh N.-C., "Evidence for strain-induced local conductance modulations in single-layer graphene on SiO₂", *Nano Lett.*, **9**, 2542, 2009.
- [284] Huang M., Pascal T. A., Kim H., Goddard W. A. and Greer J. R., "Electronic-mechanical coupling in graphene from in situ nanoindentation experiments and multiscale atomistic simulations", *Nano Lett.*, **11**, 1241, 2011.
- [285] Fu X.-W., Liao Z.-M., Zhou J. X., Zhou Y.-B., Wu H.-C., Zhang R., Jing G., Xu J., Wu X., Guo W. and Yu D., "Strain dependent resistance in chemical vapor deposition grown graphene" *Appl. Phys. Lett.*, **99**, 213107, 2011.
- [286] Zhou S. Y. et al., "Substrate-induced bandgap opening in epitaxial graphene", *Nat. Mater.*, **6**, 770, 2007.
- [287] Xiao d., Yao w. and Niu Q., "Valley-Contrasting Physics in Graphene: Magnetic Moment and Topological Transport" *Phys. Rev. Lett.*, **99**, 236809, 2007.
- [288] Gui G., Li J. and Zhong J., "Band structure engineering of graphene by strain: First-principles calculations" *Phys. Rev. B*, **78**, 075435, 2008.
- [289] Marianetti C. A. and Yevick H. G., "Failure mechanisms of graphene under tension" *Phys. Rev. Lett.*, **105**, 245502, 2010.

Bibliography

- [290] Kotliar G. et al., "Electronic structure calculations with dynamical mean-field theory", *Rev. Mod. Phys.*, **78**, 865, 2006.
- [291] Lazzeri M., Attaccalite C., Wirtz L. and Mauri F., "Impact of the electron-electron correlation on phonon dispersion: Failure of LDA and GGA DFT functionals in graphene and graphite" *Phys. Rev. B*, **78**, 081406, 2008.
- [292] Borysenko K. M., Mullen J. T., Barry E. A., Paul S., Semenov Y. G., Zayada J. M., Nardelli M. B. and Kim K. W., "First-principles analysis of electron-phonon interactions in graphene" *Phys. Rev. B*, **81**, 121412R, 2010.
- [293] Matković A., Beltaos A., Milićević M., Ralević U., Vasić B., Jovanović Dj. and Gajić R., "Influence of transfer residue on the optical properties of chemical vapor deposited graphene investigated through spectroscopic ellipsometry" *J. Appl. Phys.*, **112**, 123523, 2012.
- [294] Silva Neto E. H., Aynajian P., Frano A., Comin R., Schierle E., Weschke E., Gyenis A., Wen J., Schneeloch J., Xu Z., Ono S., Gu G., Le Tacon M. and Yazdani A., "Ubiquitous Interplay Between Charge Ordering and High-Temperature Superconductivity in Cuprates" *Science*, **343**, 6169, 2014 .
- [295] Comin R., Frano A., Yee M. M., Yoshida Y., Eisaki H., Schierle E., Weschke E., Sutarto R., He F., Soumyanarayanan A., He Yang, Le Tacon M., Elfimov I. S., Hoffman J. E., Sawatzky G. A., Keimer B. and Damascelli A., "Charge order driven by Fermi-arc instability in Bi2201" *Science*, **343**, 6169, 2014.
- [296] Chang J., Blackburn E., Holmes A. T., Christensen N. B., Larsen J., Mesot J., Liang R., Bonn D. A., Hardy W. N., Watenphul A., Zimmermann M. v., Forgan E. M. and Hayden S. M., "Direct observation of competition between superconductivity and charge density wave order in $\text{YBa}_2\text{Cu}_3\text{O}_y$ " *Nat. Phys.*, **8**, 871, 2012 .
- [297] Roy B. and Sau D. J., "Competing charge-density-wave, magnetic and topological ground states at and near Dirac points in graphene in axial magnetic fields" *Phys. Rev. B*, **90**, 075427, 2014.
- [298] Kotov N. V., Uchoa B., Pereira M. V., Guinea F. and Castro Neto A. H., "Electron-Electron Interactions in Graphene: Current Status and Perspectives" *Rev. Mod. Phys.*, **84**, 1067, 2012.

Bibliography

- [299] Khevshchenko D. V., "Ghost excitonic insulator transition in layered graphite", *Phys. Rev. Lett.*, **87**, 246802, 2001.
- [300] Toke C. and Falko V. I., "Charge-density-wave states in double-layer graphene structures at a high magnetic field", *Phys. Rev. B*, **90**, 035404, 2014.
- [301] Rahnejat K. C., Howard C. A., Shuttleworth N. , Schofield S. R., Iwaya K., Hirjibehedin C., Renner Ch., Aeppli G. and Ellerby M., "Charge density waves in the graphene sheets of the superconductor CaC_6 " *Nat. Commun.*, **2**, 558, 2011.
- [302] Hennig, G.R., "Optical transmission of graphite compounds". *J. Chem. Phys.* **43**, 1201-1206, 1965.
- [303] Efetov, D.K., Kim, P. "Controlling electron-phonon interactions in graphene at ultrahigh carrier densities". *Phys. Rev. Lett.* **105**, 256805-256809, 2010.
- [304] Khrapach, I., Withers, F., Bointon, T.H., Polyushkin, D.K., Barnes, W.L., Russo, S., Craciun, M.F.: "Novel highly conductive and transparent graphene-based conductors". *Adv. Mat.*, **24**, 2844-2849, 2012.
- [305] Kim, K.S., Zhao, Y., Jang, H., Lee, S.Y., Kim, J.M., Kim, K.S., Ahn, J.-H., Kim, P., Choi, J.-Y., Hong, B.H.: "Large-scale pattern growth of graphene films for stretchable transparent electrodes". *Nature*, **457**, 706-710, 2009.
- [306] Wang, F., Zhang, Y., Tian, C., Girit, C., Zettl, A., Crommie, M., Shen, Y.R.: "Gate-variable optical transitions in graphene". *Science*, **320**, 206-209, 2008.
- [307] Bao, W., Wan, J., Han, X., Cai, Xi, Zhu, H., Kim, D., Ma, D., Xu, Y., Munday, J.N., Drew, H.D., Fuhrer, M. Hu, L.: "Approaching the limits of transparency and conductivity in graphitic materials through lithium intercalation". *Nat. Commun.*, **5**, 4224, 2014.
- [308] Liu, Y., Ren, L., He, Y., Cheng, H.P.: "Titanium-decorated graphene for high-capacity hydrogen storage studied by density functional simulations". *J. Phys. Condens. Matter* **22**, 445301, 2010.
- [309] Sivek, J., Leenaerts, O., Partoens, B., Petters, F.M., "Adsorption of Titanium and Titanium Dioxide on Graphene: n and p-type doping". *arXiv:1301.3654 [cond-mat.mtrl-sci]*, 2013.

Bibliography

- [310] Mak, K.F., Lee, C., Hone, J., Shan, J., Heinz, T.F.: "Atomically thin MoS₂: a new direct-gap semiconductor". *Phys. Rev. Lett.* **105**, 136805, 2010.
- [311] Krack, M. "Pseudopotentials for H to Kr optimized for gradient-corrected exchange-correlation functionals", *Theor. Chem. Acc.* **114**, 145-152, 2005.
- [312] Brenner, N.E., "Random-phase-approximation dielectric function for diamond, with local field effects included", *Phys. Rev. B* **12**, 1487-1492, 1975.
- [313] Kumar, A., Ahluwalia, P.K., "A first principle comparative study of electronic and optical properties of 1H- MoS₂ and 2H-MoS₂", *Mater. Chem. Phys.* **135**, 755-761, 2012.
- [314] Li, W., Birdwell, A.G., Amani, M., Burke, R.A., Ling, X., Lee, Y.-H., Liang, X., Peng, L., Richter, C.A., Kong, J., Gundlach, D.J., Nguyen, N.V., "Broad-band optical properties of large-area monolayer CVD molybdenum disulfide", *Phys. Rev. B*, **90**, 195434, 2014.
- [315] Marinopoulos, A.G., Reining, L., Rubio, A., Olevano, V., "Ab initio study of the optical absorption and wave-vector-dependent dielectric response of graphite", *Phys. Rev. B*, **69**, 245419, 2004.
- [316] Isić, G., Jakovljević, M., Filipović, M., Jovanović, Dj, Vasić, B., Lazović, S., Puač, Nevena, Lj Petrović, Z., Kostić, R., Gajić, R., Humlcek, J., Losurdo, M., Bruno, G., Bergmair, I., Hingerl, K., "Spectroscopic ellipsometry of few-layer graphene", *J. Nanophoton.*, **5**, 051809, 2011.
- [317] Kostić, R., Mirić, M., Radić, T., Radović, M., Gajić, R., Popović, Z.V. "Optical characterization of graphene and highly oriented pyrolytic graphite", *Acta Phys. Pol. A*, **116**, 718-721, 2009.
- [318] Sedelnikova, O.V., Bulusheva, L.G., Okotrub, A.V. "Ab initio study of dielectric response of rippled graphene", *J. Chem. Phys.*, **134**, 244707, 2011.
- [319] Trevisanutto, P.E., Holzmann, M., Ct, M., Olevano, V. "Ab initio high-energy excitonic effects in graphite and graphene", *Phys. Rev. B*, **81**, 121405, 2010.
- [320] Bulusheva, L.G., Sedelnikova, O.V., Okotrub, A.V. "Many-body effects in optical response of graphene- based structures", *Int. J. Quantum Chem.*, **116**, 270-281, 2016.

Bibliography

- [321] Chen, N.-X., Rabii, S. "Theoretical investigation of the optical spectra of LiC_6 ", *Phys. Rev. B*, **31**, 4784-4791, 1985.
- [322] Rani, P., Dubey, G.S., Jindal, V.K.: "DFT study of optical properties of pure and doped graphene", *Phys. E* **62**, 28-35, 2014.
- [323] Eklund, P.C., Yang, M.H., Doll, G.L., Dresselhaus, M.S. "Optical Properties of Donor-Type Graphite Intercalation Compounds-Intercalation in Layered Materials", 257-270. Springer, Boston, 1986.
- [324] Nagamatsu, J., Nakagawa, N., Muranaka, T., Zenitani, Y. and Akimitsu, "Superconductivity at 39 K in magnesium diboride", *J., Nature*, **410**, 63, 2001.
- [325] Kong Y., Dolgov O.V., Jepsen O. and Andersen O.K., "Electron-phonon interaction in the normal and superconducting states of MgB_2 " *Phys. Rev. B*, **64**, 020501, 2001.
- [326] Bohnen K.-P., Heid R. and Renker B., "Phonon Dispersion and Electron-Phonon Coupling in MgB_2 and AlB_2 " *Phys. Rev. Lett.*, **86**, 5771, 2001.
- [327] Kunc. K, Loa I., Syassen K., Kremer R.K. and Ahn K., "MgB₂ under pressure: phonon calculations, Raman spectroscopy, and optical reflectance" *J.Phys. Condens. Matter*, **13**, 9945, 2001.
- [328] Choi H.J., Roundy D., Sun H., Cohen M.L. and Louie S. G., "First-principles calculation of the superconducting transition in MgB_2 within the anisotropic Eliashberg formalism" *Phys. Rev. B*, **66**, 020513(R), 2002.
- [329] V. V. Moshchalkov and J. Fritzsche, *Nanostructured Superconductor*, 2011.
- [330] E. Babaev, J. Carlstrom, M. Silaev, J.M. Speight, "Type-1.5 superconductivity in multicomponent systems", *Physica C*, **533**, 15, 2017.
- [331] M. Zehetmayer, "A review of two-band superconductivity: materials and effects on the thermodynamic and reversible mixed-state properties" *Supercond. Sci. Technol.*, **6**, 043001, 2013.
- [332] Canfield P.C., Crabtree G. W., "Magnesium Diboride: Better Late than Never" *Phys. Today*, **56**, 34, 2003.

Bibliography

- [333] Hyoungh Joon Choi, David Roundy, Hong Sun, Marvin L. Cohen, Steven and G. Louie, "The origin of the anomalous superconducting properties of MgB_2 " *Nature*, **418**, 758, 2002.
- [334] I. I. Mazin, V.P. Antropov, "Electronic structure, electronphonon coupling, and multiband effects in MgB_2 " *Physica C: Superconductivity*, **385**, 49, 2003.
- [335] Yildirim T., Gulseren O., Lynn J.W., Brown C.M., Udovic T.J., Huang Q., Rogado N., Regan K.A., Hayward M.A., Slutsky J.S., Haas M.K., Khalifah P., Inumaru K. and Cava R.J., "Giant anharmonicity and nonlinear electron-phonon coupling in MgB_2 : a combined first-principles calculation and neutron scattering study." *Phys. Rev. Lett.*, **87**, 3, 2001.
- [336] Tupitsyn I. I., "Structure and Density of States of Light-Metal Diborides." *Sov. Phys. Solid State*, **18**, 1688, 1976.
- [337] Armstrong D.R., Perkins P.G., "Electronic band structure of magnesium diboride" *J. Chem. Soc., Faraday Trans. II*, **75**, 12, 1979.
- [338] De la Pena-Seaman O., de Cross R., Heid R. and Bohnen K.-P., "Effects of Al and C doping on the electronic structure and phonon renormalization in MgB_2 " *Phys. Rev. B*, **79**, 134523, 2009.
- [339] Kortus J., "Current progress in the theoretical understanding of MgB_2 " *Phys. C*, **456**, 54, 2007.
- [340] Sighn P.P., "From E_{2g} to Other Modes: Effects of Pressure on Electron-Phonon Interaction in MgB_2 " *Phys. Rev. Lett.*, **97**, 247002, 2006.
- [341] R. Arita, K. Kuroki, and H. Aoki, "Spin-fluctuation exchange study of superconductivity in two- and three-dimensional single-band Hubbard models" *Phys. Rev. B*, **60**, 14585, 1999.
- [342] R. Arita, K. Kuroki, and H. Aoki, "Magnetic-field induced triplet superconductivity in the Hubbard model on a triangular lattice" *J. Phys. Soc. Jpn.*, **69**, 1181, 2000.
- [343] Morshedloo T., Roknabadi M.R. and Behdani M., "First-principles study of the superconductivity in MgB_2 bulk and in its bilayer thin film based on electronphonon coupling" *Physica C*, **509**, 1, 2015.

Bibliography

- [344] Ponce S., E.R. Margine, Verdi C. and Giustino F., "EPW: Electron-phonon coupling, transport and superconducting properties using maximally localized Wannier functions" *Comp. Phys. Commun.*, **209**, 116, 2016.
- [345] J.M. Soler, E. Artacho, J.D. Gale, A. Garcia, J. Junquera, P. Ordejón, and D. Sanchez-Portal, "The SIESTA method for ab initio order-N materials simulation" *J. Phys. Condens. Matter*, **14**, 2745, 2002.
- [346] N. Troullier and J.L. Martins, "Efficient pseudopotentials for plane-wave calculations" *Phys. Rev. B*, **43**, 1991 .
- [347] S. Nose, "A unified formulation of the constant temperature molecular dynamics methods" *J. Chem.Phys.*, **81**, 511, 1984.
- [348] F.A. Lindemann, "A unified formulation of the constant temperature molecular dynamics methods" *Phys. Z.*, **11**, 609, 1910.
- [349] V. Damjanović and R. Gajić, "Existence of Dirac cones in the Brillouin zone of diperiodic atomic crystals according to group theory" *J. of Phys.: Condens. Matter.*, **28**, 085502, 2016.
- [350] V. Damjanović and R. Gajić, " Addendum to: Existence of Dirac cones in the Brillouin zone of diperiodic atomic crystals according to group theory" *J. of Phys.: Condens. Matter.*, **28**, 439401, 2016.
- [351] A. Q. R. Baron, H. Uchiyama, Y. Tanaka, S. Tsutsui, D. Ishikawa, S. Lee, R. Heid, K.-P. Bohnen, S. Tajima, and T. Ishikawa, "Kohn Anomaly in MgB₂ by Inelastic X-Ray Scattering" *Phys. Rev. Lett.*, **92**, 197004, 2004.
- [352] Bingyun a., Zhengjun z., Tao T. and Yiping Z., "Potential enhancement of superconductivity in MgB₂ nanosheets: First-principles calculations" *Chem. Phys. Let.*, **591**, 185, 2014.
- [353] C. Zhang, Y. Wang, D. Wang, Y. Zhang, Z.-H. Liu, Q.-R. Feng, and Z.-Z. Gan, "Suppression of superconductivity in epitaxial MgB₂ ultrathin films", *J. of App. Phys.*, **114**, 023903, 2013.
- [354] M. A. Wolak, N. Acharya, D. P. Cunnane, B. S. Karasik, and X. X. Xi, "Fabrication and Characterization of Ultrathin MgB₂ Films for Hot-Electron Bolometer Applications" *APL Materials*, **4**, 086114, 2016.

Bibliography

- [355] A. Romero-Bermudez and A. M. Garca-Garca, "Shape resonances and shell effects in thin-film multiband superconductors" *Phys. Rev. B*, **89**, 024510, 2014.
- [356] A. Romero-Bermudez and A. M. Garca-Garca, "Size effects in superconducting thin films coupled to a substrate" *Phys. Rev. B*, **89**, 064508, 2014.
- [357] D. Valentinis, D. van der Marel, and C. Berthod, "BCS superconductivity near the band edge: Exact results for one and several bands" *Phys. Rev. B*, **94**, 054516, 2016.
- [358] K. Szalowski, "Critical temperature of MgB₂ ultrathin superconducting films: BCS model calculations in the tight-binding approximation" *Phys. Rev. B*, **74**, 094501, 2006.
- [359] A.V. Narlikar, "Small Superconductors: Introduction in The Oxford Handbook of Small Superconductors", *First Edition*. Edited by A.V. Narlikar, 2017.
- [360] S. Gariglio, M. Scheurer, J. Schmalian, A.M.R.V.L. Monteiro, S. Goswami, and A. Caviglia, "Surface and Interface Superconductivity in The Oxford Handbook of Small Superconductors", *First Edition*. Edited by A.V. Narlikar, 2017.
- [361] MPI: A Message-Passing Interface Standard Version 3.0, Message Passing Interface Forum, September 21, 2012. Available from: <http://www.mpi-forum.org> Accessed: 04.06.2017.
- [362] The OpenMP API Specification for Parallel Programming. Available from: <http://openmp.org/wp/openmp-specifications/> Accessed: 04.06.2017.
- [363] "Tesla gpu accelerators" Available at: <http://www.nvidia.com/object/tesla-servers.html> Accessed: 02.06.2017.
- [364] "Electronic Structure Calculations on Graphics Processing Units: From Quantum Chemistry to Condensed Matter Physics" edited by Ross C. Walker, Andreas W. Goetz (2016).
- [365] J. Owens, M. Houston, D. Luebke, S. Green, J. Stone, and J. Phillips, "GPU computing," *Proceedings of the IEEE* **96**, 5, 879–899, 2008.
- [366] A. Harju, T. Siro, F. Canova, S. Hakala, T. Rantalaiho, Computational physics on graphics processing units, in: P. Manninen, P. Aster (Eds.), Applied "Parallel

Bibliography

- and Scientific Computing”, Vol. 7782 of Lecture Notes in Computer Science, Springer Berlin Heidelberg, 2013, pp. 3–26.
- [367] Nvidia Corporation (2017) ”What is GPU Computing?”. Available from: <http://www.nvidia.com/object/what-is-gpu-computing.html> Accessed: 02.06.2017.
- [368] G.M. Amdahl ”Validity of Single-Processor Approach to Achieving Large-Scale Computing Capability”. Proceedings of AFIPS Conference, Reston (VA) 483485, 1967.
- [369] J.L. Gustafson, ”Reevaluating Amdahls law.” Communications of the ACM 31, 5, 532533, 1988.
- [370] I. Girotto, N. Varini, F. Spiga, C. Cavazzoni, D. Ceresoli, L. Martin-Samos, T. Gorni, Enabling of quantum espresso to petascale scientific challenges, PRACE.
- [371] F. Spigga, I.Girotto, Phigemm: A cpu-gpu library for porting quantum espresso on hybrid systems, 16th Euromicro Conference on Parallel, Distributed and Network-Based Processing.
- [372] Quantum Chemistry GPU Benchmarking Report April 2017 Available from:<http://images.nvidia.com/content/tesla/pdf/Quantum-Chemistry-April-2017-MB-slides.pdf> Accessed: 02.06.2017.
- [373] S. Goedecker, M. Teter, J. Hutter, Separable dual-space gaussian pseudopotentials, Phys. Rev. B 54, 1703–1710, 1996.
- [374] C. Hartwigsen, S. Goedecker, J. Hutter, ”Relativistic separable dual-space gaussian pseudopotentials from H to Rn”, Phys. Rev. B 58, 3641–3662, 1998.
- [375] X. Gonze, et al., Abinit: First-principles approach to material and nanosystem properties, Computer Physics Communications 180, 2582, 2009.
- [376] <http://nvidianews.nvidia.com/news/nvidia-launches-revolutionary-volta-gpu-platform-fueling-next-era-of-ai-and-high-performance-computing> Accessed: 01.06.2017.
- [377] K. S. Novoselov, V. I. Falko, L. Colombo, P. R. Gellert, M. G. Schwab, and K. Kim, A roadmap for graphene *Nature*, 490, 192200, 2012.

Bibliography

- [378] C. Hurlbut, and C. S. Klein, "*Manual of mineralogy*", 20th ed., Wiley New York, 1985.
- [379] G.H. Lee et al, "High-strength chemical-vapor-deposited graphene and grain boundaries" *Science*, **340**, 1073-6, 2013.
- [380] Kw.-S. Kim, H.-J. Lee, C. Lee, S.-K. Lee, H. Jang, J.-H. Ahn, J.-H. Kim, and H.-J. Lee, "Chemical vapor deposition-grown graphene: the thinnest solid lubricant", *ACS Nano*, **5**, 510714, 2011.
- [381] D. Berman, A. Erdemir and A. V. Sumant, "Graphene: a new emerging lubricant *Mater. Today*, 17, 31-42, 2014.
- [382] A. Klemenz, L. Pastewka, S. G. Balakrishna, A. Caron, R. Bennewitz, and M. Moseler, "Atomic scale mechanisms of friction reduction and wear protection by graphene" *Nano Lett.* **14**, 714552, 2014.
- [383] T. Filleter, J. L. McChesney, A. Bostwick, E. Rotenberg, K. V. Emtsev, Th. Seyller, K. Horn, and R. Bennewitz, "Friction and dissipation in epitaxial graphene films" *Phys. Rev. Lett.*, **102**, 086102, 2009.
- [384] C. Lee, Q. Li, W. Kalb, X.-Z. Liu, H. Berger, R. W. Carpick and J. Hone, "Frictional characteristics of atomically thin sheets" *Science*, **328**, 7680, 2010
- [385] H. Lee, N. Lee, Y. Seo, J. Eom and S. Lee, "Comparison of frictional forces on graphene and graphite" *Nanotechnology*, **20**, 325701, 2009.
- [386] D. Berma, A. Erdemir and A. V. Sumant, "Few layer graphene to reduce wear and friction on sliding steel surfaces" *Carbon*, **54** 454-9 2013.
- [387] L. Y. Lin, D.-E. Kim, W-K. Kim and S.-C. Jun, "Friction and wear characteristics of multi-layer graphene films investigated by atomic force microscopy" *Surf. Coat. Tech.*, **205**, 48649, 2011.
- [388] N.T. Kirkland, T. Schiller, N. Medhekar and N. Birbilis, "Exploring graphene as a corrosion protection barrier" *Corros. Sci.*, **56**, 14, 2012.
- [389] R. Kempaiah, S. Salgado, W. L. Chung and V. Maheshwari, "Graphene as membrane for encapsulation of yeast cells: protective and electrically conducting" *Chem. Commun.*, **47**, 114802, 2011.

Bibliography

- [390] N. Mohanty, M. Fahrenholtz, A. Nagaraja, D. Boyle, and V. Berry, "Impermeable graphenic encasement of bacteria" *Nano Lett.*, **11**, 12705, 2011.
- [391] K. Xu, P. Cao and J. R. Heath, "Graphene visualizes the first water adlayers on mica at ambient conditions" *Science*, **329**, 118891, 2010
- [392] P. Cao, K. Xu, J. O. Varghese and J. R. Heath, "The microscopic structure of adsorbed water on hydrophobic surfaces under ambient conditions" *Nano Lett.*, **11**, 55816, 2011.
- [393] P. Cao, J. O. Varghese, K. Xu, and J. R. Heath, "Visualizing local doping effects of individual water clusters on gold(111)- supported graphene" *Nano Lett.*, **12**, 145963, 2012.
- [394] J. Shim, C. H. Lui, T. Y. Ko, Y.-J. Yu, P. Kim, T. F. Heinz, and S. Ryu, "Water-gated charge doping of graphene induced by mica substrates" *Nano Lett.*, **12**, 64854, 2012.
- [395] N. Severin, P. Lange, I. M. Sokolov, and J. P. Rabe, "Reversible dewetting of a molecularly thin fluid water film in a soft graphene-mica slit pore" *Nano Lett.*, **12**, 7749, 2012.
- [396] K. T. He, J. D. Wood, G. P. Doidge, E. Pop, and J. W. Lyding, "Scanning tunneling microscopy study and nanomanipulation of graphene coated water on mica" *Nano Lett.*, **12**, 266572, 2012.
- [397] H. Komurasaki, T. Tsukamoto, K. Yamazaki, and T. Ogino, "Layered structures of interfacial water and their effects on Raman spectra in graphene-on-sapphire systems" *J. Phys. Chem. C*, **116**, 100849, 2012.
- [398] Mi. J. Lee, J. S. Choi, J.-S. Kim et al., "Characteristics and effects of diffused water between graphene and a SiO₂ substrate" *Nano Res.*, **5**, 7107, 2012.
- [399] Q. Li, J. Song, F. Besenbacher and M. Dong, "Two-dimensional material confined water" *Acc. Chem. Res.*, **48**, 11927, 2015 .
- [400] J. Song, Q. Li, X. Wang, J. Li, S. Zhang, J. Kjems, F. Besenbacher and M. Dong, "Evidence of Stranski-Krastanov growth at the initial stage of atmospheric water condensation" *Nat. Commun.*, **5**, 4837, 2014.

Bibliography

- [401] P. Lange, M. Dorn, N. Severin, Da. A. Va. Bout and J. P. Rabe, "Single- and double-layer graphenes as ultrabarriers for fluorescent polymer films" *J. Phys. Chem. C*, **115**, 2305761, 2011 .
- [402] N. Severin, M. Dorn, A. Kalachev, and J. P. Rabe, "Replication of single macromolecules with graphene" *Nano Lett.*, **11**, 24369, 2011.
- [403] Y. Moon, J. Shin, S. Seo, J. Park, S. R. Dugasani, S. H. Woo, T. Park, S. H. Park and J. R. Ahn, "Nanoscale topographical replication of graphene architecture by artificial DNA nanostructures" *Appl. Phys. Lett.*, **104**, 231904, 2014 .
- [404] A. Matković, "Investigating the optical properties of graphene with spectroscopic ellipsometry", *PhD Thesis*, 2015
- [405] D. Han, S. Pal, J. Nangreave, Z. Deng, Y. Liu and H. Yan, "DNA origami with complex curvatures in three-dimensional space" *Science*, **332**, 3426, 2011.
- [406] Y. Ke, L. L. Ong, W. M. Shih and P. Yin, "Three-dimensional structures self-assembled from DNA bricks" *Science*, **338**, 117783, 2012 .
- [407] B. Wei, M. Dai and P. Yin, "Complex shapes self-assembled from single-stranded DNA tiles" *Nature*, **485**, 6236, 2012 .
- [408] I. Bald and A. Keller, "Molecular processes studied at a single-molecule level using DNA origami nanostructures and atomic force microscopy" *Molecules*, **19**, 1380323, 2014.
- [409] H. Li, S. H. Park, J. H. Reif, T. H. LaBean and H. Yan, "DNA-templated self-assembly of protein and nanoparticle linear arrays" *J. Am. Chem. Soc.*, **126**, 4189, 2004.
- [410] Y. Geng, J. Liu, E. Pound, S. Gyawali, J. N. Harb and A. T. Woolley, "Rapid metallization of lambda DNA and DNA origami using a Pd seeding method" *J. Mater. Chem.*, **21**, 1212631, 2011.
- [411] R. Schreiber, S. Kempter, S. Holler, V. Schller, D. Schiffels, S. S. Simmel, P. C. Nickels and T. Liedl, "DNA origami-templated growth of arbitrarily shaped metal nanoparticles" *Small* **7**, 17959, 2011.

Bibliography

- [412] J. B. Knudsen et al, "Routing of individual polymers in designed patterns" *Nat. Nanotechnol.*, **10**, 8928, 2015.
- [413] J. Prinz, B. Schreiber, L. Olejko, J. Oertel, J. Rackwitz, A. Keller, and I. Bald, "DNA origami substrates for highly sensitive surfaceenhanced Raman scattering" *J. Phys. Chem. Lett.*, **4**, 41405, 2013.
- [414] H. A. Becerril and A. T. Woolley, "DNA shadow nanolithography" *Small*, **3**, 15348, 2007.
- [415] Z. Deng and C. Mao, "Molecular lithography with DNA nanostructures" *Angew. Chem. Int. Ed.*, **43**, 406870, 2004.
- [416] S. P. Surwade, S. Zhao and H. Liu, "Molecular lithography through DNA-mediated etching and masking of SiO₂" *J. Am. Chem. Soc.*, **133**, 1186871, 2011.
- [417] S. P. Surwade, F. Zhou, B. Wei, W. Sun, A. Powell, C. O'Donnell, P. Yin, and H. Liu, "Nanoscale growth and patterning of inorganic oxides using DNA nanostructure templates" *J. Am. Chem. Soc.*, **135**, 677881, 2013.
- [418] Z. Jin, W. Sun, Y. Ke, C-J. Shih, G. L. C.Paulus, Q. H. Wang, B. Mu, P. Yin and M. S. Strano, "Metallized DNA nanolithography for encoding and transferring spatial information for graphene patterning" *Nat. Commun.*, **4**, 1663, 2013.
- [419] G. Zhang, S. P. Surwade, F. Zhou and H. Liu, "DNA nanostructure meets nanofabrication" *Chem. Soc. Rev.*, **42**, 248896, 2013.
- [420] J. Liu, Y. Geng, E. Pound, S. Gyawali, J. R. Ashton, J. Hickey, A. T. Woolley, and J. N. Harb, "Metallization of branched DNA origami for nanoelectronic circuit fabrication" *ACS Nano*, **5**, 22407, 2011.
- [421] H. Kim, S. P. Surwade, A. Powell, C. O'Donnell, and H. Liu, "Stability of DNA origami nanostructure under diverse chemical environments" *Chem. Mater.*, **26**, 526573, 2014.
- [422] P. Blake, E. W. Hill, A. H. Castro Neto, K. S. Novoselov, D. Jiang, R. Yang, T. J. Booth, and A. K. Gaim, "Making graphene visible", *Appl. Phys. Lett.*, **97**, 231901–231904, 2007.

Bibliography

- [423] A. Matković, B. Vasić, J. Pešić, J. Prinz, I. Bald, A. R. Milosavljević, R. Gajić, "Enhanced structural stability of DNA origami nanostructures by graphene encapsulation" *New Journal of Physics*, **18**, 2, 025016, 2016.
- [424] J. Prinz, A. Matković, J. Pešić, R. Gajić, I. Bald, "Hybrid Structures for Surface-Enhanced Raman Scattering: DNA Origami/Gold Nanoparticle Dimer/-Graphene" *Small* **12**, 39, 5458-5467, 2016.
- [425] A. Matković, Institute of Physics, University of Belgrade, Serbia, "Micromechanical Exfoliation procedure". *Image published on* <http://www.graphene.ac.rs>, 2015.
- [426] J. Vujin, Institute of Physics, University of Belgrade, Serbia, "UV Photolithographic Au contacts on monolayer graphene", *Unpublished material*, 2017.
- [427] Koichi Momma and Fujio Izumi, "VESTA3 for three-dimensional visualization of crystal, volumetric and morphology data" *J. of App. Crys.*, **44**, 12721276, 2011.
- [428] Official Quantum Espresso support forum: http://qe-forge.org/pipermail/pw_forum/2015-August/107595.html Accessed: 20.6.2017.

A. APPENDIX

A.1. Graphene

A.1.1. Tight-Binding Model

Derivations of the nearest neighbor hopping Hamiltonian components $H_{AB}(\vec{k})$ and $H_{BA}(\vec{k})$, and the detailed derivation of the dispersion relation for graphene are presented in this section. The Hamiltonian $H_{AB}(\vec{k})$ addresses nearest neighbor hopping from B site to three neighboring A sites: A, A' and A''

We start with the equation:

$$H_{AB}(\vec{k}) = \int \phi_A^*(\vec{r} - \vec{r}_A) \hat{H} \phi_B(\vec{r} - \vec{r}_B) d\vec{r} = t_{AB} \cdot \exp(i \vec{k} (\vec{r}_A - \vec{r}_B)) \quad (\text{A.1})$$

If we consider only nearest neighbors:

$$H_{AB}(\vec{k}) = t_{AB} \sum_{A^i=A, A', A''} \exp(i(k_x \hat{x} + k_y \hat{y})(\vec{r}_B - \vec{r}_{A^i})) \quad (\text{A.2})$$

We assign an appropriate coordinates for the atomic sites and by doing this we define the exact atomic positions, assigning the symmetry of a hexagonal structure. If the center of a (\hat{x}, \hat{y}) coordinating system is placed at the site A (Fig A. 1)), then all atomic site coordinates are:

$$\begin{aligned} A &= (0, 0) \\ B &= (\frac{a}{\sqrt{3}}, 0), \\ A' &= (\frac{a\sqrt{3}}{2}, \frac{a}{2}) \\ A'' &= (\frac{a\sqrt{3}}{2}, -\frac{a}{2}) \end{aligned} \quad (\text{A.3})$$

Using this coordinates, we rewrite nearest neighbor Hamiltonian and sum it to obtain:

A. APPENDIX

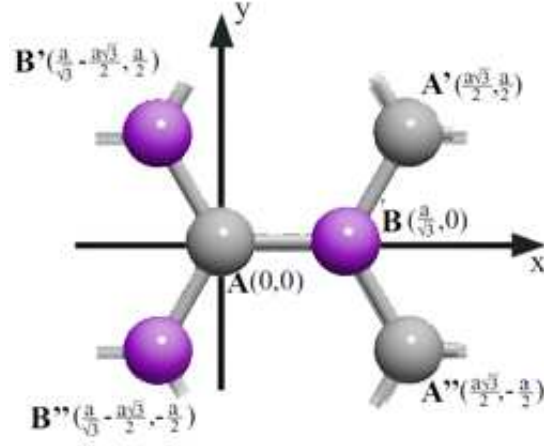


Figure A.1.: A (gray) and B (violet) atomic sites and nearest neighbor sites. The a stands for a length of a unit vector, and relates to carbon-carbon distance as: $a = a_0\sqrt{3}$

$$H_{AB}(\vec{k}) = t_{AB} \cdot [e^{i(k_x\hat{x}+k_y\hat{y})\frac{a}{\sqrt{3}}\hat{x}} + e^{i(\frac{a}{\sqrt{3}}\hat{x}-\frac{a\sqrt{3}}{2}\hat{x}-\frac{a}{2}\hat{y})k_x\hat{x}+k_y\hat{y}+e^{i(k_x\hat{x}+k_y\hat{y})(\frac{a}{\sqrt{3}}\hat{x}-\frac{a\sqrt{3}}{2}\hat{x}+\frac{a}{2}\hat{y})}], \quad (\text{A.4})$$

$$H_{AB}(\vec{k}) = t_{AB} \cdot [e^{i(\frac{k_x a}{\sqrt{3}})} + e^{i(\frac{k_x a}{\sqrt{3}} - \frac{k_x a \sqrt{3}}{2} - \frac{k_y a}{2})} + e^{i(\frac{k_x a}{\sqrt{3}} - \frac{k_x a \sqrt{3}}{2} + \frac{k_y a}{2})}], \quad (\text{A.5})$$

$$H_{AB}(\vec{k}) = t_{AB} \cdot [e^{i\frac{k_x a}{\sqrt{3}}} + e^{i\frac{k_x a}{\sqrt{3}}} e^{-i\frac{k_x a \sqrt{3}}{2}} e^{-i\frac{k_y a}{2}} + e^{i\frac{k_x a}{\sqrt{3}}} e^{-i\frac{k_x a \sqrt{3}}{2}} e^{i\frac{k_y a}{2}}], \quad (\text{A.6})$$

$$H_{AB}(\vec{k}) = t_{AB} e^{i\frac{k_x a}{\sqrt{3}}} [1 + e^{-i\frac{k_x a \sqrt{3}}{2}} (e^{-i\frac{k_y a}{2}} + e^{i\frac{k_y a}{2}})], \quad (\text{A.7})$$

$$H_{AB}(\vec{k}) = t_{AB} e^{i\frac{k_x a}{\sqrt{3}}} [1 + e^{-i\frac{k_x a \sqrt{3}}{2}} \cos \frac{k_y a}{2}] \quad (\text{A.8})$$

The same procedure is repeated for $H_{BA}(\vec{k})$, which corresponds for nearest neighbor hopping from A site to three neighboring B, B' and B'' sites.

$$B' = (\frac{a}{\sqrt{3}} - \frac{a\sqrt{3}}{2}, \frac{a}{2})$$

$$B'' = (\frac{a}{\sqrt{3}} - \frac{a\sqrt{3}}{2}, -\frac{a}{2}),$$

that gives:

$$H_{BA}(\vec{k}) = t_{BA} e^{-i\frac{k_x a}{\sqrt{3}}} [1 + e^{+i\frac{k_x a \sqrt{3}}{2}} \cos \frac{k_y a}{2}]. \quad (\text{A.9})$$

A. APPENDIX

Combining the H_{AB} and H_{BA} to equation (1.8) we get:

$$\Delta_k = \begin{pmatrix} 0 & t^* e^{i\frac{k_x a}{\sqrt{3}}} (1 + 2e^{(\frac{-i\sqrt{3}}{2}k_x a)} \cos \frac{k_y a}{2}) \\ t e^{-i\frac{k_x a}{\sqrt{3}}} (1 + 2e^{(\frac{i\sqrt{3}}{2}k_x a)} \cos \frac{k_y a}{2}) & 0 \end{pmatrix} = \begin{pmatrix} 0 & \Delta_k \\ \Delta_k^* & 0 \end{pmatrix} \quad (\text{A.10})$$

The eigenvalues are:

$$E(k) = \pm \sqrt{tt^* \cdot e^{(\frac{\pm i\sqrt{3}}{2}k_x a)} e^{(\frac{\mp i\sqrt{3}}{2}k_x a)} \cdot (1 + 2e^{(\frac{-i\sqrt{3}}{2}k_x a)} \cos \frac{k_y a}{2}) \cdot (1 + 2e^{(\frac{\pm i\sqrt{3}}{2}k_x a)} \cos \frac{k_y a}{2})} \quad (\text{A.11})$$

$$E(k) = \pm t \sqrt{(1 + 2e^{(\frac{-i\sqrt{3}}{2}k_x a)} \cos \frac{k_y a}{2}) \cdot (1 + 2e^{(\frac{\pm i\sqrt{3}}{2}k_x a)} \cos \frac{k_y a}{2})} \quad (\text{A.12})$$

To make it simpler to handle we define:

$$\begin{aligned} \frac{\sqrt{3}}{2} k_x a &= \phi \\ \cos \frac{k_y a}{2} &= C, \end{aligned}$$

$$\begin{aligned} E(k) &= \pm t \sqrt{(1 + 2e^{-i\phi} C)(1 + 2e^{+i\phi} C)} \\ &= \pm t \sqrt{1 + 4C^2 + 2C(e^{i\phi} + e^{-i\phi})}, \\ &= \pm t \sqrt{1 + 4C^2 + 2C \cos \phi} \end{aligned} \quad (\text{A.13})$$

Finally, if we return back from ϕ and C , to \vec{k} , the dispersion relation of graphene is obtained:

$$E(k) = \pm t \sqrt{1 + 4 \cos^2 \frac{k_y a}{2} + 2 \cos \frac{k_y a}{2} \cos \frac{\sqrt{3} k_x a}{2}} \quad (\text{A.14})$$

A.2. Superconductivity

A.2.1. Eliashberg Equations

Nambu [124] demonstrated how the formalism used for normal state can be rewritten in such a way that the diagrams used for normal state can be applicable also to the superconductive state. The inclusion of Coulomb interaction causes the electron-phonon interaction to be screened and this causes a significant reduction. Although there is a strong electron-phonon coupling, and phonons' correction to the electron-phonon vertex are small. Moreover, the Coulombic correction is not necessarily small, but constant factors, so they can be included in the coupling constant. In the Nambu formalism, a 2-component spinor for the electron and a bare-phonon field operator are defined as:

$$\psi_k = \begin{pmatrix} c_{k\uparrow} \\ c_{-k\downarrow}^\dagger \end{pmatrix} \quad \psi_k^\dagger = \begin{pmatrix} c_{k\uparrow}^\dagger & c_{-k\downarrow} \end{pmatrix} \quad (\text{A.15})$$

$$\varphi_{q\nu} = b_{q\nu} + b_{-q\nu}^\dagger \quad (\text{A.16})$$

The Hamiltonian of an electron-phonon interacting system can be written in terms of ψ and ϕ , including the Coulomb interactions [126]:

$$H = \sum_k \varepsilon_k \psi_k^\dagger \sigma_3 \psi_k + \sum_{q\lambda} \Omega_{q\lambda} b_{q\lambda}^\dagger b_{q\lambda} \sum_{k,k',\lambda} g_{kk'\lambda} \varphi_{k-k'\lambda} \psi_{k'}^\dagger \sigma_3 \psi_k + \frac{1}{2} \sum_{k_1 k_2 k_3 k_4} \langle k_3 k_4 | V_C | k_1 k_2 \rangle \left(\psi_{k_3}^\dagger \sigma_3 \psi_{k_1} \right) \left(\psi_{k_4}^\dagger \sigma_3 \psi_{k_2} \right) \quad (\text{A.17})$$

where ε_k is the one-electron Bloch energy relative to Fermi energy E_F , σ_3 is a Pauli matrix, Ω is the bare phonon energy of wavevector \mathbf{q} and mode ν , $g_{k,k',\nu}$ are electron-phonon matrix elements and V_C is the Coulomb potential. Translational invariance of V_C restrict $k_1+k_2-k_3-k_4$ to be either zero or a reciprocal lattice vector \mathbf{K} . (The electrons are described in an extended zone scheme and phonons are described in a reduced zone scheme which is extended periodically through \mathbf{q} -space) In order to apply the perturbation method to superconductors, the possibility of the existence of Cooper pairs has to be included and this is done by taking anomalous propagators. Green function becomes [127]:

$$\widehat{G}(k, \tau) = -\langle T \{ \psi_k(\tau) \psi_k^\dagger(0) \} \rangle \widehat{D}(q, \tau) = -\langle T \{ \varphi_{q\lambda}(\tau) \varphi_k^\dagger(0) \} \rangle \quad (\text{A.18})$$

A. APPENDIX

Where the average is over the grand canonical ensemble ($\beta=1/T$, T is the temperature)

$$\langle Q \rangle = \frac{\text{Tr} e^{-\beta H} Q}{\text{Tr} e^{-\beta H}} \quad (\text{A.19})$$

where the operators develop with imaginary time and T represents the usual time-ordered product. As the matrix operator $\psi_k(\tau)\psi_k^\dagger(0)$ does not conserve the number of particles, the definition of a new operator U that adjusts the number of particles is necessary:

$$U=1+R^\dagger+R$$

where R converts a given state in an N -particle system into the corresponding state in $N+2$ particle system.

The Green function for electrons is a 2×2 matrix, the diagonal elements are the conventional Green functions for spin-up electrons and spin-down holes, while G_{12} and G_{21} describe the pairing properties. We have:

$$\hat{G}(k, \tau) = - \begin{pmatrix} \langle T \{ c_{k\uparrow}(\tau) c_{k\uparrow}^\dagger(0) \} \rangle & \langle UT \{ c_{k\uparrow}(\tau) c_{-k\downarrow}(0) \} \rangle \\ \langle UT \{ c_{-k\downarrow}^\dagger(\tau) c_{k\uparrow}^\dagger(0) \} \rangle & \langle T \{ c_{-k\downarrow}^\dagger(\tau) c_{-k\uparrow}(0) \} \rangle \end{pmatrix} \quad (\text{A.20})$$

The diagonal elements are the "normal" propagators, while off-diagonal elements are Gor'kov's F and F bar, respectively [101].

The phonon and the electron Green function could be expanded in a Fourier series

$$D_\lambda(q, \tau) = \frac{1}{\beta} \sum_{n=-\infty}^{\infty} e^{i\nu_n \tau} D_\lambda(q, i\nu_n) G(k, \tau) = \frac{1}{\beta} \sum_{n=-\infty}^{\infty} e^{i\omega_n \tau} G(k, i\omega_n) \quad (\text{A.21})$$

where

$$\nu = 2n\pi/\beta \quad , \quad \omega_n = (2n+1)\pi/\beta \quad (\text{A.22})$$

ν_n and ω_n are the Matsubara frequencies [128] and n is an integer. The Matsubara frequencies are odd multiplies of π/β for fermions while for bosons they are even. The Midgal-Eliashberg theory [98, 129, 130, 131, 132, 133, 134] is based on the propagators. In momentum and the imaginary frequencies space, the one-electron Green function for the non-interacting system is given by:

$$\hat{G}_0(k, i\omega_n) = [i\omega_n \mathbb{I} - \varepsilon_k \sigma_3]^{-1} \quad (\text{A.23})$$

A. APPENDIX

And for phonons

$$D_0(q, i\nu_n) = [M [\omega^2(q) + \nu_n^2]]^{-1} \quad (\text{A.24})$$

Where M is the ion mass and $\omega(\mathbf{q})$ is the phonon dispersion. For the electron and phonon, the Green functions can be written:

$$\left[\widehat{G}(k, i\omega_n)\right]^{-1} = \left[\widehat{G}_0(k, i\omega_n)\right]^{-1} - \widehat{\Sigma}(k, i\omega_n) \left[\widehat{D}(q, i\nu_n)\right] = \left[\widehat{D}_0(q, i\nu_n) - \widehat{\Pi}(q, i\nu_n)\right]^{-1} \quad (\text{A.25})$$

where Σ is the electron self-energy and Π the bosonic one. The Migdal's approximation sets the vertex values equal to the bare vertex, and the electron-phonon interaction is truncated at order $\sqrt{\frac{m}{M}} \sim \frac{\omega_D}{E_F}$. We began from Hamiltonian, then the Coulomb interaction can be included and discussion can be generalized to a temperature different from zero obtaining:

$$\begin{aligned} \widehat{\Sigma}(k, i\omega_n) = & -\frac{1}{\beta} \sum_{k', n'} \sigma_3 G(k', i\omega_{n'}) \sigma_3 \\ & \times \left[\sum_{\nu} |g_{k, k', \nu}|^2 D_{\nu}(k - k', i\omega_n - i\omega_{n'}) + V_C(k - k') \right] \end{aligned} \quad (\text{A.26})$$

where $V_C(k-k')$ is screened Coulomb potential which depends only on the momentum transfer $k-k'$. Since σ are Pauli matrices, this equation consists of actually four coupled equations, one per each component of matrix Σ . If we use the linear combination of the Pauli matrices, we can rewrite it as:

$$\widehat{\Sigma}(k, i\omega_n) = i\omega_n [1 - Z(k, i\omega_n)\mathbb{I}] + \chi(k, i\omega_n)\sigma_3 + \phi(k, i\omega_n)\sigma_1 + \bar{\phi}(k, i\omega_n)\sigma_2 \quad (\text{A.27})$$

We can solve Σ by using the Green function. But before that, we transform it using the Dyson equation, and it becomes:

$$\left[\widehat{G}(k, i\omega_n)\right]^{-1} = i\omega_n Z\mathbb{I} - (\varepsilon_k + \chi)\sigma_3 - \phi\sigma_1 - \bar{\phi}\sigma_2 \quad (\text{A.28})$$

There is always a solution for $\phi = \bar{\phi} = 0$, and it corresponds to the normal state. For non-zero ϕ or $\bar{\phi}$, the solution has lower free energy and describes a state with Cooper-pairs condensation. After the matrix inversion we have:

A. APPENDIX

$$\begin{aligned}\hat{G}(k, i\omega_n) &= \frac{1}{\Theta} [i\omega_n Z \mathbb{I} + (\varepsilon_k + \chi)\sigma_3 + \phi\sigma_1 + \bar{\phi}\sigma_2] = \\ &\frac{1}{\Theta} \begin{pmatrix} i\omega_n Z + (\varepsilon_k - \mu + \chi) & \phi - i\bar{\phi} \\ \phi + i\bar{\phi} & i\omega_n Z - (\varepsilon_k - \mu + \chi) \end{pmatrix}\end{aligned}\quad (\text{A.29})$$

where,

$$\Theta = (i\omega_n Z)^2 - (\varepsilon_k - \mu + \chi)^2 - \phi^2 - \bar{\phi}^2 \quad (\text{A.30})$$

The importance of the Eliashberg theory lies in its validity in the normal state [129] where \hat{G} is diagonal. In that case, ϕ and $\bar{\phi}$ vanish and Z and χ are determined by the normal state self-energy. χ shifts electronic energies and Z is a renormalization function.

From the Green function we have that the poles, the electrons (and holes) elementary excitations are given by:

$$E_k = \sqrt{\left(\frac{\varepsilon_k - \mu + \chi}{Z}\right)^2 + \left(\frac{\phi + \bar{\phi}}{Z}\right)^2} \quad (\text{A.31})$$

And then the gap function is:

$$\Delta(k, i\omega_n) = \frac{\phi - i\bar{\phi}}{Z} \quad (\text{A.32})$$

After inserting the Green equation into self-energy and comparing the result with the general expression, we get set of equations for Z , χ , ϕ and $\bar{\phi}$, called the Eliashberg equations:

$$[1 - Z(k, i\omega_n)]i\omega_n = \frac{1}{\beta} \sum_{k', n', \nu} |g_{k, k', \nu}|^2 \frac{i\omega_{n'} Z(k, i\omega_n) D_\nu(k - k', i\omega_n - i\omega_{n'})}{\Theta(k', i\omega_{n'})} \quad (\text{A.33})$$

$$\chi(k, i\omega_n) = \frac{1}{\beta} \sum_{k', n', \nu} |g_{k, k', \nu}|^2 \frac{\chi(k', i\omega_{n'}) + \varepsilon_{k'}}{\Theta(k', i\omega_{n'})} D_\nu(k - k', i\omega_n - i\omega_{n'}) \quad (\text{A.34})$$

$$\begin{aligned}\phi(k, i\omega_n) &= \frac{1}{\beta} \sum_{k', n', \nu} [|g_{k, k', \nu}|^2 D_\nu(k - k', i\omega_n - i\omega_{n'}) - V_C(k - k')] \frac{\phi(k', i\omega_{n'})}{\Theta(k', i\omega_{n'})} \\ &\quad (\text{A.35})\end{aligned}$$

A. APPENDIX

$$\bar{\phi}(k, i\omega_n) = -\frac{1}{\beta} \sum_{k', n', \nu} [|g_{k, k', \nu}|^2 D_\nu(k - k', i\omega_n - i\omega_{n'}) - V_C(k - k')] \frac{\bar{\phi}(k', i\omega_{n'})}{\Theta(k', i\omega_{n'})} \quad (\text{A.36})$$

With addition of one more equation that represents the electron number equation and determines the chemical potential μ :

$$n = 1 - \frac{2}{\beta} \sum_{k', n'} \frac{\chi(k', i\omega_{n'}) + \varepsilon_{k'} - \mu}{\Theta(k', i\omega_{n'})} \quad (\text{A.37})$$

For elemental superconductors good approximation is in the averaging of these equations over energy isosurface in k-space and solving it in one dimension. Yet this is not sufficient for more complex systems. We can fix $\bar{\phi} = 0$ and k-dependence in \hat{G} comes mainly from explicit ε_k dependence of θ but it can be averaged out in Z and φ (fixing $\varepsilon_k = E_F$ because they are non-zero only near Fermi surface) and we get:

$$\begin{aligned} Z(k, i\omega_n) &\rightarrow \langle Z(k, i\omega_n) \rangle_{\varepsilon=E_F} = Z(i\omega_n) \\ \phi(k, i\omega_n) &\rightarrow \langle \phi(k, i\omega_n) \rangle_{\varepsilon=E_F} = \phi(i\omega_n) \\ \chi(k, i\omega_n) &\rightarrow \langle \chi(k, i\omega_n) \rangle_{\varepsilon=E_F} = \chi(i\omega_n) \end{aligned} \quad (\text{A.38})$$

We can use the same k average in the right side of the Eliashberg equations by applying an operator

$$\frac{1}{N(0)} \sum_k \delta(\varepsilon_k) \quad (\text{A.39})$$

where $N(0)$ is the normal density of state at the Fermi level and by introducing a unity factor

$$\int d\omega \delta(\omega - \omega_{q,v}) \quad (\text{A.40})$$

where $q = k - k'$ is the phonon wavevector and we get:

$$\begin{aligned} i\omega_n = -\frac{1}{\beta N^2(0)} \sum_{n'} \int d\omega \sum_{k, \nu} \sum_{k'} \frac{|g_{k, k', \nu}|^2 \delta(\varepsilon_{k'}) \delta(\varepsilon_k) \delta(\omega - \omega_{q, \nu}) 2\omega_{q, \nu}}{(\omega_n - \omega'_n)^2 + \omega_{q, \nu}^2} \\ \times \int_{-\infty}^{\infty} d\varepsilon \frac{N(\varepsilon) i\omega_{n'} Z(i\omega_{n'})}{\Theta(\varepsilon, i\omega_{n'})} \end{aligned} \quad (\text{A.41})$$

$$\begin{aligned} \phi(i\omega_n) = \frac{1}{\beta N^2(0)} \sum_{n'} \int d\omega \sum_{k, \nu} \sum_{k'} \frac{|g_{k, k', \nu}|^2 \delta(\varepsilon_{k'}) \delta(\varepsilon_k) \delta(\omega - \omega_{q, \nu}) 2\omega_{q, \nu}}{(\omega_n - \omega'_n)^2 + \omega_{q, \nu}^2} \\ \times \int_{-\infty}^{\infty} d\varepsilon \frac{N(\varepsilon) \phi(i\omega_{n'})}{\Theta(\varepsilon, i\omega_{n'})} \end{aligned} \quad (\text{A.42})$$

A. APPENDIX

$$\chi(i\omega_n) = -\frac{1}{\beta N^2(0)} \sum_{n'} \int d\omega \sum_{k,\nu} \sum_{k'} \frac{|g_{k,k',\nu}|^2 \delta(\varepsilon_{k'}) \delta(\varepsilon_k) \delta(\omega - \omega_{q,\nu}) 2\omega_{q,\nu}}{(\omega_n - \omega'_n)^2 + \omega_{q,\nu}^2} \times \int_{-\infty}^{\infty} d\varepsilon \frac{N(\varepsilon)(\varepsilon - \mu + \chi(i\omega_{n'}))}{\Theta(\varepsilon, i\omega_{n'})} \quad (\text{A.43})$$

$$n = 1 - \frac{2}{\beta N(0)} \sum_{n'} \int_{-\infty}^{\infty} d\varepsilon \frac{N(\varepsilon)[\varepsilon - \mu + \chi(i\omega_{n'})]}{\Theta(\varepsilon, i\omega_{n'})} \quad (\text{A.44})$$

Now we specify always positive-definite function, the electron-boson spectral function:

$$\alpha^2 F(\omega) = N(0) \sum_{q,\nu} g_{q,\nu}^2 \delta(\omega - \omega_{q,\nu}) = \frac{1}{N(0)} \sum_{k,k'} \sum_{\nu} |g_{k,k',\nu}|^2 \delta(\varepsilon_{k'}) \delta(\varepsilon_k) \delta(\omega - \omega_{q,\nu}) \quad (\text{A.45})$$

Where the electron-phonon coupling is:

$$g_{q,\nu}^2 = \frac{1}{N^2(0)} \sum_{k'} |g_{k,k',\nu}|^2 \delta(\varepsilon_{k+q}) \delta(\varepsilon_k) \quad (\text{A.46})$$

After applying this, the Eliashberg equations changes its form to:

$$[1 - Z(i\omega_n)]i\omega_n = -\frac{\pi}{\beta} \sum_{\omega_{n'}} \frac{Z(i\omega_{n'})i\omega_{n'}}{\Xi(i\omega_{n'})} \int d\omega \frac{2\omega\alpha^2 F(\omega)}{(\omega_n - \omega_{n'})^2 + \omega^2} \quad (\text{A.47})$$

$$\phi(i\omega_n) = \frac{\pi}{\beta} \sum_{\omega_{n'}} \frac{\phi(i\omega_{n'})}{\Xi(i\omega_{n'})} \left[\int d\omega \frac{2\omega\alpha^2 F(\omega)}{(\omega_n - \omega_{n'})^2 + \omega^2} - N(0)V_{col} \right] \quad (\text{A.48})$$

$$\Xi(i\omega_n) = \sqrt{[Z(i\omega_n)\omega_n]^2 + [\phi(i\omega_n)]^2} \quad (\text{A.49})$$

V_{col} is Fermi surface average of the V_C . The sum over the Matsubara's frequencies can be cut off at an energy ω_C . After solving these equations, we get the electron self-energy at the Fermi level.

Now we discuss the reduction of the Eliashberg theory to BCS limit where all calculations in this dissertation are performed. We introduce several approximations. The first is that real boson scattering is not taken into account. The next approximation is in setting:

$$\Delta(\omega, T) = \begin{cases} \Delta_0(T) & \text{for } \omega < \omega_D \\ 0 & \text{for } \omega \geq \omega_D \end{cases},$$

A. APPENDIX

Where $\Delta_0(T)$ is real number and ω_D is the Deybe energy. $Z(w, T)$ can be replaced with its form for the normal state at $w=0$ and $T=0$, so we get:

$$Z(0, T) - 1 = 2 \int_0^\infty d\omega' \int_0^\infty d\Omega \alpha^2 F(\Omega) \left[\frac{f(-\omega')}{(\omega' + \Omega)^2} + \frac{f(\omega')}{(\omega' + \Omega)^2} \right] \equiv \lambda(T) \quad (\text{A.50})$$

And for $T \rightarrow 0$ it becomes:

$$Z(0, 0) - 1 = \int_0^\infty d\Omega \alpha^2 F(\Omega) \int_0^\infty \frac{2d\omega'}{(\omega' + \Omega)^2} \equiv \lambda(T) \quad (\text{A.51})$$

The gap equation becomes:

$$\Delta_0(T) = \int_{\delta_o(T)}^{\omega_D} d\omega' \frac{\Delta_0(T)}{\sqrt{\omega'^2 - \Delta_0^2(T)}} \frac{\lambda - \mu}{1 + \lambda} [1 - 2f(\omega')] \quad (\text{A.52})$$

For $\varepsilon = \sqrt{\omega'^2 - \delta_0^2}$ we can rewrite it to the usual BCS equation at finite temperature:

$$\Delta_0(T) = \frac{\lambda - \mu}{1 + \lambda} \int_0^{\omega_D} d\varepsilon \frac{\Delta_0(T)}{\sqrt{\omega'^2 + \Delta_0^2(T)}} \left[1 - 2f(\sqrt{\varepsilon^2 + \Delta_0^2(T)}) \right] \quad (\text{A.53})$$

For $T \rightarrow 0$ we get BCS gap equation as we know:

$$\Delta_0(T) = \frac{\lambda - \mu^*}{1 + \lambda} \int_0^{\omega_C} d\varepsilon \frac{\Delta_0}{\sqrt{\varepsilon^2 + \Delta_0^2}} \quad (\text{A.54})$$

The renormalization factor $1/(1+\lambda)$ comes from the Z term in the Eliashberg equation i.e. the inclusion of electron-phonon interaction. The Eliashberg equation can be solved numerically with the iterative method until convergence is reached.

A.3. Numerical Methods

A.3.1. Derivation of the Hartree-Fock equations

Derivation of the Hartree-Fock equations starts with the case of two electrons in many-body Schrödinger equation:

$$\left[-\int_i \frac{\nabla_i^2}{2} + \sum_i V_n(r_i) + \sum_{i<j} \frac{1}{|r_i - r_j|} \right] \Psi = E\Psi \quad \text{for } N = 2 \quad (\text{A.55})$$

and for the single-electron Hamiltonian

$$\hat{H}_0(r) = -\frac{1}{2}\nabla^2 + V_n(r) \quad (\text{A.56})$$

it can be written as:

$$[\hat{H}_0(\mathbf{r}_1) + \hat{H}_0(\mathbf{r}_2) + \frac{1}{|\mathbf{r}_1 - \mathbf{r}_2|}] \Psi = E\Psi,$$

The single-particle wavefunctions defined by ψ_1 and ψ_2 is:

$$\Psi(\mathbf{r}_1, \mathbf{r}_2) = \frac{1}{\sqrt{2}}[\psi_1(\mathbf{r}_1)\psi_2(\mathbf{r}_2) - \psi_1(\mathbf{r}_2)\psi_2(\mathbf{r}_1)]. \quad (\text{A.57})$$

Ψ is the solution with the lowest energy, E , i.e. the electronic ground state.

In order to find the functions ψ_1 and ψ_2 which minimize the total energy, E is written an explicit functiona of the wavefunctions. Knowing that energy E is:

$$E = \int d\mathbf{r}_1 \dots d\mathbf{r}_N \Psi^* \hat{H} \Psi \quad (\text{A.58})$$

and combining equations 1 and 2 in this expression we get:

$$\begin{aligned} E = & \{\psi_1 | \hat{H}_0 | \psi_1\} \{\psi_2 | \psi_2\} + \{\psi_2 | \hat{H}_0 | \psi_2\} \{\psi_1 | \psi_1\} - \\ & \{\psi_1 | \hat{H}_0 | \psi_2\} \{\psi_2 | \psi_1\} - \{\psi_2 | \hat{H}_0 | \psi_1\} \{\psi_1 | \psi_2\} \\ & + \int d\mathbf{r}_1 d\mathbf{r}_2 \frac{|\psi_1(\mathbf{r}_1)|^2 |\psi_2(\mathbf{r}_2)|^2}{|\mathbf{r}_1 - \mathbf{r}_2|} - \int d\mathbf{r}_1 d\mathbf{r}_2 \frac{\psi_1^*(\mathbf{r}_1) \psi_2^*(\mathbf{r}_2) \psi_1(\mathbf{r}_2) \psi_2(\mathbf{r}_1)}{|\mathbf{r}_1 - \mathbf{r}_2|}, \end{aligned} \quad (\text{A.59})$$

The $\psi_1(\mathbf{r})$ and $\psi_2(\mathbf{r})$ need to be orthonormal and this requirement corresponds to setting:

$$\{\psi_1 | \psi_1\} = \{\psi_2 | \psi_2\} = 1, \quad \text{and} \quad \{\psi_1 | \psi_2\} = \{\psi_2 | \psi_1\} = 0. \quad (\text{A.60})$$

Applying this conditions we get:

$$\begin{aligned} E = & \int d\mathbf{r} \psi_1^*(\mathbf{r}) \hat{H}_0(\mathbf{r}) \psi_1(\mathbf{r}) + \int d\mathbf{r} \psi_2^*(\mathbf{r}) \hat{H}_0(\mathbf{r}) \psi_2(\mathbf{r}) \\ & + \int d\mathbf{r}_1 d\mathbf{r}_2 \frac{\psi_1^*(\mathbf{r}_1) \psi_2^*(\mathbf{r}_2) \psi_1(\mathbf{r}_1) \psi_2(\mathbf{r}_2)}{|\mathbf{r}_1 - \mathbf{r}_2|} - \int d\mathbf{r}_1 d\mathbf{r}_2 \frac{\psi_1^*(\mathbf{r}_1) \psi_2^*(\mathbf{r}_2) \psi_1(\mathbf{r}_2) \psi_2(\mathbf{r}_1)}{|\mathbf{r}_1 - \mathbf{r}_2|}. \end{aligned} \quad (\text{A.61})$$

A. APPENDIX

Since $E = E[\psi_1, \psi_2]$ functional of ψ_1 and ψ_2 and we can find the functions ψ_1 and ψ_2 which minimize this functional. In order to achieve this functional derivatives of E with respect to ψ_1 and ψ_2 should be equal to zero ie.

$$\frac{\delta E}{\delta \psi_1} = 0 \quad \frac{\delta E}{\delta \psi_2} = 0 \quad (\text{A.62})$$

The functional derivative is:

$$\int dr h(r) \frac{\delta F}{\delta g}(r) = \frac{d}{d\epsilon} F[g(r) + \epsilon h(r)] \Big|_{\epsilon=0} \quad (\text{A.63})$$

Using the method of Lagrange multipliers we make sure constraints (A.62) are fulfilled. We introduce a new functional which automatically incorporates the constraints:

$$L[\psi_1, \psi_2, \lambda_{11}, \dots, \lambda_{22}] = E[\psi_1, \psi_2] - \sum_{ij} \lambda_{ij} [\langle \psi_i | \psi_j \rangle - \delta_{ij}], \quad (\text{A.64})$$

where the Lagrange multipliers $\lambda_{11}, \lambda_{12}, \lambda_{21}$ and λ_{22} should be calculated. For constraints to be fulfilled it is necessary for L and λ to be:

$$\begin{aligned} \frac{\delta L}{\delta \psi_i} &= 0, i = 1, 2, \\ \frac{\delta L}{\delta \lambda_{ij}} &= 0, \quad i, j = 1, 2. \end{aligned} \quad (\text{A.65})$$

The Hamiltonian is Hermitian and it allows ψ_i and ψ_i^* , (though they are not independent) to be effectively be treated as independent and we calculate functional derivative of each term of (A.63). Beginning with the first term of equation and using expression (A.65), we get:

$$G = \int dr \psi_1^*(r) \hat{H}_0(r) \psi_1(r) \quad (\text{A.66})$$

$$\int dr h(r) \frac{\delta G}{\delta \psi_1^*} = \frac{d}{d\epsilon} \int dr [\psi_1^*(r) + \epsilon h(r)] \hat{H}_0(r) \psi_1(r) = \int dr h(r) \hat{H}_0(r) \psi_1(r) . \quad (\text{A.67})$$

$$\frac{\delta G}{\delta \psi_1^*} = \hat{H}_0(r) \psi_1(r) . \quad (\text{A.68})$$

For the second term of equation and using expression (A.65) we get:

$$I = \int dr \psi_2^*(r) \hat{H}_0(r) \psi_2(r) \quad (\text{A.69})$$

A. APPENDIX

$$\int dr h(r) \frac{\delta I}{\delta \psi_2^*} = \frac{d}{d\epsilon} \int dr [\psi_2^*(r) + \epsilon h(r)] \hat{H}_0(r) \psi_2(r) = \int dr h(r) \hat{H}_0(r) \psi_2(r) . \quad (\text{A.70})$$

$$\frac{\delta I}{\delta \psi_2^*} = \hat{H}_0(r) \psi_2(r) . \quad (\text{A.71})$$

and so on...

Applying this procedure to all terms of the equation (A.63) and then conditions (A.66) we get:

$$\begin{aligned} \frac{\delta L}{\delta \psi_1^*} &= \hat{H}_0(r) \psi_1(r) + \int dr' \frac{|\psi_2(r')|^2}{|r-r|} \psi_1(r) - \int dr' \frac{\psi_2^*(r') \psi_2(r)}{|r-r|} \psi_1(r') - \lambda_{11} \psi_1(r) - \\ &\quad \lambda_{12} \psi_2(r) \cdot \frac{\delta L}{\delta \psi_2^*} = \\ \hat{H}_0(r) \psi_2(r) + \int dr' \frac{|\psi_1(r')|^2}{|r-r|} \psi_2(r) - \int dr' \frac{\psi_1^*(r') \psi_1(r)}{|r-r|} \psi_2(r') - \lambda_{21} \psi_1(r) - \lambda_{22} \psi_2(r) \cdot \frac{\delta L}{\delta \lambda_{ij}} &= \\ &\quad \delta_{ij} - \{\psi_i | \psi_j\} \quad \text{for any } i, j=1,2. \end{aligned} \quad (\text{A.72})$$

By setting all these derivatives to zero we obtain the conditions that the functions ψ_1 and ψ_2 have to satisfy in order to minimize the energy:

$$\hat{H}_0(r) \psi_1(r) + \int dr' \frac{|\psi_2(r')|^2}{|r-r|} \psi_1(r) - \int dr' \frac{\psi_2^*(r') \psi_2(r)}{|r-r|} \psi_1(r') = \lambda_{11} \psi_1(r) + \lambda_{12} \psi_2(r) \quad (\text{A.73})$$

$$\hat{H}_0(r) \psi_2(r) + \int dr' \frac{|\psi_1(r')|^2}{|r-r|} \psi_2(r) - \int dr' \frac{\psi_1^*(r') \psi_1(r)}{|r-r|} \psi_2(r') = \lambda_{21} \psi_1(r) + \lambda_{22} \psi_2(r) \quad (\text{A.74})$$

$$\int dr \psi_i^*(r) \psi_j(r) = \delta_{ij} \text{ for any } i, j=1,2. \quad (\text{A.75})$$

If we set:

$$V_H(r) = \sum_j \int dr' \frac{|\psi_j(r')|^2}{|r-r|}, \quad (\text{A.76})$$

$$V_X(r, r') = - \sum_j \frac{\psi_j^*(r') \psi_j(r)}{|r-r|}, \quad (\text{A.77})$$

with $j = 1, 2$ and return it to equations (A.73) and (A.74) we get:

A. APPENDIX

$$\left[-\frac{\nabla^2}{2} + V_n(r) + V_H(r)\right]\psi_1(r) + \int dr' V_X(r, r')\psi_1(r') = \lambda_{11}\psi_1(r) + \lambda_{12}\psi_2(r) \quad (\text{A.78})$$

$$\left[-\frac{\nabla^2}{2} + V_n(r) + V_H(r)\right]\psi_2(r) + \int dr' V_X(r, r')\psi_2(r') = \lambda_{21}\psi_1(r) + \lambda_{22}\psi_2(r) \quad (\text{A.79})$$

To eliminate one of the two functions on the right-hand side of both equations we introducing a 2×2 matrix, S , which diagonalizes the Lagrange multipliers:

$$\begin{pmatrix} \lambda_{11} & \lambda_{12} \\ \lambda_{21} & \lambda_{22} \end{pmatrix} S^{-1} = \begin{pmatrix} \epsilon_1 & 0 \\ 0 & \epsilon_2 \end{pmatrix} \quad (\text{A.80})$$

Since the Hamiltonian, \hat{H} , is Hermitian, the Lagrange multipliers are also Hermitian, i.e. $\lambda_{ij}^* = \lambda_{ji}$ making S a unitary matrix and the eigenvalues ϵ_1, ϵ_2 real numbers.

Now define new wavefunctions, ϕ_1 and ϕ_2 , as follows:

$$\phi_i = \sum_j S_{ij}\psi_j,$$

we can rewrite equations (A.73) and (A.74) as:

$$\left[-\frac{\nabla^2}{2} + V_n(r) + V_H(r)\right]\phi_1(r) + \int dr' V_X(r, r')\phi_1(r') = \epsilon_1\phi_1(r) \quad (\text{A.81})$$

$$\left[-\frac{\nabla^2}{2} + V_n(r) + V_H(r)\right]\phi_2(r) + \int dr' V_X(r, r')\phi_2(r') = \epsilon_2\phi_2(r) \quad (\text{A.82})$$

Because of the fact S is a unitary matrix it makes the orthonormality condition for ϕ_1 and ϕ_2 , as:

$$\int dr \phi_i^*(r)\phi_j(r) = \delta_{ij} \quad \text{for } i, j=1,2 \quad (\text{A.83})$$

And Hartree and exchange potentials are:

$$V_H(r) = \sum_j \int dr' \frac{|\phi_j(r')|^2}{|r - r'|}, \quad (\text{A.84})$$

$$V_X(r, r') = - \sum_j \frac{\phi_j^*(r')\phi_j(r)}{|r - r'|} \quad (\text{A.85})$$

This way we obtained the Hartree-Fock equations.

A.3.2. Proof of the first HK Theorem

We suppose two external potentials V_1^{ext} and V_2^{ext} and they differ by more than a constant and give rise to the same electron density $n(r)$. This two potentials are associated with two Hamiltonians, H_1 and H_2 , and wavefunctions Φ_1 and Φ_2 , respectively. According to the variationaal principle, only ground state wavefunction gives the lowest energy, such that:

$$E_1 = \langle \Phi_1 | \hat{H}_1 | \Phi_1 \rangle < \langle \Phi_2 | \hat{H}_1 | \Phi_2 \rangle \quad (\text{A.86})$$

Assuming non-degenerate ground state, this statement strictly holds. As the two Hamiltonians are related to an identical ground state density, there is:

$$\langle \Phi_2 | \hat{H}_1 | \Phi_2 \rangle = \langle \Phi_2 | \hat{H}_2 | \Phi_2 \rangle + \langle \Phi_2 | \hat{H}_1 - \hat{H}_2 | \Phi_2 \rangle = E_2 + \int [V_1^{ext}(r) - V_2^{ext}(r)] n(r) dr \quad (\text{A.87})$$

The same goes for:

$$\langle \Phi_1 | \hat{H}_2 | \Phi_1 \rangle = E_1 + \int [V_2^{ext}(r) - V_1^{ext}(r)] n(r) dr \quad (\text{A.88})$$

When we add those two expressions, we get:

$$E_1 + E_2 < E_2 + E_1 \quad (\text{A.89})$$

Which is nonsense and thus we have proven that for external potential V , there is a single ground state.

A.3.3. Proof of the second HK Theorem

Supposing there is $n(r)$, an electron density other than the ground state one, associated to the wavefunction Φ . By using the variational principle for the wavefunction, there is:

$$E[n] = \langle \Phi | \hat{H} | \Phi \rangle < \langle \Phi' | \hat{H} | \Phi' \rangle = E[n'] \quad (\text{A.90})$$

Therefore the evaluation of $E[n]$ at the ground state electron density yields the lowest energy value. Although HK theorems put particle density $n(r)$ as the basic variable, it is still impossible to calculate any property of a system because the universal functional $F[n(r)]$ is unknown. This difficulty was overcome by Kohn and Sham [206] in 1965, who proposed the well-known Kohn-Sham scheme.

A.3.4. Derivation of the Kohn-Sham equations

From the Hohenberg-Kohn theorem we know that the total energy, E , in the electronic ground state is a functional of the electron charge density, $n(\mathbf{r})$, $E = F[n]$.

In the Kohn-Sham approach the functional F is decomposed as :

$$E = F[n] = \int d\mathbf{r} n(\mathbf{r})V_n(\mathbf{r}) - \sum_i \int d\mathbf{r} \phi_i^*(\mathbf{r}) \frac{\nabla^2}{2} \phi_i(\mathbf{r}) + \frac{1}{2} \int \int d\mathbf{r} d\mathbf{r}' \frac{n(\mathbf{r})n(\mathbf{r}')}{|\mathbf{r} - \mathbf{r}'|} + E_{xc}[n] \quad (\text{A.91})$$

The first term is the external potential that describes interaction of the electrons with the nuclei, the second is kinetic energy, the third is Hartree energy and the fourth is exchange-correlation energy. The index i runs over N wavefunctions

The density, $n(\mathbf{r})$, is expressed in terms of the Kohn-Sham wavefunction as:

$$n(\mathbf{r}) = \sum_i |\psi_i(\mathbf{r})|^2 \quad (\text{A.92})$$

From the Hohenberg-Kohn theorem it is known that the total energy, E , reaches its minimum value in correspondence with the ground-state electron density. This can be expressed using a functional derivative as:

$$\frac{\delta F}{\delta n} = 0 \quad (\text{A.93})$$

Functional derivative is:

$$\int d\mathbf{r} h(\mathbf{r}) \frac{\partial F}{\partial g}(\mathbf{r}) = \left. \frac{d}{d\epsilon} F[g(\mathbf{r}) + \epsilon h(\mathbf{r})] \right|_{\epsilon=0} \quad (\text{A.94})$$

We apply the chain rule to the functional derivative of F with respect to any of the wavefunctions, ψ_i^* , and we get:

$$\frac{\delta F}{\delta \psi_i^*} = \frac{\delta F}{\delta n} \frac{\delta n}{\delta \psi_i^*} = \frac{\delta F}{\delta n} \psi_i, \quad (\text{A.95})$$

The derivatives with respect to ψ_i or ψ_i^* can be treated as independent. By combining above two equations, we see that the Kohn-Sham orbitals must satisfy:

$$\frac{\delta F}{\delta \psi_i^*} = 0 \quad (\text{A.96})$$

The Kohn-Sham wavefunctions must satisfy the orthonormality constraints as:

$$\{\psi_i | \psi_j\} = \delta_{ij}, \quad (\text{A.97})$$

A. APPENDIX

which guarantees that the density we defined in the beginins, is correctly normalized to N electrons. This is the problem of constrained minimization and as shown in derivation of Hartree-Fock equation we use the method of Lagrange multipliers.

$$L = F - \sum_{ij} \lambda_{ij} [\{\psi_i | \psi_j\} - \delta_{ij}], \quad (\text{A.98})$$

with λ_{ij} the Lagrange multipliers.

$$\frac{\delta L}{\delta \psi_i^*} = 0 \rightarrow \frac{\delta F}{\delta \psi_i^*} = \sum_j \lambda_{ij} \psi_j. \quad (\text{A.99})$$

The functional derivatives $\delta F / \delta \psi_i^*$ is:

$$-\frac{\nabla^2}{2} \psi_i(\mathbf{r}) + \frac{\delta}{\delta n} \left\{ \int d\mathbf{r} n(\mathbf{r}) V_n(\mathbf{r}) + \frac{1}{2} \iint d\mathbf{r} d\mathbf{r}' \frac{n(\mathbf{r}) n(\mathbf{r}')}{|\mathbf{r} - \mathbf{r}'|} + E_{xc}[n] \right\} \psi_i(\mathbf{r}) = \sum_j \lambda_{ij} \psi_j(\mathbf{r}). \quad (\text{A.100})$$

By using the definition of functional derivative this equation can be written:

$$\left[-\frac{\nabla^2}{2} + V_n(\mathbf{r}) + \int d\mathbf{r}' \frac{n(\mathbf{r}')}{|\mathbf{r} - \mathbf{r}'|} + \frac{\delta E_{xc}}{\delta n} \right] \psi_i(\mathbf{r}) = \sum_j \lambda_{ij} \psi_j(\mathbf{r}) \quad (\text{A.101})$$

The third term is the Hartree potential, $V_H(\mathbf{r})$, and the fourt is exchange and correlation potential, $V_{xc}(\mathbf{r})$. The matrix λ_{ij} of the Lagrange multipliers can be diagonalized. Introducing the 2x2 matrix, that diagonalize Lagrange multipliers as:

$$\begin{pmatrix} \lambda_{11} & \lambda_{12} \\ \lambda_{21} & \lambda_{22} \end{pmatrix} S^{-1} = \begin{pmatrix} \epsilon_1 & 0 \\ 0 & \epsilon_2 \end{pmatrix} \quad (\text{A.102})$$

The Hamiltonian, \hat{H} , is Hermitian, the Lagrange multipliers are also Hermitian, i.e. $\lambda_{ij}^* = \lambda_{ji}$ making S a unitary matrix.

We define wavefunctions, ϕ_1 and ϕ_2 , as follows:

$$\phi_i = \sum_j S_{ij} \psi_j,$$

we can rewrite equations above and obtain Kohn-Sham equations:

$$\left[-\frac{1}{2} \nabla^2 + V_n(\mathbf{r}) + V_H(\mathbf{r}) + V_{xc}(\mathbf{r}) \right] \phi_i(\mathbf{r}) = \epsilon_i \phi_i(\mathbf{r}) \quad (\text{A.103})$$

B. Quantum ESPRESSO inputs

In this appendix are presented the most relevant inputs for Quantum Espresso calculations of doped graphene. Here are presented inputs for the run for electron-phonon interaction, superconductivity and phonon dispersion and dos in LiC₆-mono. Other calculations (Ba, Ca-doped graphene) are made according to this model.

B.1. Li-doped graphene

QE run: Superconductivity in LiC₆.

1. SCF run on fine grid of kpoints:

```
mpirun np -8 /home/...path-to-qe-directroy.../bin/pw.x <lic6.scf.fine.in>  
lic6.scf.fine.out
```

```
&control  
  calculation= 'scf',  
  restart_mode='from_scratch',  
  prefix= 'lic6',  
  pseudo_dir = './',  
  outdir = './',  
  tstress = .true.,  
  tprnfor = .true.,  
  verbosity= 'high',  
  wf_collect= .true.,  
/  
&system  
  ibrav = 4, celldm(1)=8.05, celldm(3)=2.8,  
  nat= 7, ntyp= 2,  
  ecutwfc = 65,  
  occupations = "smearing",  
  smearing = "fd",
```

B. Quantum ESPRESSO inputs

```
degauss      = 0.01,
la2F=.true.,
/
&electrons
  mixing_beta = 0.7
  conv_thr = 1.0d-12
/
&IONS
  ion_dynamics = 'bfgs',
/
&CELL
  cell_dynamics = 'bfgs',
/
ATOMIC_SPECIES
Li  6.914      Li.pz-n-vbc.UPF
C   12.0107    C.pz-vbc.UPF
ATOMIC_POSITIONS {crystal}
Li      0.666666667  0.666666660  0.143500000
C       0.000090063  0.000090063  0.001279709
C       0.666666667  0.000090063  0.001279709
C       0.333243270  0.333243270  0.001279709
C       0.666666667  0.333243270  0.001279709
C       0.000090063  0.666666667  0.001279709
C       0.333243270  0.666666667  0.001279709
K_POINTS AUTOMATIC
48 48 1 0 0 0
```

2. SCF calculation on the coarse grid of kpoints:

```
mpirun np -8 /home/...path-to-qe-directroy.../bin/pw.x <lic6.scf.in>
      lic6.scf.out
```

```
&control
  calculation= 'scf',
  restart_mode='from_scratch',
  prefix= 'lic6',
  pseudo_dir = './',
  outdir = './',
```

B. Quantum ESPRESSO inputs

```
tstress = .true.,
tprnfor = .true.,
verbosity= 'high',
wf_collect= .true.,
/
&system
ibrav = 4, celldm(1)=8.05, celldm(3)=2.8,
nat= 7, ntyp= 2,
ecutwfc = 65,
occupations = "smearing",
smearing    = "fd",
degauss     = 0.01,
/
&electrons
mixing_beta = 0.7
conv_thr = 1.0d-12
/
&IONS
ion_dynamics = 'bfgs',
/
&CELL
cell_dynamics = 'bfgs',
/
ATOMIC_SPECIES
Li  6.914      Li.pz-n-vbc.UPF
C   12.0107    C.pz-vbc.UPF
ATOMIC_POSITIONS {crystal}
Li      0.666666667  0.666666660  0.143500000
C       0.000090063  0.000090063  0.001279709
C       0.666666667  0.000090063  0.001279709
C       0.333243270  0.333243270  0.001279709
C       0.666666667  0.333243270  0.001279709
C       0.000090063  0.666666667  0.001279709
C       0.333243270  0.666666667  0.001279709
K_POINTS AUTOMATIC
24 24 1 0 0 0
```

B. Quantum ESPRESSO inputs

3. PHonon run on the q-points grid with "electron_phonon= interpolated"

```
mpirun np -8 /home/...path-to-qe-directroy.../bin/ph.x <lic6.ph.in>
    lic6.ph.out
```

Electron-phonon coefficients for LiC\$_6\$-monolayer

```
&inputph
  prefix= 'lic6',
  tr2_ph=1.0d-15,
  fildvscf='lic6fildvscf',
  amass(1)=6.914,
  amass(2)=12.0107,
  outdir='./',
  fildyn='lic6.dyn',
  electron_phonon= 'interpolated',
  trans=.true.,
  ldisp=.true.
  nq1=24, nq2=24, nq3=1
/
```

4. q2r.x reads the dynamical matrices produced in the preceding step and Fourier-transform them, writing a file of Interatomic Force Constants in real space

```
mpirun np -8 /home/...path-to-qe-directroy.../bin/q2r.x <q2r.in> q2r.out
```

```
&INPUT
  zasr= 'crystal',
  fildyn= 'lic6.dyn',
  flfrc='lic6.fc',
  la2F= .true.
/
```

4. matdyn produce phonon modes and frequencies at any q using the Interatomic Force Constants file as input

a) phonon dos:

```
mpirun np -8 /home/...path-to-qe-directroy.../matdyn.x <matdyn.dos.in>
    matdyn.dos.out
```

B. Quantum ESPRESSO inputs

&INPUT

```
asr= 'crystal',
amass(1)= 6.914,
amass(2)= 12.0107,
flfrc= 'lic6.fc',
flfrq= 'lic6.freq',
dos= .true.,
fldos= 'phonon.dos',
la2F= .true.,
nk1=16, nk2=16, nk3=1, ndos=500
```

/

b) phonon dispersion:

```
mpirun np -8 /home/...path-to-qe-directroy.../bin/matdyn.x
<matdyn.freq.in> matdyn.freq.out
```

&INPUT

```
asr= 'simple',
amass(1)= 6.914 ,
amass(2)= 12.0107,
flfrc= 'lic6.fc',
flfrq= 'lic6.freq',
dos= .false.,
```

/

200

```
0.0000000 0.0000000 0.0000000 0.0
0.0068493 0.0039545 0.0000000 0.0
0.0136986 0.0079089 0.0000000 0.0
```

...

.....

/

5. Using `lambda.x` we calculate α^2F function, the electron-phonon coefficient λ and an estimate of the critical temperature T_c

```
/home/\textit{...path-to-qe-directroy...}/lambda.x <lambda.in> lambda.out
```

B. Quantum ESPRESSO inputs

```

50 0.12 1
    10
    0.0000000 0.0000000 0.0000000 1.00
    0.1250000 0.0721688 0.0000000 6.00
    0.2500000 0.1443376 0.0000000 6.00
    0.3750000 0.2165064 0.0000000 6.00
    0.5000000 0.2886751 0.0000000 3.00
    0.1250000 0.2165064 0.0000000 6.00
    0.2500000 0.2886751 0.0000000 12.00
    0.3750000 0.3608439 0.0000000 12.00
    0.2500000 0.4330127 0.0000000 6.00
    0.3750000 0.5051815 0.0000000 6.00
    elph. 0.000000. 0.000000. 0.000000
    elph. 0.000000. 0.144338. 0.000000
    elph. 0.000000. 0.288675. 0.000000
    elph. 0.000000. 0.433013. 0.000000
    elph. 0.000000.-0.577350. 0.000000
    elph. 0.125000. 0.216506. 0.000000
    elph. 0.125000. 0.360844. 0.000000
    elph. 0.125000. 0.505181. 0.000000
    elph. 0.250000. 0.433013. 0.000000
    elph. 0.250000. 0.577350. 0.000000

0.112

! INPUT from standard input:
!   emax degaussq ngaussq
!   nks
!   q(1,1)  q(2,1)  q(3,1)  wk(1)
!   ...      ...      ...      ...
!   q(1,nks) q(2,nks) q(3,nks) wk(nks)
!   filelph(1)
!   ...
!   filelph(nks)
!
! emax (THz) : alpha2F is plotted from 0 to "emax" in "nex" steps
! degaussq (THz): gaussian smearing for sum over q

```

B. Quantum ESPRESSO inputs

```
!           NB: not the same used in phonon !
! ngaussq   : 0 for simple gaussian, 1 for Methfessel-Paxton etc.
! nks       : number of q-points used in the sum
! q, wk     : q-points and weights
! filelph   : output files from phonon, one for each q-point
!           May contain "nsig" calculations done with different
!           broadenings for the sum over k - all of them are used
!
```

CV and list of publications

Jelena Pešić je diplomirala na Fizičkom Fakultetu, Univerzitet u Beogradu u Januaru 2013 sa diplomskim radom "Primena GPU programiranja u DFT propačunima" mentor, Radoš Gajić. Upisla je doktorske studije na Fizičkom Fakultetu u užoj naučnoj oblasti "Fizika kondenzovane materije i statistička fizika". Od novembra 2013. godine Jelena Pešić je zaposlena na Insitutu za Fiziku Beograd, u Laboratoriji za grafen i druge dvodimenzione materijale u okviru Centra za Fiziku Čvrstog Stanja i Nove Materijale. Izabrana je za istraživača saradnika u decembru 2014. Tema doktorske disertacije Jelena Pešić je "Istraživanje superprovodnosti u grafenu i sličnim materijalima koriscenjem ab-initio metoda" koji radi pod supervizijom Prof. dr. Radoša Gajića. Za vreme doktorskih studija Jelena Pešić je učestvovala u tri projekta madjunarodne saradnje: bilateralni projekar sa NR Kinom, bilateralni projekat sa Austrijom i projekat Texas A & M Univerziteta u Katru. Tokom 2015. Jelena Pešić je učestvovala i na bilateralnom projektu sa Nemačkom i Univerzitetom u Potsdamu. U Januaru 2017 je pohađjala školu "Advanced Workshop on High-Performance & High-Throughput Materials Simulations using Quantum ESPRESSO" u Internacionalnom Centru za Teorijsku Fiziku u Trstu, Italija. Tokom doktoskih studija Jelena je učestvovala u saradnji sa Johannes Kepler Univerzitetom u Lincu, Austrija, sa Zentrum fr Oberflächen- und Nanoanalytik koji vodi Prof. dr. Kurt Hingerl. Pored teorijskog istraživanja ima i eksperimentalna zaduženja u Laboratoriji za grafen. Bavi se mehaničkom eksfolijacijom grafena i drugih Van der Waals materijala. U periodu 2014-2015 ucestvovala je u inovacionom projektu Ministarstva Prosvete, Nauke i Tehnološkog Razvoja Republike Srbije, koji je istraživao korišćenje tečne disperzije grafena kao mastila za štampanu elektroniku.

LIST OF PUBLICATIONS

- **Pešić J.** , Gajić R., Hingerl K. and Belić M., "*Strain-enhanced superconductivity in Li-doped graphene*", EPL 108 67005 (2014)
- **Pešić J.**, and R. Gajić. "*Advantages of GPU technology in DFT calculations of intercalated graphene*" Phys. Scr.T162 014027 (2014)
- **Pešić J.**, Damljanović V., Gajić R., Hingerl K. and Belić M., "*Density functional theory study of phonons in graphene doped with Li, Ca and Ba*", EPL, 112 6 67006 (2015)
- **Pešić J.** and Gajić R., "*Ab-initio study of the optical properties of the Li-intercalated graphene and MoS₂*", Opt Quant Electron, 48:368 (2016)
- **Pešić J.**, Popov I., Damljanović V., , Hingerl K., Belić M. and Gajić R. "*Ab-Initio Study of Superconductivity in Magnesium-Diboride Monolayer*", EPL, in press, (2017).
- **Pešić J.**, and R. Gajić, "*GPU accelerations in DFT codes in 2D-materials research*" in press, 2017.
- Prinz, J., Matković, A., **Pešić J.**, Gajić, R. and Bald, I, "*Hybrid Structures for Surface-Enhanced Raman Scattering: DNA Origami/Gold Nanoparticle Dimer/Graphene*" Small, doi:10.1002/sml.201601908 (2016)
- Tomašević-Ilić T., **Pešić J.**, Milošević I., Vujin J., Matković A., Spasenović M., Gajić R. "*Transparent and conductive films from liquid phase exfoliated graphene*", Opt. Quant. Electron. 48:319 (2016)
- Matković A., Milošević I., Milićević M., Tomašević-Ilić T., **Pešić J.**, Musić M., Spasenović M., Jovanović , Vasić B., Deeks C., Panajotović R., Belić M. and Gajić R., "*Enhanced sheet conductivity of Langmuir-Blodgett assembled graphene thin films by chemical doping*" 2D Mater. 3 015002 (2016)
- Matković A., Vasić B., **Pešić J.**, Prinz J., Bald I., Milosavljević A. and Gajić R., "*Enhanced structural stability of DNA origami nanostructures by graphene encapsulation*", New J. Phys. 18 025016 (2016)

CONFERENCES AND SCHOOLS:

- January 2017 "Advanced Workshop on High-Performance & High-Throughput Materials Simulations using Quantum ESPRESSO" , ICTP, Trieste, Italy
- January 2017 "18th International Workshop on Computational Physics and Materials Science: Total Energy and Force Methods" ICTP, Trieste, Italy
Poster presentation: *"Enhancement of electron-phonon coupling in alkali-doped graphene and thin MgB_2 layers"*
- September 2015 "Symposium on Condensed Matter Physics", Belgrade, Serbia
Poster presentation: *"Density Functional Theory Study of Li and Ti-Intercalated Graphene"*
- August 2015 Photonica 2015 Belgrade, Serbia
Poster presentation: *"Ab-initio study of optical properties of alkali metal-intercalated graphene and MoS_2 "*
- July 2014 - "10 years from the discovery of graphene" Summer School, Patras, Greece
Poster presentation: *"Density Functional Theory Study of Phonons in mono and bilayer intercalated graphene"*
- December 2013 Thirteenth Young Researchers Conference - Materials Science and Engineering Belgrade, Serbia
Presentation: *"First principle calculation of phonons and electron-phonon interaction in graphene"*
- August 2013 Photonica 2013 Belgrade, Serbia
Poster presentation: *"Advantages of GPU technology on the DFT calculations on Intercalated Graphene"*

Прилог 1.

Изјава о ауторству

Потписани-а _____

број уписа D-37/2012 _____

Изјављујем


да је докторска дисертација под насловом

ab-initio

- резултат сопственог истраживачког рада,
- да предложена дисертација у целини ни у деловима није била предложена за добијање било које дипломе према студијским програмима других високошколских установа,
- да су резултати коректно наведени и
- да нисам кршио/ла ауторска права и користио интелектуалну својину других лица.

Потпис докторанда

У Београду, 22. 11. 2017.



Прилог 2.

**Изјава о истоветности штампане и електронске
верзије докторског рада**

Име и презиме аутора _____

Број уписа D-37/2012

Студијски програм _____

Наслов рада _____

ab-initio

Потписани _____

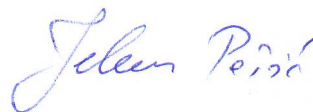
изјављујем да је штампана верзија мог докторског рада истоветна електронској верзији коју сам предао/ла за објављивање на порталу **Дигиталног репозиторијума Универзитета у Београду**.

Дозвољавам да се објаве моји лични подаци везани за добијање академског звања доктора наука, као што су име и презиме, година и место рођења и датум одбране рада.

Ови лични подаци могу се објавити на мрежним страницама дигиталне библиотеке, у електронском каталогу и у публикацијама Универзитета у Београду.

Потпис докторанда

У Београду, 22. 11. 2017.



Прилог 3.

Изјава о коришћењу

Овлашћујем Универзитетску библиотеку „Светозар Марковић“ да у Дигитални репозиторијум Универзитета у Београду унесе моју докторску дисертацију под насловом:

ab-initio

која је моје ауторско дело.

Дисертацију са свим прилозима предао/ла сам у електронском формату погодном за трајно архивирање.

Моју докторску дисертацију похрањену у Дигитални репозиторијум Универзитета у Београду могу да користе сви који поштују одредбе садржане у одабраном типу лиценце Креативне заједнице (Creative Commons) за коју сам се одлучио/ла.

① Ауторство

- 2. Ауторство - некомерцијално
- 3. Ауторство – некомерцијално – без прераде
- 4. Ауторство – некомерцијално – делити под истим условима
- 5. Ауторство – без прераде
- 6. Ауторство – делити под истим условима

(Молимо да заокружите само једну од шест понуђених лиценци, кратак опис лиценци дат је на полеђини листа).

У Београду, 22. 11. 2017.

Потпис докторанда

